Evaluation of Scour around Isolated and Two Circular Piers using Semi-Empirical and Machine Learning Approaches

Thesis Submitted by

BUDDHADEV NANDI

Index No.: D-7/ISLM/124/19

Doctor of Philosophy (Engineering)

School of Water Resources Engineering

Faculty of Interdisciplinary Studies, Law & Management

Jadavpur University

Kolkata, India

2025

Dedicated to the loving memory of My Mother and Grand Mother

JADAVPUR UNIVERSITY
KOLKATA – 700 032, INDIA

INDEX NO.: **D-7/ISLM/124/19**

Title of Thesis:

Evaluation of Scour around Isolated and Two Circular Piers using Semi-Empirical and Machine Learning Approaches

Name, Designation & Institution of the Supervisors

Dr. Subhasish Das
Associate Professor and Joint Director
School of Water Resources Engineering
Jadavpur University
Kolkata 700 032, West Bengal, India

Dr. Rajib Das
Assistant Professor
School of Water Resources Engineering
Jadavpur University
Kolkata 700 032, West Bengal, India

Publications

1. List of journal Publications

- Nandi, B., and Das, S. (2025). Predicting Max Scour Depths near Two-Pier Groups Using Ensemble Machine-Learning Models and Visualizing Feature Importance with Partial Dependence Plots and SHAP. ***Journal of Computing in Civil Engineering***, ASCE, *39*(2), 04025007. https://doi.org/10.1061/JCCEE5/CPENG-6150. (Q1, SCIE, Scopus)
- Nandi, B., and Das, S. (2025). Developing new equations for maximum scour depth near tandem, side-by-side, and eccentric piers. ***Canadian Journal of Civil Engineering***. (Manuscript in second revision) (Q3, SCIE, Scopus).
- Nandi, B., Patel, G. and Das, S. (2024). Prediction of maximum scour depth at clear water conditions: Multivariate and robust comparative analysis between empirical equations and machine learning approaches using extensive reference metadata. ***Journal of Environmental Management***, Elsevier, *354*(3), 120349. https://doi.org/10.1016/j.jenvman.2024.120349 (Q1, SCIE, Scopus)
- Nandi, B., and Das, S. (2023). Identify most promising temporal scour depth formula for circular piers proposed over last six decades. ***Ocean Engineering***, Elsevier, *286*, 115639. https://doi.org/10.1016/j.oceaneng.2023.115639. (Q1, SCIE, Scopus)

2. List of conference publications

- Nandi, B., Das, S., Paul, S. (2025). Estimation of Clear Water Flow Induced Maximum Scour Depth Using Random Forest and XGBoost. In: *Mukhopadhyay, A., Ghosh, K. (eds) Advances in Thermo-Fluid Engineering. INCOM 2024. Lecture Notes in Mechanical Engineering. Springer, Singapore.* https://doi.org/10.1007/978-981-97-7296-4_6.
- Nandi, B., and Das, S. (2024). Estimation of clear water maximum scour depth at eccentric pier using light gradient boosting machine and random forest regressor. Sustainable Materials, Environment and Technologies under climate change scenario (SMET-2024) 25-27 July 2024, NIT Kurukshetra. Haryana, India.
- Nandi, B., Sasmal, K. and Das, S. (2024). Evolution of Four Formulae Derived Over Five Decades to Predict Temporal Scour at Circular Pier. In: *Swain, B.P., Dixit, U.S. (eds) Recent Advances in Civil Engineering. ICSTE 2023. Lecture Notes in Civil Engineering, vol 431, pp. 131-139. Springer, Singapore.* https://doi.org/10.1007/978-981-99-4665-5_14.

PROFORMA – 1

"Statement of Originality"

I, **Buddhadev Nandi** (D-7/ISLM/124/19) registered on **07th November 2019**, do hereby declare that this thesis entitled "**Evaluation of Scour around Isolated and Two Circular Piers using Semi-Empirical and Machine Learning Approaches**" contains literature survey and original research work done by the undersigned candidate as part of Doctoral studies.

All information in this thesis have been obtained and presented in accordance with existing academic rules and ethical conduct. I declare that, as required by these rules and conduct, I havefully cited and referred all materials and results that are not original to this work.

I also declare that I have checked this thesis as per the "Policy on Anti Plagiarism, Jadavpur University, 2019", and the level of similarity as checked by iThenticate software is **06**%.

Buddhadev Nandi

Signature of Candidate:

Date: 27.01.2025

Certified by Supervisor(s):(Signature with date, seal)

1. Subhasish Das. 27/01/25

Dr. Subhasish Das
Associate Professor & Joint Director
School of Water Resources Engineering
Jadavpur University
Kolkata - 700032

2. Rajib Das 27/01/2025

Dr. RAJIB DAS
Assistant Professor
School of Water Resources Engineering
Jadavpur University
Kolkata-700 032

PROFORMA – 2

CERTIFICATE FROM THE SUPERVISORS

This is to certify that the thesis entitled "**Evaluation of Scour around Isolated and Two Circular Piers using Semi-Empirical and Machine Learning Approaches**" submitted by **Mr. Buddhadev Nandi**, who got his name registered on **07th November, 2019** for the award of the Ph.D. degree of Jadavpur University is absolutely based upon his own work under the supervisions of **Dr. Subhasish Das**, Associate Professor, and Joint Director and **Dr. Rajib Das**, Assistant Professor of School of Water Resources Engineering, Jadavpur University and that neither his thesis nor any part of the thesis has been submitted for any degree or any other academic award anywhere before.

1. Subhasish Das 27/01/25

THESIS ADVISOR
Dr. Subhasish Das
Associate Professor and Joint Director
School of Water Resources Engineering
Jadavpur University

Dr. Subhasish Das
Associate Professor & Joint Director
School of Water Resources Engineering
Jadavpur University
Kolkata - 700032

2. Rajib Das 27/01/2025

THESIS ADVISOR
Dr. Rajib Das
Assistant Professor
School of Water Resources Engineering
Jadavpur University

Dr. RAJIB DAS
Assistant Professor
School of Water Resources Engineering
Jadavpur University
Kolkata-700 032

ACKNOWLEDGEMENTS

The author wishes to express his heartfelt gratitude towards his thesis supervisors Dr. Subhasish Das, Associate Professor & Joint Director and Dr. Rajib Das, Assistant Professor of the School of Water Resources Engineering (SWRE), Jadavpur University (JU), for their valuable guidance and continuous encouragement in planning, wholehearted involvement, advice, support execution and presentation of this thesis. It was their initiation, constant encouragement and help rendered in developing the experimental facilities in the Fluvial Hydraulics Laboratory of the School of Water Resources Engineering, Jadavpur University which enabled the author to carry out a major part of the present thesis work. It would also be very difficult to inculcate this work in pen and paper without their valuable advice.

The author is also indebted to his supervisors for helping and providing moral support during the tenure of his Ph.D. work.

Heartfelt gratitude to Prof. (Dr.) Asis Mazumdar, Professor & Director, School of Water Resources Engineering, Jadavpur University for his encouragement during the research.

Thanks, are also due to all the staff members of the SWRE, JU, for their cooperation during the investigation.

Thanks, are also extended to Dr. Asim Kuila, former Ph.D. student, Mr. Gaurav Patel, Mr. Saikat Mondal, Mr. Plaban Sen, Mr. Tanmoy Das, Ph.D. students, and other research scholars of SWRE, JU, for their unwavering support and assistance during the preparation of this thesis. The author expresses heartfelt gratitude to his friend, Mr. Sudarsan Laha, for his moral support throughout the academic journey. Furthermore, the author is deeply thankful to his teachers, Mr. Manilal Mondal, Mr. Srikanta Goswami, and Mr. Subhankar Ghosh, for their foundational support, and to all the teachers who guided him throughout his academic journey.

Last but not least, the author would like to dedicate this thesis to his parents, family and friends without whose motivation and constant backup, the completion of this thesis might be a distant dream to the author.

Date:
Place: SWRE, Jadavpur University

Buddhadev Nandi

Buddhadev Nandi
Doctoral Research Fellow
School of Water Resources Engineering
Jadavpur University

Table of Contents

Abstract

The obstruction of water flow by bridge piers increases sediment transport, resulting in local scour that can compromise bridge stability. During floods, it may take less time to create extensive scour around the pier than normal flow where the temporal effect can be considered rather than the equilibrium scour. So, temporal scour depth (d_{st}) measurement at bridge piers is crucial for engineers due to the need for accurate real-time monitoring. However, temporal conditions offer more cost-effective solutions for pier construction. Despite various predictive formulas, there is a need to identify the most promising method and develop a new one combining metadata from the literature.

However, the actual occurrence of d_{se} near the bridge piers theoretically takes an infinitely long time (t). However, the quasi-equilibrium state can be reached in a certain period, which is useful for designing bridge piers. Previous studies have developed formulas for predicting the time to reach d_{se} at bridge piers. These equilibrium time (t_e) formulas match well with the datasets they were originally based on, they often produce significant deviations when applied to a wider range of datasets. This serves as one of the research gaps to propose a new formula to calculate the quasi-state of equilibrium scour time (T_e).

There are two primary approaches to predicting scour depth (d_s), one focuses on understanding hydraulic processes and their influencing factors, while the other one is data-driven soft computing models. Researchers may select their approach based on the objectives and resources available. However, there is a lack of robust ensemble machine-learning models using extensive metadata collected from various laboratory conditions.

A significant research gap exists in understanding the interference effects on d_s in side-by-side, tandem, and eccentric pier arrangements. This is critical for bridge design, as these configurations can alter scouring patterns and impact structural integrity.

To improve d_s near two-pier configurations, researchers have created regression-based formulas specific to their datasets. This highlights the need for new formulas that consider the influence of different parameters. Furthermore, ensemble machine learning (ML) techniques can provide more reliable predictions. However, more thorough studies are needed to understand how the spacing and positioning of piers affect d_s.

Therefore, to fulfill these research gaps, first of all here, a comparative analysis of *temporal* prediction formulas, at circular piers in clearwater steady flow conditions, is performed using laboratory datasets for evolution over 57 years based on seven parameters: sediment coarseness (d/d_{50}), flow shallowness (h/d), constriction ratio (d/W), flow intensity(u/u_c), sediment uniformity (σ), relative density (Δ), t. The main aim is to select the best formula that provides accurate d_{st} estimation. Therefore, 11 selected literature formulas with a newly proposed formula are assessed and ranked using different performance indicators. The weightage of each performance indicator is calculated using equal weightage and CRITIC methods. The ranking of each formula is determined using compromise programming. Overall study shows that the NCHRP (2011) formula is still most useful to determine d_{st} when equilibrium d_s (d_{se}) and equilibrium time (t_e) are assumed the same as experimental d_s and duration. The newly developed formula is independent of d_{se} and t_e and most accurately predicts the d_{st} without presuming the d_{se} and t_e.

Secondly to improve d_{sm} estimation new ensemble models which includes a Support Vector Machine for Regression (SVMR), Random Forest Regression (RFR), and Reduced Error Pruning Tree (REPTree) as base learners, alongside Bagging Regression Tree (BRT) and Stochastic Gradient Boosting (SGB) as meta learners. These ensembles are developed to analyze maximum d_s (d_{sm}) in clear water conditions, utilizing 35 literature experimental data published in the last 63 years. The proposed models are also compared with the six promising formulas from the literature. Performance evaluation considering training, testing, and the entire dataset, SGB(REPTree), BRT(SVMR-PUK: Pearson VII Universal Kernel), and SGB(REPTree) showed the highest performance, securing the top rank among all ML models and empirical formulas. Sensitivity analysis identified σ, and u/u_c as the most influential variables for predicting d_{sm} during both the training and testing, respectively.

Furthermore, a new formula is established to calculate the T_e depending on the parameter function. The new formula is based on analyzing over six decades of clearwater data collected from the literature. It considers five hydraulic characteristics h/d, u/u_c, d/d_{50}, σ, and d/W. This new formula of T_e has promising efficiency, outperforming five literature formulas. The formula of T_e helps to accurately predict d_{se} and d_{st} in clear water around circular piers using a promising literature formula.

In addition, how these hydraulic parameters affect the d_{sm} near the group of the pier is studied. The key parameters are identified: u/u_c, h/d, d/d_{50}, σ, t, pier spacing (r), and flow skew angle ($\varphi°$). Three different sets of formulas are established for determining d_{sm} around side-by-side, tandem, and eccentric pier groups, considering multiple factors and comparing them to existing literature. The accuracies of formulas are assessed using different performance indicators. The newly proposed formula shows the most accurate method over the literature for all the arrangements.

On the other hand, two ensemble ML models, Random Forest (RF), and Extreme Gradient Boosting (XGBoost), are used to estimate the d_{sm} for both the front and rear piers. The key input parameters are u/u_c, d/d_{50}, t, r, and φ. Partial Dependence Plots (PDP) and SHapley Additive exPlanations (SHAP) are used to visualize feature importance and effects on predicting d_{sm} after training ML models, providing insights into the individual influence of features on predictions. Results demonstrate that RF outperformed XGBoost in both training and testing phases with Random Search Cross Validation (RSCV) optimization for both piers using performance indicators. The u/u_c is identified as the most influential variable making the phenomenon highly vulnerable during model training with Sequential Feature Selection (SFS) and SHAP.

Moreover, in this final chapter, a series of carefully designed experiments take center stage, exploring how different eccentricities (e), h/d and u/u_c affect the d_{st} and d_{sm}, in the rear and eccentric pier to minimize scour. Single-pier experiments are also conducted to compare the scour with the eccentric positioning of piers. The key parameters assessed here are h/d, u/u_c, Fr, t, and e. The lowest d_{sm} occurs at front pier when the eccentric pier is located at e = 3.5d and h = 1.65d, while the d_{sm} of the eccentric pier is 25% higher in that position. Conversely, the lowest d_{sm} for the eccentric pier occurs when e = 2d and h = 1.65d, where the d_s of the front pier is 14% lower in that position. Upon considering all pier arrangements in terms of e, the minimum d_s for the safe bridge pier design is found when the eccentric pier is positioned at e = 2.5d and h = 1.2d. Multi-non-linear regression (MNLR) and, multi-linear

regression (MLR) analyses are performed based on the integrative data from the literature and this study. MLR-based new formula outperformed MNLR-based and all literature formulas for eccentric piers.

The applications of this study might be that designers and engineers can use the most accurate method for the estimation of d_{st} around the isolated pier and may consider the effect most critical hydraulic parameter when designing the foundation. Researchers may also consider the reference of more than 80 isolated d_{sm}, 12 formulas of d_{st}, or more than 10 two-pier arrangement formulas along with the extensive clear water data associated with it for the improvement in the formula near future. The practical application of the two piers arrangements study shows where new bridges are needed next to old bridges for traffic in growing cities. Experts and practitioners can utilize the existing models to improve bridge placements by predicting how pier interference affects d_s, enhancing safety in the design process. This research can help to choose dimensions (mainly eccentric distance e and φ) to reduce the scour needed for safe pier construction. Researchers may use different novel ensemble, physics-informed deep learning models to accurately predict d_s around such interfering piers.

Chapter 1

Introduction

1.1. Research background

Scouring around bridge piers is a destructive phenomenon that arises from the dynamic interaction of water flow and obstructions such as bridge piers, which increase local shear stress and displace sediment particles. This erosion process, which can severely undermine the foundation of the bridge, is responsible for approximately 50~60% of bridge failures in history (Melville and Coleman 2000, Wardhana and Hadipriono 2003, Xiong et al. 2023). To safeguard the stability of bridges, it becomes necessary to estimate the scour depth (d_s) accurately. While semi-empirical approaches have long been used, there is an emerging necessity to improve this or integrate machine learning (ML) techniques to enhance the precision of d_s predictions, especially for isolated piers and two-pier configurations.

Moreover, scour is a complex, evolving process. These dynamic effects start from temporal changes to the development of maximum d_s (d_{sm}) and equilibrium d_s (d_{se}). Key hydraulic parameters must be examined to understand their role in influencing scour. The additional parameters, which are more useful at capturing the complicated behavior of sediment transport and scour may be considered.

As urban areas continue to expand and traffic congestion increases, the demand for new bridge construction also increases. These new bridges are often built near the existing old bridges and this leads even more complex challenge to predict d_s. In cities like Kolkata, where the Nivedita and Vivekananda bridges are positioned near one another, the flow interference between nearby piers can lead to eccentric scour patterns (Das et al. 2019). These bridge arrangements, like side-by-side, tandem, or eccentric, create different flow patterns that are very difficult to predict, but at the same time, these are important to understand for safe bridge design (Das et al. 2016, Das and Mazumdar 2018).

To address this, the focus should be on creating semi-empirical and ML models instead of traditional regression models to study the scour around these complex two-pier arrangements. However, predicting scour alone is not sufficient. In practice, it is important to identify the location where scour is least, which helps to determine the best place to position new piers for maximum stability and safety. This goal is closely linked to the complexity of real-world flow conditions and bridge pier arrangements. Therefore, it is essential to conduct experimental investigations that reveal the precise locations where scour risk is minimized. Thus to ensure safety, bridges will be placed in the safest possible locations.

The next section explains the importance of the study, points out the research gap, and describes why this research is being conducted.

1.1.1. Significance of temporal scour

Bridge piers obstruct the flow of water, which increases sediment transport and causes local scour which further leads to the weakening of the bridge pier foundation (Breusers et al. 1977). During floods, scour can form faster than in normal flow conditions in less time, so it is important to measure temporal d_s (d_{st}) in real time (Chabert and Engeldinger 1956, Melville and Chiew 1999). In theory, the d_{se} at bridge piers takes an infinite amount of time to occur (Franzetti et al. 1982). Previous studies have provided formulas for predicting d_{st} at circular bridge piers, but these formulas often produce inconsistent results under varying sediment types, flow rates, and other dynamic conditions (Franzetti et al. 2022).

The limitations in current research are the lack of accuracy when evaluating d_{st} in non-equilibrium conditions, particularly under clearwater scour. Most of these studies were established based on less experimental data and fewer hydraulic parameters (Mia and Nago 2003). There are many formulas for predicting scour, a better method is needed that combines temporal meta data from past studies. This study aims to address this gap by investigating how different variables, such as sediment characteristics (σ), flow intensity (u/u_c), time (t), flow shallowness (h/d), and sediment coarseness (d/d_{50}) along with an additional influential parameter constriction ratio (d/W), are influencing the evolution of d_{st}. The key focus will be on comparing existing formulas and proposing a new formula derived from a comprehensive analysis of experimental data, which spans several decades. By evaluating the performance of these formulas using experimental datasets, the study aims to provide a more reliable d_{st} estimation that can be applied to bridge design and management scenarios.

1.1.2. Need for maximum scour prediction

In recent decades, soft computing like ML techniques have been increasingly used to predict d_{sm} at bridge piers. These data-driven methods, like Artificial Neural Networks (ANNs), Adaptive Neuro-fuzzy Inference Systems (ANFIS), and evolutionary algorithms, offer significant advantages over traditional formulas (Bateni et al. 2007, Cheng et al. 2014). For example, ANFIS models have demonstrated high accuracy in predicting d_{sm}, outperforming traditional empirical formulas from several studies (Firat and Gungor 2009). Similarly, genetic programming and Support Vector Machines (SVMs) have shown good performance in improving d_{sm} predictions by accounting for nonlinear relationships between input variables, such as sediment size (d_{50}), flow depth (h), and pier geometry (Choi et al. 2017). However, recent research suggests that the integration of ensemble learning techniques, which combine multiple ML models, could further improve the accuracy and robustness of d_s predictions (Chou and Nguyen 2022, Kumar et al. 2023, Baranwal et al. 2024). Moreover, there has been an emphasis on sensitivity analysis and uncertainty quantification in ML approaches to account for the variability of input parameters and their influence on d_{sm} predictions (Singh et al. 2022). The motivation for this study is to combine the strengths of both base and meta learning models to predict d_{sm} under clear water scouring conditions. The research aims to develop ensemble models that integrate various standalone ML techniques with different ensemble ML to improve the accuracy of d_{sm} predictions.

1.1.3. Equilibrium scour challenges

The d_{se} near bridge piers theoretically takes an infinite time to occur. So considering some experimental conditions from different research, different equilibrium time (t_e) formulas have been developed over years by different groups of researchers. Sumer et al. (1992) used 18 datasets from lab experiments to calculate t_e, but they overestimated d_{se}. Melville and Chiew (1999) analyzed 84 datasets and developed formulas for d_{st} and t_e, though their experiments were not conducted over a long period. Here, Chabert and Engeldinger (1956) defined equilibrium as the point where d_s increases very little over time (t). Ettema (1980) described equilibrium time (t_e) as the time when less than 1 mm of d_s is added in 4 hours. Franzetti et al. (1982) noted that reaching this equilibrium could take an infinite amount of t. According to Melville and Chiew (1999), equilibrium can be reached when d_s increases by less than 5% of the pier diameter (d) in 24 hours. Grimaldi (2005) defined equilibrium as a scour rate of less than (0.05×width of the channel)/3 within 24 hours. Lança et al. (2010) suggested using long-term data and a six-parameter polynomial function to estimate d_{se} at circular piers. Different research groups have varying definitions to estimate t_e, creating ambiguity in considering a single formula.

However, a quasi-equilibrium state can be reached in a stipulated period. Previous formulas predict the t to reach d_{se}, but they often do not fit well when applied to new data. To address this research gap, new formulas are needed to accurately calculate quasi-equilibrium scour time (T_e). Thus, this study focusing on T_e can help in designing more economical scour solutions. Existing formulas predict this time well for specific datasets but often fail with broader datasets. This study aims to develop a new formula for T_e using dimensional analysis and functional relationships.

1.1.4. Dealing with interference around two piers

Studies have shown the importance of flow patterns and structures around piers, such as vortices, in determining d_s and patterns for single and two piers in eccentric arrangements (Das et al. 2013, Das et al. 2016, Das and Mazumdar 2018). Research on scouring around side-by-side, tandem, and eccentric pier arrangements highlights the complexities of flow structures and sediment movement (Wang et al. 2016, Malik and Setia 2020, Devi and Kumar 2022). Existing studies on these configurations have not fully captured the dynamics in natural river environments, emphasizing the need for further research (Namaee and Sui 2019, Sahu et al. 2023). The existing formulas often overestimate d_s compared to real-world observations (Liang et al. 2017). Tandem pier studies have explored mutual interference effects and developed empirical formulas for d_{se}, but further validation is required (Beg and Beg 2015, Liu et al. 2018). On the other side, using ML method, Baranwal et al. (2024) showed that XGBoost outperforms SVM-PSO for the d_s estimations.

This research gap can be fulfilled by developing robust formulas either by semi empirically or by ML model. In this study, we have focused on the both semi empirical approach as well as Ensemble ML models, like Random Forest (RF) and XGBoost. These ML models have demonstrated superior performance in d_s, but more research is needed to

apply these methods to complex pier groups (Kumar et al. 2023, Eini et al. 2023). Given the limitations of existing empirical formulas and ML models, there is a need for a robust d_s prediction model that integrates data from multiple two pier configurations into a unified method. Therefore, this study aims to fulfill the research gap by using ensemble methods, combined with feature selection techniques to improve the accuracy of d_{sm} predictions and enhance our understanding of key contributing influential parameters through different visualization tools. However, the semi empirical models aim to establish a robust understanding of different interference effects such as reinforcing, sheltering, and effect of shed vortices.

1.1.5. Need for experimental study

The urban growth increases traffic congestion, which often requires building new bridges next to existing ones, creating eccentric pier combinations (Das et al. 2016, Das et al. 2019, Nandi and Das 2024). The scouring process around such pier groups creates complex interactions, making it challenging to predict the d_{sm}. Four key scour mechanisms that occur around pier groups can be seen as reinforcing, shed vortices, sheltering, and compressed horseshoe vortices (Hannah 1978). After different studies on such pier groups, a complete understanding of scour geometry around piers with eccentric arrangements is still limited. Most studies on pier groups have focused on tandem (Beg and Beg 2015, Wang et al. 2016, Liu et al. 2018) or side-by-side (Malik and Setia 2014, Devi and Kumar 2022) arrangements to study the effect of pier spacing on d_{sm}. Some studies examined the impact of longitudinal spacing (l) variations in eccentric arrangments of piers (Das et al. 2016, Khaple et al. 2017), but fewer have studied variations in transverse spacing or eccentric spacings (e) (Beg 2004).

There is a gap in studies on eccentric piers when it comes to identifying the minimum scour locations. Building new bridges next to older ones is often necessary in rapidly growing cities, and understanding how to reduce scour is crucial for safe construction. This research focuses on experimentally reducing scour around bridge piers placed eccentrically at different e while keeping fixed $l = 5.2d$ (Das et al. 2016) to simulate the worst-case scenario as they found the maximum scour at such l. The aim is to find the position with the least scour for eccentric piers at various e. Experts and practitioners can use this model to better plan bridge placements, and predict how pier interference affects d_s and improve safety in the design process.

1.2. Scopes of this research

The scope of this research focuses on advancing the prediction of d_s around isolated bridge piers, which is critical for ensuring the safety of bridges. This study also aims to develop improved formulas/ML models for predicting d_s at various two pier configurations, including eccentric, side-by-side, and tandem piers. The earlier research provides an overview of the areas of study that can be further explored in the present research are given below:

- To develop new formulas for predicting d_{st} at isolated circular and d_{sm} around two pier arrangements, improving on existing models.

- To use ML techniques, including XGBoost and RF, SVM, REP Tree, Bagging and Boosting to analyze meta datasets from several studies for d_{sm} prediction at the isolated pier and two pier groups.
- To identify key hydraulic parameters in isolated as well as two pier combinations, that influence d_s.
- To introduce the Multiple Attribute Decision-Making (MADM) to rank the formula and different advanced feature selection methods, to identify the parameter influence which enhances prediction accuracy.
- To study the temporal evolution of d_s at circular mono piers with a new formula that includes six hydraulic parameters including constriction ratio (d/W).
- To evaluate the effects of e and u/u_c on d_s at two piers experimentally in the lab scale bridge pier model.
- To investigate the interference between piers and its impact on d_s at side-by-side, tandem, and eccentric pier arrangements.
- To identify optimal configurations for minimizing d_s in twin pier setups experimentally varying eccentricity.
- To add knowledge to practical applications for improved bridge design and scour management.
- To suggest future research directions for further refining scour prediction models and addressing their limitations.

1.3. Main objectives of this study

The main objectives of this research are centred on addressing critical gaps in the prediction of d_s around bridge piers, both isolated and in two-pier arrangements. The combining past research hydraulic parameters with new parameters, along with a comparison with the empirical approaches with advanced ML techniques, this study aims to enhance the accuracy of d_s estimation under various hydraulic conditions. The research also seeks to develop new predictive formulas and methods that can guide practical applications in bridge design, ensuring safer and more reliable infrastructure in urban and natural settings. Below is a detailed outline of the key objectives that drive this study.

- To evaluate and rank d_{st} prediction formulas for isolated circular piers under clear water steady flow conditions using a dataset spanning 57 years. This study considers almost 6800 temporal data points. The study aims to identify the most accurate formula, including a newly proposed one, based on performance indicators and compromise programming.
- To improve the prediction of d_{sm} by developing an ensemble ML model combining Support Vector Machine for Regression (SVMR), Random Forest Regression (RFR), and Reduced Error Pruning Tree (REPTree) as base learners, with Bagging Regression Tree (BRT) and Stochastic Gradient Boosting (SGB) as meta learners. The objective is to compare these models with existing empirical formulas and identify key influential variables using sensitivity analysis.

- To establish a novel formula for predicting the quasi-equilibrium scour time (T_e) for circular piers under clear water conditions. This formula development aims to synthesize metadata from six decades and compare existing literature formulas.
- To study how hydraulic parameters, affect d_{sm} around side-by-side, tandem, and eccentric pier groups. The objective is to develop accurate semi empirical formulas for these configurations and compare them with existing regression-based formulas from the literature.
- To apply ensemble ML models such as Random Forest (RF) and Extreme Gradient Boosting (XGBoost) to predict d_{sm} around front and rear piers in two pier setups. The study aims to identify the most influential variables using Partial Dependence Plots (PDP) and SHapley Additive exPlanations (SHAP).
- To conduct experiments assessing the impact of e and u/u_c on d_{st} and d_{sm} in eccentric pier arrangements. The objective is to identify the optimal positioning of piers to minimize scour and develop a new predictive formula based on multi-linear and multi-nonlinear regression analyses.
- Lastly, to provide insights for designers and engineers on using accurate d_s estimation methods and considering critical hydraulic parameters in bridge pier foundation design. The objective is to assist in the safe construction of new bridges adjacent to existing ones in urban areas, reducing scour through best pier positioning or predictive ensemble models.

1.4. Thesis outline

This thesis includes six research papers, three of which have been published in international scientific journals, while the others are in the communication phase. It begins with an introduction that covers the background and motivation for the study and ends with a chapter that shows the main conclusions from the research. Below is a summary of each chapter, highlighting the key contributions and findings.

Chapter 2: Basic theories that are related to fluid kinematics, flow structure interaction around isolated cylinders, and two cylindrical pier groups importance of different dimensional and non-dimensional parameters. The chapter also includes formulas used in the literature to estimate scour around isolated and eccentric pier arrangements.

Chapter 3: This chapter explains the identification of the most promising d_{st}. It compares 11 literature formulas with a newly proposed one using 6784 clear water data points. A new parameter, the constriction ratio (d/W), is introduced along with six others from the past. These formulas are ranked using compromise programming based on weighted performance indicators using the Criteria Importance Through Intercriteria Correlation (CRITIC) method.

Chapter 4: This chapter focuses on predicting the maximum clearwater d_s using metadata analysis of 850 datasets from 35 past studies. It compares the six most promising empirical formulas with novel ML techniques. This chapter compares promising literature formulas. The standalone and novel ensemble ML models are developed to predict scour accurately.

The sensitivity analysis is done to identify the influential parameter. Ranked the model/formula using multi attribute decision making using different influential parameters.

***Chapter 5*:** This chapter presents a novel formula to revisit the time scale formula to estimate quasi-equilibrium time (T_e) for scour at circular mono piers. Five hydraulic parameters are identified through dimensional analysis. The formula is validated through rigorous training and validation of time-scale data. It also shows enhanced accuracy in predicting the magnitudes of statistically influential parameters compared to existing formulas. A numerical example is provided to illustrate how to compute d_s more accurately.

***Chapter 6*:** This chapter introduces new formulas to predict the d_{sm} at side-by-side, tandem, and eccentric piers. An analysis of 12 studies and 486 datasets is conducted to evaluate various d_s predictors. Key factors such as interference, compressed horseshoe vortex, reinforcement, and sheltering effects on flow between piers are examined. The newly developed formulas are compared statistically along with literature formulas. Pier spacing (r) and flow skew angle ($\varphi°$), along with previously identified parameters, are analyzed to study their influence on d_s.

***Chapter 7*:** This chapter develops two ensemble ML models, XGBoost and RF, to predict d_s at twin piers. It evaluates existing formulas using data from 12 studies and 431 datasets. The PDPs and SHAP are employed to visualize the impact of different features on scour prediction. The most influential hydraulic parameters are identified through Sequential Feature Selection (SFS) and SHAP analysis, providing deeper insights into the factors affecting d_s.

***Chapter 8*:** This chapter explores the interference effects on eccentric circular piers when two parallel bridges are constructed alongside. It examines how varying transverse spacing (e) and flow intensity (u/u_c) influence the d_s at each pier. The study focuses on understanding the combined effects of horseshoe vortices and wake vortices between the piers. By analyzing the transverse spacing ratios (e/d), it aims to identify the conditions that minimize the d_s, providing insights into optimal bridge design to reduce scour-related risks.

***Chapter 9*:** This chapter presents the conclusions and key findings of the research, along with future directions. It also discusses the practical applications in the field. The limitations of this study are also discussed.

References

Baranwal, A., Gaurav, P., Reddy, L., Das, B. S., and Naik, B. (2024). Predicting temporal clear water scour depth around bridge piers with XGBoost and SVM–PSO approaches. *Journal of Hydroinformatics*, *26*(12), 3109–3129.

Bateni, S. M., Borghei, S. M., and Jeng, D. S. (2007). Neural network and neuro-fuzzy assessments for scour depth around bridge piers. *Engineering Applications of Artificial Intelligence, 20*(3), 401–414.

Beg, M. (2004). Mutual interference of bridge piers on local scour. In *Proceedings of the Second International Conference on Scour and Erosion, Singapore* (pp. 111–118).

Beg, M., and Beg, S. (2015). Scour hole characteristics of two unequal size bridge piers in tandem arrangement. *ISH Journal of Hydraulic Engineering*, *21*(1), 85-96.

Breusers, H. N. C., Nicollet, G., and Shen, H. W. (1977). Local scour around cylindrical piers. *Journal of Hydraulic Research*, *15*(3), 211-252.

Hannah, C. R. (1978). *Scour at pile groups*. Research Report No. 28–3, Civil Engineering Dept., University of Canterbury, Christchurch, New Zealand.

Chabert, J., and Engeldinger, P. (1956). *Étude des affouillements autour des piles de ponts* [Study of scour around bridge piers]. Technical Report. Laboratoire National d'Hydraulique, Chatou, France.

Chabert, J., and Engeldinger, P. (1956). Etude des affouillements autourdes piles des ponts. Laboratoire d'Hydraulique, Chatou, France (in French)

Cheng, M. Y., Cao, M. T., and Wu, Y. W. (2014). Predicting equilibrium scour depth at bridge piers using evolutionary radial basis function neural network. *Journal of Computing in Civil Engineering, 29*(5), 04014070.

Choi, S. U., Choi, B., and Lee, S. (2017). Prediction of local scour around bridge piers using the ANFIS method. *Neural Computing and Applications, 28*(2), 335–344.

Chou, J. S., and Nguyen, N. M. (2022). Scour depth prediction at bridge piers using metaheuristics-optimized stacking system. *Automation in Construction, 140*, 104297.

Das, R., Das, S., Jaman, H., and Mazumdar, A. (2019). Impact of upstream bridge pier on the scouring around adjacent downstream bridge pier. *Arabian Journal for Science and Engineering*, *44*, 4359–4372.

Das, S., and Mazumdar, A. (2018). Evaluation of hydrodynamic consequences for horseshoe vortex system developing around two eccentrically arranged identical piers of diverse shapes. *KSCE Journal of Civil Engineering*, *22*, 2300-2314.

Das, S., Das, R., and Mazumdar, A. (2016). Comparison of local scour characteristics around two eccentric piers of different shapes. *Arabian Journal of Science and Engineering, 41*(4), 1199-1213.

Devi, G., and Kumar, M. (2022). Experimental study of the local scour around the two piers in the tandem arrangement using ultrasonic ranging transducers. *Ocean Engineering*, *266*, 112838.

Ettema, R. (1980). *Scour at bridge piers*. Ph.D. thesis. Department of Civil Engineering, University of Auckland.

Firat, M., and Gungor, M. (2009). Generalized regression neural networks and feed forward neural networks for prediction of scour depth around bridge piers. *Advances in Engineering Software, 40*(8), 731–737.

Franzetti, S., Larcan, E., and Mignosa, P. (1982). Influence of tests duration on the evaluation of ultimate scour around circular piers. In: *Proceedings of the International Conference on the Hydraulic Modelling of Civil Engineering Structures* (editors, HS Stephens, CA Stapleton), *BHRA Fluid Engineering, Coventry, Inghilterra, Settembre 1982.* (pp. 381-396).

Franzetti, S., Radice, A., Rebai, D., and Ballio, F. (2022). Clear water scour at circular piers: A new formula fitting laboratory data with less than 25% deviation. *Journal of Hydraulic Engineering*, *148*(10), 04022021.

Grimaldi, C. (2005). *Non-conventional countermeasures against local scouring at bridge piers*. Ph.D. thesis. Hydraulic Engineering for Environment and Territory, University of Calabria, Cosenza, Italy.

Khaple, S., Hanmaiahgari, P. R., Gaudio, R., and Dey, S. (2017). Interference of an upstream pier on local scour at downstream piers. *Acta Geophysica*, *65*, 29-46.

Kumar, S., Goyal, M. K., Deshpande, V., and Agarwal, M. (2023). Estimation of time-dependent scour depth around circular bridge piers: Application of ensemble machine learning methods. *Ocean Engineering, 270*, 113611.

Lança, R., Fael, C., and Cardoso, A. H. (2010). Assessing equilibrium clear water scour around single cylindrical piers. *River Flow*, 1207–1214.

Liang, F., Wang, C., and Yu, X. (2019). Performance of existing methods for estimation and mitigation of local scour around bridges: case studies. *Journal of Performance of Constructed Facilities*, *33*(6), 04019060.

Liang, F., Wang, C., Huang, M., and Wang, Y. (2017). Experimental observations and evaluations of formulae for local scour at pile groups in steady currents. *Marine Georesources & Geotechnology*, *35*(2), 245-255.

Liu, Q. S., Tang, H. W., Wang, H., and Xiao, J. F. (2018). Critical velocities for local scour around twin piers in tandem. *Journal of Hydrodynamics*, *30*, 1165-1173.

Malik, R., and Setia, B. (2014). Experimental study on behaviour of closely placed bridge pier models. In *Proceedings of the National Conference in Department of Civil Engineering, National Institute of Technology Kurukshetra, Kurukshetra, India.*

Malik, R., and Setia, B. (2020). Interference between pier models and its effects on scour depth. *SN Applied Sciences*, *2*, 68.

Melville, B. W., and Chiew, Y. M. (1999). Time scale for local scour at bridge piers. *Journal of Hydraulic Engineering, 125*(1), 59–65.

Melville, B. W., and Coleman, S. E. (2000). *Bridge scour*. Water Resources Publication.

Mia, F., and Nago, H. (2003). Design method of time-dependent local scour at circular bridge pier. *Journal of Hydraulic Engineering, 129*(6), 420–427.

Namaee, M., and Sui, J. (2019). Local scour around two side-by-side cylindrical bridge piers under ice-covered conditions. *International Journal of Sediment Research, 34*(4), 355-367.

Nandi, B., and Das, S. (2024). Equation for time-dependent local scour at pier-like structures with eccentric in-line arrangements. In *Proceedings of the Institution of Civil Engineers-Water Management*, *177*(6), 361-374.

Sahu, C., Eldho, T. I., and Mazumder, B. S. (2023). Experimental study of flow hydrodynamics around circular cylinder arrangements using particle image velocimetry. *Journal of Fluids Engineering, 145*(1), 011302.

Singh, U. K., Jamei, M., Karbasi, M., Malik, A., and Pandey, M. (2022). Application of a modern multi-level ensemble approach for the estimation of critical shear stress in cohesive sediment mixture. *Journal of Hydrology, 607*, 127549.

Sumer, B. M., Christiansen, N., and Fredsoe, J. (1992). Time scale of scour around a vertical pile. In *Proceedings of the Second International Offshore and Polar Engineering Conference* (pp. 179-184). International Society of Offshore and Polar Engineers.

Wang, C., Yu, X., and Liang, F. (2017). A review of bridge scour: mechanism, estimation, monitoring and countermeasures. *Natural Hazards*, *87*, 1881-1906.

Wardhana, K., and Hadipriono, F. C. (2003). Analysis of recent bridge failures in the United States. *Journal of performance of constructed facilities*, *17*(3), 144-150.

Xiong, W., Cai, C. S., Zhang, R., Shi, H., and Xu, C. (2023). Review of hydraulic bridge failures: Historical statistic analysis, failure modes, and prediction methods. *Journal of Bridge Engineering*, *28*(4), 03123001.

Chapter 2

Theoretical Background

2.1. General

The aim of this chapter is to introduce the basic concept behind the scour at the alluvial river bed, the theoretical concept behind the sediment transport phenomenon, mechanisms of flow structure interaction, scour influential parameters, dynamics of flow structure interaction around an isolated pier, and two pier arrangement. The information provided here is mostly derived from the laboratory studies. This chapter may lead the designer, engineer, or technician to know: What are the causes of bridge failure? How important to design safe and economical structures in a stream bed? How semi the empirical formula derived for scour problems? What cutting-edge soft computing method should be used for scour problems?

An alluvial riverbed constantly changes as flowing of water erodes, moves, and deposits sediment, reshaping the bed of river elevation and boundaries. These changes can occur naturally or result from human activities that alter the riverbed or its geometry. One significant impact of human intervention is the development of scour holes around bridge piers, which are a leading cause of bridge foundation failures (Xiong et al. 2023). Different processes can change the bed elevation or level at the bridge pier sites, with scour being a key factor. More than 60% of bridges fail in the USA due to scour related reasons (Lagasse et al. 2007).

Local scour depth (d_s) around bridge piers is the primary cause of many bridge failures in river systems. Accurately estimating the maximum d_s (d_{sm}) around a pier is essential for ensuring the safe design of the structure (Melville and Coleman 2000). Bridge component failures are most often attributed to pier failure, accounting for approximately 61% of such cases (Fig. 2.1). This statistic emphasizes the critical importance of addressing scour at bridge piers, as they are the most vulnerable to the erosive forces of flowing water. When piers fail, the structural integrity of the entire bridge is compromised, highlighting the need for thorough monitoring and mitigation strategies to prevent scour-related damage. Abutments and other components also face risks, but the high failure rate of piers makes them a primary concern in bridge safety and design (Lin et al. 2014). It has been observed that in free surface flow around a bridge pier, horseshoe vortices form, intensifying turbulence in the areas in front, around, and behind the piers (Das et al. 2013). Moreover, a distinct scour hole develops in the loose bed surrounding the pier. The experimental investigations have shown that the flow dynamics and sediment transport involved in the formation of the scour hole are complex phenomena. Another critical aspect of this scour process is the downstream movement of sediments. Despite many research into understanding the mechanisms of scour and developing methods to predict d_s, new bridges continue to fail due to excessive scour.

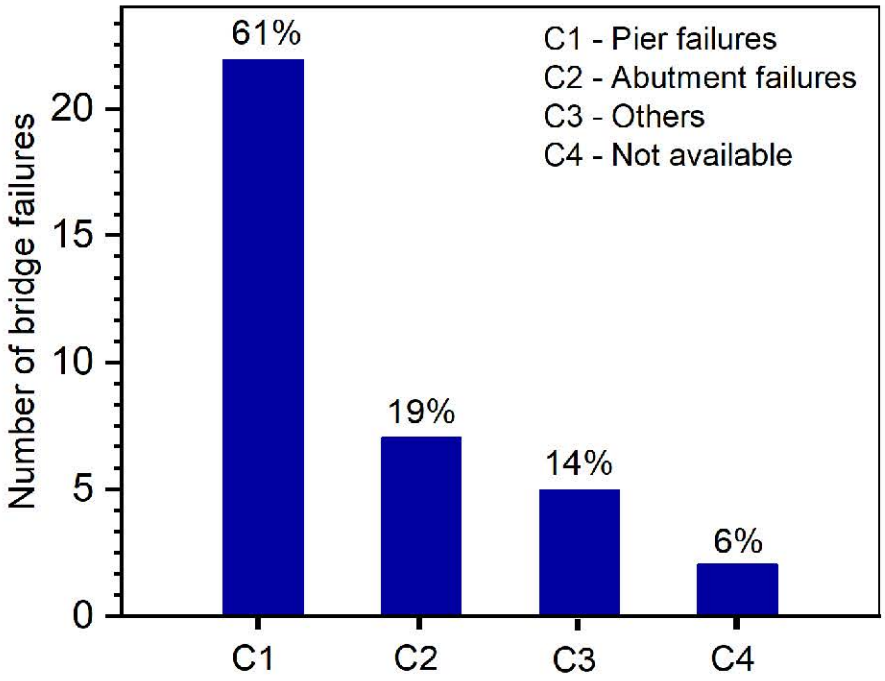

Fig. 2.1. Failures of bridge components due to scour (Lin et al. 2014).

While hydraulic and bridge engineers have methods for estimating d_s in sand and gravel beds under controlled flow conditions using empirical approaches, but accurately predicting the d_s near a pier using metadata is still limited. Furthermore, the application of machine learning (ML) techniques to estimate d_s remains limited. When scour poses a risk to the foundations of a bridge, it is essential to implement effective prevention and protection measures based on precise scour estimation.

Findings from single pier studies cannot be directly applied to two-pier groups due to hydraulic, geotechnical, and economic factors in bridge design. Furthermore, accelerated urban development and increased traffic volumes create a necessity for new bridges to be built next to existing ones, leading to issues related to pier interference and arrangements such as side-by-side, tandem, and eccentric pier configurations. In some cases, a new bridge pier is positioned downstream in an eccentric arrangement relative to an existing bridge pier. An example of this can be seen in Kolkata, West Bengal, India, where the Nivedita Setu (constructed in 2007) was built just downstream of the Vivekananda Setu (constructed in 1931). When bridges are closely spaced, the pier of one bridge influences the other. The horseshoe vortex formed around the rear eccentric pier is interacting with wake vortex of the front pier. The combined effect of both vortices enhances the scour hole around the rear pier, increasing sediment transport. This natural interaction could be explored for its suitability and efficiency in improving d_s prediction in such two pier groups in eccentric arrangements.

In many river channels, sediment accumulation can reduce the depth, making navigation difficult. This sediment buildup often results from the natural water flow carrying particles that settle in the channel. If sediment could be redirected to one side of the bank, it could help maintain the required depth for vessels. When studying scour near bridge piers, particularly in eccentric arrangements, it is important to understand how sediment transport affects scour development. Managing sediment movement can help reduce scour and improve bridge

foundation stability. Another benefit is that this method could be a better alternative to traditional dredging after studying the bed morphology of such arrangements. Understanding the bed morphology of pier combinations, like eccentric arrangements, is also important for preventing sediment buildup and keeping bridges stable over time.

2.2. Scour

Scouring is a natural dynamic process driven by the flow of water in streams and rivers. It results from the erosive action of flowing water, which gradually removes and erodes material from the bed and banks of watercourses. This process can occur in various areas, including the vicinity of bridge piers and abutments. While scouring is a natural aspect of river morphology, it is often amplified by human-made structures, such as bridges and dams. During peak flow events, such as floods, the flow velocity (u) increases dramatically, which significantly enhances the erosive power of the water. These high-u flows can create deep scour holes around piers, leading to more substantial material removal and posing a greater risk to the integrity of riverbed structures in a very short time which leads to the importance of examining the temporal aspect of the scour (Melville and Chiew 1999).

Regardless of the flow conditions, scour can occur at any time, and its effects can lead to the washing away of materials around the pier abutments, often disrupting the natural level of the riverbed. Over time, the cumulative impact of scour can compromise the stability of bridges, foundations, and other infrastructure, making it a critical factor in river and bridge engineering.

2.2.1. Why should we be concerned about scour?

Why should we worry about scour? Because it can wash away the sediment near foundation under a bridge, making the structure weak and unsafe. Imagine crossing a bridge when the ground beneath its foundation has been eroded by a strong river. This exact situation happened in 1987 when the Interstate Highway Bridge over Schoharie Creek in New York collapsed during a flood, leading to tragic loss of lives and severe damage. After this disaster, the Federal Highway Administration required all states to find and address bridges at risk of scouring to prevent such tragedies from happening again.

In India, the collapse of the Jahu Bridge in Himachal Pradesh is another example. In 2007, heavy rains damaged and washed away the concrete bridge. A new Bailey bridge was built in its place, but on August 14, 2014, it also collapsed due to scour. How many more such incidents must happen before we fully understand the serious threat that scour poses?

Understanding the threat of scour is not just about knowing the problem, it is about taking action. By finding the bridges most at risk, we can monitor and improve them, making sure our infrastructure stays safe before it is too late. It is our duty to keep the bridges we use every day safe, no matter how strong the river beneath them. The Houfeng Bridge over the Da-Chia River in Taiwan collapsed due to scour during the 2008 typhoon flood (Fig. 2.2). To monitor this, we need an accurate estimation of scour as well as a clear knowledge of the interference effect near two pier groups.

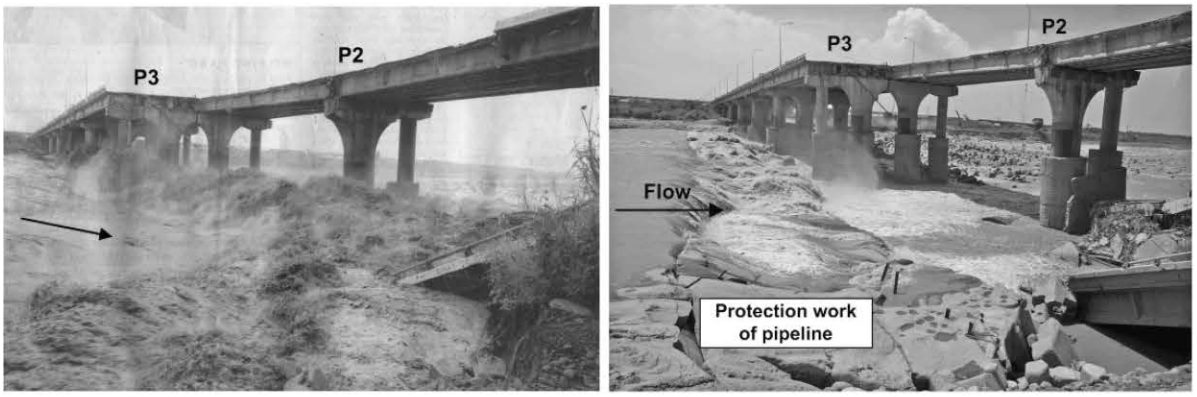

Fig. 2.2. Photographs of Houfeng bridge failure due to scour (Hong et al. 2012). Here, P2 represents the second pier, and P3 represents the third pier failed due to a typhoon flood.

2.2.2. Classification of scours

Scouring is a natural process occurring as part of the morphological changes of rivers or may be due to man-made structures. The criteria for scour involve physical conditions related to the threshold at which materials begin to move, often determined using the well-known Shields diagram. Scour types are categorized based on their location and the sediment transport capacity of rivers and streams. The two main types are general scour and localized scour, with further subdivisions illustrated in Fig. 2.3.

(a) General scour

General scour refers to changes in riverbeds caused by natural or human activities, leading to a lowering of the profile of river channels. It happens when the flow pattern of river changes, causing the bed to erode. General scour can occur with or without a bridge pier or abutments and is divided into short-term and long-term scour. Short-term scour happens during a single or a series of floods, while long-term scour lasts for several years, involving ongoing bed or bank erosion.

(b) Localized scour

Melville and Coleman (2000) described localized scour as a combination of contraction scour and local scour, both caused by the presence of a bridge pier or in one-word obstruction towards the flow. When river flow converges at a bridge, it narrows, accelerates at the narrowest point (vena contracta), and then slows as it spreads out downstream. This acceleration causes contraction scour. Local scour occurs when flow interacts with structures like piers and abutments, leading to material being eroded around these areas. The local scour at piers can be classified into clear-water scour and live-bed scour, based on the ability to transport bed material by the flow.

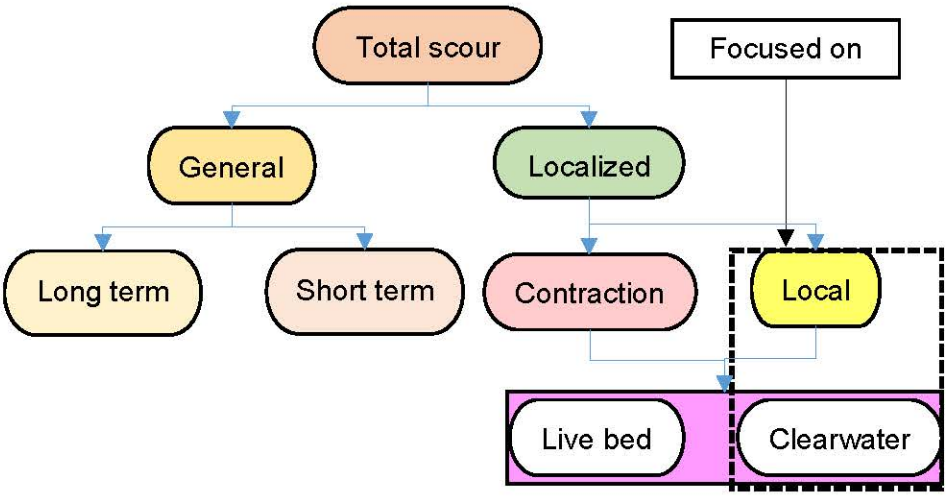

Fig. 2.3. Classification of scour (Melville and Coleman 2000).

(c) Clear water scour

Clear water scour occurs when the upstream bed material remains stationary, preventing any replacement of the scour hole. In this scenario, the bed shear stress (τ_o) beyond the scour hole is at or below the critical shear stress (τ_{oc}) required to initiate particle movement. The scour hole deepens until equilibrium is achieved, where the combined effects of mean τ_o and turbulent agitation near the bed can no longer dislodge material. Figure 2.4 shows a schematic diagram with selected boundary/key points around the pier used to determine scour contours.

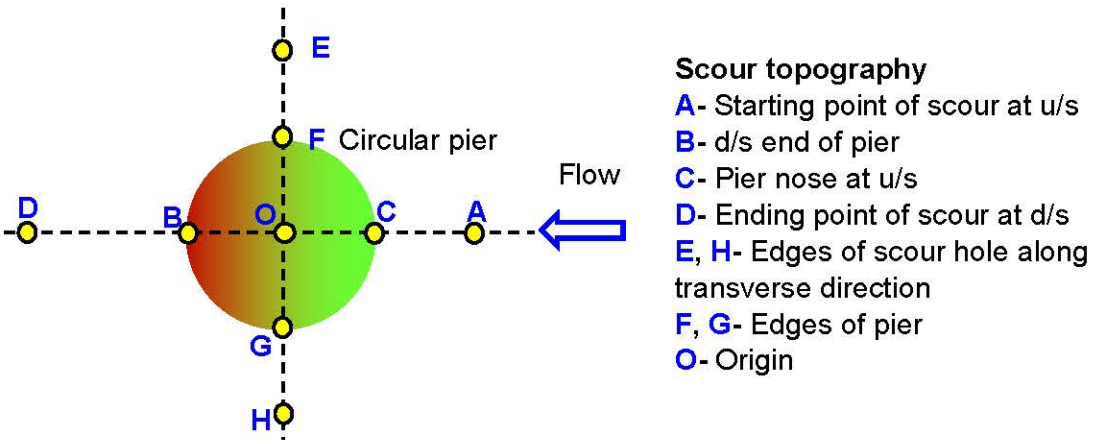

Fig. 2.4. Schematic diagram showing the boundary around the pier to determine scour contours.

(d) Live bed scour

Live bed scour occurs when sediment is actively transported both into and out of the scour hole. In this case, the τ_o exceeds the τ_{oc} of the bed material, leading to the formation of bed forms on the channel bed. Equilibrium in live bed scour is reached when the average sediment inflow into the scour hole matches the average outflow.

Figure 2.5 shows the two scour types and the equilibrium scour depth (d_{se}) over time (t). It shows that d_{se} in clear water scour is reached asymptotically, whereas live bed scour shows

non-periodic oscillations around the d_{se}. Shen et al. (1969) noted that the d_{se} for live bed scour is approximately 10% less than that for clear water scour.

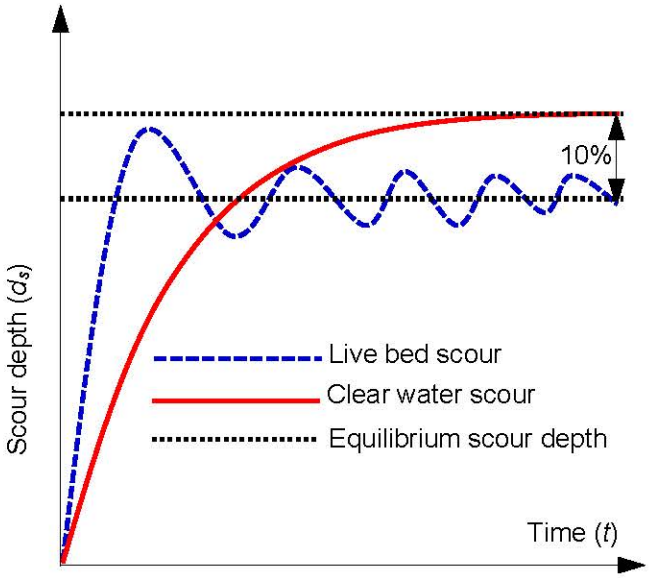

Fig. 2.5. Time evolution of scour depth in clear water and live bed conditions.

2.2.3. Local scour mechanism

The boundary layer flow around a cylindrical pier experiences three-dimensional separation, leading to the formation of a vortex system in front of the pier, which is carried downstream by the river flow. From an overhead view, this system looks like a horseshoe, thus termed a horseshoe vortex. The development of this vortex and the associated down flow around the pier which increases the τ_o, enhancing the sediment transport capacity and resulting in the formation of a deep scour hole around the pier. This alteration in the flow pattern subsequently reduces τ_o, diminishing sediment transport capacity. The temporal variation (d_{st}) and d_{sm} of scour at bridge elements are influenced primarily by the flow characteristics, pier geometry, and riverbed material. The formation of the horseshoe vortex and down flow contributes to local scour around cylindrical piers, abutments, and spur dikes. The local scour mechanism is predominantly driven by the vortex system surrounding the pier, with the strength of vortex and size depending on the "bluffness of the pier."

Understanding the flow field around piers is crucial to comprehending the scour mechanism. As noted by Ettema (1980), this flow field represents a type of junction flow characterized by interactions among three-dimensional turbulence structures. Melville and Coleman (2000) identified key features of the flow field at a bridge pier: the down-flow at the upstream side, the horseshoe vortex at the base of the pier, the surface roller at the upstream side, and wake vortices downstream. These vortices are further divided into components based on their specific characteristics and roles in the flow dynamics (Fig. 2.6).

(a) Horseshoe vortex and downflow

The horseshoe vortex is a common flow pattern seen around bridge piers during scour, where water flowing past a pier creates a circular flow resembling a horseshoe. This flow separates

at the upstream face of the pier, forming a vortex trail called the horseshoe vortex. The water u decreases from the surface to the riverbed, with the highest u at the surface and the lowest at the bottom. This results in reduced stream pressure in the downward direction, which leads to the development of a downward flow at the front of the pier. This downward flow, caused by the presence of the pier, can intensify scour by increasing water u and accelerating the erosion of sediment around the pier. Understanding the dynamics of this downflow is crucial for predicting and mitigating pier scour. The erosive action of the downflow and bed erosion continues until a quasi-stable state is reached, where the dynamic angle of repose is 10-20% greater than in still water. The primary horseshoe vortex, which forms in front of a circular pier, is a key factor in the scour process (Das et al. 2013, Dey 2014). This vortex can significantly increase sediment erosion, compromising the stability of the bridge. Therefore, understanding and mitigating the effects of the horseshoe vortex is critical in bridge design and maintenance.

(b) Wake vortex

Wake vortices are formed on the downstream side of piers as a result of flow separation, often referred to as cast-off vortices (Raudkivi 1986). These vortices, which have vertical axes, shed alternately from each side of the pier and are carried downstream (Fig. 2.6). As they move, wake vortices dissipate, with the shedding frequency being directly proportional to the u and inversely proportional to the d. Wake vortices play a significant role, alongside horseshoe vortices, in multi-pier configurations. When two wake vortex streams intersect, scour is greatly enhanced. The vortices weaken as they approach the centreline of the flow, and their alternating shedding creates lateral forces that decrease as they near the centreline (Das et al. 2013). Furthermore, scour is intensified when the wake vortices from adjacent piers intersect downstream, creating local scour. A similar effect occurs at the confluence of a main channel and its side channel, known as confluence scour.

(c) Bow wave

The bow wave forms at the free surface near the pier face, rotating in the opposite direction to the horseshoe vortex (Fig. 2.6). This phenomenon is more significant in shallow flows and helps reduce the downflow u. The bow wave arises due to the obstruction of the flowing stream at the upstream free surface adjacent to the pier. Unlike other flow-induced vortices, the bow wave does not contribute to scour and is considered relatively harmless in terms of erosion (Khaple et al. 2017).

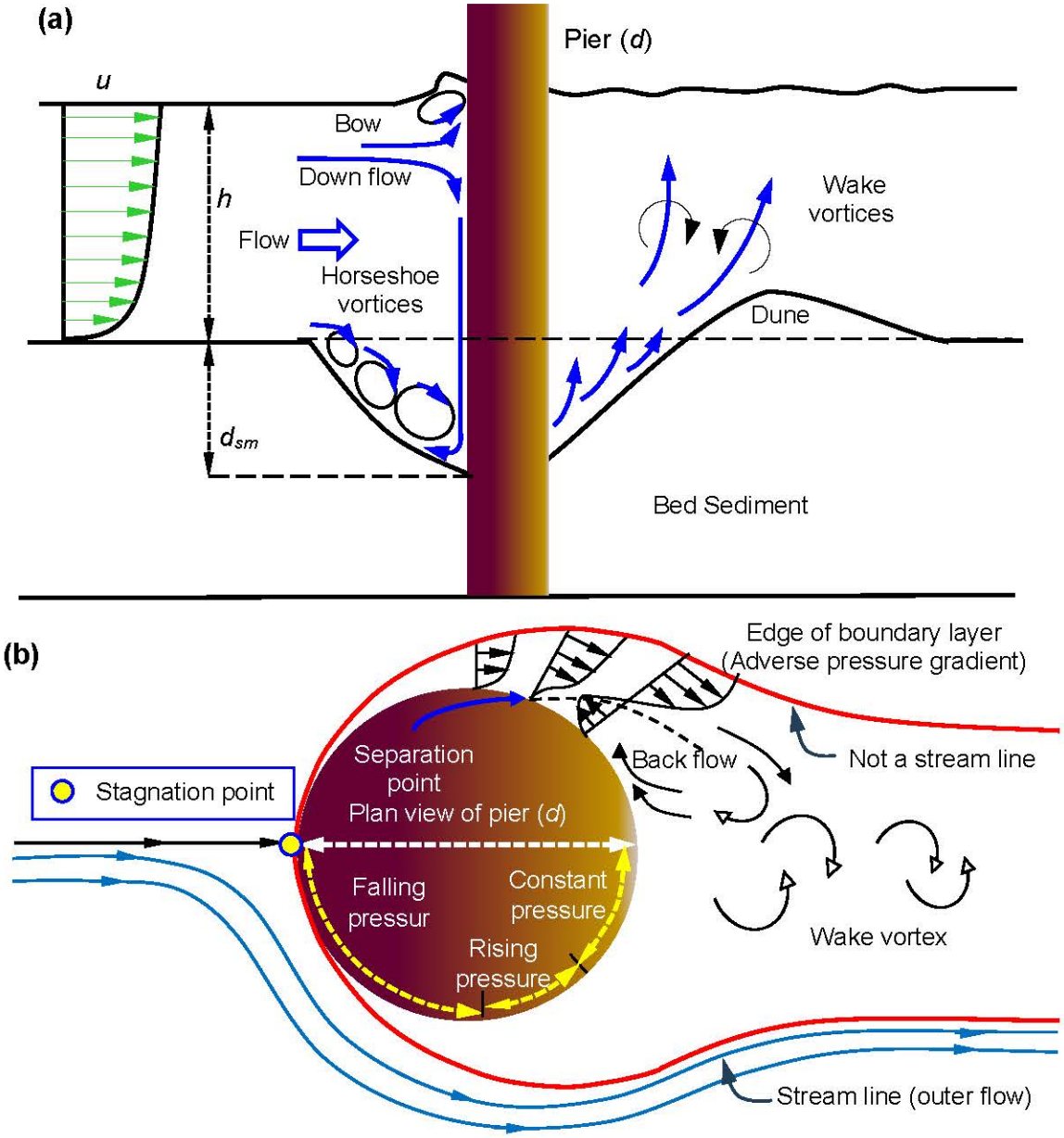

Fig. 2.6. Schematic diagrams of flow structures around a single circular pier showing **(a)** side view, and **(b)** top view.

2.2.4. Sediment transport

When the τ_o of an alluvial channel exceeds the critical tractive stress for the bed material, the particles begin to move. Sediment transport can be divided into two main types: *bed load* (where particles move in contact with the bed) and *suspended load* (where particles are carried in suspension by the turbulent flow). The amount of sediment transported at any cross-section is determined by two factors: the *geology of the upstream area* (sediment supply) and the *stream power* (ability to transport sediment).

The rate of sediment transport depends on particle shape, size, and density, as well as how the particles are distributed among each other. In *bed-load transport*, particles glide, roll, or briefly jump, staying close to the bed. *Suspended-load transport* occurs when finer particles

make larger jumps and remain surrounded by fluid. *Wash-load* involves particles that are rarely in contact with the bed and are carried through the flow. The *saltation load* refers to particles that jump in and out of contact with the bed. A review on bed-load transport is available in Raudkivi (1998) and Chien and Wan (1999).

Sediment transport can also vary over time. In a natural stream, fine and coarse materials are mixed, and under lower flow velocities, fine particles are transported downstream while coarse particles remain stationary and form *armor* layer. This armor layer, composed of coarse particles, acts as a protective shield for the streambed, reducing further erosion, enhancing the stability of bed and impacting the flow dynamics. Other processes affecting sediment transport include *overpassing* and *embedment*. *Overpassing* occurs when larger or smaller particles move over an immobile bed, and *embedment* refers to the burial of larger particles by finer material.

If τ_o = the time average of the applied shear stress, τ_c = the critical shear stress of the bed material, τ_i = the minimum shear stress required to move a particular exposed sand on the surface of the bed then there are four possible conditions:

- $\tau_i > \tau_c > \tau_o$ and $\tau_c > \tau_i > \tau_o$ no sand movement, the immobile bed.
- $\tau_o > \tau_c > \tau_i$ and $\tau_o > \tau_i > \tau_c$ all sands are in motion.
- $\tau_i > \tau_o > \tau_c$, embedment condition.
- $\tau_c > \tau_o > \tau_i$, overpassing condition.

2.2.5. Parameters affecting local scour

Pier scour is primarily influenced by fluid parameters, flow conditions, stream bed materials, and the characteristics of the pier. The time of scour also plays a significant role under these conditions. The parameters that influence the scour phenomena include: *Parameters characterizing the approach flow*, *channel geometry*, *bridge pier*, *fluid* (*water*), *bed material*, *time*, *and parameters related to the unsteadiness of the flow*.

According to Ettema et al. (2011), the parameters influencing d_s can be classified into primary and secondary categories. Primary parameters are directly related to the structure and geometric scales of the pier and the flow field, which determine the d_{sm}. These parameters have a direct impact on the development of d_s around the pier. On the other hand, secondary parameters influence the sensitivity of d_s within the limits of the geometric scale and typically lead to d_s that are less than the d_{sm}. Secondary parameters, while still important, generally have a lesser impact compared to the primary parameters in determining the ultimate d_s. The influence of parameters with dimension and dimensionless form is discussed in the following section.

2.2.6. Parameter influences

This section reviews how individual parameters affect scour and highlights knowledge gaps. Local d_s around pier is influenced by many interrelated factors, meaning the effect of one parameter may be overshadowed by others. This explains the wide variation in measured d_s under similar conditions. Factors such as sediment type, flow, and pier/channel geometry all

play crucial roles. While many studies have explored these factors (e.g., Laursen and Toch 1953, Ettema 1980, Melville and Sutherland 1988, Ettema et al. 2011) note that gaps still exist in fully understanding scour and predicting its depth.

(a) Pier diameter, d

One of the most significant factors affecting d_s is the d, which is commonly used to normalize d_s and allow data from different piers to be compared on a single curve. The d_s generally increases in proportion to the d (Raudkivi and Ettema 1983). Their research showed that the time to reach d_{se} also increases with d because the volume of the scour hole is proportional to the cube of the d, meaning larger piers create larger scour holes that take longer to erode. Franzetti et al. (2022) also reference circular piers in their study, as they provide a standard condition for considering various factors that can be adjusted with correction factors.

(b) Flow velocity, u

When discussing the relationship between u and d_s, it is essential to distinguish between the clear water and live bed regimes. The flow intensity (u/u_c) (where u_c is the critical u for the sediment motion), is a non-dimensional u parameter that indicates the u condition relative to the u_c, and helps differentiate between the live bed and clear water flow based on u/u_c. Some researchers prefer to shear velocity (u_*) with the corresponding critical value of it u_{*c}, as these are the true drivers for scour. However, the trends are similar, and the u/u_c is more commonly used due to its ease of measurement. According to Melville (2008), Chiew (1984), Raudkivi and Ettema (1983), and Raudkivi (1986), d_{se} increases almost linearly with u in the clear water regime (Fig. 2.7).

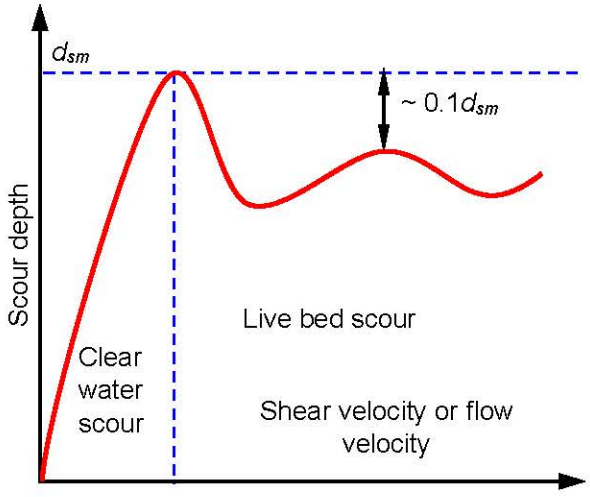

Fig. 2.7. Scour depth in clear water and live bed (Melville 2008).

(c) Sediment size, d_{50}

Sediment size (d_{50}) plays a crucial role in bridge pier scour. Larger sediment particles tend to settle and accumulate around the pier. In contrast, smaller particles are more easily carried away by the water flow, which could increase d_s. However, smaller sediment can fill in gaps

between larger particles, leading to denser accumulation and worsening scour. The effect of sediment size on scour depends on various factors, including u, sediment supply, and pier geometry. In non-cohesive sediment, erosion is influenced by factors like grain size distribution, d_{50}, sediment fall u, and mass density.

(d) Flow depth, *h*

The influence of h on d_s has been studied by many researchers (Chabert and Engeldinger 1956, Laursen and Toch 1956, Breusers et al. 1977, Melville and Chiew 1999). The presence of the pier in the channel creates a surface roller and a horseshoe vortex around the pier. The h affects local d_s by influencing the formation of these rollers. In deep flow conditions, where there is minimal interference between the two rollers (the bow wave and the horseshoe vortex), the local d_s depend primarily on the d. However, as the h decreases, the surface roller becomes more dominant, reducing the ability of the horseshoe vortex to entrain sediment. Consequently, in shallower flows, the local d_s is reduced, and in very shallow flows, the d_s becomes more dependent on h, particularly at wider piers.

(e) Pier shape

Piers come in various shapes, including circular, rectangular, square, rectangular with chamfered ends, oblong, lenticular, and Joukowski. The impact of pier shape on scour has been studied by different researchers (Breusers 1977, Breusers and Raudkivi 1991, Melville and Coleman 2000). A general conclusion is that blunter piers tend to cause deeper local scour. The shape of the downstream end of the pier is considered to have little effect on d_{sm}. To account for these variations, a shape factor is often used (Table 2.1). Melville and Chiew (1999) proposed shape factors for uniform piers (those with constant sections throughout their depth). Their results showed that for piers with the same projected width (140 mm), a circular pier caused the least scour, while a rectangular pier with blunt ends caused the most.

Table 2.1. Pier shape factor (Shukur and Obeid 2016).

Pier shape	Shape factor
Circular	1.00
Lenticular	0.80
Joukowski profile	0.88
Oblong	0.85
Rectangular	1.11
Streamlined	0.48
Elliptical	0.80
Chamfered	1.01

(f) Effect of pier alignment, *a*°

The pier alignment, or the $a°$, significantly impacts the local d_s, especially for non-circular pier shapes. As the angle of attack increases, the d_s also increases due to the larger projected

width of the pier (Melville and Coleman 2000). For example, d_s at a rectangular pier nearly triples at a 30° angle compared to a pier with zero angle. Breusers and Raudkivi (1991) noted that the effect of $a°$ could be ignored for values up to 5° to 10°, but Ettema et al. (2011) reported that the influence of parameters like h and sediment grain size can affect the d_s in combination with the angle of attack.

(g) Angle of repose, φ_r

The angle of repose, also called the angle of friction, is the maximum stable slope formed by sediments, determined by friction, cohesion, and particle shapes. It represents the internal angle between the surface of a material pile and the horizontal surface, forming a conical shape. The angle of repose is influenced by the density of material, surface area, and coefficient of friction, with materials having a low angle forming flatter piles than those with a high angle. This property is essential for understanding the stability of loose materials, such as sand or rock, and is crucial for engineering and landscaping purposes.

(h) Effect of time, t

Different studies have investigated the d_{st}, with key findings that indicate that d_s development is typically asymptotic. Ettema et al. (2011) highlighted that the scour rate and equilibrium depth differ between clear water and live bed conditions. Under clear water, d_s gradually approaches an equilibrium value over time, while in live bed conditions, equilibrium is reached more quickly, but d_s can fluctuate due to the movement of bed material. As a result, the time variation in d_s is less significant in live bed conditions. Chabert and Engeldinger (1956) suggested that equilibrium occurs when the d_s stops changing noticeably. Ettema (1980) identified three distinct phases of the scour process:

- *Initial phase*: Rapid scouring occurs due to the downflow at the upstream face of pier, with sediment transport starting at the sides of piers. The horseshoe vortex is not yet significant.
- *Principal phase*: The horseshoe vortex becomes the dominant factor, creating a narrow scour hole around the pier. As the hole deepens, the vortex and downflow are less effective at removing sediment.
- *Equilibrium phase*: Scour stops developing significantly, and the scour hole stabilizes.

(i) Densimetric Froude number, F_d

The densimetric Froude number is defined as $F_d = u/(g'h)^{0.5}$ [$g' = g(\Delta - 1)$], where $\Delta = \rho_s/\rho_f - 1$, ρ_s/ρ_f is the relative density of sand, ρ_s is the bed material density, ρ_f is the density of water, g is acceleration due to gravity and g' is the reduced g. The theoretical critical value is unity, therefore, if $F_d > 1$, no saline wedge will form. In practice, values of F_d as well as 0.6 to 0.7 prevent the formation of a saline wedge. Therefore, for the condition, $F_d < 0.6$, a salt wedge will form.

2.2.7. Influence of non-dimensional parameters

This could be attributed to challenges in performing laboratory flume experiments on large geometric scales or the lack of reliable field data. Melville and Coleman (2000) published comprehensive works that detail the factors influencing scour at bridge piers.

(a) Effect of sediment non-uniformity, σ

Sediment non-uniformity is characterized using the geometric standard deviation (σ) of sediment particles, calculated as $\sigma = (d_{84}/d_{16})^{0.5}$. Melville and Coleman (2000) noted some experimental studies on non-uniform sediment under live-bed conditions, conducted by Chiew (1984). These studies were performed at the threshold motion condition for the sediment used. The results show that as the geometric standard deviation (σ) increases, the rate of scouring and equilibrium d_s decrease. Furthermore, for non-uniform sediment, near the threshold condition ($u/u_c \approx 1$), armoring occurs at the base of the scour hole, significantly reducing the local d_s. The effect of non-uniformity is less significant at higher u/u_c values when the flow can carry most sediment particles. At intermediate u/u_c values, the effect of sediment non-uniformity diminishes as the u increases and transports more sediment. This trend is visually summarized in Fig. 2.8, which shows the impact of u/u_c on local d_s.

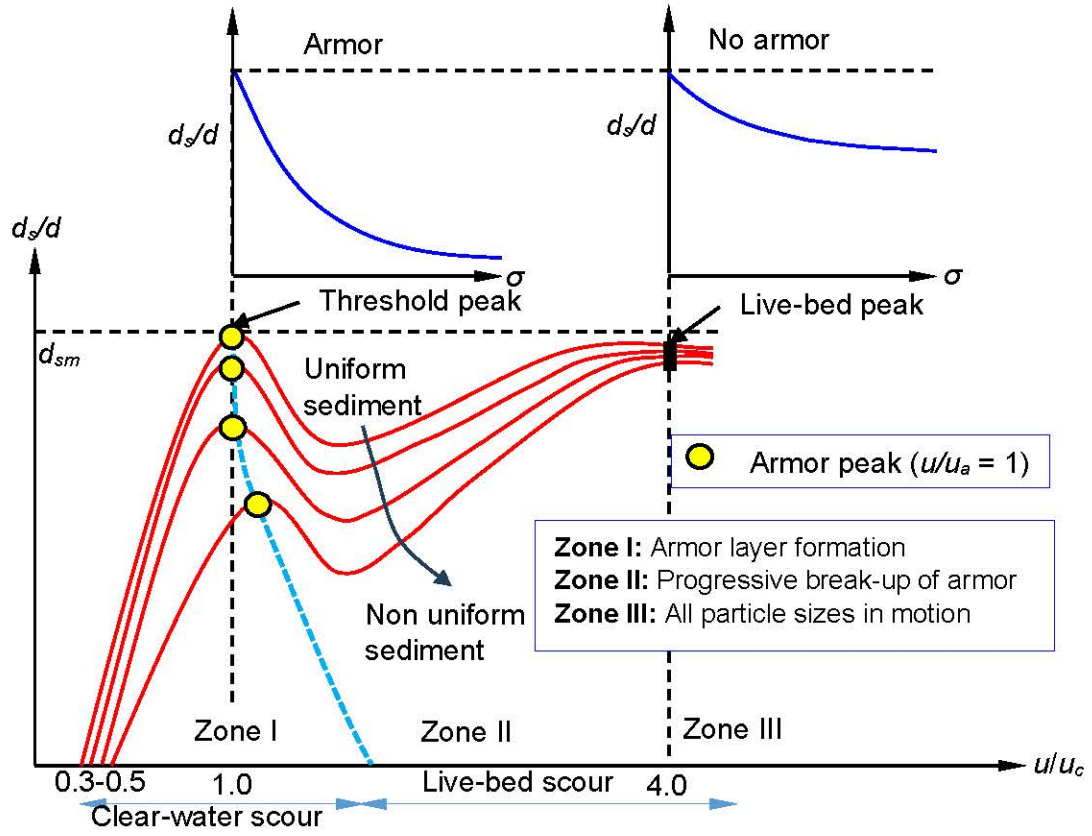

Fig. 2.8. Local scour depth variation with flow intensity and sediment non-uniformity (Melville 2008).

(b) Effect of flow intensity, u/u_c

Melville and Coleman (2000) defined u/u_c as the ratio of the free stream u to the u_c of the sediment. This ratio helps classify local scour at piers into two conditions: clear water scour

and live bed scour. Clear water scour occurs when the u is up to the threshold condition, where $u/u_c \approx 1$. In this condition, no sediment is supplied to the scour hole, and sediment movement occurs only around the obstruction (e.g., bridge piers). In contrast, live bed scour happens when the ratio u/u_c is greater than 1, and sediment is continuously supplied to the scour hole from the upstream side. Under clear-water conditions, the local d_s in uniform sediment increases almost linearly with u, reaching a maximum at the threshold u, called the threshold peak. As the u exceeds the u_c, the d_s decreases initially and then increases again to a second peak, known as the live-bed peak. However, the threshold peak is not exceeded if the sediment is uniform. The second peak occurs when sediment transport transitions to a flatbed stage. The variation of d_s with u/u_c is schematically shown in Fig. 2.9.

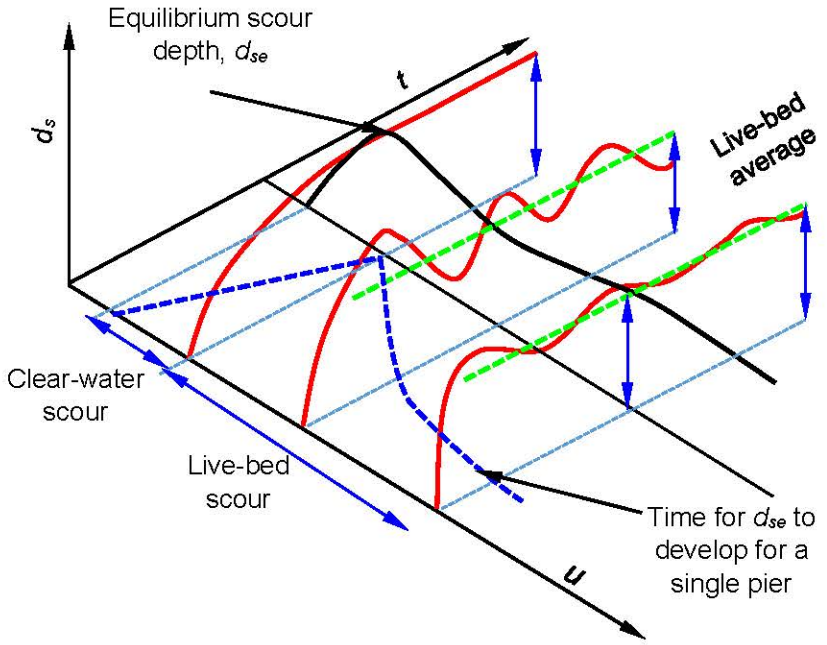

Fig. 2.9. Variation of local scour depth with flow velocity and time (Melville and Chiew 1999).

(c) Effect of flow shallowness, *h*/*d*

According to Raudkivi (1998), d_s is not affected by h when it exceeds three times the d. He reported that decreasing h increases the surface roller (bow wave), which reduces the strength of the downflow. As a result, d_s does not depend exactly on h. The h/d represents the relationship between h and d. Ettema et al. (2011) classified scour processes into three categories based on h/d ratio (Table 2.2). For narrow piers or deep flow (large h compared to pier width), d_s is proportional to pier width and independent of h. For shallow flow or wide piers, d_s is proportional to h and independent of pier width. For intermediate h, d_s depends on both h and d (Fig. 2.10).

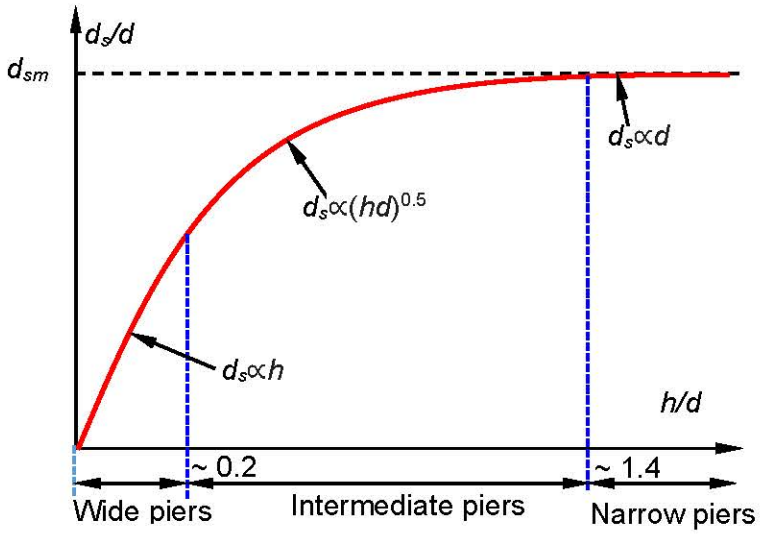

Fig. 2.10. Local scour depth variation with flow shallowness (Melville 2008).

Table 2.2. Classification of local scour processes at bridge piers (Ettema et al. 2011).

Pier class	Flow shallowness	Local scour dependence
Narrow	$h/d > 1.4$	$d_s \infty d$
Intermediate/Transitional	$0.2 < h/d < 1.4$	$d_s \infty (dh)^{0.5}$
Wide	$h/d < 0.2$	$d_s \infty h$

(d) Effect of pier Froude number, F_B and Reynolds number, R_p

According to Ettema et al. (2006), the Pier Froude number $F_B = u/(gd)^{0.5}$, and pier Reynolds number $R_p = ud/v$, are key parameters used to characterize the turbulence structure and vortex shedding frequency around piers. They suggested that d_s does not scale linearly with pier width unless there is complete similitude in pier, flow, and sediment conditions, leading to deeper scour in laboratory flumes. While the R_p does not significantly affect d_s, it influences the vortex shedding frequency. Ettema et al. (2006) also found that the Fr can describe the energy gradient around the pier, with narrower piers resulting in a higher Fr and, consequently, a smaller d_s. A correction factor for the Fr effect in laboratory tests was also defined. The variation of d_s with Fr is shown in Fig. 2.11.

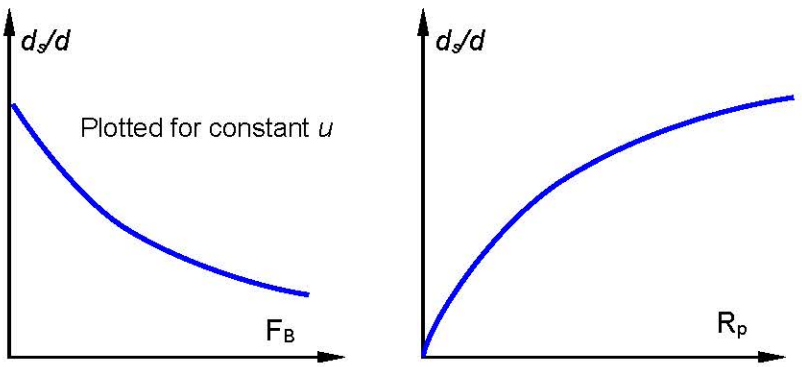

Fig. 2.11. Local scour depth variation with large-scale turbulence (Melville 2008).

(e) Effect of sediment coarseness, d/d_{50}

The parameter d/d_{50} represents the relative coarseness of the flow boundary. Melville and Coleman (2000) noted that for uniform sediments, local d_s is unaffected by coarseness, but larger sediment sizes do influence the d_s. When the d/d_{50} is less than 50, the local d_s is influenced by the sediment size. Raudkivi and Ettema (1983) classified d/d_{50} into four groups:

- $d/d_{50} \geq 130$: Sediment is fine relative to the d, with sediment entrained by both the downflow and horseshoe vortex until equilibrium is reached.
- $130 > d/d_{50} \geq 30$: Intermediate-size sediment, mainly entrained from the groove, with limited entrainment under the horseshoe vortex and sediment supply via sliding.
- $30 > d/d_{50} \geq 8$: Coarse sediment relative to the d, with significant energy dissipation in the coarse material at the base of scour hole.
- $d/d_{50} < 8$: Stones are so large that the erosion phase does not develop, with scour mainly due to entrainment at the pier flanks.

Breusers and Raudkivi (1991) found that when the mean grain size of sediment ($d_{50} < 0.7$ mm), ripples form on the bed, preventing a flatbed under clear-water conditions, while $d_{50} > 0.7$ the ripple does not form. Local scour is not maintained for ripple-forming sediments under clear water. Ettema et al. (2011) observed that for uniform sediment, local d_s is affected by d/d_{50} when the sediment is large or small. For coarse sediments, the rough bed dissipates some energy, reducing d_s. When $d/d_{50} < 8$, the sediment particles are large and scour mainly occurs at the sides of pier, further reducing d_s (Fig. 2.12).

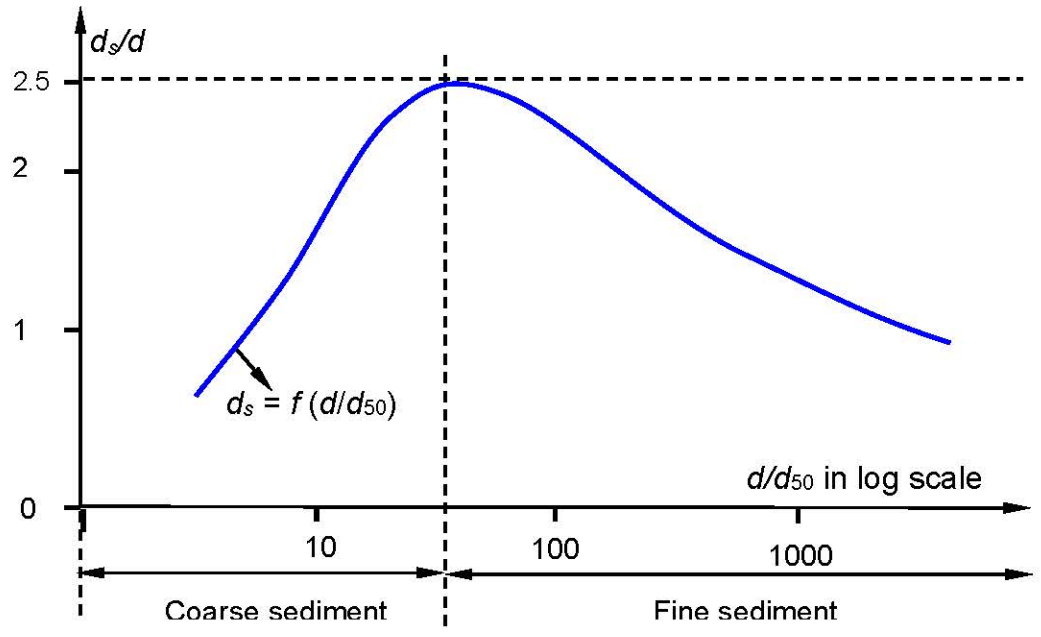

Fig. 2.12. Effect of sediment coarseness on local scour (Sheppard et al. 2006).

(f) Effect of constriction ratio, W/d

The d_{se} at a pier is influenced by the W/d, here, W is flume width. For experimental studies under clear-water scour conditions, the width of the experimental flume W should be at least eight times the d to minimize constriction effects. In the case of live-bed scour, the flume W

should be at least 10 times the d to avoid reductions in d_s caused by modifications to bed features as they propagate through the constriction (Raudkivi and Ettema 1983, Chiew and Melville 1987, Ballio et al. 2009, Ashtiani 2012).

2.2.7. Scour at pier groups

Scour patterns, depths, and extents around pier groups can differ from those around single piers due to the interaction and interference of flow and sediment transport processes. The spacing and alignment of piers are important factors that influence the scour process. In addition to local scour at individual piers, a global scour can form around the entire structure because of flow obstruction, constrictions, and increased turbulence, often resulting in deeper d_s, especially at the corners of pier groups. Four mechanisms affecting scour at pier groups, which are not seen in single pier scouring, are given below. The schematic diagram of two piers in eccentric arrangements is shown in Fig. 2.13.

(a) Reinforcing

When the scour holes from a downstream pier overlap with those of the front pier, it results in increased d_s at the front pier. This occurs because, at the base of a scour hole, a dynamic equilibrium is established where bed material is lifted by the flow but remains within the hole as the flow cannot fully remove it. If the overlap causes the bed level at the rear of the upstream hole to lower, it becomes easier for the flow to carry material away, deepening the scour. As the distance between the piers increases, this effect diminishes and eventually disappears when the bed level between the piers returns to its original state. This phenomenon can be seen in case tandem as well as for eccentric pier arrangements when piers are placed close enough where the overlapping of scour hole can occur as can be seen in Fig. 2.13.

(b) Sheltering

An upstream pier can reduce the u for downstream piers, diminishing the "horse-shoe vortex" effect and reducing scour at those piers. Another sheltering effect occurs when material scoured from the upstream pier is deposited in front of the downstream pier, causing the flow to deflect upward and around it. This deflection weakens the horse-shoe vortex at the downstream pier, reducing its impact. As the distance between the piers increases, the u deficit behind the upstream pier diminishes, and the sheltering effect becomes negligible. This also can be seen for tandem piers and eccentric piers with very low flow skew angle (φ°).

(c) Shed vortices

Vortices shed from an upstream pier are carried downstream along specific paths. If a second pier is placed near one of these paths, the vortices can help lift material from the scour hole, increasing the scouring effect. The scouring efficiency of these vortices depends on their speed and the distance between their path and the downstream pier. This effect diminishes more quickly for piers aligned with the flow than for those positioned at angles that place downstream piers in the vortex paths. Moreover, the d_s at a downstream pier may increase if

it lies in the path of vortices shed by an upstream pier, with the scouring influenced by the u and the location of the pier.

(d) Compressed horseshoe vortex

The d_s increases when multiple piers are placed close together across the flow. Each pier generates its own horseshoe vortex and as the spacing between the piers decreases, the inner arms of these vortices are compressed. This compression increases the flow velocities within the vortices, leading to deeper scour. This effect is not limited to perpendicular flow. It also occurs at other angles of attack, with the significance of the d_s depending on the spacing between the piers for any given angle.

2.2.8. Two pier group

The d_s at the front pier is relatively unaffected by changes in the flow skew angle (φ). For most configurations, especially at small angles, the front pier experiences d_s as a single pier due to the flow dynamics around it. The primary flow phenomenon influencing the front pier is the interaction of the flow with the horse-shoe vortex, which can result in an increased d_s at lower angles but becomes relatively constant for larger pier separations (Fig. 2.13). Whereas the reinforcing effect can increase the d_s at the front pier slightly higher compared to the single pier case.

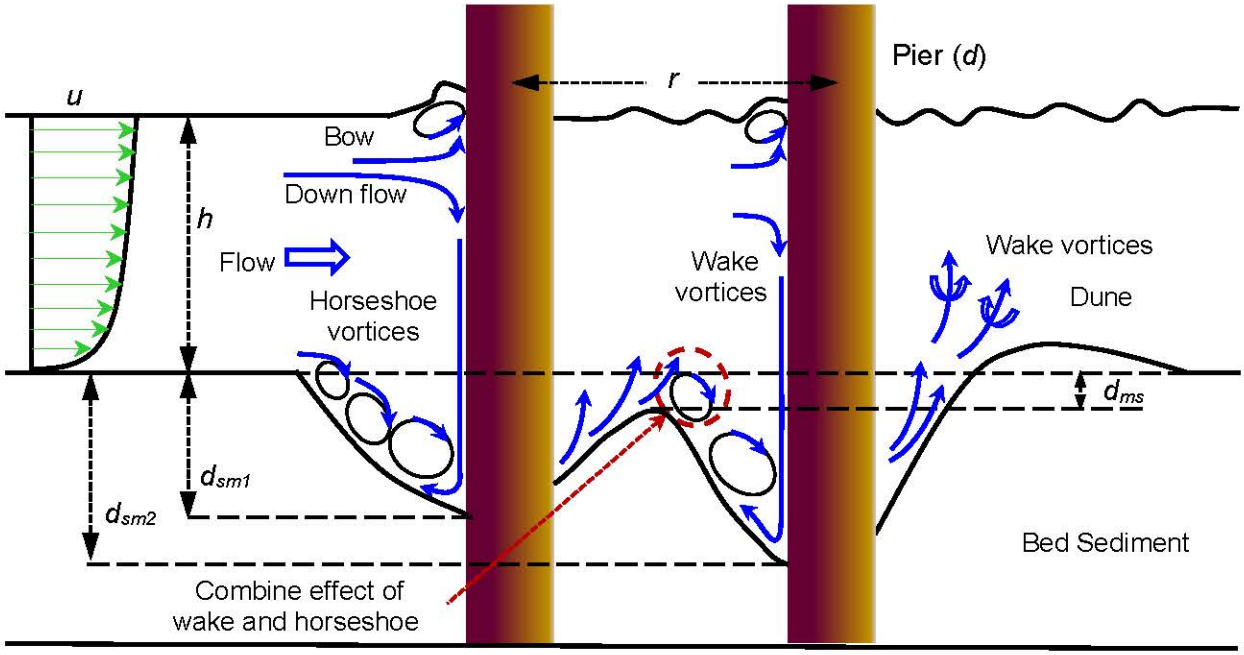

Fig. 2.13. Schematic diagram of flow pattern and local scour around two eccentric piers.

The rear pier is more sensitive to changes in the flow direction, as it is influenced by various flow effects such as sheltering from the front pier and the vortices shed from it. At small angles ($\varphi < 15°$), sheltering by the front pier reduces the d_s at the rear pier. As the angle increases, this sheltering effect decreases, and the rear pier starts to experience increased scour

due to the interaction with the shed vortices. The d_s increases to a maximum at an angle of around 45°, after which it begins to decrease as the rear pier moves away from the shed vortices, approaching the d_s seen for a single pier.

When the spacing between the two piers is small, the vortices generated by the front pier influence the d_s of rear pier. At very close spacing, the vortices become compressed between the piers, leading to higher velocities and stronger scouring effects. As the spacing increases, the piers begin to act more independently, and the d_s at both piers start to resemble those observed at a single pier. Furthermore, larger separations result in minimal interactions between the piers, and the bed level between them returns to its original state, with scour of each pier resembling that of a single pier under similar flow conditions.

(a) Tandem (φ = 0°)

- Figure 2.14(a) shows how the d_s at individual piers and the bed level between them are influenced by the relative spacing r/d, where r is the clear distance between the centerlines of the piers, and d is the common diameter of the piers.
- For two piers in contact (r/d =1), the d_s at the front pier matches that of a single pier (d_{ss}). As the separation increases, the front pier experiences a reinforcing effect, which peaks at r/d =2.5 and persists until r/d = 11. Beyond this spacing, the d_s return to that of a single pier.
- With three piers aligned and equally spaced up to r/d = 6, the middle pier experiences deeper scour, while the third pier has a shallower d_s compared to the downstream pier in a two-pier arrangement.

(b) Side by side (φ = 90°)

- Figure 2.14(b) shows test results where two piers were positioned at right angles to the flow. Both piers experienced similar d_s (±2 mm), and the average results were used to create a single curve. The d_s at the midpoint between the piers is also displayed.
- With r/d = 1, the d_s reached 1.93d_{ss}. This aligns with the idea that d_s is related to the front width of the pier. As the separation increases, the d_s decrease rapidly to 1.3d_{ss} at r/d = 1.5. When r/d > 8, the d_s becomes similar to that of a single pier. At r/d = 11, the scour holes are distinct, and the bed between the piers returns to its original level.
- At close spacing (e/d <2), increased scouring is due to the larger effective pier width. When r/d >2, separate horseshoe vortices form, and between the piers, these vortices are compressed, leading to higher velocities and more scouring. This effect diminishes as r/d increases and disappears at r/d =8.

(c) Eccentric (φ = 45°)

- Figure 2.14(c) shows that for two piers aligned at a 45° angle to the flow, the d_s were 1.77d_{ss} for twin piers. This is slightly exceeding the expected linear dependence based on frontal width.
- The d_s at the rear pier was greater than at the front pier for all r/d between 1 and 11, with piers acting independently at larger separations, resulting in d_s similar to d_{ss}.

- The increased scour at the rear pier was due to the combined effects of vortices shed from the front pier and compression of horseshoe vortices between the piers, with the maximum difference in d_s occurring at $r/d = 4$.

(d) Effect of angle of attack, φ for two pier groups

- In the tests with $r/d = 5$, the d_s at the front pier showed minimal sensitivity to the φ, varying by less than 5% across angles from 0° to 90° (Fig. 2.14d).
- The d_s at the rear pier was more sensitive to changes in φ, influenced by mechanisms like sheltering and the impact of shed vortices. The d_s increased with the angle, peaking around 45° for $r/d = 5$.
- At small angles ($\varphi < 15°$), sheltering from the front pier was the dominant effect. As φ increased, sheltering diminished, and the rear pier was affected more by shed vortices, leading to increased d_s, which then decreased as the angle approached 90°, nearing single pier scour conditions.

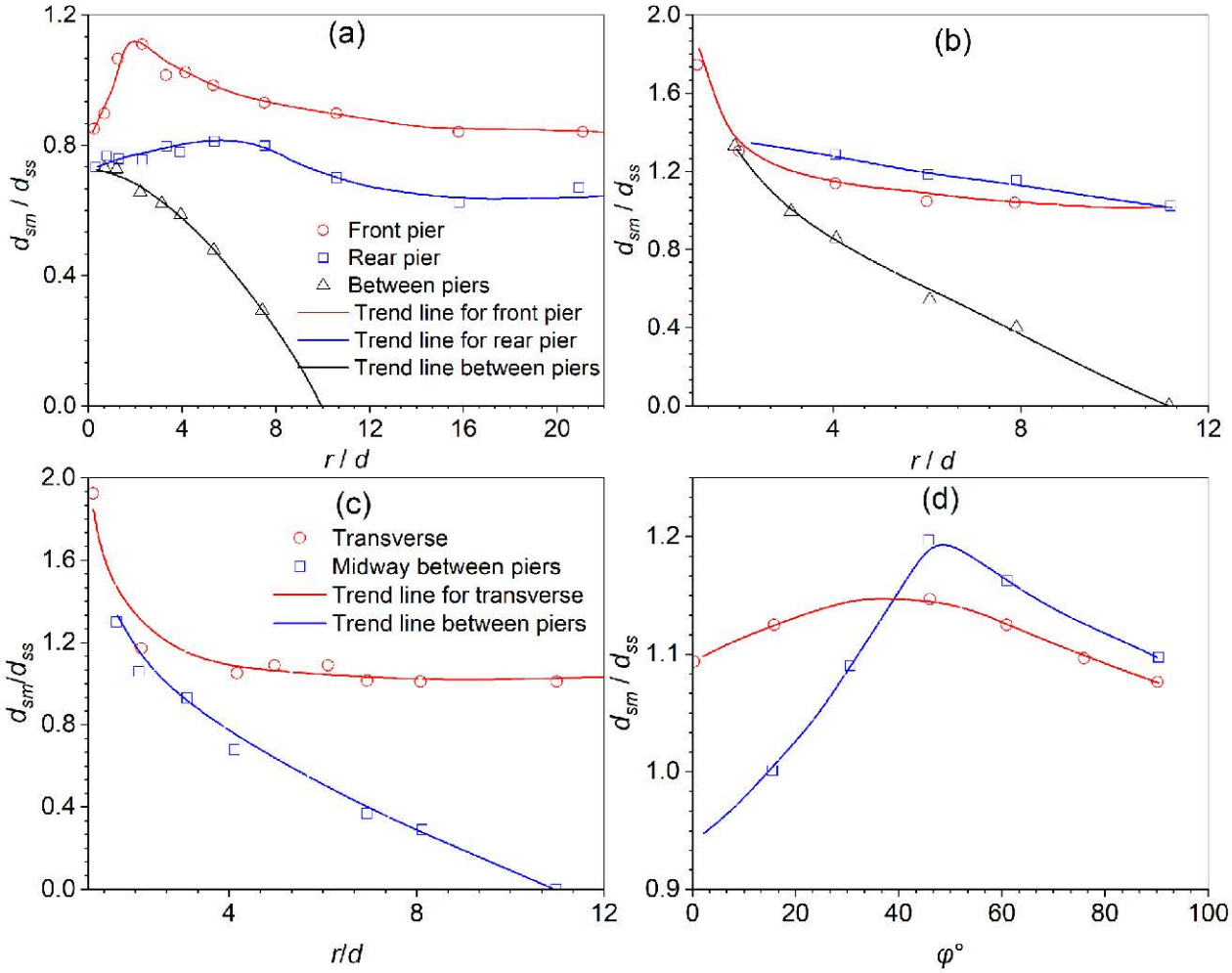

Fig. 2.14. Scour depths around **(a)** two tandem piers represented as a function of non-dimensional pier spacing (r/d), **(b)** two side by side piers represented as a function of r/d, **(c)** two piers positioned with an angle of attack of 45° represented as a function of r/d, and **(d)** two piers spaced $5d$ apart as function of φ° (Breusers and Raudkivi 2006).

2.2.9. The empirical formula for pier scour

The d_s formula developed to date along with its strengths and limitations is crucial for evaluation and establishing a new formula based on the existing scenario. The formula for temporal scour around isolated pier is given in Table 2.3, and the formula for maximum scour around isolated pier is given in Table 2.4. The formula for different two pier arrangements is given in Table 2.5. To explain each formula the following notation is used: d_{sm} is the maximum d_s, d_* is the projected width of the pier, d_{50} is median sediment size, D_* is dimensionless grain size, D_{*G} is dimensionless grain size, Froude number Fr = $u/\sqrt{(gh)}$, F_B is pier Fr (= $u/\sqrt{gd}$), F_c is critical Fr (= $u_c/\sqrt{gh}$), $F_{B,c}$ is critical F_B (= $u_c/\sqrt{gd}$), $F_{d,c}$ is critical densimetric Froude number (= $u_c/\sqrt{\Delta ghd_{50}}$), R_* is particle Reynolds number (= ud_{50}/v), R_{*c} is critical R_p (= $u_{*c}d_{50}/v$), u_a armoring u, u_p is live bed peak u, v is *k*inematic viscosity, σ is geometric standard deviation, t_R is reference time, F_{di} is F_d for threshold movement in u, d_{sl} is Lacey regime depth, Q is discharge, q is discharge per unit width.

(a) Temporal formula for isolated pier

Various studies have developed formulas to predict d_s around bridge piers over time (d_{st}). Early research created models based on limited flow and sediment parameters, while others used constants to describe the evolution of d_s. Some studies examined the influence of factors like bed-particle density and flow strength, proposing time-dependent relationships for d_s. Refinements in predictive models improved accuracy by adjusting parameters or introducing new formulas. Data collected over long durations highlighted the role of d/d_{50}, and flow conditions in d_s evolution. Recent research has introduced predictive formulas using comprehensive datasets, improving the accuracy of d_s estimates and accounting for various influencing factors (Table 2.3).

Table 2.3. The literature formulas for temporal scour analysis for isolated circular pier.

Reference	Formulas
Shen et al. (1966)	$J = 0.026\exp(-2.932h)$ $R = \left(\frac{d}{h}\right)^{0.33} \mathrm{Fr}^{0.33} \ln\left(\frac{ut}{h}\right)$
Franzetti et al. (1982)	$\frac{d_{st}}{d_{se}} = 1 - \exp\left[-p_1\left(\frac{ut}{d}\right)^{p_2}\right]$ $p_1 = 0.028$, $p_2 = 1/3$.
Sumer et al. (1992)	$\frac{d_{st}}{d_{se}} = \left[1 - \exp\left(-\frac{t}{t_e}\right)\right]$ $t_e = 0.0005\left(\frac{d^2}{\sqrt{g\Delta d_{50}^3}}\right)\left(\frac{h}{d}\right)\left(\frac{u_*^2}{g\Delta d_{50}}\right)^{-2.2}$

Melville and Chiew (1999)	$\frac{d_{st}}{d_{se}} = \exp\left\{-0.03\left\lvert\frac{u_c}{u} ln\left(\frac{t}{t_e}\right)\right\rvert^{1.6}\right\}$ $\frac{u_c}{u_{*c}} = 5.75\log\left(5.53\frac{h}{d_{50}}\right)$ $u_{*c} = 0.0115 + 0.0125 d_{50}^{1.4}$ for d_{50} = 0.1-1.0 mm, $u_{*c} = 0.0305 d_{50}^{0.5} - 0.0065 d_{50}^{-1}$ for d_{50} = 1-100 mm, $t_e\,(\text{days}) = 48.26\frac{d}{u}\left(\frac{u}{u_c} - 0.4\right)$ for, h/d>6 $t_e\,(\text{days}) = 30.89\frac{d}{u}\left(\frac{u}{u_c} - 0.4\right)\left(\frac{h}{d}\right)^{0.25}$ for, $h/d \le 6$
Oliveto and Hagar (2002, 2005)	$\frac{d_{st}}{(hd^2)^{1/3}} = 0.068 S_{hn}\sigma^{-1/2} \mathrm{F_d}^{1.5} \log\left(\frac{t}{t_R}\right)$ $t_R = \frac{(hd^2)^{1/3}}{\sigma^{1/3}\sqrt{\Delta g d_{50}}}$, where S_{hn} = shape number (=1 for CBPs and =1.25 for rectangular abutments), R_h = hydraulic radius
Kothyari et al. (2007)	$\frac{d_{st}}{(hd^2)^{1/3}} = 0.272\sigma^{-1/2}\left(\mathrm{F_d} - \mathrm{F_{d\beta}}\right)^{2/3} \log\left(\frac{t}{t_R}\right)$ $t_R = \frac{(hd^2)^{1/3}}{\sigma^{1/3}\sqrt{\Delta g d_{50}}}$ $\mathrm{F_{d\beta}} = \left[\mathrm{F_{di}} - 1.26\left(\frac{d}{W}\right)^{1/4}\left(\frac{R_h}{d_{50}}\right)^{1/6}\right]\sigma^{1/3}$ $\mathrm{F_{di}} = 2.33 D_*^{-1/4}\left(\frac{R_h}{d_{50}}\right)^{1/6}$ for, D_*< 10 $\mathrm{F_{di}} = 1.08 D_*^{1/12}\left(\frac{R_h}{d_{50}}\right)^{1/6}$ for, D_* = 10-150 $\mathrm{F_{di}} = 1.65\left(\frac{R_h}{d_{50}}\right)^{1/6}$ for, $D_* \ge 150$ Here, D_* = dimensionless grain size = $\{(S_s\text{-}1)\, g/v^2\}^{1/3} d_{50}$, $\mathrm{F_{di}} = \mathrm{F_d}$ for threshold movement in u.
Sheppard et al. (2011)	$\frac{d_{st}}{d_{se}} = \exp\left\{-0.04\left\lvert\frac{u_c}{u} \ln\left(\frac{t}{t_e}\right)\right\rvert^{1.6}\right\}$ $t_e(\text{days}) = 200(\text{days/sec})\frac{d}{u}\left(\frac{u}{u_c} - 0.4\right)$ for, h/d> 6, u/u_c>0.4 $t_e(\text{days}) = 127(\text{days/sec})\frac{d}{u}\left(\frac{u}{u_c} - 0.4\right)\left(\frac{h}{d}\right)^{0.25}$ for, $h/d \le 6$, u/u_c>0.4
Lança et al. (2013)	$\frac{d_{st}}{d_{se}} = \left[1 - \exp\left(-a_1\left(\frac{ut}{d}\right)^{a_2}\right)\right]$

	$a_1 = 1.22\left(\frac{d}{d_{50}}\right)^{-0.764}$ and, $a_2 = 0.09\left(\frac{d}{d_{50}}\right)^{0.244}$
Choi and Choi (2016)	$\frac{d_{st}}{d_{se}} = \exp\left\{0.065\left(\frac{u}{u_c}\right)^{0.95}\left(\frac{h}{d}\right)^{0.19} ln\left(\frac{t}{t_e}\right)\right\}$ $t_e\,(\min) = 18.94\left(\frac{u^2}{u_c d}\right)\left(\frac{h}{d}\right)\left(\frac{d}{d_{50}}\right)^{2.6}$ for, $h/d>6$ $t_e\,(\min) = 0.36\left(\frac{u^2}{u_c d}\right)^{-1}\left(\frac{h}{d}\right)^{0.52}\left(\frac{d}{d_{50}}\right)^{2.6}$ for, $h/d\leq 6$
Aksoy et al. (2017)	$\frac{d_{st}}{d} = 0.8\left(\frac{u}{u_c}\right)^{3/2}\left(\frac{h}{d}\right)^{0.15}\log(T_s)$ where $T_s = td_{50}(\Delta g d_{50})^{0.5}/d^2$.
Franzetti et al. (2022)	$\frac{d_{st}}{d} = af_1\left(\frac{h}{d}\right)f_2\left(\frac{d}{d_{50}}\right)f_3(\sigma)f_4\left(\frac{u}{u_c}\right)f_5\left(\frac{ut}{d\Delta^{0.5}}\right)$ $f_1\left(\frac{h}{d}\right) = 1 - 0.675e^{-1.451\left(\frac{h}{d}\right)}$ $f_2\left(\frac{d}{d_{50}}\right) = 0.849\left\{\left(\frac{d}{d_{50}}\right)^{1.815} e^{-2.990\left(\frac{d}{d_{50}}\right)^{0.235}} + 0.511\right\}$ $f_3(\sigma) = 0.740\left[e^{-0.066\sigma^{3.923}} + 0.416\right]$ $f_4\left(\frac{u}{u_c}\right) = \begin{cases} 1 - 2.017\left\{1 - \left(\frac{u}{u_c}\right)\right\}^3 & \text{if } \frac{u}{u_c} \leq 1 \\ 1 & \text{if } \frac{u}{u_c} > 1 \end{cases}$ $f_5\left(\frac{ut}{d\Delta^{0.5}}\right) = 1 - e^{-0.083\left(\frac{ut}{d\Delta^{0.5}}\right)^{0.231}}$ where, $a = 2.57$ and parameter functions f_1 to f_5 are calculated using Eqs. 2.34-2.38.

(b) Predictive maximum scour formula for isolated pier

The literature provides various formulas for estimating maximum d_s, predominantly derived from laboratory data from existing literature detailed in the following section (Table 2.4). These formulas are often utilized for calculating d_s without direct comparison to the vast literature data. Below are these formulas along with the variables upon which they are based. Additionally, when available, flume-specific formulas for calculating u_c are provided. These formulas are valuable tools for predicting d_s in different scenarios, drawing from a wealth of

experimental data compiled in the literature. However, their application warrants careful consideration and validation against specific conditions, especially in the context of flume studies.

Table 2.4. The formulas for maximum scour analysis for isolated circular pier.

Reference	Isolated pier formulas maximum scour depth
Nandi and Das (2023)	$\frac{d_{sm}}{d}=\lambda_1 f_1\left(\frac{u}{u_c}\right)f_2\left(\frac{h}{d}\right)f_3(\sigma)f_4\left(\frac{d}{d_{50}}\right)f_5\left(\frac{ut}{d\Delta^{0.5}}\right)f_6\left(\frac{d}{W}\right)$ $f_1\left(\frac{u}{u_c}\right)=\begin{cases}1.1791\left(\frac{u}{u_c}\right) & 0.4\le\frac{u}{u_c}\le 1\\ 1 & \frac{u}{u_c}>1\end{cases}$ $f_2\left(\frac{h}{d}\right)=\begin{cases}0.7786\left(\frac{h}{d}\right)^{0.1759} & \frac{h}{d}\le 4\\ 1 & \frac{h}{d}>4\end{cases}$ $f_3(\sigma)=0.3538+\frac{0.6854}{1+\exp\left[6.9924\ln\left(\frac{\sigma}{1.7196}\right)\right]}$ $f_4\left(\frac{d}{d_{50}}\right)=0.8491\left[\left(\frac{d}{d_{50}}\right)^{1.8158}\exp\left\{-2.9905\left(\frac{d}{d_{50}}\right)^{0.2350}\right\}+0.5112\right]$ $f_5\left(\frac{ut}{d\Delta^{0.5}}\right)=1-\exp\left\{-0.1000\left(\frac{ut}{d\Delta^{0.5}}\right)^{0.2000}\right\}$ $f_6\left(\frac{d}{W}\right)=\exp\left\{-2.0325\left(\frac{d}{W}\right)^{2.0211}\right\}$ where, $\lambda_1 = 2.86$.
Franzetti et al. (2022)	$\frac{d_{sm}}{d}=\lambda_2 f_1\left(\frac{h}{d}\right)f_2\left(\frac{d}{d_{50}}\right)f_3(\sigma)f_4\left(\frac{u}{u_c}\right)f_5\left(\frac{ut}{d\Delta^{0.5}}\right)$ $f_1\left(\frac{h}{d}\right)=1-0.675e^{-1.451\left(\frac{h}{d}\right)}$ $f_2\left(\frac{d}{d_{50}}\right)=0.849\left\{\left(\frac{d}{d_{50}}\right)^{1.815}e^{-2.990\left(\frac{d}{d_{50}}\right)^{0.235}}+0.511\right\}$ $f_3(\sigma)=0.740\left(e^{-0.066\sigma^{3.923}}+0.416\right)$

	$f_4\left(\frac{u}{u_c}\right)=\begin{cases}1-2.017\left\{1-\left(\frac{u}{u_c}\right)\right\}^3 & \text{if } \frac{u}{u_c}\le 1\\ 1 & \text{if } \frac{u}{u_c}>1\end{cases}$ $f_5\left(\frac{ut}{d\Delta^{0.5}}\right)=1-e^{-0.083\left(\frac{ut}{d\Delta^{0.5}}\right)^{0.231}}$ where, $\lambda_2 = 2.57$.
Hassan and Jalal (2021)	$\frac{d_{sm}}{d}=0.496-9.7\frac{u}{u_c}+0.01\frac{h}{d}-3.29\frac{d}{W}-0.388k+9.12\mathrm{F_B}-0.282\left(\frac{h}{d}\right)^2$
Vijayasree and Eldho (2021) or Modified IRC	$\frac{d_{sm}}{d}=1.34k_j\left(\frac{1}{d}\right)\left(\frac{q^2}{1.76\sqrt{d_{50}}}\right)^{1/3}$
Coscarella et al. (2020)	$\frac{d_{sm}}{d}=\frac{\Delta\mathrm{F_B}^2\left(k_b\frac{d}{d_{50}}\right)^{2/3}}{f\left(\frac{d_{50}}{\xi},\frac{d}{d_{50}}\right)}$ $f\left(\frac{d_{50}}{\xi},\frac{d}{d_{50}}\right)=k_c\left[0.22\left(\frac{d_{50}}{\xi}\right)^{-0.6}+0.12\exp\left\{-17.77\left(\frac{d_{50}}{\xi}\right)^{-0.6}\right\}\right]\left\{1+6\exp\left(-0.18\frac{d}{d_{50}}\right)\right\}$ $\xi=\left[\frac{\nu^3 d}{k_b\left(\frac{u}{u_c}\right)^3}\right]^{1/4}$, where, the drag coefficient is $k_b = 1.2$ and $k_c = 28$.
Pandey et al. (2018)	$\frac{d_{sm}}{d}=0.987\left(\mathrm{F_d}\right)^{-0.302}\left(\frac{h}{d}\right)^{0.434}\left(\frac{d}{d_{50}}\right)^{0.079}$
Aksoy et al. (2017)	$\frac{d_{sm}}{d}=0.8\left(\frac{u}{u_c}\right)^{3/2}\left(\frac{h}{d}\right)^{0.15}\log\left(T_s\right)$ where, $T_s=\frac{t_e d_{50}\left(\Delta g d_{50}\right)^{0.5}}{d^2}$
Kim et al. (2015)	$\frac{d_{sm}}{d}=0.69\left(\frac{h}{d}\right)^{0.65}\left(\frac{d_{50}}{h}\right)^{-0.10}\sigma^{0.39}\mathrm{Fr}^{0.56}$
Sheppard et al. (2014)	$\frac{d_{sm}}{d_*}=2.5f_1\left(\frac{h}{d}\right)f_2\left(\frac{u}{u_c}\right)f_3\left(\frac{d}{d_{50}}\right)$ $f_1\left(\frac{h}{d}\right)=\tanh\left[\left(\frac{h}{d}\right)^{0.4}\right]$ $f_2\left(\frac{u}{u_c}\right)=1-1.20\left[\ln\left(\frac{u}{u_c}\right)\right]^2$

	$f_3\left(\frac{d}{d_{50}}\right)=\left[\frac{\left(d/d_{50}\right)}{0.4\left(d/d_{50}\right)^{1.2}+10.6\left(d/d_{50}\right)^{-0.13}}\right]$ $u_{*c}=\left\{16.2d_{50}\left[\frac{9.09\times10^{-6}}{d_{50}}-d_{50}\left(38.76+9.6\ln\left(d_{50}\right)\right)-0.005\right]\right\}^{1/2}$ where for $R_{*c}>70$ $u_c=2.5u_{*c}d_{50}\left\{73.5\frac{h}{d_{50}}\left[R_{*c}\left(2.85-0.58\ln\left(R_{*c}\right)+0.002R_{*c}\right)+\frac{111}{R_{*c}}-6\right]^{-1}\right\}$ where for $5 < R_{*c} <70$ $u_c=2.5u_{*c}\ln\left(\frac{2.21h}{d_{50}}\right)$ To obtain a real value for u_c, $d_{50}<0.1$ mm is required.
Lança et al. (2013)	$\frac{d_{sm}}{d}=f_1\left(\frac{h}{d}\right)f_2\left(\frac{d}{d_{50}}\right)f_3\left(\frac{t}{t_e},\frac{d}{d_{50}}\right)$ $f_1\left(\frac{h}{d}\right)=\begin{cases}2\left(\frac{h}{d}\right)^{1/3} & \text{if } 0.50\le\left(\frac{h}{d}\right)\le1.45\\ 2\left(\frac{h}{d}\right)^{0.5} & \text{if } \left(\frac{h}{d}\right)>1.45\end{cases}$ $f_2\left(\frac{d}{d_{50}}\right)=\begin{cases}1 & \text{if } 60<\left(\frac{d}{d_{50}}\right)\le100\\ 5.8\left(\frac{d}{d_{50}}\right)^{-0.38} & \text{if } 100<\left(\frac{d}{d_{50}}\right)\le500\\ 0.55 & \text{if } 500<\left(\frac{d}{d_{50}}\right)\end{cases}$ $f_3\left(\frac{t}{t_e},\frac{d}{d_{50}}\right)=1-\exp\left[-a_1\left(\frac{ut}{d}\right)^{a_2}\right]$ $a_1\left(\frac{d}{d_{50}}\right)=1.22\left(\frac{d}{d_{50}}\right)^{-0.764}\quad a_2\left(\frac{d}{d_{50}}\right)=0.09\left(\frac{d}{d_{50}}\right)^{0.244}$
Arneson et al. (2012)/ (HEC-18, CSU Equation)	$\frac{d_{sm}}{d}=2k_d\left(\frac{h}{d}\right)^{0.65}(\mathrm{Fr})^{0.43}$ Here, k_d from Johnson and Torrico (1994) $k_d=2.58\left(\frac{h}{d}\right)^{0.34}(\mathrm{Fr})^{0.65}$ Therefore, the equation can be written as follows-

	$\frac{d_{sm}}{d} = 5.16\left(\frac{h}{d}\right)^{0.99}(\mathrm{Fr})^{1.08}$
Guo (2012)	$\frac{d_{sm}}{d} = \left(\frac{h}{d}\right)^{0.5}\tanh\left(\frac{D_{*G}}{3.75\sigma}\right)$, Here, $D_{*G} = \left(\frac{u}{\sqrt{\Delta g d_{50}}}\right)$
Briaud et al. (2011)	$\frac{d_{sm}}{d} = 2.2k_k k_l d^{-0.35}\left(\frac{2u-u_c}{\sqrt{g}}\right)^{0.7}$ k_k = a coefficient based on the shape of the pier nose, 1.0 for circular- or round-nosed piers and k_l = a coefficient to correct for the skew of the pier to the approach flow.
Ettema et al. (2011)	$\frac{d_{sm}}{d} = 2.5\tanh\left(\frac{d_{50}}{h}\right)^{0.4}$
Lee and Strum (2009)	$\frac{d_{sm}}{d} = 2.4 f_1\left(\frac{h}{d}\right) f_2\left(\frac{d}{d_{50}}\right) f_3\left(\frac{u}{u_c}, \frac{u_a}{u_c}\right)$ $f_1\left(\frac{h}{d}\right) = \begin{cases} 1 & \text{if } \left(\frac{h}{d}\right) \geq 2.6 \\ 0.78\left(\frac{h}{d}\right)^{0.255} & \text{if } \left(\frac{h}{d}\right) < 2.6 \end{cases}$ $f_2\left(\frac{d}{d_{50}}\right) = \begin{cases} 5\log\left(\frac{d}{d_{50}}\right) - 4.0 & \text{if } 6 \leq \left(\frac{d}{d_{50}}\right) \leq 25 \\ \frac{1.8}{\left[0.02\left(\frac{d}{d_{50}}\right) - 0.2\right]^2 + 1} + 1.3 & \text{if } 25 \leq \left(\frac{d}{d_{50}}\right) < 10^4 \end{cases}$ $f_3\left(\frac{u}{u_c}, \frac{u_a}{u_c}\right) = \begin{cases} 1 & \text{if } \left(\frac{u}{u_c} - \frac{u_a}{u_c} + 1\right) \geq 1 \\ \frac{u}{u_c} - \frac{u_a}{u_c} + 1 & \text{if } \left(\frac{u}{u_c} - \frac{u_a}{u_c} + 1\right) < 1 \end{cases}$ Here, $u_{*c} = 0.03 d_{50}^{1/2}$, $u_{*ca} = 0.03 d_a^{1/2}$, $d_a = \frac{\sigma^m d_{50}}{1.8}$, m =1.65 for $d_{max} = d_{95}$, the diameter must be expressed in millimeters. $u_c = 5.75 u_{*c}\left[\log\left(5.53\frac{h}{d_{50}}\right)\right]$ and $u_{ca} = 5.75 u_{*ca}\left[\log\left(5.53\frac{h}{d_{50}}\right)\right]$, Here eventually, $u_a = 0.8 u_{ca}$, Conditioned to the fact that if $u_a < u_c$, then $u_a = u_c$.
Kothyari et al. (2007)	$\frac{d_{sm}}{(hd^2)^{1/3}} = 0.272\sigma^{-1/2}\left(\mathrm{F_d} - \mathrm{F_{d\beta}}\right)^{2/3}\log\left(\frac{t}{t_R}\right)$

	$\frac{d_{sm}}{d} = 0.272\left(\frac{h}{d}\right)^{1/3} \sigma^{-1/2}\left(\mathrm{F_d}\text{-}\mathrm{F_{d\beta}}\right)^{2/3} \log\left(\frac{t}{t_R}\right)$ $t_R = \frac{\left(hd^2\right)^{1/3}}{\sigma^{1/3}\sqrt{\Delta g d_{50}}}$ $\qquad$ $\mathrm{F_{d\beta}} = \left[\mathrm{F_{di}} - 1.26\left(\frac{d}{W}\right)^{1/4}\left(\frac{R_h}{d_{50}}\right)^{1/6}\right]\sigma^{1/3}$ $\mathrm{F_{di}} = 2.33 D_*^{-1/4}\left(\frac{R_h}{d_{50}}\right)^{1/6}$ where $D_* < 10$ $\mathrm{F_{di}} = 1.08 D_*^{1/12}\left(\frac{R_h}{d_{50}}\right)^{1/6}$ where D_* = 10-150 $\mathrm{F_{di}} = 1.65\left(\frac{R_h}{d_{50}}\right)^{1/6}$ where $\qquad D_* \geq 150$ Here, D_* = dimensionless grain size = $\{(S_s\text{-}1)\ g/\nu^2\}^{1/3} d_{50}$, $\mathrm{F_{di}} = \mathrm{F_d}$ for threshold movement in u.
Sheppard and Miller (2006)	$\frac{d_{sm}}{d_*} = 2.5 f_1\left(\frac{h}{d}\right) f_2\left(\frac{u}{u_c}\right) f_3\left(\frac{d}{d_{50}}\right)$ $f_1\left(\frac{h}{d}\right) = \tanh\left[\left(\frac{h}{d}\right)^{0.4}\right]$ $f_2\left(\frac{u}{u_c}\right) = 1 - 1.75\left[\ln\left(\frac{u}{u_c}\right)\right]^2$ $f_3\left(\frac{d}{d_{50}}\right) = \left[\frac{\left(\frac{d}{d_{50}}\right)}{0.4\left(\frac{d}{d_{50}}\right)^{1.2} + 10.6\left(\frac{d}{d_{50}}\right)^{-0.13}}\right]$
Muller and Wagner (2005)	$\frac{d_{sm}}{d} = 2.5 k_r k_s k_t k_u \left(\frac{h}{d}\right)^{0.35} \mathrm{F}^{0.43}$ Here, $k_u = 0.35\left(d/d_{50}\right)^{0.19}$, k_r = bed condition factor =1.1 for clear water scouring, k_s = Shape factor for pier, k_t = Alignment factor, k_u = Armoring factor.
Molinas (2004*a*)	$\frac{d_{sm}}{d} = 2.5 k_r k_s k_t k_u \left(\frac{h}{d}\right)^{0.35} \mathrm{Fr}^{0.43}$ Here, $k_u = 1.25 + 3\sqrt{\frac{d_{cfm}}{d_{50}}} u_R^{0.6} \ln\left(u_R + 0.5\right)$, $u_R = \frac{u - u_j}{u_{cm} - u_{j95}}$, $u_j = 2.65 h^{1/6} d_{35}^{1/3}$, $u_{cm} = 6.625 h^{1/6} d_{cfm}^{1/3}$, $d_{cfm} = \frac{d_{85} + 2d_{90} + 2d_{95} + d_{99}}{6}$
Molinas (2004*b*)	$\frac{d_{sm}}{d} = 0.99 k_r k_s k_t k_u k_v u_R^{0.55} d_{50}^{0.66} h^{0.17}\left(\frac{1}{d}\right)$,

	Here, $k_u = 1.25 + 3\sqrt{\frac{d_{cfm}}{d_{50}}} V_R^{0.6} \ln(u_R + 0.5)$, $k_v = \left(1 - \frac{u_j}{u}\right)^{0.45}$, $u_R = \frac{u - u_j}{u_{cm} - u_{j95}}$, $u_j = 2.65 h^{1/6} d_{35}^{1/3}$, $u_{cm} = 6.625 h^{1/6} d_{cfm}^{1/3}$, $d_{cfm} = \frac{d_{85} + 2d_{90} + 2d_{95} + d_{99}}{6}$, where, k_v = Scour initiation factor.
Oliveto and Hagar (2002)	$\frac{d_{sm}}{(hd^2)^{1/3}} = 0.068 k_e \sigma^{-1/2} \mathrm{F_D^{1.5}} \log\left(\frac{t}{t_R}\right)$ $\frac{d_{sm}}{d} = 0.068 k_e \left(\frac{h}{d}\right)^{1/3} \sigma^{-1/2} \mathrm{F_D^{1.5}} \log\left(\frac{t}{t_R}\right)$ Here, $t_R = \frac{(hd^2)^{1/3}}{\sigma^{1/3}\sqrt{\Delta g d_{50}}}$, k_e = shape number (=1 for CBPs and =1.25 for rectangular abutments).
Ali and Karim (2002)	$\frac{d_{sm}}{d} = \frac{k_w D_*^{1.2} h}{\frac{ud^2}{\nu}} \left[1 - \exp\left(-5.32 \times 10^{-4} \frac{ut}{h}\right)\right]$ Here, $k_w = 0.1\sqrt{\Delta g} d_{50}^{3/2} d D_*^{-0.3}$ and, $D_* = \left(\frac{\Delta g}{\nu^2}\right)^{1/3}$
Richardson and Davis (2001) or HEC 18	$\frac{d_{sm}}{d} = 2 k_f k_g \left(\frac{d}{h}\right)^{-0.35} \mathrm{Fr}^{0.43}$ Here, a correction factor k_f for the pier nose shape and k_g for the angle of attack flow.
Sheppard-Alkhalidi [Sheppard (2001) as reported by Alkhalidi (2001)]	$\frac{d_{sm}}{d} = \begin{cases} 1.5 k_m \left[2.5\left(\frac{u}{u_c}\right) - 1\right] & \text{if } 0.4 < \frac{u}{u_c} \le 1.0 \\ k_n \left(\frac{u_p - u}{u_c}\right) + k_o & \text{if } 1.0 < \frac{u}{u_c} \le \frac{u_p}{u_c} \\ 2.4 \tanh\left(\frac{h}{d}\right) & \text{if } \frac{u_p}{u_c} > \frac{u_p}{u_c} \end{cases}$, Here, $k_m = \frac{1.1 \tanh\left[1.775\left(\frac{h}{d}\right)^{0.618}\right]}{-0.025 + 0.233 \exp\left[0.334 \log_{10}(d/d_{50})\right]} + \frac{3.098}{\exp\left[2.411 \log(d/d_{50})\right]}$ $k_n = \frac{k - 2.4 \tanh\left[1.775\left(\frac{h}{d}\right)^{0.618}\right]}{\left(\frac{u_p}{u_c} - 1\right)}$, $k_o = 2.4 \tanh\left[1.775\left(\frac{h}{d}\right)^{0.618}\right]$

	$u_{p1}=5u_c$, $u_{p2}=0.6\sqrt{gh}$ and $u_p=\begin{cases}u_{p1} & \text{if } u_{p1}\geq u_{p2}\\ u_{p2} & \text{if } u_{p1}<u_{p2}\end{cases}$
Yanmaz (2001) (LBS)	$\frac{d_{sm}}{d}=1.564\left(\frac{h}{d}\right)^{0.405}\text{Fr}^{0.413}$
IRC:78 (2014)	$\frac{d_{sm}}{d}=2\times1.34\left(\frac{1}{d}\right)\left(\frac{q^2}{k_{sf}}\right)^{1/3}$, where, k_{sf} is silt factor $=1.76(d_{50})^{1/2}$
Melville and Chiew (1999)	$\frac{d_{sm}}{d}=f_1\left(\frac{h}{d}\right)f_2\left(\frac{d}{d_{50}}\right)f_3\left(\frac{u}{u_c},\frac{u_a}{u_c}\right)f_4\left(\frac{t}{t_e},\frac{u}{u_c}\right)$ $f_1\left(\frac{h}{d}\right)=\begin{cases}1 & \text{if } \left(\frac{h}{d}\right)\geq1.42\\ 2\left(\frac{h}{d}\right)^{0.5} & \text{if } 0.2\leq\left(\frac{h}{d}\right)\leq1.42\\ 4.5\left(\frac{h}{d}\right) & \text{if } \left(\frac{h}{d}\right)<0.2\end{cases}$ $f_2\left(\frac{d}{d_{50}}\right)=\begin{cases}1 & \text{if } \left(\frac{d}{d_{50}}\right)\geq25\\ 0.57\log\left[2.24\left(\frac{d}{d_{50}}\right)\right] & \text{if } \left(\frac{d}{d_{50}}\right)<25\end{cases}$ $f_3\left(\frac{u}{u_c},\frac{u_a}{u_c}\right)=\begin{cases}1 & \text{if } \left(\frac{u}{u_c}-\frac{u_a}{u_c}+1\right)\geq1\\ \frac{u}{u_c}-\frac{u_a}{u_c}+1 & \text{if } \left(\frac{u}{u_c}-\frac{u_a}{u_c}+1\right)<1\end{cases}$ $\begin{cases}u_{*c}=0.0115+0.0125d_{50}^{1.4} & \text{if } 0.1<\frac{h}{d}\leq1\\ u_{*c}=0.0305-\frac{0.0065}{d_{50}} & \text{if } 1<\frac{h}{d}\leq100\end{cases}$ $\begin{cases}u_{*ca}=0.0115+0.0125d_a^{1.4} & \text{if } 0.1<\frac{h}{d}\leq1\\ u_{*ca}=0.0305-\frac{0.0065}{d_a} & \text{if } 1<\frac{h}{d}\leq100\end{cases}$ $d_a=\frac{\sigma^m d_{50}}{1.8}$ m =1.65 for $d_{max}=d_{95}$, the diameter must be expressed in millimeters.

	$u_c = 5.75u_{*c}\left[\log\left(5.53\frac{h}{d_{50}}\right)\right]$ $u_{ca} = 5.75u_{*ca}\left[\log\left(5.53\frac{h}{d_{50}}\right)\right]$ And eventually, $u_a = 0.8u_{ca}$, Conditioned to the fact that if $u_a<u_c$, then $u_a = u_c$ $f_4\left(\frac{t}{t_e},\frac{u}{u_c}\right) = \exp\left[-0.07\frac{u_c}{u}\left\lvert\ln\left(\frac{t}{t_e}\right)\right\rvert^{1.5}\right]$ where, time to reach equilibrium was found using the following equations- $T_e\left(\text{days}\right) = \begin{cases} 48.26\frac{d}{u}\left(\frac{u}{u_c}-0.4\right) & \text{if}\left(\frac{h}{d}\right)>6 \\ 30.89\frac{d}{u}\left(\frac{u}{u_c}-0.4\right)\left(\frac{h}{d}\right)^{0.25} & \text{if}\left(\frac{h}{d}\right)\le 6 \end{cases}$
Kandasamy and Melville (1998)	$\frac{d_{sm}}{d} = f_1\left(\frac{h}{d}\right)$ $f_1\left(\frac{h}{d}\right) = k_h\left(\frac{h}{d}\right)^n$ $\begin{cases} k_h = 1, n = 1 & \text{if } \left(\frac{h}{d}\right)\le 0.04 \\ k_h = 1, n = 0.5 & \text{if } 0.04\le\left(\frac{h}{d}\right)\le 1 \\ k_h = 1, n = 0 & \text{if } \left(\frac{h}{d}\right)>1 \end{cases}$
Ettema et al. (1998)	$\frac{d_{sm}}{d} = \left(\frac{h}{d}\right)^{0.62}\text{Fr}^{0.2}\left(\frac{d}{d_{50}}\right)^{0.08}$
Melville (1997)	$\frac{d_{sm}}{d} = f_1\left(\frac{h}{d}\right)f_2\left(\frac{d}{d_{50}}\right)f_3\left(\frac{u}{u_c},\frac{u_a}{u_c}\right)$ $f_1\left(\frac{h}{d}\right) = \begin{cases} 1 & \text{if } \left(\frac{h}{d}\right)\ge 1.42 \\ 2\left(\frac{h}{d}\right)^{0.5} & \text{if } 0.2\le\left(\frac{h}{d}\right)\le 1.42 \\ 4.5\left(\frac{h}{d}\right) & \text{if } \left(\frac{h}{d}\right)<0.2 \end{cases}$

	$$f_2\left(\frac{d}{d_{50}}\right)=\begin{cases}1 & \text{if } \left(\frac{d}{d_{50}}\right)\geq 25\\ 0.57\log\left[2.24\left(\frac{d}{d_{50}}\right)\right] & \text{if } \left(\frac{d}{d_{50}}\right)<25\end{cases}$$ $$f_3\left(\frac{u}{u_c},\frac{u_a}{u_c}\right)=\begin{cases}1 & \text{if } \left(\frac{u}{u_c}-\frac{u_a}{u_c}+1\right)\geq 1\\ \frac{u}{u_c}-\frac{u_a}{u_c}+1 & \text{if } \left(\frac{u}{u_c}-\frac{u_a}{u_c}+1\right)<1\end{cases}$$ $$\begin{cases}u_{*c}=0.0115+0.0125d_{50}^{1.4} & \text{if } 0.1\text{ mm}<d_{50}\leq 1\text{ mm}\\ u_{*c}=0.0305-\frac{0.0065}{d_{50}} & \text{if } 1\text{ mm}<d_{50}\leq 100\text{ mm}\end{cases}$$ $$\begin{cases}u_{*ca}=0.0115+0.0125d_a^{1.4} & \text{if } 0.1\text{ mm}<d_a\leq 1\text{ mm}\\ u_{*ca}=0.0305-\frac{0.0065}{d_a} & \text{if } 1\text{ mm}<d_a\leq 100\text{ mm}\end{cases}$$ $$d_a=\frac{\sigma^m d_{50}}{1.8}$$ m =1.65 for $d_{max}=d_{95}$, the diameter must be expressed in millimetres. $$u_c=5.75u_{*c}\left[\log\left(5.53\frac{h}{d_{50}}\right)\right]$$ $$u_{ca}=5.75u_{*ca}\left[\log\left(5.53\frac{h}{d_{50}}\right)\right]$$ Here, eventually, $u_a=0.8u_{ca}$, Conditioned to the fact that if $u_a<u_c$, then $u_a=u_c$
Mueller (1996)	$$\frac{d_{sm}}{d}=2.5k_rk_sk_tk_u\left(\frac{h}{d}\right)^{0.35}\text{Fr}^{0.43}$$ Here, $k_u=0.4u_R^{0.15}$, $u_R=\frac{u-u_j}{u_c-u_{j95}}$, $u_j=0.645V_c\left(\frac{d_{50}}{d}\right)^{0.053}$ $u_{j95}=0.645u_{c95}\left(\frac{d_{95}}{d}\right)^{0.053}$, $u_{c95}=6.19h^{1/6}d_{95}^{1/3}$ and, $d_{95}=d_{50}\sigma^{1.645}$
Johnson (1995) (LBS)	$$\frac{d_{sm}}{d}=2.02\left(\frac{h}{d}\right)^{0.02}\text{Fr}^{0.21}\sigma^{-0.24}$$
Richardson and Davis (1995)	$$\frac{d_{sm}}{d}=2.5k_rk_sk_tk_u\left(\frac{h}{d}\right)^{0.35}\text{Fr}^{0.43}$$, Here, $k_u=\left\{1-0.89\left(1-u_R\right)^2\right\}^{0.5}$,

	$u_R = \frac{u - u_j}{u_{c90} - u_j}$, $u_j = 0.645 u_c \left(\frac{d_{50}}{d}\right)^{0.053}$, $u_{c90} = 6.19 h^{1/6} d_{90}^{1/3}$, $d_{90} = d_{50}\sigma^{1.282}$
Wilson (1995)	$\frac{d_{sm}}{d} = 0.9 f_1\left(\frac{h}{d}\right)$, Here, $f_1\left(\frac{h}{d}\right) = \left(\frac{h}{d}\right)^{0.4}$ $u_c = \sqrt{1.2(g d_{50}\Delta)\left(\frac{h}{d_{50}}\right)^{0.16}\left(\frac{d}{d_{50}}\right)^{-0.11}}$
Ansari and Qadar (1994)	$\frac{d_{sm}}{d_*} = \begin{cases} 0.024 d_*^{\,2} & d_* < 2.2 \text{ m} \\ 2.238 d_*^{\,-0.6} & d_* > 2.2 \text{ m} \end{cases}$
Gao et al. (1993)	$\frac{d_{sm}}{d} = 0.46 d^{-0.4} h^{0.15} d_{50}^{-0.07}\left(\frac{u - u_i}{u_c - u_i}\right)$ The u_c was calculated by the following equations- $u_c = \left(\frac{h}{d_{50}}\right)^{0.14}\left[17.6\Delta d_{50} + 0.000000605\left(\frac{10 + h}{d_{50}^{0.72}}\right)\right]$ $u_i = 0.462 u_c \left(\frac{d_{50}}{d}\right)^{0.06}$
Richardson et al. (1993)	$\frac{d_{sm}}{d} = 2.5 k_r k_s k_t k_u \left(\frac{h}{d}\right)^{0.35} \mathrm{Fr}^{0.43}$
Southard (1992)	$\frac{d_{sm}}{d} = 0.827\left(\frac{1}{d}\right) d_{50}^{-0.117} u^{0.684} e^{0.476k}$ k = correction factor for the location of the pier = 0 (pier in the main channel) =1 (pier in the bank of the main channel or on the flood plain)
Kothyari et al. (1992)	$\frac{d_{sm}}{d} = 0.66 f_1\left(\frac{d}{d_{50}}\right)^{-0.25} f_2\left(\frac{h}{d_{50}}\right)^{0.16} f_3\left(\mathrm{F_D}\text{-}\mathrm{F_{D,c}}\right)$ $f_1\left(\frac{d}{d_{50}}\right) = \left(\frac{d}{d_{50}}\right)^{-0.25}$ $f_2\left(\frac{h}{d_{50}}\right) = \left(\frac{h}{d_{50}}\right)^{0.16}$ $f_3\left(\mathrm{F_d}\text{-}\mathrm{F_{d,c}}\right) = \left(\mathrm{F_d^2}\text{-}\mathrm{F_{d,c}^2}\right)^{0.40}$
Colorado State University (1990)	$\frac{d_{sm}}{d} = 2.0 k_p k_q \left(\frac{h}{d}\right)^{0.35} \mathrm{Fr}^{0.43}$ k_p = pier shape correction factor k_q = flow angle correction factor

May and Willoughby (1990)	$\frac{d_{sm}}{d} = 2.4 f_1\left(\frac{h}{d}\right) f_2\left(\frac{u}{u_c}\right)$ $f_1\left(\frac{h}{d}\right) = \begin{cases} 0.55\left(\frac{h}{d}\right)^{0.6} & \text{if } 0.7\left(\frac{h}{d}\right) \le 2.7 \\ 1 & \text{if } 0.7\left(\frac{h}{d}\right) > 2.7 \end{cases}$ $f_2\left(\frac{u}{u_c}\right) = 1 - 3.66\left(1 - \frac{u}{u_c}\right)^{1.76}$ Critical velocities were found from the following formula of Hancu (1971). $u_c = 1.2\sqrt{g d_{50} \Delta}\left(\frac{h}{d_{50}}\right)^{0.2}$
Cheremisinoff (1988*a*)	$\frac{d_{sm}}{d} = 1.05 k_x d^{-0.25}$ Here, k_x is the shape factor for the pier, for cylindrical shape, k_x = 1, and for rectangular shape, k_x = 1.4.
Cheremisinoff (1988*b*)	$\frac{d_{sm}}{d} = 3d^{-0.2}$
Chitale (1988)	$\frac{d_{sm}}{d} = 2.5$
Froehlich design (1988)	$\frac{d_{sm}}{d} = 0.32 f_1\left(\frac{h}{d}\right) f_2\left(\frac{d}{d_{50}}\right) f_3(\mathrm{Fr}) + 1$ $f_1\left(\frac{h}{d}\right) = \left(\frac{h}{d}\right)^{0.46}$ $f_2\left(\frac{d}{d_{50}}\right) = \left(\frac{d}{d_{50}}\right)^{0.08}$ $f_3(\mathrm{Fr}) = \mathrm{Fr}^{0.22}$ $u_c = 1.58\sqrt{g d_{50} \Delta}\left(\frac{h}{d_{50}}\right)^{1/6}$
Froehlich (1988)	$\frac{d_{sm}}{d} = 0.32 f_1\left(\frac{h}{d}\right) f_2\left(\frac{d}{d_{50}}\right) f_3(\mathrm{Fr})$ $f_1\left(\frac{h}{d}\right) = \left(\frac{h}{d}\right)^{0.47}$

	$f_2\left(\frac{d}{d_{50}}\right)=\left(\frac{d}{d_{50}}\right)^{0.09}$ $f_3(\mathrm{Fr})=\mathrm{Fr}^{0.22}$ $u_c=1.58\sqrt{gd_{50}\Delta}\left(\frac{h}{d_{50}}\right)^{1/6}$
Melville and Southerland (1988)	$\frac{d_{sm}}{d}=2.4f_1\left(\frac{h}{d}\right)f_2\left(\frac{d}{d_{50}}\right)f_3\left(\frac{u}{u_c},\frac{u_a}{u_c}\right)$ $f_1\left(\frac{h}{d}\right)=\begin{cases}1 & \text{if } \left(\frac{h}{d}\right)\geq 2.6\\ 0.78\left(\frac{h}{d}\right)^{0.255} & \text{if } \left(\frac{h}{d}\right)<2.6\end{cases}$ $f_2\left(\frac{d}{d_{50}}\right)=\begin{cases}1 & \text{if } \left(\frac{d}{d_{50}}\right)\geq 25\\ 0.57\log\left[2.24\left(\frac{d}{d_{50}}\right)\right] & \text{if } \left(\frac{d}{d_{50}}\right)<25\end{cases}$ $f_3\left(\frac{u}{u_c},\frac{u_a}{u_c}\right)=\begin{cases}1 & \text{if } \left(\frac{u}{u_c}-\frac{u_a}{u_c}+1\right)\geq 1\\ \frac{u}{u_c}-\frac{u_a}{u_c}+1 & \text{if } \left(\frac{u}{u_c}-\frac{u_a}{u_c}+1\right)<1\end{cases}$ $u_{*c}=0.03d_{50}^{1/2}$ $u_{*ca}=0.03d_a^{1/2}$ $d_a=\frac{\sigma^m d_{50}}{1.8}$ m =1.65 for $d_{max}=d_{95}$, the diameter must be expressed in millimeters. $u_c=5.75u_{*c}\left[\log\left(5.53\frac{h}{d_{50}}\right)\right]$ $u_{ca}=5.75u_{*ca}\left[\log\left(5.53\frac{h}{d_{50}}\right)\right]$, Here, eventually $u_a=0.8u_{ca}$, conditioned to the fact that if $u_a<u_c$, then $u_a=u_c$
Jain (1981)	$\frac{d_{sm}}{d}=1.84f_1\left(\frac{h}{d}\right)f_2(\mathrm{F_c})$

	$f_1\left(\frac{h}{d}\right)=\left(\frac{h}{d}\right)^{0.30}$ $f_2\left(\mathrm{F_c}\right)=\mathrm{F_c}^{0.25}$
Qadar (1981)	$\frac{d_{sm}}{d}=538\left(\frac{1}{d}\right)h_o^{128}$ where h_o is the initial strength of the vortex, this equation is applicable for sediments with a diameter of up to 0.5 mm.
Jain and Fischer (1980)	$\frac{d_{sm}}{d}=1.86\left(\frac{h}{d}\right)^{0.5}$
Jain and Fischer (1979)	$\frac{d_{sm}}{d}=\begin{cases}\left(\frac{d_{sm}}{d}\right)_a & \text{if } \left(\mathrm{F\text{-}F_c}\right)>0.2\\ \left(\frac{d_{sm}}{d}\right)_b & \text{if } \left(\mathrm{F\text{-}F_c}\right)<0\\ \max\left[\left(\frac{d_{sm}}{d}\right)_a,\left(\frac{d_{sm}}{d}\right)_b\right] & \text{if } 0<\left(\mathrm{F\text{-}F_c}\right)<0.2\end{cases}$ $\left(\frac{d_{sm}}{d}\right)_a=2f_{1a}\left(\frac{h}{d}\right)f_{2a}\left(\mathrm{F\text{-}F_c}\right)$ $\left(\frac{d_{sm}}{d}\right)_b=1.84f_{1b}\left(\frac{h}{d}\right)f_{2b}\left(\mathrm{F_c}\right)$ $f_{1a}\left(\frac{h}{d}\right)=\left(\frac{h}{d}\right)^{0.5}$ $f_{2a}\left(\mathrm{F\text{-}F_c}\right)=\left(\mathrm{F\text{-}F_c}\right)^{0.25}$ $f_{1b}\left(\frac{h}{d}\right)=\left(\frac{h}{d}\right)^{0.3}$ $f_{2b}\left(\mathrm{F}\right)=\mathrm{F_c}^{0.25}$ The author reported that the u_c is determined from the Shields criteria for the critical shear stress (τ_{oc}) (Vanoni 1975) and the logarithmic u distribution is given by $u_c=u_{*c}2.5\ln\left(11.02\frac{h}{d_{50}}\right)$
Breusers et al. (1977)	$\frac{d_{sm}}{d}=2f_1\left(\frac{h}{d}\right)f_2\left(\frac{u}{u_c}\right)$ $f_1\left(\frac{h}{d}\right)=\tanh\left(\frac{h}{d}\right)$

	$f_2\left(\frac{u}{u_c}\right)=2\left(\frac{u}{u_c}\right)-1$ Critical velocities can be found from the following formula- $u_c=1.2\sqrt{gd_{50}\Delta}$
Neil (1973)	$\frac{d_{sm}}{d}=1.5$
Coleman (1971)	$\frac{d_{sm}}{d}=1.49f_1(\mathrm{Fr})$ $f_1(\mathrm{Fr})=\mathrm{Fr}^{0.20}$
Hancu (1971)	$\frac{d_{sm}}{d}=2.42f_1\left(\frac{u}{u_c}\right)f_2(\mathrm{F_{B,c}})$ $f_1\left(\frac{u}{u_c}\right)=2\left(\frac{u}{u_c}\right)-1$ $f_2(\mathrm{F_{B,c}})=\mathrm{F}_{\mathrm{B,c}}^{\frac{2}{3}}$ The u_c is calculated with the following formula. $u_c=1.2\sqrt{gd_{50}\Delta}\left(\frac{h}{d_{50}}\right)^{0.2}$
Tarapore (Acres 1970)	$\frac{d_{sm}}{d}=1.35$
Veiga (1970) (LBS)	$\frac{d_{sm}}{d}=1.35\left(\frac{h}{d}\right)^{0.3}$
Shen et al. (1969)	$\frac{d_{sm}}{d}=2.34\left(\frac{h}{d}\right)^{0.381}\mathrm{Fr}^{0.619}h^{-0.06}$
Shen and Maza (Shen et al. 1969)	$\frac{d_{sm}}{d}=\begin{cases}3.4g^{-0.33}d^{-0.33}u^{0.67} & \text{if Fr>0.2}\\ 11\left(\frac{1}{d}\right)g^{-1}u^2 & \text{if Fr}\le 0.2\end{cases}$
Arunachalam (1965)	$\frac{d_{sm}}{d}=1.95\left(\frac{h}{d}\right)^{5/6}-1$
Carstens (1966)	$\frac{d_{sm}}{d}=0.546\left\{\frac{(S_N^2-1.64)}{(S_N^2-5.02)}\right\}^{0.83}$ $S_N=\frac{u}{\Delta gd_{50}}$
Shen et al. (1966)	$\frac{d_{sm}}{d}=2.5\mathrm{Fr}^{0.4}\left[1-\exp\left(JE^2\right)\right]$

	$J = 0.026\exp\left(-2.932h\right)$ $E = \left(\frac{d}{h}\right)^{0.33} \mathrm{F}^{0.33} \ln\left(\frac{ut}{h}\right)$
Breusers (1965)	$\frac{d_{sm}}{d} = 1.4$
Neil (1964) (Live bed scour)	$\frac{d_{sm}}{d} = 1.5 f_1\left(\frac{h}{d}\right)$ $f_1\left(\frac{h}{d}\right) = \left(\frac{h}{d}\right)^{0.3}$
Larras (1963)	$\frac{d_{sm}}{d} = 1.42 d^{-0.25}$
Ahmed (1962)	$\frac{d_{sm}}{d} = 1.486\left(\frac{1}{d}\right) k_i q^{2/3}$ Ahmed (1962) suggested using a k_i value between 1.7 and 2.0 to determine the total depth scoured around piers.
Blench et al. (1962)	$\frac{d_{sm}}{d} = \left(6.6\mathrm{Fr}\text{-}0.51\text{-}5.49\mathrm{Fr}^2\right)\left(\frac{h}{d}\right)$
Blench Inglis –I (1962)	$\frac{d_{sm}}{d} = \left\{1.53\left(\frac{h}{d}\right)^{0.5} u^{0.5} d_{50}^{-0.125}\right\} - \left(\frac{h}{d}\right)$
Blench Inglis –II (1962)	$\frac{d_{sm}}{d} = \left\{1.8\left(\frac{h}{d}\right)^{0.5} h^{0.25}\right\} - \left(\frac{h}{d}\right)$
Chitale (1962)	$\frac{d_{sm}}{d} = f_1\left(\frac{h}{d}\right) f_2\left(\mathrm{Fr}\right)$ $f_2\left(\mathrm{Fr}\right) = \left(6.65\mathrm{Fr} - 0.51 - 5.49\mathrm{Fr}^2\right)$
Laursen (1962)	$\frac{d_{sm}}{d} = \left(\frac{1}{d}\right)\frac{q^{2/3}}{\mathrm{F}_{\mathrm{B}}^{1/3}}$
Laursen (1962) (LBS)	$\frac{d_{sm}}{d} = 1.8\left(\frac{h}{d}\right)^{0.75}$
Bata (1960) (after Acres 1970)	$\frac{d_{sm}}{d} = 10\left(\frac{h}{d}\right)\left(\frac{u^2}{gh} - \frac{3d_{50}}{h}\right)$
Laursen (1960)	$\frac{d_{sm}}{d} = 1.11 f_1\left(\frac{h}{d}\right)$ $f_1\left(\frac{h}{d}\right) = \left(\frac{h}{d}\right)^{0.5}$

Varzeliotis (1960)	$\frac{d_{sm}}{d}=1.43\left(\frac{q^{2/3}}{d}\right)^{0.72}$
Laursen and Toch (1956)	$\frac{d_{sm}}{d}=1.35\left(\frac{h}{d}\right)^{0.3}$
Inglis (1949*a*)	$\frac{d_{sm}}{d}=2.32\left(\frac{Q^{2/3}}{d}\right)^{0.78}-\frac{h}{d}$
Inglis (1949*b*)	$\frac{d_{sm}}{d}=4.2\left(\frac{h}{d}\right)^{0.78}\mathrm{Fr}^{0.52}$
Inglis (1949)-II	$d_{sm}=2\left[0.473\left(\frac{Q}{1.76\sqrt{d_{50}}}\right)^{1/3}\right]=2\,(d_{sl})$ $\frac{d_{sm}}{d}=\left(\frac{2}{d}\right)\left[0.473\left(\frac{Q}{1.76\sqrt{d_{50}}}\right)^{1/3}\right]$
Inglis Poona-I (1949)	$\frac{d_{sm}}{d}=\left(\frac{1.7d^{0.22}h^{0.52}u^{0.52}}{d}\right)-\left(\frac{h}{d}\right)$
Inglis Poona-II (1949)	$\frac{d_{sm}}{d}=\left(1.73d^{0.88}u^{0.78}\right)-\left(\frac{h}{d}\right)$ Lacey's regime depth is $d_{sl}=0.473\left(\frac{Q}{1.76\sqrt{d_{50}}}\right)^{1/3}$

(c) Predictive maximum scour formula for two pier

The formulas are given here for the computation of d_{sm} around Pier-1 (front pier) and Pier-2 (rear pier) of the two pier arrangements given in Table 2.5. The comparison of such formulas is analyzed in detail in Chapters 6-8. Some studies are excluded from the comparison analysis due to limitations in their applicability. Empirical formulas for specific pier arrangements performed well within their datasets but lacked general applicability.

Table 2.5. The formulas for two pier arrangments for maximum scour depth estimations.

Reference	Pier arrangement	Formulas
Beg (2004)	*Eccentric pier*	$d_{sm1}/d_{ss}=1.0+0.142\varphi^{0.144}$ $\quad d_{sm2}/d_{ss}=0.83+0.7\varphi^{1.51}$
Das et al. (2016)	Eccentric pier	$\frac{d_{sm1}}{d}=-0.011\left(\frac{l}{d}\right)^2+0.145\left(\frac{l}{d}\right)+0.489$ $\frac{d_{sm2}}{d}=-0.007\left(\frac{l}{d}\right)^2+0.092\left(\frac{l}{d}\right)+0.691$

Wang et al. (2016)	*Tandem Pier*	$\frac{d_{sm1}}{d} = 2.865\frac{u}{u_c} - 1.332$ $\frac{d_{sm2}}{d} = 2.865\frac{u}{u_c} - A$ $\frac{u}{u_c} = 1.14\sqrt{gd_{50}\Delta}\left(\frac{h}{d_{50}}\right)$, Here, the deviation $P = \|B\text{-}A\|$, and $P = 0.18\{(r\text{-}d)/d\}$ when $(r\text{-}d) \leq 3d$, $P = \text{-}0.22\ln\{\text{-}(r\text{-}d)/d\} + 0.722$ when $(r\text{-}d) \geq 3d$, where, $B = 1.332$, r is center-to-center displacement between piers and d represents pier diameter.
Khaple et al. (2017)	*Tandem pier*	$\frac{d_{sm2}}{d} = \left(\frac{d_{se}}{d}\right)\exp\left[-0.0383\left\{\frac{u}{u_c}\log\left(\frac{1}{43.25}\frac{t}{T}\left(\frac{l}{d}\right)^{-0.25}\right)\right\}^2\right]$
	Three piers in staggered	$\frac{d_{sm2}}{d} = \left(\frac{d_{se}}{d}\right)\exp\left[-0.0155\left\{\frac{u}{u_c}\log\left(\frac{1}{78.68}\left(\frac{e}{d}\right)^{0.25}\frac{t}{T}\left(\frac{l}{d}\right)^{-0.25}\right)\right\}^2\right]$ $\frac{d_{sm2}}{d} = \left(\frac{d_{se}}{d}\right)\exp\left[-0.0383\left\{\frac{u}{u_c}\log\left(\frac{1}{78.68}\left(\frac{e}{d}\right)^{0.25}\frac{t}{T}\left(\frac{l}{d}\right)^{-0.25}\right)\right\}^2\right]$
Liu et al. (2018)	*Tandem Pier*	$\frac{d_{sm1}}{d} = 2.865\frac{u}{u_c} - 1.332$ $\frac{d_{sm2}}{d} = 2.865\frac{u}{u_c} - 1.332 - d_{x1}$ $d_{x1} = \frac{15.2\left(\frac{r-d}{d}\right)}{\left\{1.6\left(\frac{d}{r-d}\right)+5\right\}^2} - \frac{0.5\left(\frac{r-d}{d}\right)^2}{\left\{1.6\left(\frac{d}{r-d}\right)+5\right\}^2}$
Keshavarzi et al. (2018)	*Tandem Pier*	$\frac{d_{sm1}}{d} = \left(\frac{d_{se}}{d}\right)\frac{a_1 l^2 + a_2 l + a_3}{l^2 + a_4 l + a_5}$ where, the constant parameters are a_1=0.995, a_2=-4.165, a_3=5.249, a_4=-4.286, a_5=5.36. $\frac{d_{sm2}}{d} = \left(\frac{d_{se}}{d}\right)\frac{b_1 l^2 + b_2 l + b_3}{l^2 + b_4 l + b_5}$ where, the constant parameters are b_1=0.780, b_2=-9.155, b_3=34.010, b_4=-11.650, b_5=41.510.
Das et al. (2019)	*Eccentric pier*	$\frac{d_{sm1}}{d} = 0.0703\left(\frac{l}{d}\right) + \left(-0.243P^2 + 0.407P + 0.696\right)$ where, P represents pier position factor = 0 when the equation is accounted for calculating the front pier, P = 1 for eccentric pier, and P = 2 for inline rear pier.

		$\frac{d_{sm2}}{d} = -0.038\left(\frac{l}{d}\right) + \left(-0.243P^2 + 407P + 1.258\right)$ where, P = 0 when the equation is accounted for calculating front pier, P = 1 for eccentric pier, and P = 2 for inline rear pier.
Malik and Setia (2020)	*Tandem*	$\frac{d_{sm1}}{d} = 0.0044\left(\frac{l}{d}\right)^2 - 0.1101\left(\frac{l}{d}\right) + 1.3841$ $\frac{d_{sm2}}{d} = 0.0058\left(\frac{l}{d}\right)^2 - 0.1155\left(\frac{l}{d}\right) + 1.1711$
	Side-by-side	$\frac{d_{sm1}}{d} = -0.0473\left(\frac{e}{d}\right)^3 + 0.3128\left(\frac{e}{d}\right)^2 - 0.6867e + 1.523$ $\frac{d_{sm2}}{d} = -0.0531\left(\frac{e}{d}\right)^3 + 0.3554\left(\frac{e}{d}\right)^2 - 0.7702e + 1.5418$
	Eccentric	$\frac{d_{sm1}}{d} = 0.0342\left(\frac{s}{d}\right)^2 - 0.27\left(\frac{s}{d}\right) + 1.3581$ $\frac{d_{sm2}}{d} = 0.0342\left(\frac{s}{d}\right)^2 - 0.27\left(\frac{s}{d}\right) + 1.3581$ $\frac{d_{sm3}}{d} = 0.0479\left(\frac{s}{d}\right)^2 - 0.3774\left(\frac{s}{d}\right) + 1.4632$
Devi and Kumar (2022)	*Side-by-side pier*	$d_{se} = \exp\left\{-0.03\left\lvert\frac{u_c}{u}\ln\frac{t}{t_e}\right\rvert^{1.6}\right\}$ when, t_e is in days for $d_s/d > 6$, $u/u_c > 0.4$ $t_e = 48.26\frac{d}{u}\left(\frac{u}{u_c} - 0.4\right)$ when, t_e is in days for $d_s/d < 6$, $u/u_c > 0.4$ $t_e = 30.89\frac{d}{u}\left(\frac{u}{u_c} - 0.4\right)\left(\frac{d_s}{d}\right)^{0.25}$ $\frac{d_{sm1}}{d} = \left(\frac{1}{d}\right)\frac{a_1 + b_1x + c_1x^2}{1 + d_1x + e_1x^2}$ where, constant parameters are a_1=1.0, b_1=-0.5481, c_1=0.0793, d_1=-0.5225, e_1=0.0780. $\frac{d_{sm2}}{d} = \left(\frac{1}{d}\right)\frac{a_2 + b_2x + c_2x^2}{1 + d_2x + e_2x^2}$ where, the constant parameters are a_2=1.0693, b_2=-0.5590, c_2=0.0828, d_2=-0.5370, e_2=0.0819.
Nandi and Das (2024)		Formula is valid for the ranges $0.008 \le d_{50}/d \le 0.012$, $5.43 \le r/d \le 5.99$ and $10 \le l/d \le 10.37$, h/d=1.26-1.79 and t/T=0-36. $\frac{d_{smi}}{d} = \frac{d_{ss}}{d}K\exp\left[-0.045\left\{\ln\left(3.3\left(\frac{d_{50}}{d}\right)\left(\frac{h}{d}\right)^{-1}\left(\frac{r}{d}\right)^{-0.25}\left(\frac{l}{d}\right)^{-0.4}\left(\frac{t}{T}\right)\right)\right\}^2\right]$ where, the value of constant parameter K is given as follows: K=1, r/d, l/d are not applicable (NA) for an isolated pier.

		K=1.25, r/d=1, l/d are NA for the front pier of two piers. K=1.16, r/d=1, l/d are NA for the front pier of three piers. K=1.60, l/d are NA for the eccentric pier in two piers. K=1.78, l/d are NA for the eccentric pier in three piers. K=0.95 for the rear pier of three piers.

References

Acres, 1970. Design Transmital. East-West Interconnector Project of Bangladesh Power Development Board, Acres International Limited, Dhaka.

Ahmed, F., and Rajaratnam, N. (1998). Flow around bridge piers. *Journal of Hydraulic Engineering, 124*(3), 288–300.

Ahmed, M. (1962). Discussion on scour at bridge crossing by Laursen, E.M. *Transactions of the American Society of Civil Engineers, 127*(1).

Aksoy, A. O., Bombar, G., Arkis, T., and Guney, M. S. (2017). Study of the time-dependent clear water scour around circular bridge piers. *Journal of Hydrology and Hydromechanics, 65*(1), 26–34.

Ali, K. H., and Karim, O. (2002). Simulation of flow around piers. *Journal of Hydraulic Research, 40*(2), 161–174.

Al-Shukur, A. H. K., and Obeid, Z. H. (2016). Experimental study of bridge pier shape to minimize local scour. *International Journal of Civil Engineering and Technology*, 7(1), 162–171.

Ansari, S. A., and Qadar, A. (1994). Ultimate depth of scour around bridge piers. In *Proceedings of the ASCE National Hydraulics Conference* (pp. 51–55). Buffalo, New York.

Arneson, L. A., Zevenbergen, L. W., Lagasse, P. F., and Clopper, P. E. (2012). *Evaluating scour at bridges* (Hydraulic Engineering Circular No. 18). Washington, D.C.: U.S. Federal Highway Administration.

Arunachalam, K. (1965). Scour around bridge piers. *Journal of the Indian Roads Congress, 29*(2), 189–210.

Ballio, F., Teruzzi, A., and Radice, A. (2009). Constriction effects in clear-water scour at abutments. *Journal of Hydraulic Engineering*, *135*(2), 140 –145.

Beg, M. (2004). Mutual interference of bridge piers on local scour. In *Proceedings of the Second International Conference on Scour and Erosion, Singapore* (pp. 111-118).

Blench, T. (1969). *Mobile-bed fluviology: A regime theory treatment of canals and rivers for engineers and hydrologists*. University of Alberta Press.

Blench, T., Bardley, J. N., Joglekar, D. V., et al. (1962). Discussion of "Scour at Bridge Crossings." *Transactions of the American Society of Civil Engineers, 127*(1), 180–183.

Breusers, H. N. C. (1965). Scour around drilling platforms. *Bulletin of Hydraulics Research, 19*, 276.

Breusers, H. N. C., and Raudkivi, A. J. (1991). *Scouring*. Rotterdam: Balkema.

Breusers, H. N. C., Nicollet, G., and Shen, H. W. (1977). Local scour around bridge piers. *Journal of Hydraulic Research*, *15*(3), 211–252.

Briaud, J. L., Hurlebaus, S., Chang, K. A., Yao, C., Sharma, H., Yu, O. Y., and Price, G. R. (2011). *Realtime monitoring of bridge scour using remote monitoring technology* (Report No. 0-6060-1). Texas Transportation Institute.

Chabert, J., and Engeldinger, P. (1956). *Étude des affouillements autour des piles de ponts* [Study of scour around bridge piers]. Technical Report. Laboratoire National d'Hydraulique, Chatou, France.

Cheremisinoff, P. N. (1988). *Civil engineering practice* (Vol. 2). Technomics Publishing Company.

Chien, N., and Wan, Z. (1999). Mechanics of sediment transport.

Chiew, Y. M. (1984). *Local scour at bridge piers*. Doctoral dissertation, Department of Civil Engineering, University of Auckland, Auckland, New Zealand.

Chiew, Y. M. (1995). Mechanics of riprap failure at bridge piers. *Journal of Hydraulic Engineering, 121*(9), 635–643.

Chiew, Y. M., and Melville, B. W. (1987). Local scour around bridge piers. *Journal of Hydraulic Research, 25*(1), 15–26.

Chitale, S. V. (1988). Estimation of scour at bridge piers. *Water and Energy International, 45*(1), 57–68.

Coleman, N. L. (1971). Analyzing laboratory measurements of scour at cylindrical piers. In *Hydraulic Research and Its Impact on the Environment*.

Coscarella, F., Gaudio, R., and Manes, C. (2020). Near-bed eddy scales and clear-water local scouring around vertical cylinders. *Journal of Hydraulic Research, 58*(6), 968–981.

Cunha, L. V. D. (1970). Discussion to "Local scour around bridge piers" by Shen, H. W., Schneider, V. R., and Karaki, *Journal of the Hydraulics Division, 96*(8), 1742–1747.

Das, R., Das, S., Jaman, H., and Mazumdar, A. (2019). Impact of upstream bridge pier on the scouring around adjacent downstream bridge pier. *Arabian Journal for Science and Engineering, 44*, 4359-4372.

Das, S., Das, R., and Mazumdar, A. (2013). Circulation characteristics of horseshoe vortex in scour region around circular piers. *Water Science and Engineering, 6*(1), 59-77.

Das, S., Das, R., and Mazumdar, A. (2016) Comparison of local scour characteristics around two eccentric piers of different shapes. *Arabian Journal of Science and Engineering, 41*(4), 1199-1213.

Devi, G., and Kumar, M. (2022). Experimental study of the local scour around the two piers in the tandem arrangement using ultrasonic ranging transducers. *Ocean Engineering, 266*, 112838.

Dey, S. (2014). *Fluvial hydrodynamics: Hydrodynamic and Sediment Transport Phenomena*. Springer Berlin, Heidelberg.

Dey, S., Bose, S. K., and Sastry, G. L. (1995). Clear water scour at circular piers: A model. *Journal of Hydraulic Engineering, 121*(12), 869–876.

Ettema, R. (1980). *Scour at bridge piers*. Ph.D. thesis, Department of Civil Engineering, University of Auckland.

Ettema, R., Kirkil, G., and Muste, M. (2006). Similitude of large-scale turbulence in experiments on local scour at cylinders. *Journal of Hydraulic Engineering, 132*(1), 33–40.

Ettema, R., Melville, B. W., and Constantinescu, G. (2011). *Evaluation of bridge scour research: Pier scour processes and predictions*. Transportation Research Board of the National Academies.

Franzetti, S., Radice, A., Rebai, D., and Ballio, F. (2022). Clear water scour at circular piers: A new formula fitting laboratory data with less than 25% deviation. *Journal of Hydraulic Engineering, 148*(10), 04022021.

Froehlich, D. C. (1988). Analysis of onsite measurements of scour at piers. *Proceedings of the ASCE National Conference on Hydraulic Engineering*, Colorado Springs, CO.

Gao, D., Posada, G. L., and Nordin, C. F. (1993). *Pier scour equations used in the People's Republic of China* (Report FHWA-SA-93-076). U.S. Department of Transportation, Federal Highway Administration, Washington, D.C., U.S.

Guo, J. (2012). Pier scour in clear water for sediment mixtures. *Journal of Hydraulic Research, 50*(1), 18–27.

Hancu, S. (1971). On the estimation of local scour in the bridge piers zone. In *Proc., 14th Congress of the International Association for Hydraulic Research (IAHR)*, Vol. 3, 299–313, Madrid, Spain.

Hancu, S., and Predescu, L. (1989). Experimental results on local scour around bridge piers in free surface water currents and pressurized air currents. In *Proc., 23rd Congress of the International Association for Hydraulic Research (IAHR)*, Madrid, Spain.

Hassan, W. H., and Jalal, H. K. (2021). Prediction of the depth of local scouring at a bridge pier using a gene expression programming method. *SN Applied Sciences, 3*(2), 159.

Hong, J. H., Chiew, Y. M., Lu, J. Y., Lai, J. S., and Lin, Y. B. (2012). Houfeng bridge failure in Taiwan. *Journal of Hydraulic Engineering, 138*(2), 186–198.

Inglis, S. C. (1949). Maximum depth of scour at heads of guide banks and groynes, pier noses, and downstream of bridges—the behavior and control of rivers and canals. In *Poona, India, Indian Waterways Experimental Station*, 327–348.

IRC:78 (2014). *Standard specifications and code of practice for road bridges*. The Indian Roads Congress, New Delhi, India.

Jain, S. C. (1981). Maximum clear-water scour around circular piers. *Journal of the Hydraulics Division, 107*(5), 611–626.

Jain, S. C., and Fischer, E. E. (1979). Scour around circular piers at high Froude numbers. *Report FHWA-RD-79-104*. Washington, DC: USDOT.

Jain, S. C., and Fischer, E. E. (1980). Scour around bridge piers at high flow velocities. *Journal of Hydraulic Engineering, 106*(11), 1827–1842.

Jarrett, R. D., and Boyle, J. M. (1987). *Pilot study collection of bridge-scour data* (Vol. 86, No. 4030). U.S. Department of the Interior, U.S. Geological Survey.

Johnson, P. A. (1995). Comparison of pier-scour equations using field data. *Journal of Hydraulic Engineering, 121*(8), 626–629.

Johnson, P. A., and Torrico, E. F. (1994). Scour around wide piers in shallow water. Transportation Research Record, (1471), 66–70.

Kandasamy, J. K., and Melville, B. W. (1998). Maximum local scour depth at bridge piers and abutments. *Journal of Hydraulic Research, 36*(2), 183–198.

Keshavarzi, A., Shrestha, C. K., Melville, B., Khabbaz, H., Ranjbar-Zahedani, M., and Ball, J. (2018). Estimation of maximum scour depths at upstream of front and rear piers for two in-line circular columns. *Environmental Fluid Mechanics, 18*, 537–550.

Khaple, S., Hanmaiahgari, P. R., Gaudio, R., and Dey, S. (2017). Interference of an upstream pier on local scour at downstream piers. *Acta Geophysica, 65*, 29-46.

Kim, I., Fard, M. Y., and Chattopadhyay, A. (2015). Investigation of a bridge pier scour prediction model for safe design and inspection. *Journal of Bridge Engineering, 20*(6), 04014088.

Kothyari, U. C., Garde, R. J., and Ranga Raju, K. G. (1992). Temporal variation of scour around circular bridge piers. *Journal of Hydraulic Engineering, 118*(8), 1091–1106.

Kothyari, U. C., Hager, W. H., and Oliveto, G. (2007). Generalized approach for clear-water scour at bridge foundation elements. *Journal of Hydraulic Engineering, 133*(11), 1229–1240.

Lagasse, P. F., Clopper, P. E., Zevenbergen, L. W., and Girard, L. W. (2007). Countermeasures to protect bridge piers from scour. NCHRP Report 593, National Cooperative Highway Research Program, Transportation Research Board of The National Academies, Washington, D.C.

Lança, R. M., Fael, C. S., Maia, R. J., Pêgo, J. P., and Cardoso, A. H. (2013). Clear-water scour at comparatively large cylindrical piers. *Journal of Hydraulic Engineering, 139*(11), 1117–1125.

Lança, R., Fael, C., and Cardoso, A. H. (2010). Assessing equilibrium clear water scour around single cylindrical piers. *River Flow, 2010*, 1207–1214.

Lança, R., Simarro, G., Fael, C. M. S., and Cardoso, A. H. (2016). Effect of viscosity on the equilibrium scour depth at single cylindrical piers. *Journal of Hydraulic Engineering, 142*(3), 06015022.

Larras, J. (1963). Profondeurs maximales d'érosion des fonds mobiles autour des piles en rivière. *Annales des Ponts et Chaussées, 133*, 411–424.

Laursen, E. M. (1960). Scour at bridge crossings. *Journal of the Hydraulics Division, 86*(2), 39–54.

Laursen, E. M. (1962). Scour at bridge crossings. *Transactions of the ASCE, 127*(1), 166–180.

Laursen, E. M., and Toch, A. (1953). *A generalized model study of scour around bridge piers and abutments* (No. HR-24). State University of Iowa.

Laursen, E. M., and Toch, A. (1956). Scour around bridge piers and abutments. *Bulletin No. 4*. Ames, IA: Iowa Highway Research Board.

Lee, S. O., and Sturm, T. W. (2009). Effect of sediment size scaling on physical modeling of bridge pier scour. *Journal of Hydraulic Engineering, 135*(10), 793–802.

Lin, C., Han, J., Bennett, C., and Parsons, R. L. (2014). Case history analysis of bridge failures due to scour. In *Climatic effects on pavement and geotechnical infrastructure* (pp. 204–216).

Liu, Q. S., Tang, H. W., Wang, H., and Xiao, J. F. (2018). Critical velocities for local scour around twin piers in tandem. *Journal of Hydrodynamics, 30*, 1165-1173.

Malik, R., and Setia, B. (2020). Interference between pier models and its effects on scour depth. *SN Applied Sciences, 2*, 68.

May, R., and Willoughby, I. (1990). Local scour around large obstructions. *Technical Report*. Wallingford, UK: Hydraulics Research.

Melville, B. (2008). The physics of local scour at bridge piers. In *Fourth International conference on scour and erosion* (pp. 28–38).

Melville, B. W. (1997). Pier and abutment scour: Integrated approach. *Journal of Hydraulic Engineering, 123*(2), 125–136.

Melville, B. W., and Chiew, Y. M. (1999). Time scale for local scour at bridge piers. *Journal of Hydraulic Engineering, 125*(1), 59–65.

Melville, B. W., and Coleman, S. E. (2000). *Bridge scour*. Highlands Ranch, CO: Water Resources Publications.

Melville, B. W., and Southerland, A. J. (1988). Design method for local scour at bridge piers. *Journal of Hydraulic Engineering, 114*(10), 1210–1226.

Molinas, A. (2004). Bridge scour in nonuniform sediment mixtures and in cohesive materials: Synthesis report (No. FHWA-RD-03-083). United States: Federal Highway Administration, Office of Infrastructure Research and Development.

Monti, R. (1994). *Indagine sperimentale sulle caratteristiche fluido-dinamiche del campo di moto intorno ad una pila circolare.* Ph.D. Thesis, Dep. I.I.A.R., Politecnico di Milano, Italy.

Nandi, B., and Das, S. (2023). Identify most promising temporal scour depth formula for circular piers proposed over last six decades. *Ocean Engineering, 286*(2), 115639.

Nandi, B., and Das, S. (2024). Equation for time-dependent local scour at pier-like structures with eccentric in-line arrangements. In *Proceedings of the Institution of Civil Engineers-Water Management, 177*(6), 361–374.

Neil, C. R. (1973). *Guide to bridge hydraulics*. Roads and Transportation Association of Canada, University of Toronto Press, Toronto, Canada.

Neill, C. R. (1964). River bed scour: A review for bridge engineers. *Report*, Alberta, Canada.

Oliveto, G., and Hager, W. H. (2002). Temporal evolution of clear-water pier and abutment scour. *Journal of Hydraulic Engineering, 128*(9), 811–820.

Pandey, M., Sharma, P. K., Ahmad, Z., and Karna, N. (2018). Maximum scour depth around bridge pier in gravel bed streams. *Natural Hazards, 91*, 819–836.

Pandey, M., Zakwan, M., Sharma, P. K., and Ahmad, Z. (2020). Multiple linear regression and genetic algorithm approaches to predict temporal scour depth near circular piers in non-cohesive sediment. *ISH Journal of Hydraulic Engineering, 26*(1), 96–103.

Qadar, A. (1981). The vortex scour mechanism at bridge piers. *Proceedings of the Institution of Civil Engineers, 71*(3), 739–757.

Raikar, R. V., and Dey, S. (2005). Clear-water scour at bridge piers in fine and medium gravel beds. *Canadian Journal of Civil Engineering, 32*(4), 775–781.

Raudkivi, A. J. (1986). Functional trends of scour at bridge piers. *Journal of Hydraulic Engineering, 112*(1), 1–13.

Raudkivi, A. J., and Ettema, R. (1983). Clear-water scour at cylindrical piers. *Journal of Hydraulic Engineering, 109*(3), 338–350.

Raudkivi, A.J. 1998. Loose Boundary Hydraulics. A.A. Balkema Publishers, Netherlands.

Richardson, E. V., and Davis, S. R. (1995). *Evaluation of scour at bridges* (Report No. FHWA-IP-90-107, Hydraulic Engineering Circular No. 18, Third Edition). Federal

Highway Administration, U.S. Department of Transportation, Washington, D.C., U.S.A.

Richardson, E. V., and Davis, S. R. (2001). *Evaluating scour at bridges*. National Highway Institute (US): A review on estimation methods of scour depth around bridge piers.

Shen, H. W., Schneider, V. R., and Karaki, S. (1969). Local scour around bridge piers. *Journal of the Hydraulics Division, 95*(6), 1919–1940.

Shen, H. W., Schneider, V. R., and Karaki, S. S. (1966). *Mechanics of local scour*. U.S. Department of Commerce, National Bureau of Standards, Institute for Applied Technology, Fort Collins, Colorado.

Sheppard, D. M., Melville, B., and Demir, H. (2014). Evaluation of existing equations for local scour at bridge piers. *Journal of Hydraulic Engineering, 140*(1), 14–23.

Sheppard, D. M., Miller Jr, W. (2006). Live-bed local pier scour experiments. *Journal of Hydraulic Engineering, 132*(7), 635–642.

Sheppard, D. M., Odeh, M., and Glasser, T. (2004). Large scale clear-water local pier scour experiments. *Journal of Hydraulic Engineering, 130*(10), 957–963.

Southard, R. E. (1992). Scour around bridge piers on streams in Arkansas (Vol. 92, No. 4126). U.S. Department of the Interior, U.S. Geological Survey.

Tarapore, Z. S. (1962). *A theoretical and experimental determination of the erosion pattern around obstructions placed in an alluvial channel with particular reference to vertical circular cylinders and piers.* Ph.D. Dissertation, University of Minnesota.

Vanoni V.A. (1975) Sedimentation Engineering Practice. American Society of Civil Engineers, Manuals and Reports on Engineering Practice, No. 54, 745 p.

Vijayasree, B. A., and Eldho, T. I. (2021). A modification to the Indian practice of scour depth prediction around bridge piers. *Current Science, 120*(12), 1875–1881.

Vonkeman, J. K., and Basson, G. R. (2019). Evaluation of empirical equations to predict bridge pier scour in a non-cohesive bed under clear-water conditions. *Journal of the South African Institution of Civil Engineering, 61*(2), 2–20.

Wang, H., Tang, H., Liu, Q., and Wang, Y. (2016). Local scouring around twin bridge piers in open-channel flows. *Journal of Hydraulic Engineering, 142*(9), 06016008.

Wilson, K. V. (1995). Scour at selected bridge sites in Mississippi. *Water-Resources Investigations Report, 94-4241*. U.S. Geological Survey, Reston, VA.

Xiong, W., Cai, C. S., Zhang, R., Shi, H., and Xu, C. (2023). Review of hydraulic bridge failures: Historical statistic analysis, failure modes, and prediction methods. *Journal of Bridge Engineering, 28*(4), 03123001.

Yanmaz, A. M. (2001). Uncertainty of local scouring parameters around bridge piers. *Turkish Journal of Engineering and Environmental Sciences, 25*(2), 127–137.

Yanmaz, A. M., and Altinbilek, H. D. (1991). Study of time-dependent local scour around bridge piers. *Journal of Hydraulic Engineering, 117*(10), 1247–1268.

Chapter 3

Temporal Scour around Isolated Circular Pier

3.1. Introduction

Scour at bridge piers is a leading concern for bridge failure. This has long been a concern for engineers. When river flow encounters any obstruction like a bridge pier, it causes local scour. This process creates a system of three-dimensional vortices near the upstream face of the obstruction (Breusers et al. 1977), leading to three-dimensional flow separation. The equilibrium scour depth (d_{se}) formulas are conservative. The d_{se} is suitable for live-bed conditions. However, for clear-water scour conditions, the d_{se} is higher than live bed scour. Reaching the maximum d_{se} can take many times, and the actual scour depth (d_s) may only represent a small portion of it (Melville and Coleman 2000).

There has been significant scientific interest in predicting the temporal d_s (d_{st}) at circular bridge piers, resulting in many formulas for its calculation (Melville and Chiew 1999, Franzetti et al. 2022). Research on temporal scour at circular bridge piers was pioneered by Chabert and Engeldinger (1956) and has remained a key focus for decades. The d_{st} variation under clear-water conditions using laboratory experiments around circular piers. A Semi-empirical approach, employing sediment continuity formulas to estimate d_{st} in homogeneous beds (Yanmaz and Altinbilek 1991). A scour study using cohesionless sand under clear-water conditions examined the effect of pier diameter (d) on d_{st} (Alabi 2006). Lança et al. (2010) studied the evolution of local d_{st} and total of five experiments were performed which were stopped when the scouring rate was less than about 2 mm/day and at least seven days had passed. The experimental scour results from previous studies were compared with those scour results estimated using different empirical formulas from the literature (Choi and Choi 2016, Aksoy et al. 2017). NCHRP (2011) considered 10 temporal evolution formulas, out of which four were based on a computer program to evaluate $d_{st,}$ and the rest were based on numerical formulas from 1966 to 2007. The accuracy of some formulas compared and highlighted the need for better estimates (Vonkeman and Bason 2019). Franzetti et al. (2022) developed another d_{st} estimation formula using data acquired from 30 sources, including 247 d_{st} data series, 81 isolated data points, and 27 literature formulas for the evolution of maximum d_s (d_m). Only four studies were used for d_{st} prediction at the circular pier, in uniform and non-uniform sediment, under steady clear water flow. In the last two decades, the evolution of d_{st} has been the subject of comparative studies by different researchers (Mia and Nago 2003, Franzetti et al. 2022), using established d_{st} prediction formulas. The best formula for d_{st}, as mentioned in various manuscripts, is still unclear. Therefore, application engineers and researchers must identify the most promising formula from huge datasets from the literature that can be applied to estimate d_{st}.

This chapter evaluates 11 existing formulas from past research and introduces a newly developed formula to estimate d_{st}. The goal is to analyze how accurately each formula predicts using experimental data collected by researchers over the past 60 years. Key parameters influencing d_{st} are identified from the literature, and 329 time-series datasets from 13 research studies spanning seven decades are used for the analysis. A comparative study is conducted on 12 formulas, applying multi-attribute decision-making techniques to rank them, as no single statistical measure can fully evaluate their performance. Performance indicators are used to assess the accuracy of formulas, and sensitivity analysis is conducted to examine their reliability. The importance of each performance indicator is determined using equal weighting and the Criteria Importance Through Intercriteria Correlation (CRITIC) method. Finally, Compromise Programming (CP) ranks the formulas based on their performance.

3.2. Methods

3.2.1. Evolution of literature formulas to compute d_{st}

The d_{st} has been measured in numerical and laboratory studies, most based on controlled experiments. Researchers have proposed various formulas for calculating d_{st} around isolated circular bridge piers, considering different flow conditions and bed materials. Promising formulas for d_{st} computation have been compared and analyzed by researchers, often in combination with their own developed models. A summary of key studies from 2006 to 2022 is presented in Table 3.1.

Table 3.1. Researchers who used the formula for d_{st} proposed by other researchers.

Formulas evaluated in the present study	Researchers who analysed the time-dependent formulas											
	Yanmaz (2006)	Kothyari et al. (2007)	Lança et al. (2010)	NCHRP (2011)	Simarro et al. (2011)	Lança et al. (2013)	Guo (2014)	Choi and Choi (2016)	Aksoy et al. (2017)	Pandey et al. (2017)	Franzetti et al. (2022)	Present study
Shen et al. (1966)	×	×	×	✓	×	×	×	×	×	×	×	✓
Franzetti et al. (1982)	✓	×	×	×	✓	✓	✓	×	×	×	×	✓
Sumer et al. (1993)	×	×	×	✓	×	×	✓	✓	×	✓	×	✓
Melville and Chiew (1999)	✓	×	×	✓	✓	×	×	✓	✓	✓	✓	✓
Oliveto and Hager (2002)	✓	✓	✓	✓	×	×	×	×	✓	✓	×	✓
Kothyari et al. (2007)	×	✓	×	✓	✓	×	✓	×	×	✓	✓	✓
NCHRP (2011)	×	×	×	✓	×	×	×	×	×	×	×	✓
Lança et al. (2013)	×	×	×	×	×	✓	×	✓	×	✓	✓	✓
Choi and Choi (2016)	×	×	×	×	×	×	×	✓	×	✓	×	✓
Aksoy et al. (2017)	×	×	×	×	×	×	×	×	×	×	×	✓
Franzetti et al. (2022)	×	×	×	×	×	×	×	×	×	×	✓	✓

Note: "×" indicates "not considered", "✓" indicates "considered".

3.2.2. Dimensional analysis: Buckingham π theorem

The d_{st} is the function of the following 12 parameters (Eq. 3.1). Here, μ is the dynamic viscosity of water, h is flow depth, d is pier diameter, u is flow velocity, u_c is critical velocity, ρ_f is water density, ρ_s is sediment density, σ is sediment uniformity, g is acceleration due to gravity, W is width of flume, t is time.

$$d_{st} = f\left(h, d, u, u_c, d_{50}, \rho_f, \rho_s, \sigma, t, g, W, \mu\right) \tag{3.1}$$

The Buckingham π theorem reduces the number of variables in a physical relationship by identifying dimensionless parameters, allowing the functional relationship to be expressed in the following form (Eq. 3.2).

$$\frac{d_{st}}{d} = \lambda\left(\frac{h}{d}, \frac{u}{u_c}, \frac{d}{d_{50}}, \frac{\rho_f u h}{\mu} = \mathrm{Re}, \frac{u}{\sqrt{gh}} = \mathrm{Fr}, \sigma, \frac{ut}{d\Delta^{0.5}}, \frac{d}{W}\right) \tag{3.2}$$

Using dimensionality reduction techniques based on parameter correlation, it is seen that Reynolds number (Re) and Froude number (Fr) have minimal impact on scour in this dataset. Hence, these terms can be omitted, reducing Eq. (3.2) to the following form in Eq. (3.3).

$$\frac{d_{st}}{d} = \varphi\left(\frac{h}{d}, \frac{u}{u_c}, \frac{d}{d_{50}}, \sigma, \frac{ut}{d\Delta^{0.5}}, \frac{d}{W}\right) \tag{3.3}$$

Table 3.2 represents the functions of the formula that are used for evaluation using extensive d_{st} data. Here, F_d is densimetric Froude number, t_R is reference time, T_s time scale used by Aksoy et al. (2007), u_* is shear velocity, $F_{d\beta}$ is densimetric particle Froude number of scour entrainment, t_e is equilibrium time. The formulas of all these parameters mentioned here are given in Table 2.3 in Chapter 2.

Table 3.2. The functional relationship for the formula under consideration.

Sl. No.	Research groups	Functions
1	Shen et al. (1966)	$d_{st}/d = f\{d/h, \mathrm{Fr}, \log(ut/h)\}$
2	Franzetti et al. (1982)	$d_{st}/d_{se} = f(ut/d)$
3	Sumer et al. (1992)	$d_{st}/d_{se} = f(t/t_e)$, $t_e = f\{h/d, u_*/(g\Delta d_{50})\}$
4	Melville and Chiew (1999)	$d_{st}/d_{se} = f\{u/u_c, \ln(t/t_e)\}$
5	Oliveto and Hager (2002)	$d_{st}/(hd^2)^{1/3} = f\{F_d, \sigma, \log(t/t_R)\}$
6	Kothyari et al. (2007)	$d_{st}/(hd^2)^{1/3} = f\{F_d, F_{d\beta}, \sigma, \log(t/t_R)\}$
7	NCHRP (2011)	$d_{st}/d_{se} = f\{u/u_c, \ln(t/t_e)\}$
8	Lança et al. (2013)	$d_{st}/d_{se} = f(ut/d, d/d_{50})$
9	Choi and Choi (2016)	$d_{st}/d_{se} = f\{u/u_c, h/d, \ln(t/t_e)\}$
10	Aksoy et al. (2017)	$d_{st}/d = f\{u/u_c, h/d, \log(T_s)\}$
11	Franzetti et al. (2022)	$d_{st}/d = f\{u/u_c, d/d_{50}, \sigma, h/d, (ut/d\Delta^{0.5})\}$
12	Present study	$d_{st}/d = f\{d/W, u/u_c, d/d_{50}, \sigma, h/d, (ut/d\Delta^{0.5})\}$

This analysis relies on bulk data from previous studies. The data collection, including the parameters required for analysis, is presented in Table 3.3.

Table 3.3. Parameters affecting d_{st} as considered eleven literatures along with present study.

Research groups	Required parameters to estimate d_{st}																			
	Fr	F_d	$F_{d\beta}$	F_{di}	u	u_c	h	d	d_{50}	Δ	t	t_e	t_R	T_s	R_h	σ	u_*	u_{*c}	d/W	d_{se}
Shen et al. (1966)	Fr	--	--	--	u	--	h	d	--	--	t	--	--	--	--	--	--	--	--	--
Franzetti et al. (1982)	--	--	--	--	u	--	--	d	--	--	t	--	--	--	--	--	--	--	--	d_{se}
Sumer et al. (1992)	--	--	--	--	--	--	--	d	d_{50}	Δ	t	t_e	--	--	--	--	u_*	--	--	d_{se}
Melville and Chiew (1999)	--	--	--	--	u	u_c	h	--	d_{50}	--	t	t_e	--	--	--	--	--	--	--	d_{se}
Oliveto and Hager (2002)	--	F_d	--	--	--	--	h	d	d_{50}	Δ	t	--	t_R	--	--	σ	--	--	--	--
Kothyari et al. (2007)	--	F_d	$F_{d\beta}$	F_{di}	--	--	h	d	d_{50}	Δ	t	--	t_R	--	R_h	σ	--	--	--	--
NCHRP (2011)	--	--	--	--	u	u_c	h	--	d_{50}	--	t	t_e	--	--	--	--	--	--	--	d_{se}
Lança et al. (2013)	--	--	--	--	u	--	--	d	d_{50}	--	t	--	--	--	--	--	--	--	--	d_{se}
Choi and Choi (2016)	--	--	--	--	u	u_c	h	d	d_{50}	--	t	t_e	--	--	--	--	--	--	--	d_{se}
Aksoy et al. (2017)	--	--	--	--	u	u_c	--	d	d_{50}	--	t	--	--	T_s	--	--	--	--	--	--
Franzetti et al. (2022)	--	--	--	--	u	u_c	h	d	d_{50}	Δ	t	--	--	--	--	σ	--	--	--	--
Present study	--	--	--	--	u	u_c	h	d	d_{50}	Δ	t	--	--	--	--	σ	--	--	d/W	--

Note: "--" indicates "not considered".

3.2.3. Challenges in data curation

***Bulk velocity and depth-averaged velocity*:** Different researchers reported their studies using various types of u heterogeneity in the data. Sometimes a bulk u was provided. While, some used u profiles, which differ due to the sidewall effect, are used to determine u. The Q, h, and W are used to determine u in the current study to establish a homogenous dataset. The data analyses by NCHRP (2011) and Vonkeman and Bason (2019) used u values without considering the type of u.

***Shear and critical shear velocities*:** Several authors used u_* instead of u. This problem can be overcome by a conversion from u_* to u. Flume-specific formulas may be more appropriate, but many authors did not mention conversion formulas. Therefore, we have used a semi-logarithmic relationship for such conversion (Melville 1997).

***Threshold condition*:** The τ_o is determined by the $\tau_o = \rho_f g R_h \sin\theta$ where θ = angle between the horizontal line and tilting flume. The τ_{oc} is determined using the expression $\tau_{oc} = \Theta_c \Delta \rho_f g d_{50}$ where Θ_c is the critical Shields parameter and is computed from van Rijn's empirical formulas for Shields curve (Das et al. 2013). The d_{st} increases as a function of u/u_c and reaches the maximum for $u/u_c = 1$. The upper limit for u/u_c also strictly applies for live-bed scour, while d_{st} can vary over time. This study provides homogeneously generated u/u_c values using the

same method mentioned earlier to identify threshold conditions. Because of this homogeneity, clear water scour runs are still considered successful even when u/u_c is marginally > 1. Some experimental data show u/u_c values slightly higher than 1, with a maximum of 1.43, which is enough to develop high bedforms and cause significant variation in d_{st} as bedforms appear when u/u_c >1.2−1.3 (Franzetti et al. 2022). Oscillations are minimal in tests where ripples might form. The incipient motion condition for this study, based on different Shields curves when $\Theta > \Theta_c$, or $\tau_o > \tau_{oc}$, or $u_* > u_{*c}$ are shown in Fig. 3.1. When the shear Reynolds number ($R_* = u_* d_{50}/\nu$) is ≤ 5, the flow is smooth, and the viscous sublayer does not feel the roughness. When $R_* \geq 70$, the flow becomes turbulent, and the viscous sublayer disappears. In the range of 5 to 70, the flow is transitional, and the viscous sublayer exists. The weakness of the Shields theory is that when $R_* \geq 70$, the viscous sublayer no longer affects the u distribution. In smooth flow, μ affects u distribution in the turbulent wall shear and outer layers, while in rough flow, only boundary roughness matters. In transitional flow, both boundary roughness and μ affect the u distribution (Dey 2014). R_* widely varies from 2.41-979.14 in this study. In Fig. 3.1, the area below the dashed and dotted lines shows no sediment movement. However, this study has some data above that area. This uncertainty arises because a uniform value of u/u_c is calculated using a single criterion to identify threshold conditions.

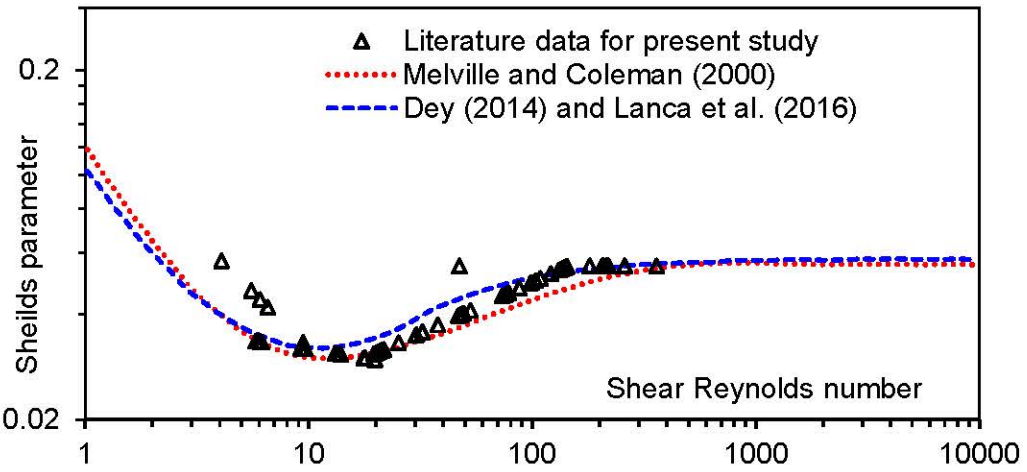

Fig. 3.1. Shields diagrams plotted for threshold conditions based on literature d_{st} data from Melville and Coleman (2002), Dey (2014), and Lança et al. (2016) as reported by Franzetti et al. (2022).

Conditions for equilibrium t and d_{se}: Scour evolves quickly in the early stages of the experiment and slows down over t, as seen in the d_{st} vs. t plot for each study. For clear water scour conditions, d_{se} is approached asymptotically but may take an infinite amount of time to reach equilibrium. In laboratory experiments, when scour slows significantly, it is considered quasi-equilibrium, but it is hard to know when it stops. To address this, some researchers use a condition where the scour rate increases by no more than 5% of d over 24 hours (Melville and Chiew 1999). But for all literature data, it is not clear when d_{se} is reached. To counter these selected data when the experimental duration was taken as t_e for simplicity of the analysis. But long duration experiments (Lança et al. 2010), t_e is taken into consideration of the fact that the t_e can be reached after an infinitely long duration.

3.2.4. Description of datasets

The performance of each formula in terms of d_{st} around a circular bridge pier is analyzed using data from laboratory experiments from various sources. The data from 13 different research groups over seven decades are Chabert and Engeldinger (1956) as CE, Ettema (1980) as ET, Mignosa (1980) as MI, Yanmaz and Altinbilek (1991) as YA, Oliveto and Hager (2002) as OH, Mia and Nago (2003) as MN, Chang et al. (2004) as CA, Raikar and Dey (2005) as RD, Alabi (2006) as AL, Sheppard et al. (2006) as SH, Lança et al. (2010) as LA, Lança et al. (2013) as LAN, and Aksoy et al. (2017) as AK have been collected for the development of new formula as well as comparison of 11 literature formulas (Table 3.4). No data screening was applied for comparing the 12 formulas. Table 3.4 shows the experimental ranges covered by the 329 data series selected for formula development and comparison. Three datasets from CE are collected from an article by MN, six datasets from another paper, and the remaining data are taken from previous literatures of those authors.

Table 3.4. Sources and experimental ranges of selected d_{st} data.

Literature	#	h/d	u/u_c	σ	d/d_{50}	Δ	$ut/d\Delta^{0.5}$	d/W
CE	3	1-4.67	0.752-0.901	1.08-1.08	50-144.23	1.65-1.65	1.63×10^{3}-6.71×10^{5}	0.075-0.15
ET	96	0.493-21.05	0.493-1.02	1.07-4.55	3.65-1000	1.65-1.66	1.32×10^{2}-6.71×10^{6}	0.019-0.157
RD	16	3.25-7.83	0.75-0.79	1.08-1.16	3.12-78.78	1.65-1.65	1.54×10^{2}-2.12×10^{6}	0.053-0.128
OH	86	0.092-6.76	0.49-1.44	1-2.35	6.73-467.27	0.42-1.65	3.15×10^{1}-1.65×10^{7}	0.022-0.5
LAN	46	0.5-5	0.66-0.82	1.65-1.65	49.22-465.12	1.36-1.46	6.52×10^{1}-1.15×10^{7}	0.025-0.2
MI	19	2.56-4.76	0.69-0.92	1.32-1.32	10.68-19.2	0.18-0.18	5.70×10^{3}-1.38×10^{7}	0.054-0.097
YA	18	1.27-3.51	0.75-0.951	1.13-1.28	43.93-79.76	1.63-1.64	1.80×10^{2}-1.32×10^{8}	0.07-0.1
SH	6	0.19-3.93	0.743-0.925	1.21-1.51	315.52-1386.4	1.65-1.65	2.59×10^{2}-9.32×10^{5}	0.05-0.15
MN	5	2.67-5	0.705-0.8	1.29-1.29	46.88-46.88	1.65-1.65	1.22×10^{2}-9.18×10^{4}	0.1-0.1
CA	10	0.15-0.3	1.02-1.43	1.20-3.00	100-140.85	1.65-1.65	1.51×10^{2}-7.17×10^{5}	0.1-0.1
AL	3	2.0-2.0	0.617-0.836	1.23-1.23	137.74-216.98	1.65-1.65	2.33×10^{2}-2.53×10^{6}	0.06-0.094
LA	5	2-2.13	0.8-0.86	1.40-1.46	49.12-93.02	1.65-1.65	2.09×10^{2}-1.28×10^{7}	0.090-0.096
AK	16	0.93-4.68	0.479-0.6	1.39-1.39	11.53-57.64	1.65-1.65	3.39×10^{1}-2.07×10^{5}	0.05-0.25
Range	329	0.092-21.05	0.479-1.44	1-4.55	3.12-1386.4	0.18-1.66	3.15×10^{1}-1.32×10^{8}	0.019-0.25

Note: # indicates number of datasets considered in selected literature.

3.2.5. Statistical performance indicators

Statistical analysis is used to evaluate the provided accuracy of the above-stated formulas. Various cost and beneficial performance indicators are used to assess. Now, the following formulas, given in Table 3.5, have been used to define the various performance indices such as Index of Agreement (IA), Kling-Gupta Efficiency (KGE), Correlation Coefficient (CC), Normalized Root Mean Square Error (NRMSE), Mean Absolute Error (MAE), Sum of Absolute Errors (SAE), Taylor Sikll Score (TSS), and Standard Deviation (SD). Here, $(d_{st}/d)_o$ is the observed and $(d_{st}/d)_c$ is the computed values. These performance indicators are chosen

to clearly evaluate the formula from the literature and the proposed one. The beneficial performance indicators are IA, KGE, CC, and TSS help us measure how well the model predicts and matches the actual data. The non-beneficial ones (NRMSE, MAE, SAE, and SD) help us see where the model makes errors or has large differences from the expected results, giving us a full picture of its performance.

Table 3.5. Performance indicators with their pertinent ranges and ideal values.

Performance indicators	Range	Ideal value
$\mathrm{SD}_o \text{or, } \mathrm{SD}_c = \sqrt{\frac{\sum_{i=1}^{N}\left\{\left(\frac{d_{st}}{d}\right)_{oi}-\overline{\left(\frac{d_{st}}{d}\right)_{oi}}\right\}^2}{N}} \text{ or, } \sqrt{\frac{\sum_{i=1}^{N}\left\{\left(\frac{d_{st}}{d}\right)_{ci}-\overline{\left(\frac{d_{st}}{d}\right)_{ci}}\right\}^2}{N}}$	0 to ∞	Closer to observed or predicted
$\mathrm{CC}=\frac{N\sum_{i=1}^{N}\left(\frac{d_{st}}{d}\right)_{oi}\times\left(\frac{d_{st}}{d}\right)_{ci}-\sum_{i=1}^{N}\left(\frac{d_{st}}{d}\right)_{oi}\sum_{i=1}^{N}\left(\frac{d_{st}}{d}\right)_{ci}}{N^2\times\mathrm{SD}_c\times\mathrm{SD}_o}$	–1 to +1	1
$\mathrm{RMSE}=\sqrt{\sum_{i=1}^{N}\frac{\left\{\left(\frac{d_{st}}{d}\right)_{oi}-\left(\frac{d_{st}}{d}\right)_{ci}\right\}^2}{N}}$	0 to ∞	0
$\mathrm{IA}=1-\frac{\sum_{i=1}^{N}\left\{\left(\frac{d_{st}}{d}\right)_{oi}-\left(\frac{d_{st}}{d}\right)_{ci}\right\}^2}{\sum_{i=1}^{N}\left\{\left\lvert\left(\frac{d_{st}}{d}\right)_{ci}-\overline{\left(\frac{d_{st}}{d}\right)_{o}}\right\rvert+\left\lvert\left(\frac{d_{st}}{d}\right)_{oi}-\overline{\left(\frac{d_{st}}{d}\right)_{o}}\right\rvert\right\}^2}$	0 to 1	1
$\mathrm{KGE}=1-\sqrt{(\mathrm{CC}-1)^2+\left\{\frac{\mathrm{SD}_c}{\mathrm{SD}_o}-1\right\}^2+\left(\frac{\overline{\left(\frac{d_{st}}{d}\right)_{c}}}{\overline{\left(\frac{d_{st}}{d}\right)_{o}}}-1\right)^2}$	–∞ to 1	1
$\mathrm{MAE}=\frac{1}{N}\sum_{i=1}^{N}\left\lvert\left(\frac{d_{st}}{d}\right)_{oi}-\left(\frac{d_{st}}{d}\right)_{ci}\right\rvert$	0 to ∞	0
$\mathrm{SSE}=\sum_{i=1}^{N}\left\{\left(\frac{d_{st}}{d}\right)_{oi}-\left(\frac{d_{st}}{d}\right)_{ci}\right\}^2$	0 to ∞	0
$\mathrm{TSS}=\frac{4(1+\mathrm{CC})}{\left\{\frac{\mathrm{SD}_o}{\mathrm{SD}_c}+\frac{\mathrm{SD}_c}{\mathrm{SD}_o}\right\}^2(1+\mathrm{CC}_{\max})}$	0 to ∞	Lower

3.2.6. Ranking techniques

The ranking of each formula is based on evaluating the weight assigned to each performance indicator in estimating d_{st}. The weight criteria are provided below, followed by the ranking method that uses these weights.

(a) Weight criteria technique

The performance of a formula cannot be judged using just one performance indicator. It is important to consider different efficiency, error and bias performance indicators and assign proper weights to understand their significance. In multi-objective optimization, weights are usually assigned equally. However, Kumar et al. (2021) explored different ways to assign weights. This study uses two methods for weighting: (i) equal weight and (ii) the CRITIC method.

CRITIC method: This method relies on the strength of the correlation between the columns in the decision matrix, as explained by Diakoulaki et al. (1995).

The decision matrix and normalized matrix are calculated using Eqs. (3.4-3.5), respectively. Here, Z_{ij} presents the performance value of i^{th} alternative on the j^{th} criterion.

$$\left[Z_{ij}\right]_{k\times l} = \begin{bmatrix} Z_{11} & Z_{12} & .. & Z_{1l} \\ Z_{21} & . & . & Z_{2l} \\ : & . & . & : \\ Z_{k1} & Z_{k2} & .. & Z_{kl} \end{bmatrix} (i = 1, 2, ..., k \ and \ j = 1, 2, .., l) \tag{3.4}$$

$$M_{ij} = \frac{Z_{ij} - Z_{ij}^{\max}}{Z_{ij}^{\max} - Z_{ij}^{\min}} \tag{3.5}$$

The weight criteria are calculated using Eqs. (3.6-3.7). Here, R_{jk} is the CC between the two criteria, and Q_j is the quantity of information contained in the j^{th} criteria.

$$Q_j = \mathrm{SD}_j \sum_{k=1}^{l} (1 - R_{jk}) \tag{3.6}$$

$$W_j = \frac{C_j}{\sum_{j=1}^{l} C_j} \tag{3.7}$$

(b) Compromise programming (CP)

Choosing the best solution emphasizes the importance of measuring distances in decision-making. The L_p metrics are the most widely used distance measurement technique in decision-making (Pomerol and Romero 2000, Ardil 2022). The distance measure $L_p(x)$ is calculated using Eq. (3.8) Here, indicator $j=1,2, ...K$, $L_p(x) = L_p$ metric for $F_j(x)$ = normalized value of indicator j for data x which is given solution, F_j^* = normalized ideal value of indicator j, W_j = weight of indicator j ($W_j > 0$) obtained from (i) equal weight and (ii) CRITIC methods.

$$L_p(x) = \left\{ \sum_{j=1}^{K} W_j \left| F_j^* - F_j(x) \right|^p \right\}^{1/p} \tag{3.8}$$

Member of the L_p metrics to be considered is determined by the parameter p, where $1 \leq p \leq \infty$ (1 for linear, 2 for squared Euclidean distance measure). In this case, $p = 2$ is used. The datasets having L_p metric values from lowest to highest are sorted from first to last.

3.3. Results and discussion

This study evaluates 11 previously proposed formulas (listed in Table 3.2) along with the newly proposed formula (Eq. 3.9) for calculating d_{st}. The performance of each formula is tested using data from 13 previous literature collected over 57 years.

$$\frac{d_{st}}{d} = \xi f_1\left(\frac{u}{u_c}\right) f_2\left(\frac{h}{d}\right) f_3(\sigma) f_4\left(\frac{d}{d_{50}}\right) f_5\left(\frac{tu}{d\Delta^{0.5}}\right) f_6\left(\frac{d}{W}\right) \tag{3.9}$$

The scour function ξ is estimated as 2.86 for the current study. The parameter functions are represented by Eqs. (3.10-3.15).

$$f_1\left(\frac{u}{u_c}\right) = \begin{cases} 1.1791\left(\frac{u}{u_c}\right) & \text{if } \frac{u}{u_c} \leq 1 \\ 1 & \text{if } \frac{u}{u_c} > 1 \end{cases} \tag{3.10}$$

$$f_2\left(\frac{h}{d}\right) = \begin{cases} 0.7786\left(\frac{h}{d}\right)^{0.1759} & \text{if } \left(\frac{h}{d}\right) \leq 4 \\ 1 & \text{if } \left(\frac{h}{d}\right) > 4 \end{cases} \tag{3.11}$$

$$f_3(\sigma) = 0.3538 + \frac{0.6854}{1 + \exp\left[6.9924 \ln\left(\frac{\sigma}{1.7196}\right)\right]} \tag{3.12}$$

$$f_4\left(\frac{d}{d_{50}}\right) = 0.8491\left\{\left(\frac{d}{d_{50}}\right)^{1.8158} e^{-2.9905\left(\frac{d}{d_{50}}\right)^{0.235}} + 0.5112\right\} \tag{3.13}$$

$$f_5\left(\frac{tu}{d\Delta^{0.5}}\right) = 1 - e^{-0.1000\left(\frac{tu}{d\Delta^{0.5}}\right)^{0.2000}} \tag{3.14}$$

$$f_6\left(\frac{d}{W}\right) = \exp\left\{-2.0325\left(\frac{d}{W}\right)^{2.0211}\right\} \tag{3.15}$$

All the parameter functions considered in Eq. (3.9), are shown in Figs. 3.2(a–e) for isolated data series. The parameter function of u/u_c has taken a linear relationship as taken by Melville (1997). The effect of the u/u_c is similar to the previous literature (Fig. 3.2a). Sheppard and Miller (2006) and Sheppard et al. (2014) used a logarithmic trend while Franzetti et al.

(2022) took a polynomial trend to plot u/u_c. In the present study, we have used the linear relations given in Eq. (3.10).

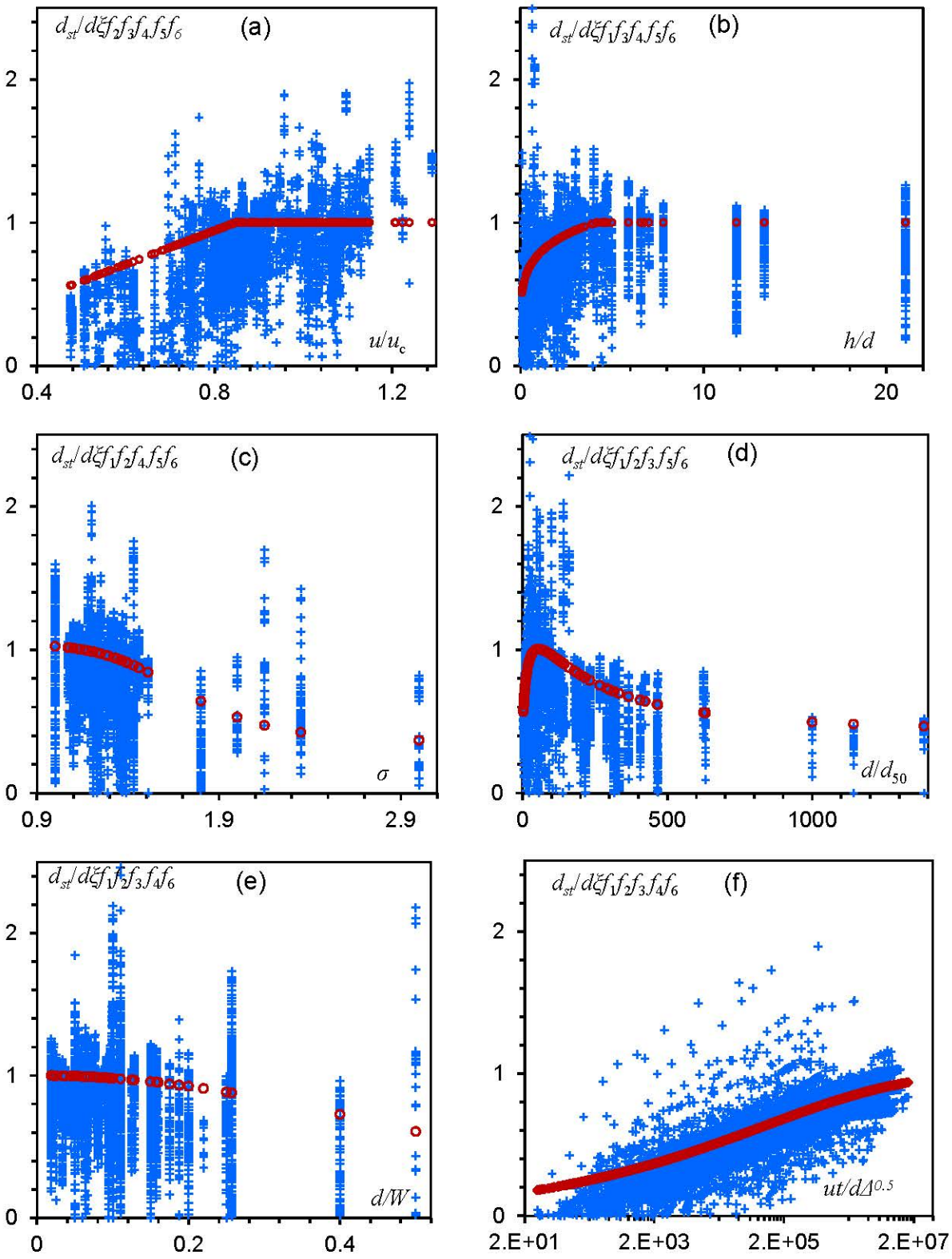

Fig. 3.2. Parameter functions **(a)** $f_1(u/u_c)$, **(b)** $f_2(h/d)$, **(c)** $f_3(\sigma)$, **(d)** $f_4(d/d_{50})$, **(e)** $f_5(ut/d\Delta^{0.5})$, and **(f)** $f_6(d/W)$ for isolated points.

The dimensionless d_s increases with respect to the increase of the flow shallowness (h/d) and yields a maximum value when the h/d value reaches approximately 4 (Fig. 3.2b). The parameter function of h/d follows the power law and after $h/d > 4$, the function value is taken as 1, given in Eq. (3.11). The trend of the parameter function of h/d is represented in power law by different previous researchers (Laursen and Toch 1956, Jain and Fischer 1979, Sheppard et al. 2014).

The parameter function σ is represented by the logistic growth formula in Eq. (3.12). The trend of the parameter function of σ plot follows a similar trend as shown by Raikar and Dey (2005) and Franzetti et al. (2022) (Fig. 3.2c).

The envelope of the d/d_{50} has a rising limb initially and reaches a maximum d/d_{50} value approximately equal to 50 and after the peak point, it has a recession limb extended up to d/d_{50} value of 750 (Fig. 3.2d). This parameter function is similar to Franzetti et al. (2022) given in Eq. (3.13). The rise in the coarse sediment limb is constant by many researchers but the decrease after the peak point has an ambiguity among many researchers (Lança et al. 2013, Lee and Strum 2009).

The parameter function of dimensionless time ($ut/d\Delta^{0.5}$) has an exponential trend used by different researchers (Lança et al. 2013, Franzetti et al. 2022) (Fig. 3.2e). This study considers the exponential formulas given in Eq. (3.14).

The logarithm trend was used by Melville (1997) and Oliveto and Hager (2002). The parameter function of the d/W has an exponential trend shown in the graph (Fig. 3.2f). Some studies have been made considering the side wall effect (Sheppard et al. 2004). If one cannot want to consider the effect of the constriction ratio in their study just take the parameter function of d/W =1 given in Eq. (3.15) and the scour function ξ = 2.82 will give a good agreement between computed and measured values.

3.3.1. Comparison between literature and present formulas

These comparisons are between measured and calculated scour values using the newly proposed Eq. (3.9) and literature formulas based on the complete 329-time series dataset, which includes 6,784 data points.

The accuracy of 11 formulas, along with the formula from this study, is evaluated both graphically and using various statistical parameters. The black short dashed line in Figs. 3.3 to 3.5 shows the ±20% deviation from the perfect fit line between the observed and predicted normalized d_{st} values. In Fig. 3.3(a-f), the abscissa shows the normalized observed $d_s(d_{st}/d_{se})_o$, and the ordinate shows the dimensionless computed $d_s(d_{st}/d_{se})_c$. The d_{st} data were either taken from graphs in the same literature or directly from research groups who used d_{st} data of other researchers. Since the data were extracted from figures in the respective studies, there may be slight differences from the original d_{st} data, including small variations in the time step. It is important to note that very few d_{st}/d_{se} values from the literature exceeded 1.

Figure 3.3(a-f) shows the relationship between the observed d_{st} data from various literature and the estimated d_{st} data using formulas from Franzetti et al. (1982), Sumer et al. (1992), Melville and Chiew (1999), Sheppard et al. (2011), Lança et al. (2013), and Choi and Choi (2016).

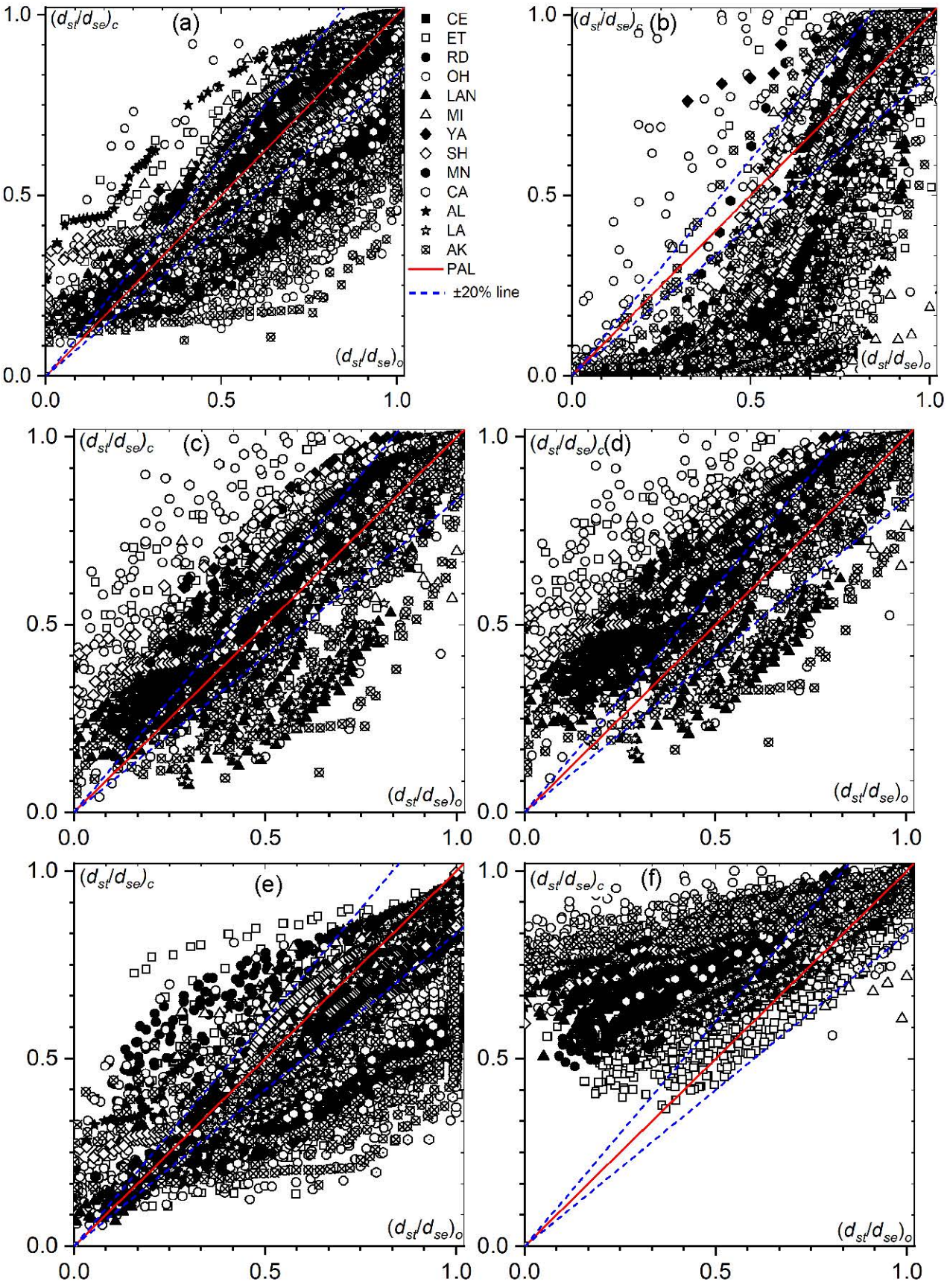

Fig. 3.3. Observed versus computed normalized d_{st} with d_{se} using formulas of **(a)** Franzetti et al. (1982), **(b)** Sumer et al. (1992), **(c)** NCHRP (2011), **(d)** Melville and Chiew (1999), **(e)** Lança et al. (2013), and **(f)** Choi and Choi (2016).

The selected data from the literature are plotted as computed normalized d_{st} versus measured normalized d_{st}. From the figure, it can be seen that 67% of the observed d_{st} data from the literature fall within the 80% accuracy band when compared to the computed d_{st} data using the formula by Franzetti et al. (1982). Similarly, 64%, 73%, 63%, 62%, and 53% of the observed d_{st} data from the literature fall within the 80% accuracy band when compared to the d_{st} data based on the formulas mentioned above.

Figure 3.4(a-b) shows the observed normalized d_s $(d_{st}/(hd^2)^{1/3})_o$ in the abscissa direction and normalized computed d_s $(d_{st}/(hd^2)^{1/3})_c$ in the ordinate direction. The normalization was done with h and d. Figure 3.4(a) shows the observed and predicted d_{st} data plotted using the formula given by Oliveto and Hager (2002) while Fig. 3.4(b) shows the predicted d_{st} plot using the formula of Kothyari et al. (2007). Here, 35% and 34% of the d_{st} data are found to lie within the 80% accuracy band respectively.

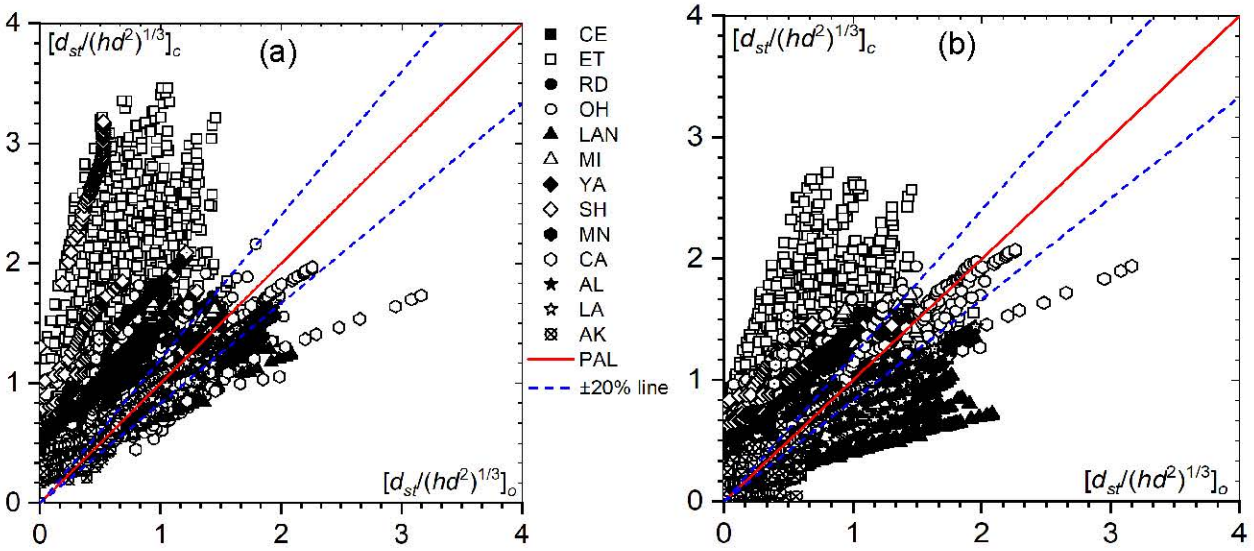

Fig. 3.4. Plots of observed versus computed normalized d_{st} with $(hd^2)^{1/3}$ using formulas of (a) Oliveto and Hager (2002), and (b) Kothyari et al. (2007).

The d_{st} data of SH and ET throughout the series are dispersed with considerable amounts as clearly shown in Fig. 3.4(a) and Fig. 3.4(b) respectively. The rest of the other d_{st} data, more or less follow the 80% accuracy band in the case of Fig. 3.4(a). However, for Fig. 3.4(b), initially, they are more scattered but in later stages, it follows the 80% accuracy band.

Figures 3.5(a-d) show the normalized computed d_s $(d_{st}/d)_c$ in the ordinates and the observed normalized d_s $(d_{st}/d)_o$ in the abscissa. Figure 3.5(a) shows the observed and predicted d_{st} data plot using the formula of Shen et al. (1966). Figure 3.5(b) shows the d_{st} plot using the formula of Aksoy et al. (2017) and Fig. 3.5(c) shows the d_{st} plot using the formula of Franzetti et al. (2022). It is found that 21%, 49%, and 60% of the measured d_{st} data from the literature lie within the ±80% accuracy band when compared to the predicted d_{st} data for Shen et al. (1966), Aksoy et al. (2017), and Franzetti et al. (2022).

The performance of the d_{st} datasets is also examined considering the average percentage of d_{st} data falling within the ±80% accuracy range. A total of 329 d_{st} data series have been collected to measure the accuracy of each literature formula. It is noticed that the d_{st} data

series satisfies the literature formula minimum of 21% to a maximum of 73%, where the minimum is 21% of d_{st} data series is satisfied by the Shen et al. (1966) formula and the maximum of 73% satisfied by NCHRP (2011) formula as shown in Fig. 3.6(a).

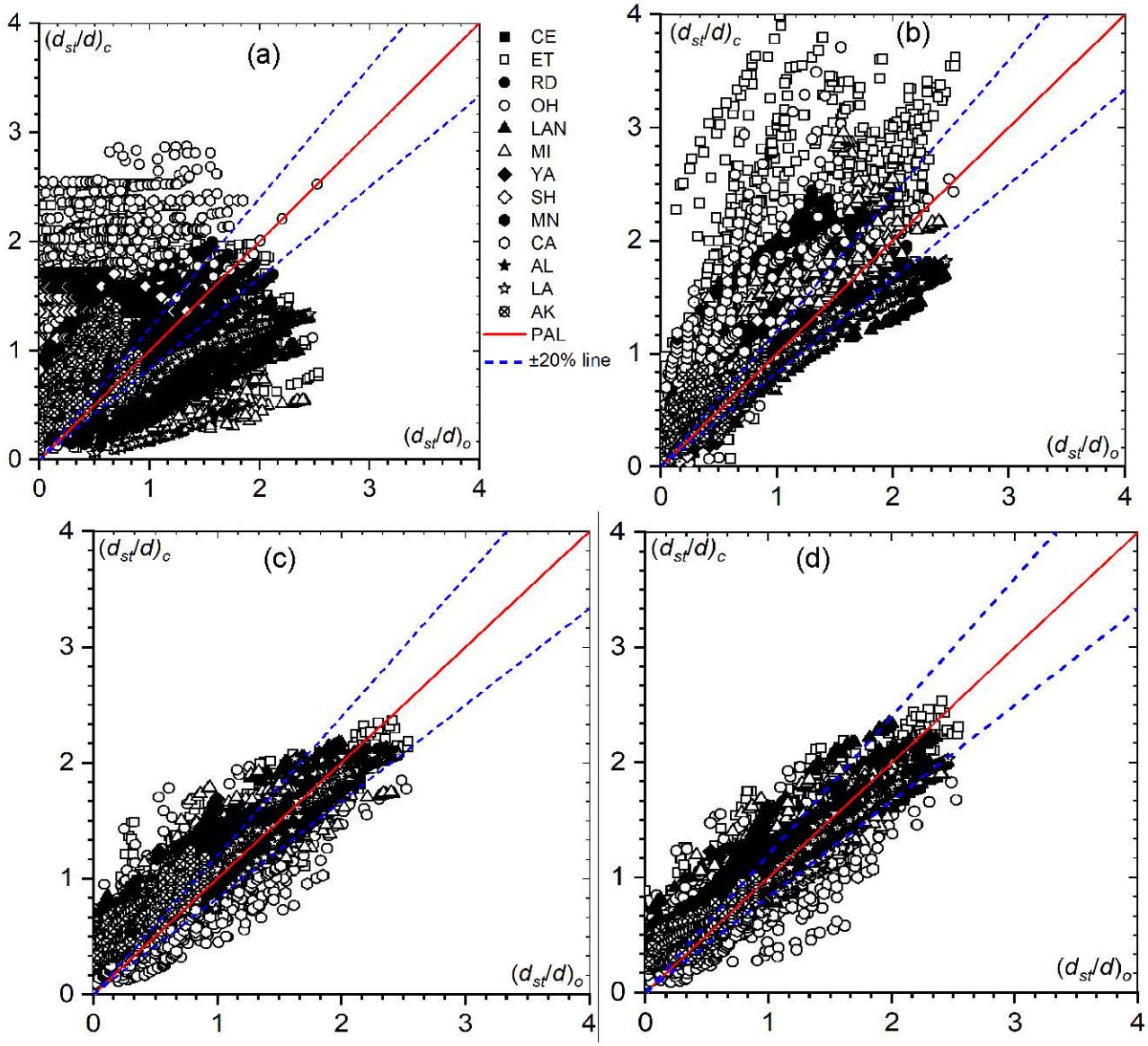

Fig. 3.5. Plots of observed versus computed normalized d_{st} with d using formulas of **(a)** Shen et al. (1966), **(b)** Aksoy et al. (2017), **(c)** Franzetti et al. (2022), and **(d)** present study.

There are a total of four formulas given by Shen et al. (1966), Oliveto and Hager (2002), Kothyari et al. (2007), and Aksoy et al. (2017) who have d_{st} data series agreement in terms of percentage d_{st} data in and out is less than 50% and the rest of the formulas are in agreement greater than 50%. Figure 3.6(b) indicates average, 31% of d_{st} of the data of OH falls under the 80% accuracy band. The d_{st} data by CE has the highest agreement, with almost 57% of d_{st} data points falling under the 80% accuracy band compared to the computed d_{st} from the rest of the literature. In all, three data series, LAN, SH, MI, LA, and CE have average d_{st} data series agreements in terms of percentage in and out that are greater than equal to 50%, compared to the remaining d_{st} data series, which all have agreements less than 50%. Under

prediction of d_{st} is insufficiently conservative and should be avoided in real-field applications, on the other hand, too much over-prediction is also problematic for the application engineers to construct such circular bridge piers, as it is not economical in engineering concerns.

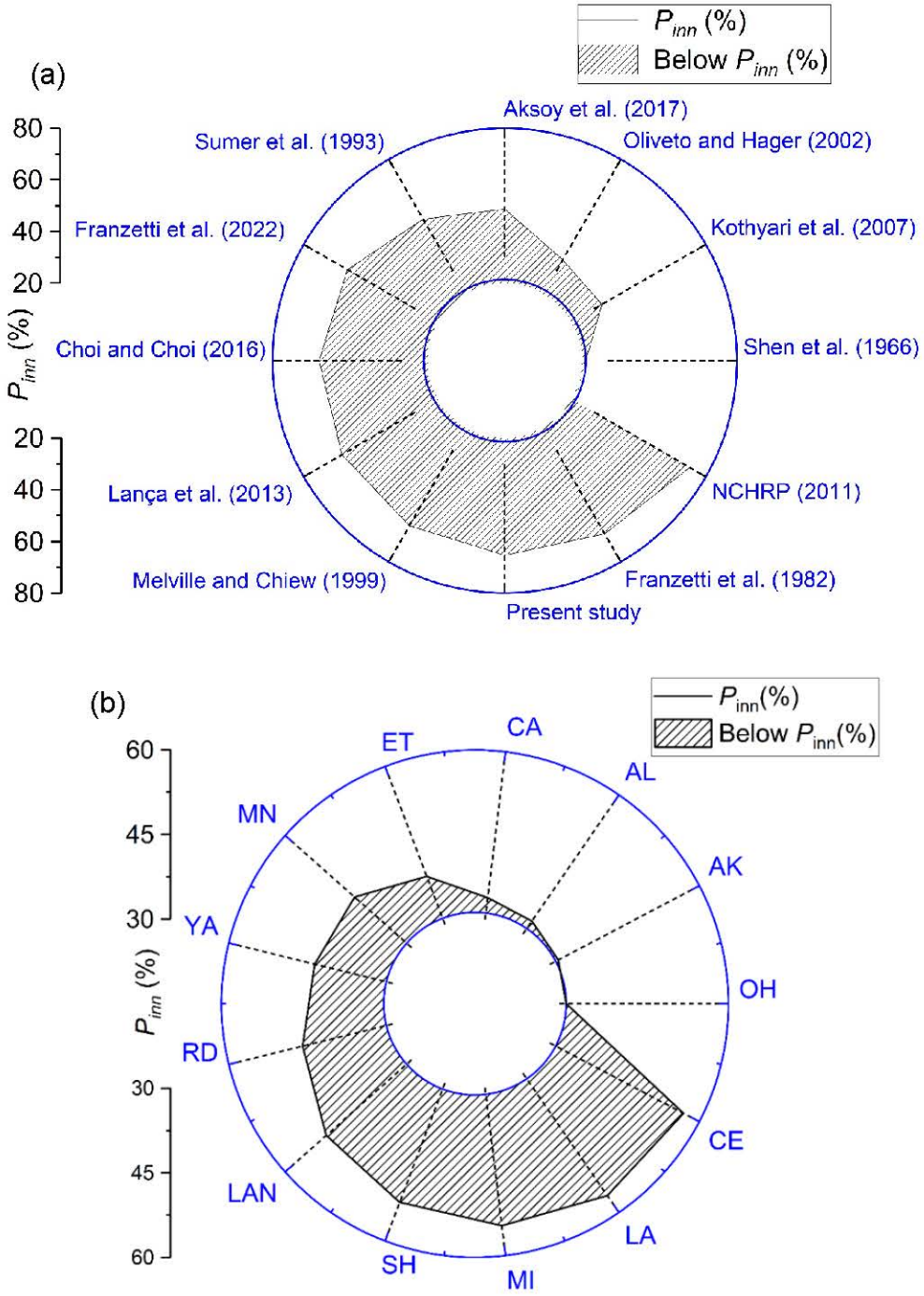

Fig. 3.6. (a) Percentage of d_{st} data series satisfied by the respective formulas, and **(b)** average percentage of d_{st} data of research groups classified within the ±80% accuracy band.

However, a higher value for structural design can be used to achieve a higher factor of safety. Both problems were encountered by Franzetti et al. (2022), to estimate upper-bound, the scour formula must be multiplied by 1.6, i.e., the constant a = 4.1 instead of 2.57.

3.3.2. Performance of formulas and sensitivity analysis

Literature data of d_{st} are analyzed to assess the accuracy of the computed d_{st} datasets by the 12 formulas in terms of eight statistical performance indicators SD, CC, IA, KGE, TSS, SSE, MAE, and NRMSE using CP given in Table 3.6. The weights are calculated by equal weight, and CRITIC methods are given in Figs. 3.7(a-b). The rankings for each d_{st} computation formula are achieved using CP.

Table 3.6. The performance indicators used for finding the ranking formula using CP.

Authors	Beneficial criteria				Non-beneficial criteria			
	Correlation coefficient (CC)	Index of agreement (IA)	Kling-Gupta efficiency (KGE)	Tailor skill score (TSS)	Sum of squared errors (SSE)	Mean absolute error (MAE)	Normalized root mean squared error (NRMSE)	Standard deviation (SD)
Shen et al. (1966)	0.02	0.40	0.00	0.50	4061.13	0.62	0.73	0.51
Franzetti et al. (1982)	0.95	0.97	0.92	0.97	247.64	0.14	0.18	0.59
Sumer et al. (1992)	0.86	0.89	0.65	0.89	1223.29	0.27	0.40	0.71
Melville and Chiew (1999)	0.96	0.97	0.87	0.98	272.10	0.14	0.19	0.54
Oliveto and Hager (2002)	0.51	0.52	-0.37	0.44	10122.05	0.69	1.16	1.22
Kothyari et al. (2007)	0.52	0.65	0.25	0.64	4159.17	0.50	0.74	0.87
NCHRP (2011)	0.96	0.98	0.93	0.98	205.05	0.11	0.16	0.56
Lança et al. (2013)	0.93	0.95	0.83	0.96	427.08	0.19	0.24	0.52
Choi and Choi (2016)	0.92	0.93	0.76	0.93	539.24	0.19	0.27	0.48
Aksoy et al. (2017)	0.70	0.82	0.63	0.84	1709.50	0.34	0.48	0.63
Franzetti et al. (2022)	0.92	0.95	0.84	0.94	385.79	0.18	0.23	0.50
Present study	0.93	0.96	0.84	0.94	326.54	0.17	0.21	0.49

The weight ranges of eight statistical performance indicators SD, CC, IA, KGE, TSS, SSE, MAE, and NRMSE using these two different weight criteria are 13-17%, 13-14%, 11-13%, 8-13%, 9-13%, 9-13%, 13-24%, and 8-13%, respectively. The highest weight is carried by MAE and the lowest weight by KGE.

The L_p values are used to rank the d_{st} datasets for each formula, with a lower L_p value considered to indicate greater accuracy and vice versa. The L_p metric is observed to vary between 0.012 (first rank) and 0.460 (last rank) for the equal weight method, and 0.014 (first rank) and 0.434 (last rank) for the CRITIC method throughout 12 formulas' ranks. The weight distribution results of the three such methods are shown in Fig. 3.7.

Using the NCHRP (2011) formula, it is found that within the 20% error band total of 73% of data points lie which is the highest of all. The lowest data agreement has been found for Shen et al. (1966) with 21% of data points lying within the 20% error band. Using CP it is found that NCHRP (2011) formula performed best considering both weightage methods, after normalizing the performance indicators with Z-score normalization (Fig. 3.8). Here, the Z-Score = (value of i^{th} influence parameter - mean of the sample)/ SD of the sample. The

accuracy of Melville and Chiew's (1999) formula is found very close to NCHRP (2011). The formula of Franzetti et al. (1982) ranked third due to the slightly higher value of SSE.

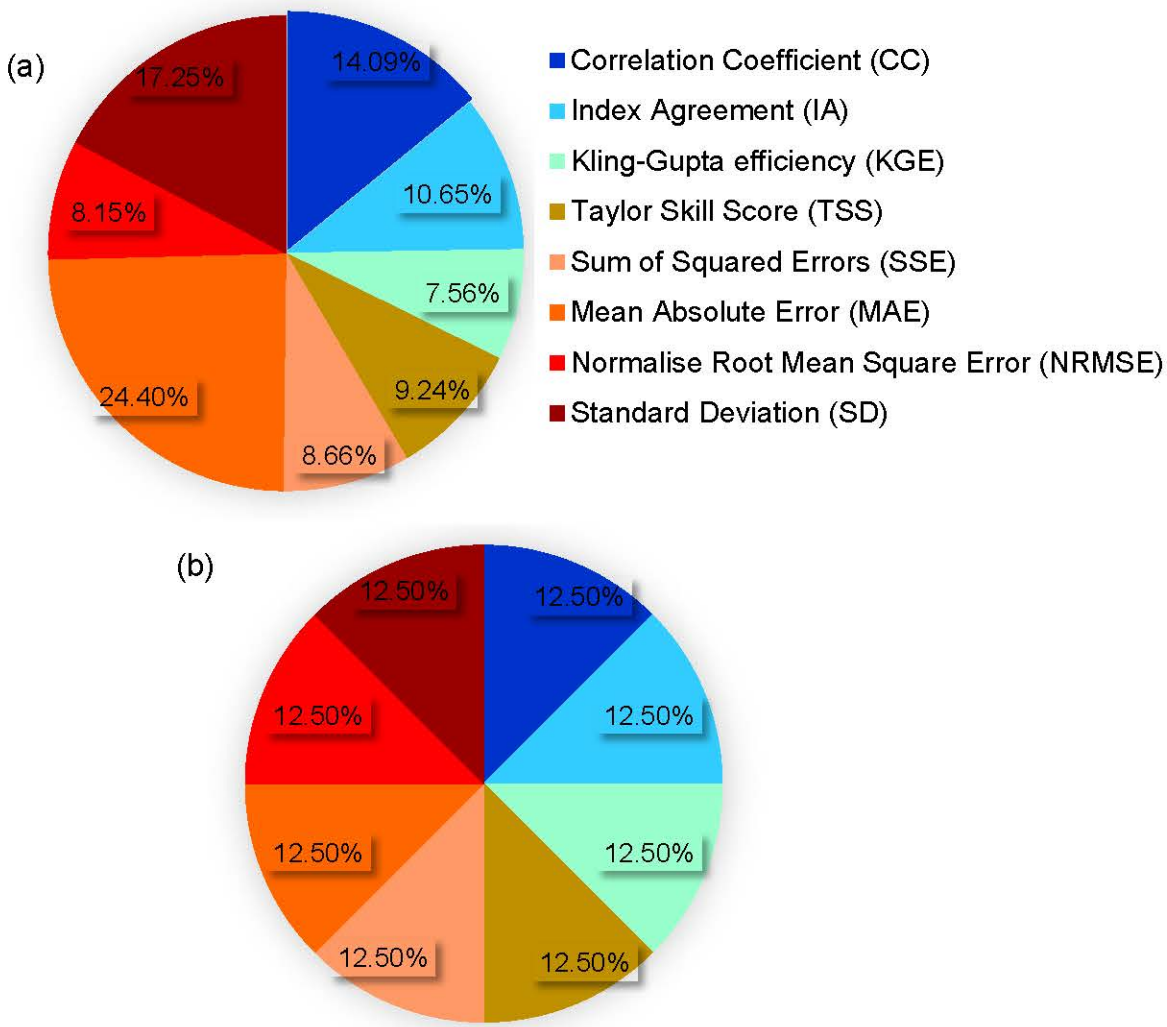

Fig. 3.7. Weight of beneficial and unfavourable criteria highlighted in pie charts for (a) CRITIC, and (b) equal weight methods.

These formulas compute the d_{st}/d_{se} as a dependent parameter with u/u_c and t/t_e as independent parameters, here d_{se} and t_e must be known to compute d_{st}. Here, d_{se} and t_e are considered as experimental d_s and experimental time respectively for the present study, though there are separate formulas given for the calculation of t_e. Calculated t_e is high and may cause a significant error to compute d_{st}. The parameter d_{st} in the formulas of Oliveto and Hager (2002) and Kothyari et al. (2007) is non-dimensionalized with $(hd^2)^{1/3}$. In the present study, these two formulas $d_{st}/(hd^2)^{1/3}$ have been normalized by multiplying $(h/d)^{1/3}$ to make it into the form d_{st}/d. These two formulas are then compared with four other formulas from Lança et al. (2013), Choi and Choi (2016), Franzetti et al. (2022), and the present study, using the same scale of d_{st}/d. The advantage of using these formulas is that they do not require any assumptions about d_{se} or t_e to compute d_{st}. Among these six d_{st}/d formulas, the newly developed formula provides the best accuracy when using CP, while the beneficial and non-beneficial criteria are equal to or better than those of the other five formulas. The formula of

Franzetti et al. (2002) is ranked just after the present formula using both weighting methods. The formula of Oliveto and Hager (2002) is ranked the lowest, with the poorest agreement of data, mainly due to the negative KGE and very high SSE.

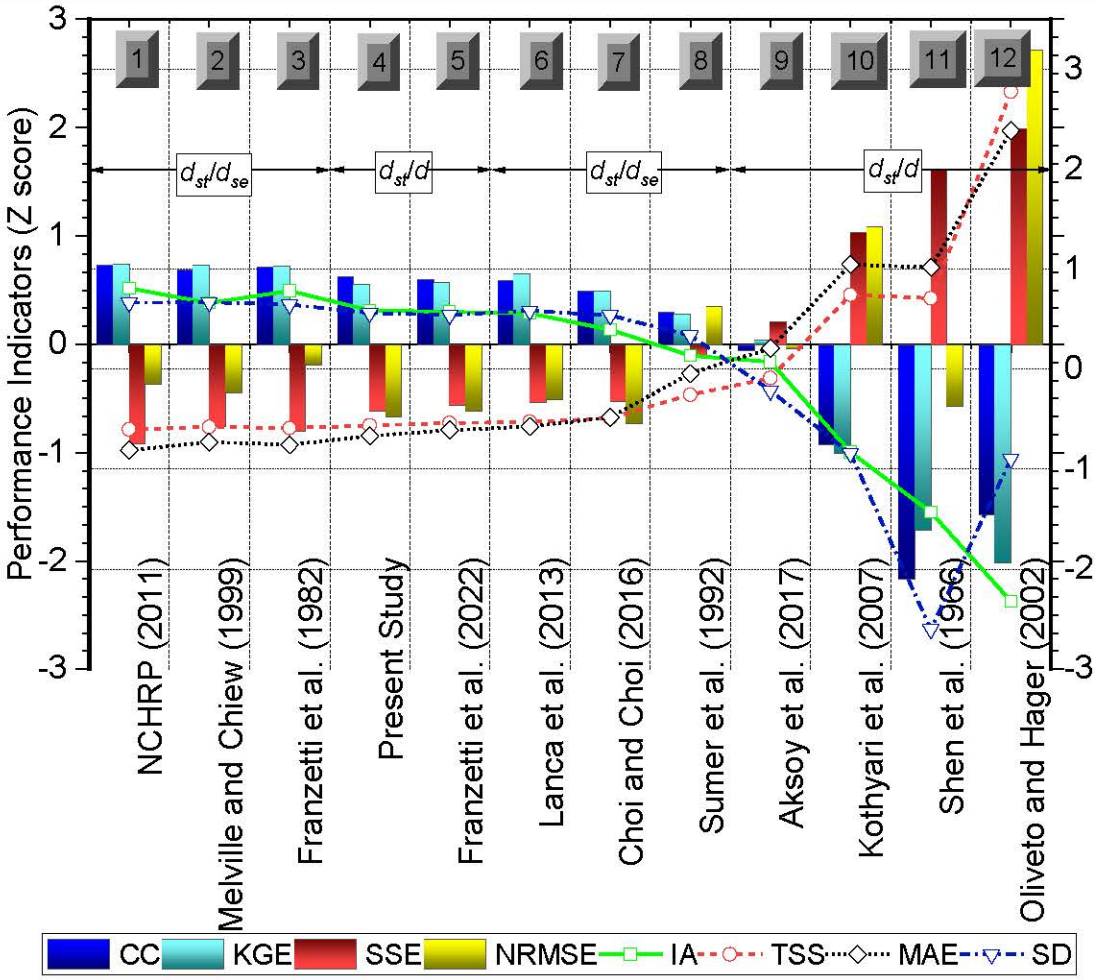

Fig. 3.8. Ranking of formulas based on d_{st}/d_{se} and d_{st}/d by compromise programming using critic and equal weight methods.

However, the observations may vary slightly depending on the selected data sets. Therefore, it is important to use as many data sets as possible to make more reliable conclusions. Overall, the data that show the most agreement are from Chabert and Engeldinger (1956), Mignosa (1980), Sheppard et al. (2006), and Lança et al. (2010), with agreement rates greater than 50%. The data from other researchers show less than or equal to 50% agreement.

3.4. Conclusions

To estimate temporal and maximum scour depths (d_{sm}) around bridge piers, many researchers have studied clear water scour under steady flow conditions. Over the years, various formulas have been developed to predict temporal scour (d_{st}). In this study, 11 of the most promising

formulas from the past six decades, along with the formula proposed in this research, are analyzed. The goal is to identify the most accurate formula for estimating d_{st}. The formulas are evaluated using eight different statistical performance measures. Further, a multi-attribute decision-making technique using compromise programming is used to rank each formula for estimating d_{st}. The observations of this study are given below-

- The key factors influencing d_s are flow characteristics, bed sediment properties, pier geometry, and time. Specifically, these include parameters like Reynolds number, Froude number, flow shallowness (u/u_c), pier slenderness (h/d), sediment coarseness (d/d_{50}), sediment uniformity (σ), and dimensionless time (ut/d). These parameters are used in various combinations in the formulas to develop computational models for estimating d_{st}. Additionally, this study highlights the significance of the constriction ratio (d/W).
- It is observed that Shen et al. (1966) formula satisfies at least 21% of the d_{st} data, while NCHRP's (2011) formula satisfies up to 73%. On average, d_{st} data from all selected studies fall within a 20% error margin, ranging from 31% to 57% agreement when compared with the d_{st} data from the formulas of all 12 research groups.
- The L_p metric, a key factor in ranking, ranges from 0.012 to 0.460 for the equal weight method and from 0.014 to 0.434 for the CRITIC method across the 12 computational formulas. This study shows that weight factors have minimal impact on the ranking of d_{st} prediction formulas.
- The study highlights that several d_{st} prediction formulas relying on d_{se} and t_e have been developed since 1999. The formula proposed by NCHRP (2011) remains the most reliable for computing d_{st}, with Melville and Chiew's (1999) formula showing accuracy that is very close to it.
- To achieve a prediction formula for d_{st} that is independent of d_{se} and t_e, the present formula shows the highest accuracy, outperforming Franzetti et al. (2022) and other related formulas.
- Overall, d_{st}/d_{se} predictors give slightly better accuracy than the d_{st}/d predictors. Though without knowing the values of d_{se} and t_e, it is difficult to use d_{st}/d_{se} predictors.
- Among the 13 selected studies, the experimental data from Chabert and Engeldinger (1956), Mignosa (1980), Sheppard et al. (2006), and Lança et al. (2010) show strong agreement with both the existing and newly proposed formulas.

This study provides valuable insights into clear-water temporal scour based on laboratory data. It offers a detailed analysis of scour prediction formulas used globally, giving hydraulic engineers and designers useful tools for estimating scour.

References

Aksoy, A.O., Bombar, G., Arkis, T., and Guney, M.S. (2017). Study of the time-dependent clear water scour around circular bridge piers. *Journal of Hydrology and Hydromechanics, 65*(1), 26–34.

Alabi, P.D. (2006). *Time development of local scour at a bridge pier fitted with a collar* (M.Sc. thesis). Department of Civil and Geological Environmental Engineering, University of Saskatchewan.

Ardil, C. (2022). Comparison of composite programming and compromise programming for aircraft selection problem using multiple criteria decision making analysis method. *International Journal of Aerospace and Mechanical Engineering, 15*(11), 479–485.

Breusers, H.N.C., Nicollet, G., and Shen, H.W. (1977). Local scour around cylindrical pier. *Journal of Hydraulic Research, 15*(3), 211–252.

Chabert, J., and Engeldinger, P. (1956). Étude des affouillements autour des piles de ponts. Technical Report. Chatou, France: Laboratoire National d'Hydraulique.

Chang, W.Y., Lai, J.S., and Yen, C.L. (2004). Evolution of scour depth at circular bridge piers. *Journal of Hydraulic Engineering, 130*(9), 905–913.

Choi, S.U., and Choi, B. (2016). Prediction of time-dependent local scour around bridge piers. *Water and Environment Journal, 30*(1–2), 14–21.

Das, S., Das, R., and Mazumdar, A. (2013). Circulation characteristics of horseshoe vortex in the scour region around circular piers. *Water Science and Engineering, 6*(1), 59–77.

Dey, S. (2014). *Fluvial hydrodynamics*. Berlin: Springer-Verlag.

Dey, S., Bose, S.K., and Sastry, G.L.N. (1995). Clear water scour at circular piers: A model. *Journal of Hydraulic Engineering, 121*(12), 869–876.

Diakoulaki, D., Mavrotas, G., and Papayannakis, L. (1995). Determining objective weights in multiple criteria problems: The critic method. *Computational Operations Research, 22*(7), 763–770.

Ettema, R. (1980). *Scour at bridge piers*. Ph.D. thesis. Department of Civil Engineering, University of Auckland.

Franzetti, S., Larcan, E., and Mignosa, P. (1982). Influence of tests duration on the evaluation of ultimate scour around circular piers. In: *Proceedings of the International Conference on the Hydraulic Modelling of Civil Engineering Structures* (editors, HS Stephens, CA Stapleton), *BHRA Fluid Engineering, Coventry, Inghilterra, Settembre 1982.* (pp. 381-396).

Franzetti, S., Radice, A., Rebai, D., and Ballio, F. (2022). Clear water scour at circular piers: A new formula fitting laboratory data with less than 25% deviation. *Journal of Hydraulic Engineering, 148*(10), 04022021.

Guo, J. (2014). Semi-analytical model for temporal clear-water scours at prototype piers. *Journal of Hydraulic Research, 52*(3), 366–374.

Jain, S.C., and Fischer, E.E. (1979). Scour around circular piers at high Froude numbers. Report No. FHWARD-79-104. Washington, DC: USDOT.

Kothyari, U.C., Hager, W.H., and Oliveto, G. (2007). Generalized approach for clear-water scour at bridge foundation elements. *Journal of Hydraulic Engineering, 133*(11), 1229–1240.

Kumar, R., Singh, S., Bilga, P.S., Singh, J., Singh, S., Scutaru, M.L., and Pruncu, C.I. (2021). Revealing the benefits of entropy weights method for multi-objective optimization in machining operations: A critical review. *Journal of Materials Research and Technology, 10*, 1471–1492.

Lança, R., Fael, C., and Cardoso, A.H. (2010). Assessing equilibrium clear water scour around single cylindrical piers. *River Flow 2010*, 1207-1214.

Lança, R., Fael, C.S., Maia, R.J., Pêgo, J.P., and Cardoso, A. (2013). Clear-water scour at comparatively large cylindrical piers. *Journal of Hydraulic Engineering, 139*(11), 1117–1125.

Lança, R., Simarro, G., Fael, C.M.S., and Cardoso, A.H. (2016). Effect of viscosity on the equilibrium scour depth at single cylindrical piers. *Journal of Hydraulic Engineering, 142*(3), 06015022.

Laursen, E.M., and Toch, A. (1956). *Scour around bridge piers and abutments* (Bulletin No. 4). Ames, IA: Iowa Highway Research Board.

Lee, S.O., and Sturm, T.W. (2009). Effect of sediment size scaling on physical modeling of bridge pier scour. *Journal of Hydraulic Engineering, 135*(10), 793–802.

Melville, B.W. (1997). Pier and abutment scour: Integrated approach. *Journal of Hydraulic Engineering, 123*(2), 125–136.

Melville, B.W., and Chiew, Y.M. (1999). Time scale for local scour at bridge piers. *Journal of Hydraulic Engineering, 125*(1), 59–65.

Melville, B.W., and Coleman, S.E. (2000). *Bridge scour*. Highlands Ranch, CO: Water Resources Publications.

Melville, B.W., and Raudkivi, A.J. (1977). Flow characteristics in local scour at bridge piers. *Journal of Hydraulic Research, 15*(4), 373–380.

Mia, F., and Nago, H. (2003). Design method of time-dependent local scour at circular bridge pier. *Journal of Hydraulic Engineering, 129*(6), 420–427.

Mignosa, P. (1980). *Fenomeni di erosione locale alla base delle pile dei ponti* (M.Sc. thesis). Politecnico di Milano.

Miller, W., and Sheppard, D.M. (2002). Time rate of local scour at a circular pile. In *First International Conference on Scour of Foundations*, College Station, Texas, USA, 827–841.

NCHRP. (2011). *Scour at Wide Piers and Long Skewed Piers*. Authored by Sheppard, D.M., Demir, H., and Melville, B. National Cooperative Highway Research Program (NCHRP). Washington, DC: The National Academies Press.

Oliveto, G., and Hager, W.H. (2002). Temporal evolution of clear-water pier and abutment scour. *Journal of Hydraulic Engineering, 128*(9), 811–820.

Oliveto, G., and Hager, W.H. (2005). Further results to time-dependent local scour at bridge elements. *Journal of Hydraulic Engineering, 131*(2), 97–105.

Pandey, M., Sharma, P.K., Ahmad, Z., and Singh, U.K. (2017). Evaluation of existing equations for temporal scour depth around circular bridge piers. *Environmental Fluid Mechanics, 17*(5), 981–995.

Pomerol, J.C., and Barba-Romero, S. (2000). *Multicriterion decision in management: principles and practice* (Vol. 25). Springer Science & Business Media.

Raikar, R.V., and Dey, S. (2005). Clear-water scour at bridge piers in fine and medium gravel beds. *Canadian Journal of Civil Engineering, 32*, 775–781.

Shen, H.W., Schneider, V.R., and Karaki, S.S. (1966). *Mechanics of local scour*. U.S. Department of Commerce, National Bureau of Standards, Institute for Applied Technology, Fort Collins, Colorado.

Sheppard, D.M., Melville, B., and Demir, H. (2014). Evaluation of existing equations for local scour at bridge piers. *Journal of Hydraulic Engineering, 140*(1), 14–23.

Sheppard, D.M., and Miller, W.J. (2006). Live-bed local pier scour experiments. *Journal of Hydraulic Engineering, 132*(7), 635–642.

Sheppard, D.M., Odeh, M., and Glasser, T. (2002). Clearwater local sediment scour experiments. *Coastal Engineering Technical Report No. 131*. Gainesville, FL: Department of Civil and Coastal Engineering, University of Florida.

Sheppard, D.M., Odeh, M., and Glasser, T. (2004). Large scale clear-water local pier scour experiments. *Journal of Hydraulic Engineering, 130*(10), 957–963.

Simarro, G., Fael, C.M.S., and Cardoso, A.H. (2011). Estimating equilibrium scour depth at cylindrical piers in experimental studies. *Journal of Hydraulic Engineering, 137*(9), 1089–1093.

Sumer, B.M., Christiansen, N., and Fredsoe, J. (1992). Time scale of scour around a vertical pile. In *Second International Offshore and Polar Engineering Conference*. International Society of Offshore and Polar Engineers.

Sumer, B.M., Christiansen, N., and Fredsoe, J. (1993). Influence of cross section on wave scour around piles. *Waterways, Port, Coastal, and Ocean Engineering, 119*(5), 477–495.

Vonkeman, J.K., and Basson, G.R. (2019). Evaluation of empirical equations to predict bridge pier scour in a non-cohesive bed under clear-water conditions. *Journal of the South African Institution of Civil Engineering, 61*(2), 2–20.

Yanmaz, A.M. (2006). Temporal variation of clear water scour at cylindrical bridge piers. *Canadian Journal of Civil Engineering, 33*(8), 1098–1102.

Yanmaz, A.M., and Altinbilek, H.D. (1991). Study of time-dependent local scour around bridge piers. *Journal of Hydraulic Engineering, 117*(10), 1247–1268.

Chapter 4

Maximum Scour around Isolated Circular Pier

4.1. Introduction

In hydraulic environments, an obstruction like bridge piers can cause sediment to be washed away by fast-moving water. These obstructions change the flow nearby, leading to flow contractions, the formation of vortices upstream and downstream, and turbulence (Das and Mazumdar 2018). These changes increase the local sediment transport, causing scour, which can damage hydraulic structures (Sumer 2007). Scour depth (d_s) assessment relies on two main methods: *physical process-based models* and *soft computing or data-driven models*. The first method focuses on the physics of hydraulic processes. The second uses data-driven algorithms for predictions without detailed physical explanations.

Many scour prediction formulas have been developed for maximum d_s (d_{sm}) and temporal d_s (d_{st}) (Melville and Chiew 1999, Lança et al. 2013, Franzetti et al. 2022, Nandi and Das 2023), around cylindrical piers. A widely used formula recommended by the Federal Highway Administration (FHWA) (Arneson et al. 2012) was derived from laboratory data for cylindrical piers by Chabert and Engeldinger (1956) and data from Colorado State University (CSU). The CSU (HEC-18) formula has been modified over the years and used for predicting d_{sm}. In India, the formula is based on the regime theory for d_s calculation (IRC:78 2000). Chinese scour formula by Gao et al. (1993) has been used by engineers for over 20 years. Froehlich (1988) used 83 scour data and derived a formula based on laboratory studies of scour around large obstructions. Melville (1997) proposed a promising method using extensive laboratory data from the University of Auckland and other sources. Empirical formulas often lack a solid physical foundation and are valid mainly for the experimental conditions they were based on. To address this, Coscarella et al. (2020) combined theoretical processes with empirical data to better understand the physics of local scour around piers. Sheppard et al. (2014) evaluated 23 formulas from the literature, using 441 laboratory and 760 field data, and proposed a new formula for estimating d_s.

To improve d_s prediction models, researchers have turned to soft computing techniques to estimate d_{sm}. Recent studies have focused on applying these methods to predict scour around hydraulic structures, such as isolated bridge piers, pier groups, abutments, spur dikes, sluice gates, and grade control structures showing promising results in engineering applications. Bateni et al. (2007) proposed using Artificial Neural Networks (ANNs) and Adaptive Neuro-Fuzzy Inference Systems (ANFIS) to predict equilibrium d_s (d_{se}) and d_{st}. Generalized regression and Feed-Forward Neural Networks (FFNN) were used to predict d_s around cylindrical bridge piers, finding that generalized regression outperformed Multiple

Linear Regression (MLR) and empirical formulas (Firat and Gungor 2009). Researchers used ANFIS to predict d_s, showing that ANFIS provided good predictions compared to RBFNN and linear regression respectively (Akib et al. 2014). Cheng et al. (2015) introduced an Evolutionary RBFNN (ERBFNN) that combined RBFNN with Artificial Bee Colony Optimization (ABCO), outperforming four other techniques and four mathematical methods in predicting d_s. Choi et al. (2017) used ANFIS to predict d_{se} using five variables and found that it improved predictions compared to both ANN and empirical formulas. Ebtehaj et al. (2019) employed Extreme Learning Machines (ELM) for predicting d_s and found better against regression models. Choi and Choi (2022) applied Support Vector Machines (SVM) for predicting d_s and found that SVM outperformed ANFIS, Gene Expression Programming (GEP), and other methods. A Metaheuristics-Optimized Stacking System (MOSS), combined metaheuristic optimization with machine learning (ML) models to improve d_s prediction (Chou and Nguyen 2022). A multi-level ML method, including Extreme Gradient Boosting (XGBoost) and Random Forest (RF), found these methods outperformed the standalone models (Singh et al. 2022) used. Kumar et al. (2023) used ensemble and standalone ML approaches, showing that ensemble techniques outperformed traditional methods.

The goal is to identify a robust model for d_{sm} estimation with a minimal uncertainty band. The aim is to use ensemble methods that combine the strengths of individual ML models to enhance prediction accuracy considering a range of data. The study aims to develop novel ensemble models integrating Support Vector Machine for Regression (SVMR), Random Forest Regression (RFR), and Reduced Error Pruning Tree (REPTree) as base learners, with Boosted Regression Tree (BRT) and Stochastic Gradient Boosting (SGB) as meta-learners. A total of 634 experimental datasets from 35 studies over 63 years are analyzed for d_{sm} prediction under clear-water conditions. Model performance is evaluated using statistical metrics like Correlation Coefficient (CC), Modified Kling-Gupta Efficiency (MKGE), Absolute Normalized-Mean Bias Error (ANMBE), and Persistence Index (PI).

4.2. Methods

4.2.1. Curation of scour data

We reviewed over 35 research papers for the initial data collection, gathering more than 850 isolated data samples. A total of six d_{sm} formulas are also collected from the literature (Table 4.1). After screening the data to focus on variables influencing d_s, the sample size was reduced to 634 data points, as shown in Table 4.2. We encountered several variations in the reported parameters across studies during data curation given below.

***Velocity* (u):** Different studies reported velocities in various forms, such as bulk u, depth-averaged u, or central mean u. To ensure consistency, we used the original u provided by the same research group, regardless of the type. For studies that did not provide u directly, we derived it using other available parameters.

Critical velocity (u_c): Some studies reported results in terms of shear velocity (u_*) or critical shear velocity (u_{*c}) instead of critical u (u_c). To resolve this, we converted u_{*c} to u_c

using a promising logarithmic formula of u/u_* or u_c/u_{*c}= 5.75log ($h/2d_{50}$) + 6, d_{50} is median diameter of sediment particle.

***Sediment gradation* (σ):** In cases where σ data was missing, we assumed the sediment is uniform if reported as such, assigning σ a value of less than 1.4, typically 1.3. For non-uniform sediment, we used values greater than 1.4.

***Relative density of sediments* (ρ_f/ρ_s):** If sediment density was not provided, we used a standard value of 2.65, as recommended for coarse sediment or sand. Here, ρ_f and ρ_s is densities of water and sediment.

***Flume width* (W):** If the W was provided, we used it directly. Otherwise, we estimated W based on discharge (Q) or u and the cross-section given.

***Threshold condition for incipient motion* (u/u_c):** To maintain data consistency, we adjusted u/u_c values using the logarithmic formula. Slightly higher values are considered (~1) but values of u/u_c > 1.2, are excluded.

4.2.2. Dimensional analysis: Buckingham π theorem

The d_{sm} for the cylindrical isolated pier is the function of the following variables (Eq. 4.1). Here, d is pier diameter, h is flow depth, t is time, g is gravitational acceleration, μ is dynamic viscosity of water.

$$d_{sm} = f\left(h, d, u, u_c, d_{50}, \rho_f, \rho_s, \sigma, t, g, W, \mu\right) \tag{4.1}$$

The relationship can then be modified, adjustments include inverting the numerator and denominator of a ratio, as well as converting one variable into another if both are present in the same relationship (Eq. 4.2).

$$\frac{d_{sm}}{d} = f\left(\frac{h}{d}, \frac{u}{u_c}, \frac{d}{d_{50}}, \frac{\rho_f u h}{\mu}, \frac{u}{\sqrt{gh}}, \sigma, \frac{ut}{d\Delta^{0.5}}, \frac{d}{W}\right) \tag{4.2}$$

4.2.3. Promising maximum scour depth formulas

To assess the predictive ability of each formula in combination with our proposed non-tuned ML model, six empirical formulas from previous literature for d_{sm} of scour at bridge piers are taken (Table 4.1).

Table 4.1. Functional relationships of empirical formulas

References	Functions
Nandi and Das (2023)	$D_{sm} = f(u/u_c, h/d, \sigma, d/d_{50}, ut/d\Delta^{0.5}, d/W)$
Franzetti et al. (2022)	$D_{sm} = f(u/u_c, h/d, \sigma, d/d_{50}, ut/d\Delta^{0.5})$
Sheppard and Miller (2006)	$D_{sm} = f(u/u_c, h/d, d/d_{50})$
Melville and Southerland (1988)	$D_{sm} = f(u/u_c, h/d, d/d_{50})$
Froehlich (1988)	$D_{sm} = f(h/d, d/d_{50})$
Jain and Fischer (1979)	$D_{sm} = f(h/d, \mathrm{Fr})$

Table 4.2. Sources of information for relevant experiments and appropriate *non-dimensional* ranges.

Literatures	#	u/u_c – intensity of flow	h/d – flow shallowness	σ– sediment gradation	d/d_{50} – sediment coarseness	dimensionless time– $ut/d\Delta^{0.5}$	Constriction ratio– d/W	Fr – Froude number	Re–Reynolds number
Chabert and Engeldinger (1956)	12	0.74-0.90	0.67-7.00	1.08-1.08	16.67-384.62	5.85×10^{4}-2.28×10^{6}	0.05-0.15	0.12-0.40	4.00×10^{3}-1.04×10^{5}
Ettema (1980)	115	0.55-1.15	0.20-21.05	1.07-4.55	3.65-1000.00	7.32×10^{4}-1.23×10^{7}	0.02-0.16	0.07-1.03	7.52×10^{3}-9.40×10^{5}
Mignosa (1980)	19	0.78-1.05	2.56-4.76	1.32-1.32	10.68-19.20	1.51×10^{5}-1.38×10^{7}	0.05-0.10	0.12-0.16	1.71×10^{4}-2.50×10^{4}
Chiew (1984)	1	0.50-0.50	4.67-4.67	1.88-1.88	14.06-14.06	4.04×10^{5}-4.04×10^{5}	0.10-0.10	0.25-0.25	7.00×10^{4}-7.00×10^{4}
Franzetti et al. (1989)	1	0.82-0.82	3.00-3.00	1.32-1.32	19.20-19.20	3.63×10^{7}-3.63×10^{7}	0.09-0.09	0.12-0.12	2.11×10^{4}-2.11×10^{4}
Hancu and Predescu (1989)	6	0.77-0.99	0.77-1.67	1.22-1.72	15.00-260.00	2.07×10^{5}-1.80×10^{6}	0.03-0.13	0.20-0.63	2.00×10^{4}-6.20×10^{4}
Dargahi (1990)	1	0.92-0.92	1.33-1.33	1.37-1.37	394.74-394.74	5.83×10^{4}-5.83×10^{4}	0.15-0.15	0.14-0.14	5.20×10^{4}-5.20×10^{4}
Yanmaz and Altinbilek (1991)	47	0.44-0.90	0.67-3.51	1.10-1.30	43.87-79.83	3.13×10^{4}-1.06×10^{5}	0.07-0.10	0.18-0.37	7.46×10^{3}-4.88×10^{5}
Graf 1995	3	1.02-1.02	1.55-2.32	1.30-1.30	47.62-71.43	1.18×10^{6}-1.76×10^{6}	0.10-0.15	0.40-0.45	9.84×10^{4}-1.41×10^{5}
Chiew (1995)	12	0.55-1.20	0.66-2.86	1.25-1.31	72.92-131.03	1.15×10^{5}-3.31×10^{6}	0.09-0.12	0.15-0.38	4.30×10^{4}-8.62×10^{4}
Dey et al. (1995)	18	0.75-1.01	0.46-0.88	1.31-1.39	98.28-292.31	7.61×10^{5}-1.54×10^{5}	0.07-0.09	0.29-0.37	6.02×10^{3}-1.31×10^{4}
Melville (1997)	13	0.45-0.84	0.60-12.62	1.30-1.30	17.61-222.17	3.65×10^{4}-1.78×10^{6}	0.01-0.13	0.12-0.27	2.76×10^{4}-5.85×10^{4}
Melville and Chiew (1999)	45	0.43-0.94	0.60-12.50	1.30-1.30	17.78-222.22	3.30×10^{4}-1.80×10^{6}	0.02-0.20	0.12-0.38	1.16×10^{4}-6.48×10^{4}
Oliveto and Hager (2002)	77	0.54-1.13	0.12-6.76	1.00-2.35	6.73-467.27	7.99×10^{3}-1.65×10^{7}	0.02-0.50	0.13-1.05	6.97×10^{3}-1.30×10^{4}
Mia and Nago (2003)	5	0.70-0.80	2.67-5.00	1.29-1.29	46.88-46.88	3.63×10^{4}-8.17×10^{4}	0.10-0.10	0.23-0.25	4.98×10^{4}-1.16×10^{5}
Chang et al. (2004)	23	0.77-1.09	0.75-1.50	1.20-3.00	100.00-142.86	4.45×10^{4}-7.16×10^{5}	0.10-0.10	0.26-0.39	1.69×10^{4}-5.31×10^{4}
Sheppard et al. (2004)	6	0.74-0.92	0.19-3.93	1.21-1.51	315.52-1386.36	1.71×10^{5}-9.33×10^{5}	0.05-0.15	0.09-0.38	8.37×10^{4}-9.19×10^{5}
Raikar and Dey (2005)	38	0.86-0.91	3.25-7.81	1.08-2.93	2.25-18.78	6.65×10^{5}-2.38×10^{6}	0.05-0.13	0.49-0.70	1.90×10^{5}-2.76×10^{5}
Alabi (2006)	3	0.62-0.84	2.00-2.00	1.23-1.23	137.74-216.98	4.64×10^{5}-2.52×10^{6}	0.06-0.09	0.13-0.21	3.62×10^{4}-5.71×10^{4}
Ettema (2006)	6	0.90-0.90	2.46-15.75	1.30-1.30	60.48-387.05	1.02×10^{5}-4.87×10^{5}	0.06-0.40	0.15-0.15	4.60×10^{5}-4.60×10^{5}

Sheppard and Miller (2006)	4	0.56-0.88	2.76-3.22	1.32-1.33	180.95-562.96	8.98×10^{4}-1.51×10^{6}	0.10-0.10	0.08-0.18	7.49×10^{4}-1.83×10^{5}
Link et al. (2008)	1	0.85-0.85	1.50-1.50	1.37-1.37	769.23-769.23	6.76×10^{4}-6.76×10^{4}	0.20-0.20	0.26-0.26	7.41×10^{4}-7.41×10^{4}
Lee and Sturm (2009)	37	0.60-1.09	3.07-7.49	1.25-1.25	8.18-104.53	2.23×10^{5}-4.44×10^{6}	0.01-0.01	0.14-0.60	2.42×10^{4}-1.15×10^{5}
Lança et al. (2010)	5	0.80-0.86	2.00-2.13	1.40-1.46	49.22-93.02	7.84×10^{6}-1.20×10^{7}	0.08-0.10	0.23-0.30	4.45×10^{4}-5.66×10^{4}
Coleman from NCHRP (2011)	2	1.02-1.04	0.13-0.25	1.30-1.30	378.57-378.57	2.37×10^{5}-2.43×10^{5}	0.32-0.32	0.37-0.48	1.20×10^{4}-2.66×10^{4}
Jones from NCHRP (2011)	17	0.58-1.17	1.75-1.76	1.37-1.37	30.366-505.97	2.39×10^{5}-2.08×10^{6}	0.15-0.15	0.18-0.48	7.71×10^{4}-2.09×10^{5}
Khosronejad et al. (2012)	1	0.68-0.68	1.13-1.13	1.30-1.30	194.24-194.24	5.09×10^{4}-5.09×10^{4}	0.17-0.17	0.07-0.07	4.65×10^{4}-4.65×10^{4}
Beg (2013)	6	1.04-1.04	1.94-4.20	1.20-1.20	35.05-75.80	3.64×10^{5}-7.88×10^{5}	0.04-0.10	0.33-0.33	5.46×10^{4}-3.27×10^{5}
Das et al. (2013)	16	0.74-1.03	0.60-1.60	1.80-1.80	60.61-133.33	3.86×10^{5}-1.06×10^{6}	0.06-0.14	0.22-0.40	1.48×10^{4}-3.09×10^{4}
Lança et al. (2013)	46	0.74-0.91	0.50-5.00	1.36-1.46	49.22-465.12	5.19×10^{5}-1.15×10^{7}	0.03-0.20	0.17-0.39	1.35×10^{4}-1.32×10^{5}
Ettmer et al. (2015)	5	0.85-1.06	1.57-1.57	1.19-1.19	35.00-35.00	9.07×10^{4}-1.13×10^{5}	0.07-0.07	0.07-0.19	7.92×10^{3}-9.90×10^{3}
Shalmani and Hakimzadeh (2015)	13	0.76-0.89	1.50-2.51	1.25-1.25	149.38-250.00	3.15×10^{5}-5.82×10^{5}	0.06-0.10	0.19-0.27	1.26×10^{4}-1.90×10^{4}
Lança et al. (2016)	8	0.74-0.89	1.00-1.51	1.18-1.50	58.14-58.59	1.37×10^{6}-2.67×10^{6}	0.01-0.04	0.33-0.34	1.36×10^{4}-1.39×10^{5}
Aksoy et al. (2017)	16	0.48-0.60	0.93-4.68	1.39-1.39	11.53-57.64	3.26×10^{4}-2.06×10^{5}	0.05-0.25	0.26-0.33	6.48×10^{4}-8.22×10^{4}
Link et al. (2019)	6	0.65-1.07	1.53-3.33	1.18-1.45	18.75-416.67	2.88×10^{5}-7.17×10^{5}	0.02-0.11	0.19-0.35	1.58×10^{4}-6.67×10^{4}
Total	634	0.43-1.20	0.12-21.05	1.00-4.55	2.25-1386.36	7.99×10^{3}-3.63×10^{7}	0.01-0.50	0.07-1.05	4.00×10^{3}-9.40×10^{5}

– Number of experimental data samples take

4.2.4. Data pre-processing

The raw data is transformed into a collection of independent dimensionless variables: u/u_c, h/d, σ, d/d_{50}, $ut/d\Delta^{0.5}$, d/W, Fr, and Re during the processing phase. These variables served as input variables in the analysis of subset regression. The d_{sm}/d is the response variable. Table 4.3 gives descriptive statistical measures of the dataset. Among these variables, $ut/d\Delta^{0.5}$ has the most pronounced skewness, with a value of 6.54, which indicates a significant deviation from the normal distribution. Furthermore, the kurtosis of variable $ut/d\Delta^{0.5}$ is very high at 71.82, which indicates heavy-tailedness.

The Anderson-Darling (AD) test is an alternative to the chi-square and Kolmogorov-Smirnov goodness-of-fit tests (Table 4.3). The Shapiro-Wilk test is the best normality test, but studies from Razali and Wah (2011), indicated that for sample sizes bigger than 500, the AD test performed well and was comparable to the Shapiro-Wilk test. *Null hypothesis* (H_0): the data are normally distributed, and *Alternate hypothesis* (H): the data are not normally distributed, considered significance level α=0.05, for all cases, we have rejected null hypothesis (H_0) as p<0.005 and accepted the alternate hypothesis.

Table 4.3 Descriptive statistics matrices when p <0.005.

Variable	Mean	SD	Minimum	Maximum	Range	IQR	Skewness	Kurtosis	AD
d_{sm}/d	1.3424	0.5979	0.0475	2.963	2.9155	0.8693	0.06	-0.57	1.24
u/u_c	0.8461	0.16745	0.43041	1.19659	0.76618	0.24098	-0.25	-0.54	2.72
h/d	3.465	3.756	0.118	21.053	20.935	3.167	2.44	6.99	50.81
σ	1.3761	0.3527	1	4.55	3.55	0.130	3.55	17.72	70.95
d/d_{50}	103.61	133.87	2.25	1386.36	1384.12	102.20	3.87	23.85	56.85
$ut/d\Delta^{0.5}$	1338007	2447154	7987	36325107	36317120	1358457	**6.54**	**71.82**	84.51
d/W	0.0956	0.0717	0.00472	0.5	0.49528	0.05621	2.12	6.81	25.65
Fr	0.31717	0.17383	0.06931	1.04562	0.97631	0.18956	1.54	2.76	22.86
Re	116950	161847	6020	940363	934343	100187	2.80	8.73	73.77

A correlation matrix showing the relationships between independent and dependent variables for best subset regression (Fig. 4.1). The correlation matrix highlights significant correlations: CC = 0.315 between d_{sm}/d and h/d, CC = 0.406 for u/u_c, and CC = -0.493 for d/W, showing h/d, u/u_c and d/W are key predictors of d_{sm}/d. Some predictors show moderate dependencies, capturing only linear interactions.

4.2.5. Selection of effective predictors

The best subset regression technique is a powerful mathematical tool for selecting effective independent predictors for the ML model. This method employs six metrics, R^2, adjusted R^2 [R^2(adj)], predicted R^2 [R^2(pred)], Mallow's coefficient (C_p), and standard error (S) and mean squared error (MSE). The methodology adopted for determining the best subset of input variables is given in Eqs. (4.3-4.12).

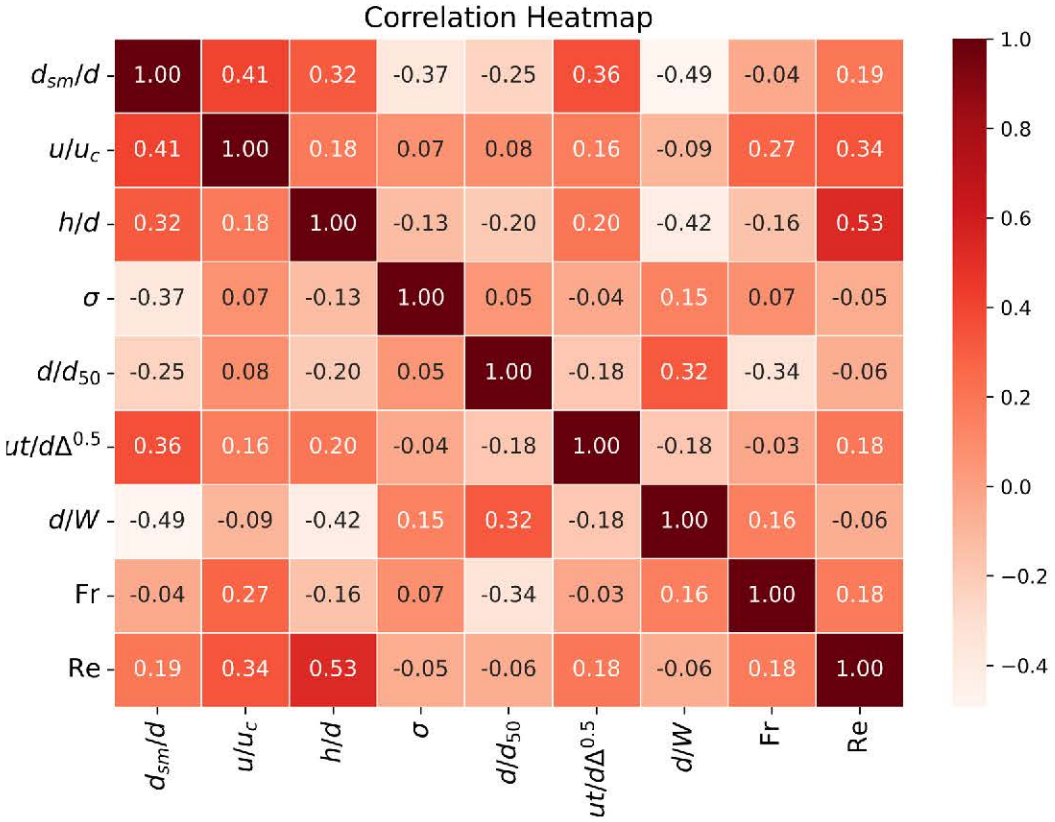

Fig. 4.1. Correlation plot for all 35 literature

The sum of square residual = $$\mathrm{SS_R} = \sum_{i=1}^{N}\left\{\left(\frac{d_{sm}}{d}\right)_{oi} - \left(\frac{d_{sm}}{d}\right)_{ci}\right\}^2 \tag{4.3}$$

The sum of square regression = $$\mathrm{SS_G} = \sum_{i=1}^{N}\left\{\left(\frac{d_{sm}}{d}\right)_{ci} - \overline{\left(\frac{d_{sm}}{d}\right)_{o}}\right\}^2 \tag{4.4}$$

The sum of square total = $$\mathrm{SS_T} = \sum_{i=1}^{N}\left\{\left(\frac{d_{sm}}{d}\right)_{oi} - \overline{\left(\frac{d_{sm}}{d}\right)_{o}}\right\}^2 \tag{4.5}$$

$$\mathrm{SS_R} + \mathrm{SS_G} = \mathrm{SS_T} \tag{4.6}$$

$$\mathrm{R^2} = 1 - \frac{\mathrm{SS_R}}{\mathrm{SS_T}} = \frac{\mathrm{SS_G}}{\mathrm{SS_T}} \tag{4.7}$$

$$\mathrm{R^2(adj)} = 1 - \frac{\mathrm{SS_R}/df_{\mathrm{R}}}{\mathrm{SS_T}/df_{\mathrm{T}}} = 1 - \frac{\mathrm{R^2}(N-1)}{N-J-1} \tag{4.8}$$

where, df_{R} (degree of freedom of residual) = (N-J-1), df_{G} (degree of freedom of regression) = J and df_{T} (degree of freedom of total) = N-1.

$$\mathrm{R^2(pred)} = 1 - \frac{\mathrm{PRESS}}{\mathrm{SS_T}} \tag{4.9}$$

$$\mathrm{PRESS} = \sum_{i=1}^{N}\left\{\left(\frac{d_{sm}}{d}\right)_{oi} - \left(\frac{d_{sm}}{d}\right)_{ci,-i}\right\}^2 \tag{4.10}$$

$$C_p = \frac{\mathrm{SS}_{\mathrm{R(P)}}}{\mathrm{MSE}} + 2(J+1) - N \tag{4.11}$$

$$\mathrm{MSE} = \frac{1}{N}\sum_{i=1}^{N}\left\{\left(\frac{d_{sm}}{d}\right)_{oi} - \left(\frac{d_{sm}}{d}\right)_{ci}\right\}^2 \tag{4.12}$$

Step 1: There are many possible regression models based on different predictor combinations. With 8 predictors, there are 256 possible models ($2^8 = 256$) to consider. Step 2: To identify the best-performing regression models, evaluate one-predictor, two-predictor, and higher-order models based on criteria such as the highest R^2, highest adjusted R^2, lowest MSE or S, and additional statistics like Mallow's C_p, PRESS, and R^2 (pred) from the PRESS statistic. For each model, remove one observation at a time, update the model with the remaining data, and calculate the PRESS statistic, with lower values indicating better performance. Subsets with low C_p values suggest minimal variation in the expected responses, and a C_p value close to J + 1 indicates negligible bias. Values significantly higher than J + 1 imply significant bias, while values lower than J + 1 indicate sampling error. Since the full model always has C_p = J + 1, it should not be used to evaluate the overall model, and C_p does not help select a model with all predictors. Step 3: After evaluating and refining the handful of models considering all the above-mentioned criteria identify the best predictor at the last step (Table 4.4).

Table 4.4. Selection of optimal input combination.

J	R^2	R^2 (adj)	R^2 (pred)	C_p	J+1	S	S^2 = MSE	Model variable	Model
1	24.3	24.2	23.9	448.9	2	0.17852	0.031869	$f(d/W)$	S1
2	37.3	37.1	36.7	265.4	3	0.16258	0.026432	$f(u/u_c, d/W)$	S2
3	48.7	48.5	48	105.1	4	0.14719	0.021665	$f(u/u_c, \sigma, d/W)$	S3
4	53.3	53	51.1	41.6	5	0.14055	0.019754	$f(u/u_c, \sigma, ut/d\Delta^{0.5}, d/W)$	S4
5	54.6	54.2	52.5	25.6	6	0.13875	0.019252	$f(u/u_c, \sigma, d/d_{50}, ut/d\Delta^{0.5}, d/W)$	S5
6	56.1	**55.7**	**53.9**	**6.3**	7	0.13656	0.018649	$f(u/u_c, \sigma, d/d_{50}, ut/d\Delta^{0.5}, d/W$, Fr)	S6
7	**56.2**	**55.7**	53.6	7.2	8	**0.13654**	**0.018643**	$f(u/u_c, h/d, \sigma, d/d_{50}, ut/d\Delta^{0.5}, d/W$, Fr)	S7
8	56.2	55.6	53.5	9	9	0.13663	0.018668	$f(u/u_c, h/d, \sigma, d/d_{50}, ut/d\Delta^{0.5}, d/W$, Fr, Re)	S8

J – Number of model-independent variables.

The sixth combination, which included all influential parameters, had the highest correlation (R^2-adj = 55.7%, R^2-pred = 53.9%), as well as the lowest C_p (= 6.3). Furthermore, the seven parameters models, which also included all relevant variables, had the best features, with the highest correlation (R^2 = 56.2%, R^2-adj = 55.7%) and the lowest C_p (= 7.2), indicating best model. However, to identify the single model with the best input condition, KNN algorithm (Kumbure and Luukka 2021) has been employed with NN=1, Euclidean distance metrics and 10-fold cross-validation. If the input data contains more outliers, a higher value of NN would be preferable, although the non-tuned KNN utilized in

this study was sufficient. The evolution metrics of CC, mean absolute error (MAE), root MSE (RMSE), relative absolute error (RAE), and root relative squared error (RRSE).

Figure 4.2 highlights the seventh numerical model, which can be identified by a set of variable functions: u/u_c, h/d, σ, d/d_{50}, $ut/d\Delta^{0.5}$, d/W, and Fr. This model appears as the best option for furthering computations incorporating $d_{sm}/d = f(u/u_c, h/d, \sigma, d/d_{50}, ut/d\Delta^{0.5}, d/W,$ Fr). The dataset for this study is split into two parts: 80% for training and 20% for testing. Min-max normalization is applied to scale the data between 0 and 1, enhancing the accuracy of the analysis.

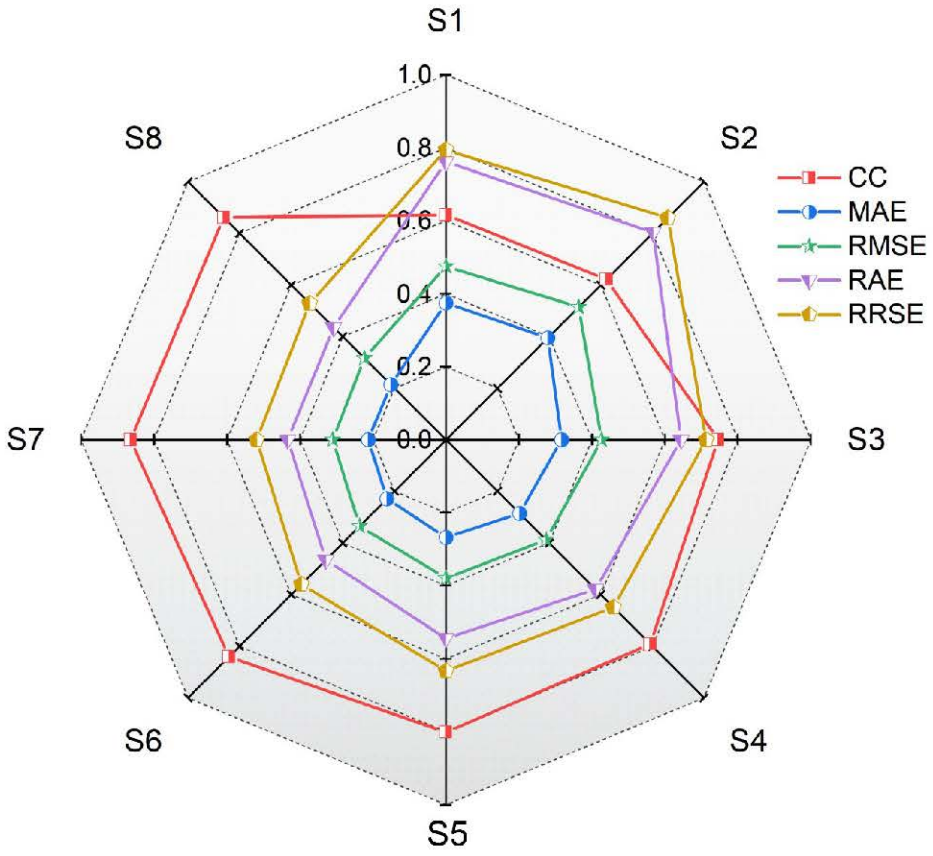

Fig. 4.2. Evolution metrics plot for KNN.

4.2.6. Description of machine learning models

Support Vector Machine for Regression (SVMR): SVMR, a supervised machine learning algorithm, predicts continuous target variables by minimizing errors and maximizing prediction accuracy (Vapnik 1995). Using the kernel trick, SVMR transforms non-linear data into a higher-dimensional space for accurate regression. It employs kernel functions like radial basis (RBF), polynomial, and Pearson VII universal (PUK) to identify optimal hyperplanes. Key parameters include complexity (C), margin of error (ε), and kernel-specific settings like exponent, gamma (γ), omega (ω), and sigma (σ). This study evaluates SVMR alone and in combination with Boosted Regression Trees (BRT) and Stochastic Gradient Boosting (SGB), showing its versatility in managing complex data patterns and improving prediction accuracy. Random Forest Regression (RFR): The RFR is a machine learning technique for regression that uses an ensemble of de-correlated decision trees built

from random subsets of data and features, reducing overfitting and improving generalization (Breiman 2001). It averages tree predictions for accurate and consistent results and is effective for handling non-linear relationships and large datasets. This study evaluates RFR as a standalone method and as a base learner in BRT and SGB. Reduced Error Pruning Tree (REPTre): The REPTree algorithm combines decision-tree methods with reduced error pruning for efficient classification and regression tasks (Quinlan 1987). It builds and prunes regression trees to maximize the information-gain ratio, creating a robust model that handles complex data interactions effectively (Bui et al. 2020). This study evaluates REPTree as a standalone hybrid strategy and as a base learner in Boosted Regression Trees (BRT) and Stochastic Gradient Boosting (SGB). The detailed methodology for this study is given in Fig. 4.3.

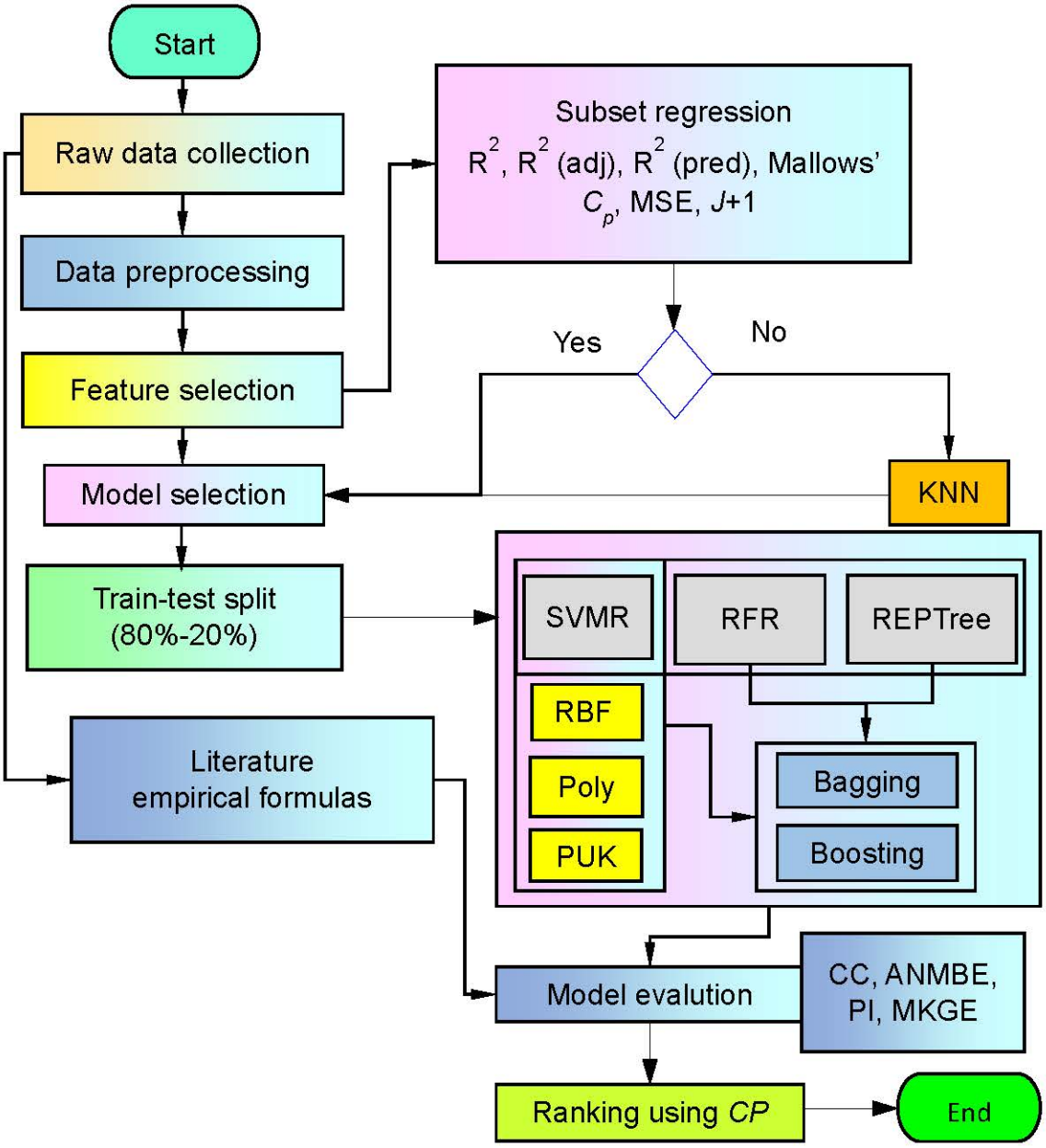

Fig. 4.3. Methodology designed for the present study.

4.2.7. Statistical performance indicators

This study employs a comprehensive set of performance metrics to evaluate model accuracy and reliability, including SD, Coefficient of Variance (CV), Persistence Index (PI), CC, MKGE, ANMBE, RSE, RMSE, and RAE. Each metric serves a specific purpose: the CC assesses the linear relationship between predictions and observations, highlighting the ability to capture trends of the model. MKGE provides evaluation by incorporating correlation, bias, and variability, making it particularly relevant for environmental hydraulics studies. ANMBE evaluates predictive accuracy by measuring bias and identifying over- or underestimation in the prediction. The PI focuses on time-series data, measuring the effectiveness of models. These metrics together offer a strong method to analyze error, bias, and variability, giving a detailed understanding of how well the model performs, specifically suitable to the focus of the present study. Formulas of some performance indicators (CV_o, CV_c, CC, RMSE, and MAE) are given in Table 3.5 while formulas of new PIs are listed in Table 4.5.

Table 4.5. Performance indicators with their pertinent ranges and ideal values.

Performance indicator	Range	Ideal value
$PI = 1 - \frac{\sum_{i=1}^{N}\left\{\left(\frac{d_{sm}}{d}\right)_{ci} - \left(\frac{d_{sm}}{d}\right)_{oi}\right\}^2}{\sum_{i=1}^{N}\left\{\left(\frac{d_{sm}}{d}\right)_{oi} - \left(\frac{d_{sm}}{d}\right)_{oi-1}\right\}^2}$	$-\infty$ to 1	1
$MKGE = 1 - \sqrt{(CC-1)^2 + \left\{\frac{CV\left\{\left(\frac{d_{sm}}{d}\right)_c\right\}}{CV\left\{\left(\frac{d_{sm}}{d}\right)_o\right\}} - 1\right\}^2 + \left(\frac{\overline{\left(\frac{d_{sm}}{d}\right)_c}}{\overline{\left(\frac{d_{sm}}{d}\right)_o}} - 1\right)^2}$	$-\infty$ to 1	1
$ANMBE = \frac{1}{N}\sum_{i=1}^{N}\frac{\left\lvert\left(\frac{d_{sm}}{d}\right)_{ci} - \left(\frac{d_{sm}}{d}\right)_{oi}\right\rvert}{\left(\frac{d_{sm}}{d}\right)_{oi}} \times 100$	0 to ∞	0
$RRSE = \frac{\sqrt{\sum_{i=1}^{N}\left\{\left(\frac{d_{sm}}{d}\right)_{ci} - \left(\frac{d_{sm}}{d}\right)_{oi}\right\}^2}}{\sqrt{\sum_{i=1}^{N}\left\{\overline{\left(\frac{d_{sm}}{d}\right)_o} - \left(\frac{d_{sm}}{d}\right)_{oi}\right\}^2}}$	0 to ∞	0

$\mathrm{RAE}=\frac{\sum_{i=1}^{N}\left\lvert\left(\frac{d_{sm}}{d}\right)_{ci}-\left(\frac{d_{sm}}{d}\right)_{oi}\right\rvert}{\sum_{i=1}^{N}\left\lvert\overline{\left(\frac{d_{sm}}{d}\right)_{o}}-\left(\frac{d_{sm}}{d}\right)_{oi}\right\rvert}$	0 to ∞	0

4.3. Results and discussion

4.3.1. Performance of models

This study explores advanced ML techniques to estimate d_{sm}, focusing on data-driven models. It uses several methods, including empirical formulas from previous studies, SVMR, RFR, REPTree, and ensemble methods like Bagging and Boosting. The dataset used in this study is developed to estimate d_{sm}. The models are evaluated using several performance measures, including CC, MKGE, ANMBE, and PI. The ML models in this study are not tuned, and the goal is to compare the accuracy of individual models with ensemble methods like BRT and SGB. The tuning variables are listed in Table 4.6.

The study also compares the performance of individual models and combined model in predicting d_{sm}. Table 4.7 shows the performance metrics (CC, MKGE, ANMBE, and PI) for training, testing, and overall data. While empirical formulas do not follow the training and testing split like ML models, they are still included in Table 4.7 for comparison with the ML models. Table 4.7 shows that Nandi and Das's (2023) formula gives the best results for the training dataset when compared to the other empirical formulas. It has CC, MKGE, ANMBE, and PI values of 0.855, 0.751, 0.026, and 0.859, outperforming the other five formulas. For the testing dataset, it also performs the best, with CC, MKGE, ANMBE, and PI values of 0.841, 0.726, 0.023, and 0.841, respectively. This higher performance continues in the overall data evolution matrices.

Table 4.6. Selected hyper-variables for non-tuned ML model.

ML model	Tuning variable
SVM-RBF	Kernel: RBF; C: 1.0; Filter type: Normalize training data; γ: 0.01; ε 0.001; Tolerance: 0.001; Number of seed:1
SVM-Poly	Kernel: Poly; C: 1.0; Filter type: Normalize training data; Exponent: 1; ε 0.001; Tolerance: 0.001; Number of seed:1
SVM-PUK	Kernel: PUK; C: 1.0; Filter type: Normalize training data; ω: 1.0; σ': 1.0; ε 0.001; Tolerance: 0.001; Number of seed:1
RFR	Maximum depth: 0 (i.e., no restriction on tree depth); Number of execution slot: 1.0; Number of trees in RF: 100; Number of seed: 1.0; Number of randomly chosen attribute: 0 (i.e., int($\log_2$(#) +1)

REPTree	Initial count: 0; Maximum depth: -1 (i.e., no restriction on tree depth); Minimum weight of the instance leaf: 2.0; No pruning: True; Number of seed: 1.0; Minimum variance probability: 0.001; Number of folds: 3.0;
BRT	Number of execution slots to constructing ensemble: 1.0; Number of iterations: 10.0; Number of seed: 1.0; Base learner: SVMR-RBF, SVMR-Poly, SVMR-PUK, RFR, REPTree.
SGB	Number of iterations: 10; Shrinkage rate: 1.0 (Smaller value prevents overfitting but increases learning time); Base learner: SVM-RBF, SVMR-Poly, SVMR-PUK, RFR, REPTree.

Note: # - Numbers of variables

When comparing the ML models in Table 4.7, SGB (RFR) stands out with CC = 0.998, MKGE = 0.861, ANMBE = 0.002, and PI = 0.988. The values for CC and PI are higher than those of the other 14 ML models in the training dataset. SGB (REPTree) shows CC = 0.965, MKGE = 0.956, ANMBE = 0.00001, and PI = 0.965. MKGE and ANMBE are the best values in the training dataset, and the ANMBE value for REPTree is the same as that of SGB (REPTree).

For the testing data evolution matrices in Table 4.7, SGB (RFR) shows CC = 0.930, MKGE = 0.718, ANMBE = 0.016, and PI = 0.909. The values for CC and PI are higher than those of the other ML models and the empirical and functional formulas. SGB(SVMR-PUK) performs well with matrices like CC = 0.860, MKGE = 0.841, ANMBE = 0.001, and PI = 0.862. The MKGE and ANMBE values are the best among the ML and empirical models for the testing dataset. When considering all data, RFR has matrices such as CC = 0.973, MKGE = 0.886, ANMBE = 0.006, and PI = 0.969, with PI being the best. SGB(RFR) has CC = 0.982, MKGE = 0.831, ANMBE = 0.004, and PI = 0.971, with CC being the best. SGB(REPTree) shows CC = 0.941, MKGE = 0.9184, ANMBE = 0.001, and PI = 0.940, where MKGE and ANMBE are the best values among all models in the study (see Table 4.7). ML models individually, SGB(RFR) and SGB(REPTree) perform best during training, while SGB(RFR) and SGB(SVMR-PUK) perform best in testing. RFR and SGB(RFR) outperform others using overall data.

Figure 4.4 shows scatter plots for observed vs. predicted data across the entire dataset. Figure 4.5 shows residual errors for the best-performing empirical and ML models. The optimal method should have more points near the zero line, which indicates reduced error. The residual error values are divided by a horizontal line at zero. Among all ML models, BRT(SVMR-PUK) in the testing phase, SGB(REPTree) in training, and RFR for overall data perform better than other models. Compared to empirical models, Nandi and Das (2023) achieve better residual error in percentage.

Table 4.7. Evolution variables of isolated pier scour models for training, testing, and for overall data.

References	Train data (80%)				Test data (20%)				All data (100%)			
	CC	MKGE	ANMBE	PI	CC	MKGE	ANMBE	PI	CC	MKGE	ANMBE	PI
Nandi and Das (2023)	0.855	0.751	0.026	0.859	0.841	0.726	0.023	0.841	0.852	0.747	0.026	0.856
Franzetti et al. (2022)	0.825	0.653	0.059	0.822	0.808	0.637	0.069	0.802	0.822	0.651	0.061	0.820
Sheppard and Miller (2006)	0.646	0.502	0.200	0.597	0.728	0.660	0.131	0.729	0.660	0.534	0.188	0.624
Froehlich (1988)	0.429	0.092	0.127	0.562	0.499	0.145	0.130	0.619	0.444	0.104	0.128	0.575
Melville and Southerland (1988)	0.520	0.461	-0.013	0.621	0.528	0.478	-0.030	0.655	0.521	0.464	-0.015	0.629
Jain and Fischer (1979)	0.410	0.044	0.743	-1.890	0.487	0.056	0.773	-1.806	0.427	0.048	0.750	-1.861
SVMR-RBF	0.714	0.437	0.001	0.727	0.687	0.425	0.050	0.703	0.709	0.436	0.010	0.724
BRT(SVMR-RBF)	0.739	0.466	0.008	0.743	0.712	0.455	0.037	0.721	0.734	0.465	0.000	0.741
SGB(SVMR-RBF)	0.752	0.676	0.001	0.775	0.707	0.660	0.020	0.721	0.742	0.675	0.003	0.766
SVMR-Poly	0.749	0.684	0.002	0.772	0.691	0.661	0.022	0.700	0.736	0.681	0.006	0.758
BRT(SVMR-Poly)	0.751	0.676	0.000	0.774	0.697	0.657	0.020	0.710	0.739	0.674	0.003	0.762
SGB(SVMR-Poly)	0.749	0.691	0.001	0.772	0.692	0.667	0.018	0.699	0.736	0.688	0.003	0.758
SVMR-PUK	0.939	0.901	0.009	0.939	0.874	0.810	0.005	0.876	0.925	0.883	0.007	0.925
BRT(SVMR-PUK)	0.943	0.889	0.012	0.943	0.889	0.825	0.006	0.888	0.932	0.877	0.008	0.931
SGB(SVMR-PUK)	0.962	0.936	0.015	0.961	0.860	0.841	0.001	0.862	0.940	0.9181	0.012	0.939
RFR	0.990	0.917	0.005	0.987	0.916	0.769	0.011	0.907	0.973	0.886	0.006	0.969
BRT(RFR)	0.976	0.864	0.008	0.970	0.919	0.744	0.017	0.906	0.963	0.839	0.010	0.956
SGB(RFR)	0.998	0.861	0.002	0.988	0.930	0.718	0.016	0.909	0.982	0.831	0.004	0.971
REPTree	0.964	0.949	0.00001	0.963	0.841	0.765	0.005	0.846	0.938	0.910	0.001	0.938
BRT(REPTree)	0.968	0.892	0.006	0.965	0.886	0.764	0.014	0.881	0.950	0.865	0.008	0.947
SGB(REPTree)	0.965	0.956	0.00001	0.965	0.849	0.778	0.004	0.854	0.941	0.9184	0.001	0.940

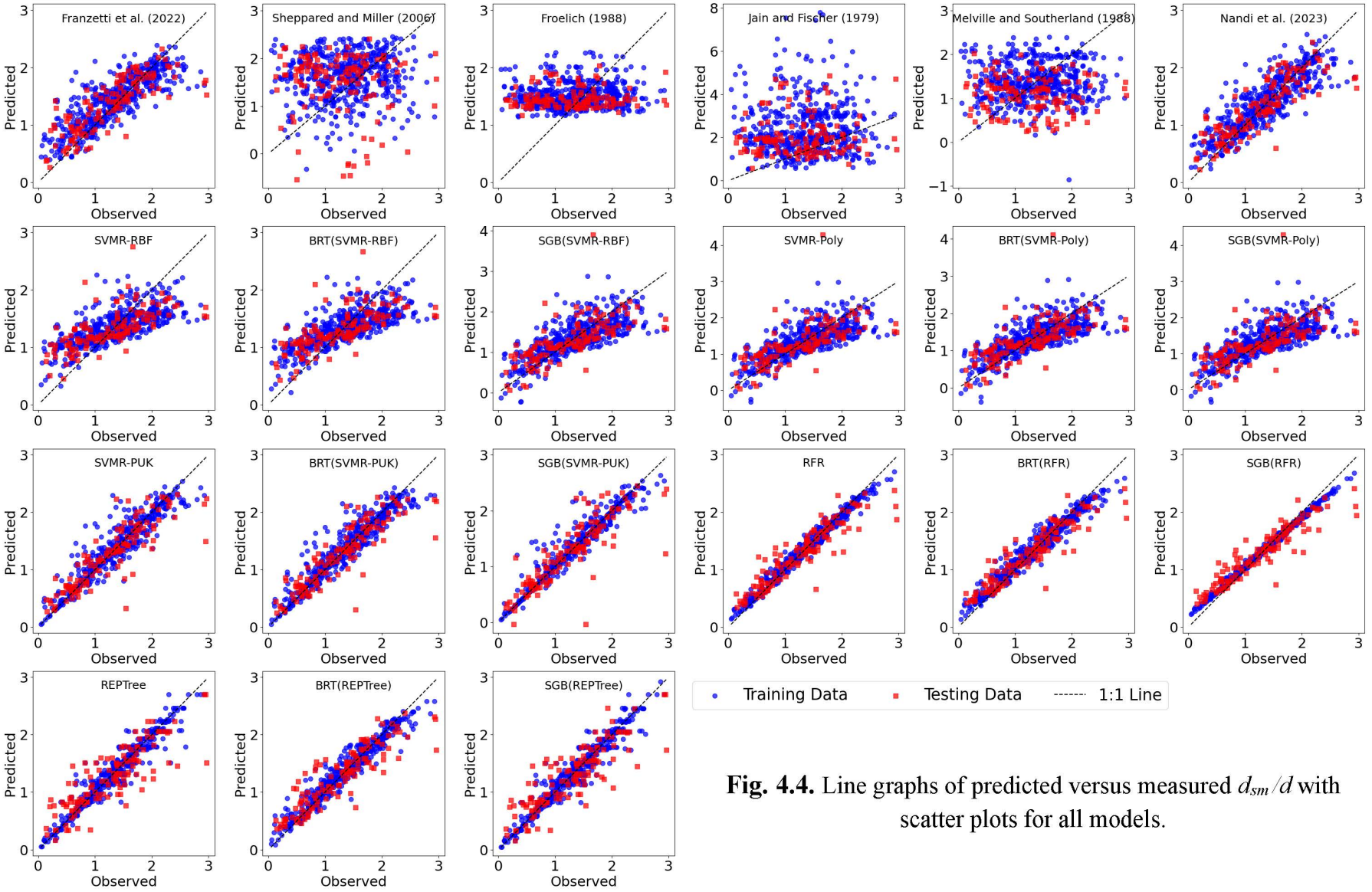

Fig. 4.4. Line graphs of predicted versus measured d_{sm}/d with scatter plots for all models.

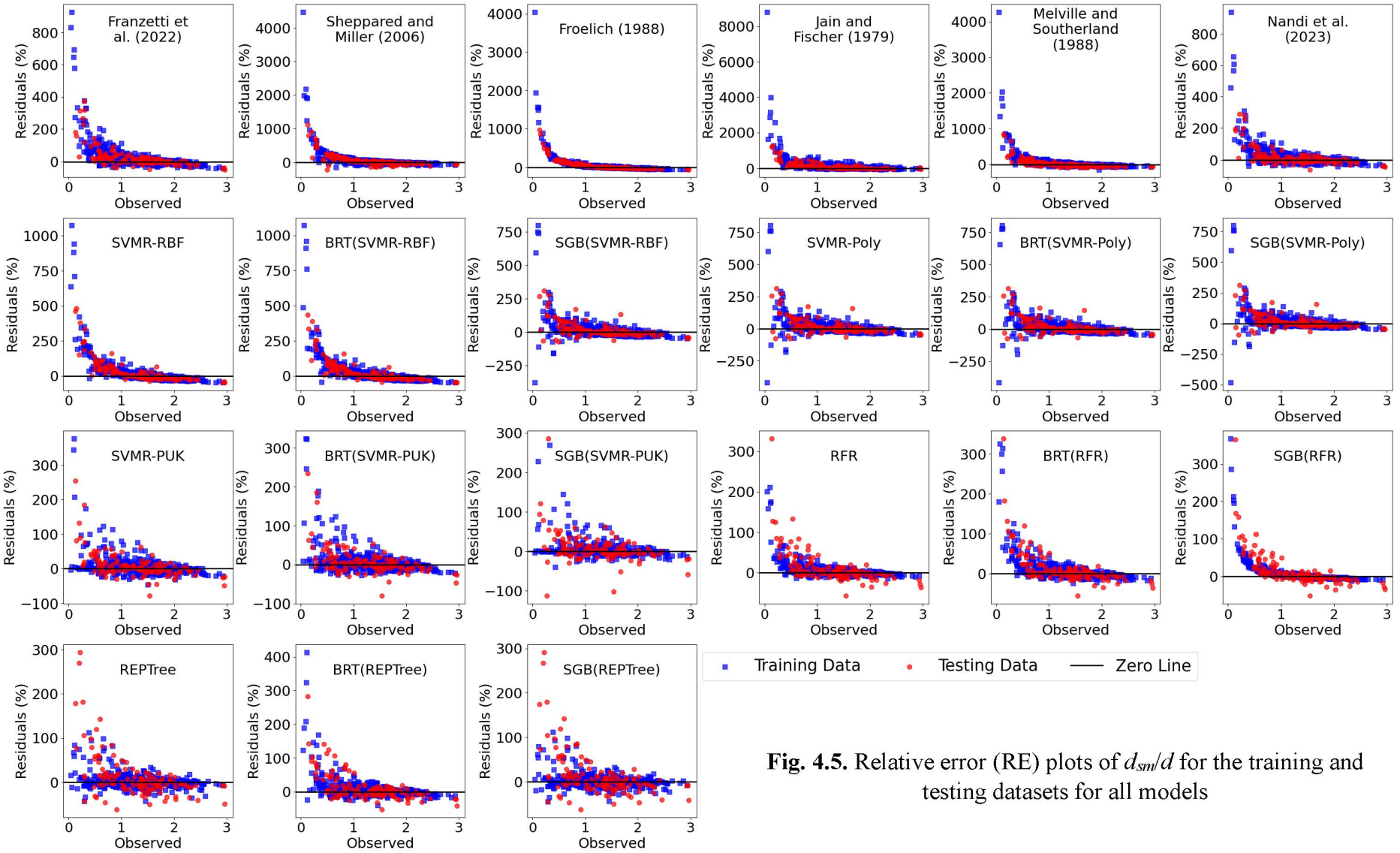

Fig. 4.5. Relative error (RE) plots of d_{sm}/d for the training and testing datasets for all models

In Fig. 4.6, Taylor diagrams show the performance of different ML models across training, testing, and overall datasets. The distance between the points representing the ML models and the observed point, which is closer to the higher correlation line, indicates the robustness of the model. In the training phase, both RFR and SGB(RFR) models have points that closely match the observed data, performing better than the other models. However, the performances of RFR and SGB(RFR) are very similar to the other ML models in the testing stage. When considering all data, RFR and SGB(RFR) remain closer to the observed point.

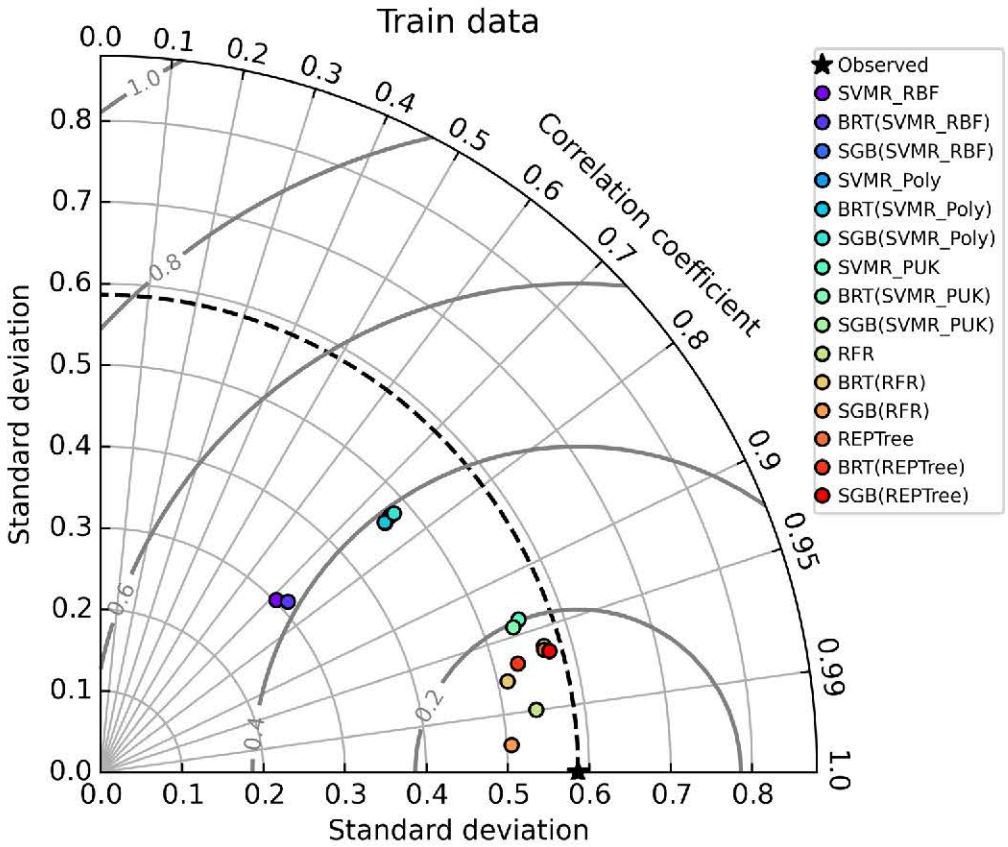

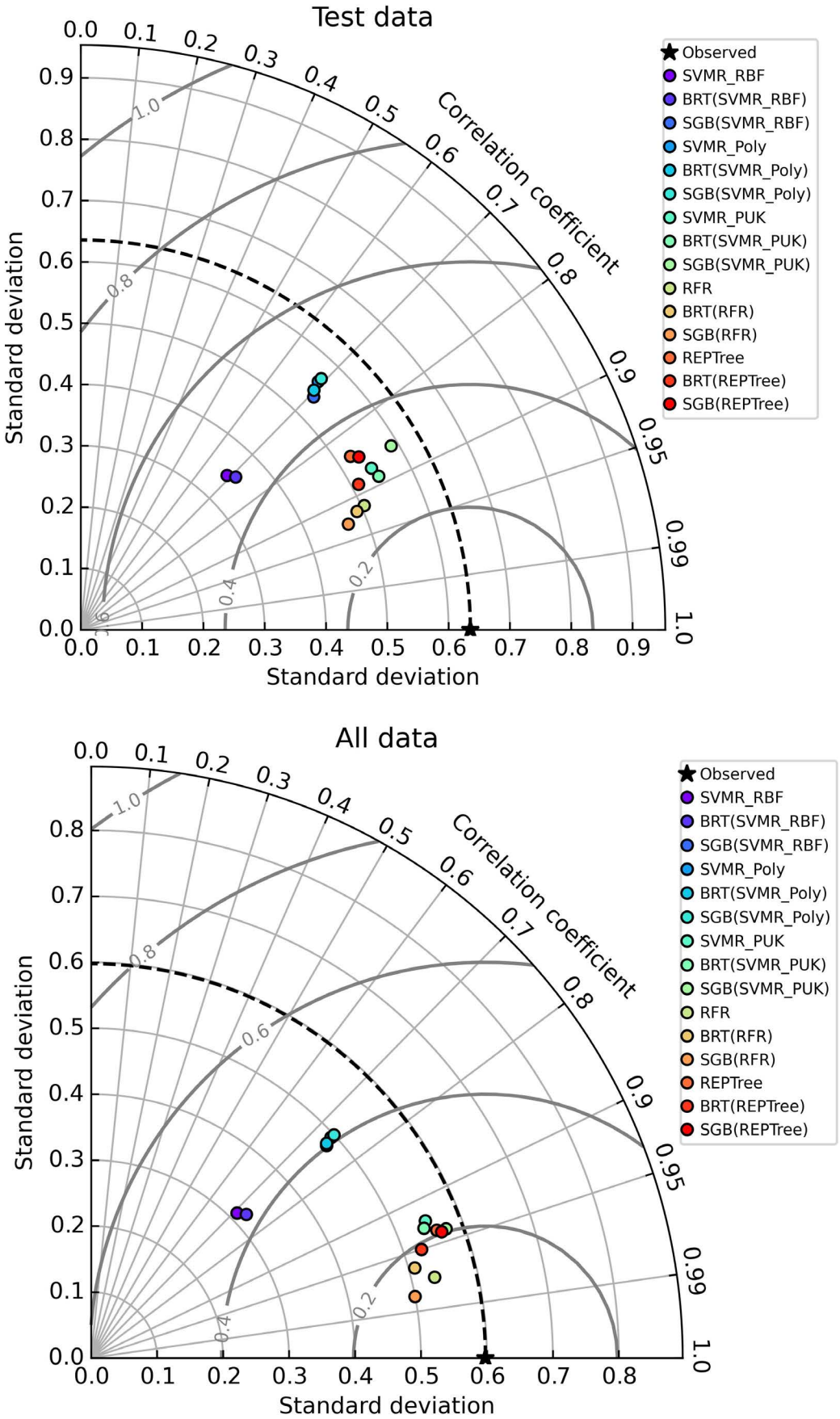

Fig. 4.6. Taylor diagrams for training, testing and all data for ML models.

4.3.2. Rankings of models

This method depends on the correlation between the columns of the decision matrix (Diakoulaki et al. 1995). For the test data, the highest weight is assigned to CC at 39.40%, while PI has the lowest weight at 15.31%. Similarly, for the train data, CC receives the maximum weight of 32.96%, and PI has the minimum weight of 15.96%. The same pattern is observed for the overall data, as illustrated in Fig. 4.7.

The ranking of ML models using Compromise Programming (CP) (see Chapter 3), the weightage is calculated using CRITIC method (methodology given in Chapter 3) and empirical models are shown in Fig. 4.8, along with their performance bars for the same base learner in BRT and SGB, grouped as I to VI.

Group I: Among the empirical formulas, Nandi and Das (2023) (Rank 10) perform best across all three phases training, testing, and overall data.

Group II: Models with SVMR-RBF as a standalone learner and as a base learner for BRT and SGB are compared. SGB (SVMR-RBF) (Rank 13) shows the best performance, while SVMR-RBF (Rank 17) performs the worst across training, testing, and overall data.

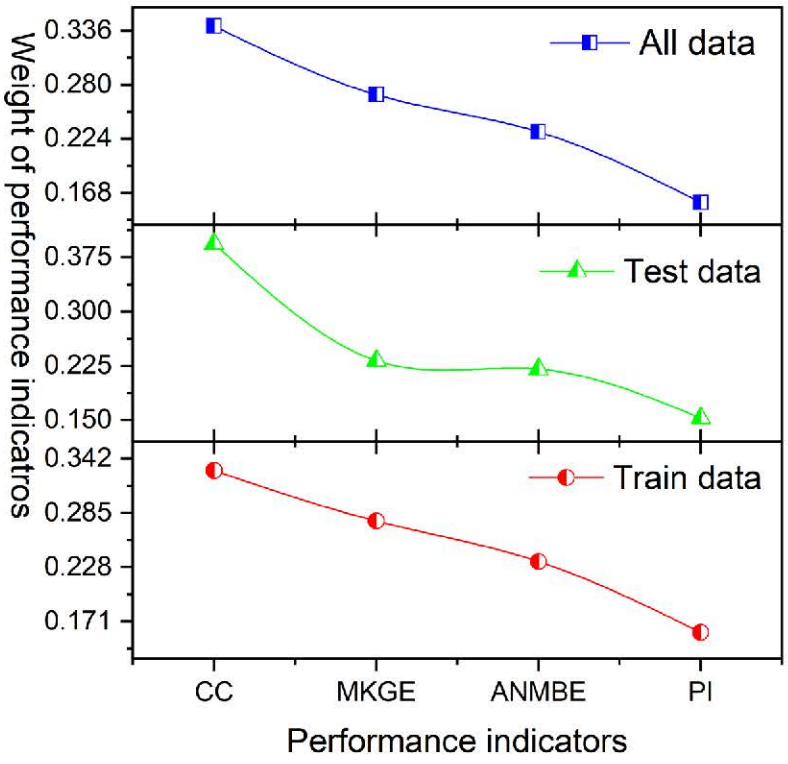

Fig. 4.7. Weight of performance indicators using CRITIC method.

Group III: Models using SVMR-Poly as a standalone learner and as a base learner for BRT and SGB are compared. SGB (SVMR-Poly) performs best [Rank 11 (training, overall), Rank 12 (testing)], while BRT (SVMR-Poly) performs the worst [Rank 14 (training, overall), Rank 13 (testing)].

Group IV: Models using SVMR-PUK as a standalone learner and as a base learner for BRT and SGB are analyzed. BRT (SVMR-PUK) [Rank 1 (testing)] performs best during

testing, while SGB (SVMR-PUK) [Rank 3 (testing), Rank 8 (overall)] shows the lowest performance in testing and overall data. However, for training data, SGB (SVMR-PUK) performs best [Rank 6], while BRT (SVMR-PUK) shows the lowest performance [Rank 9].

Group V: RFR performs best across all scenarios [Rank 3 (training), 4 (testing), 3 (overall)], while BRT (RFR) shows the lowest performance for training and overall data [Rank 8 (training), 9 (overall)]. For testing data, SGB (RFR) has the weakest performance [Rank 9 (testing), 5 (training), 6 (overall)].

Group VI: SGB (REPTree) achieves the highest performance for training and overall data [Rank 1 (training, overall)], while BRT (REPTree) performs best during testing [Rank 5 (testing)] but shows lower performance for training and overall data [Rank 4 (training, overall)]. REPTree has the lowest performance in the testing phase [Rank 8 (testing)] but ranks well for training and overall data [Rank 2 (training), 4 (overall)].

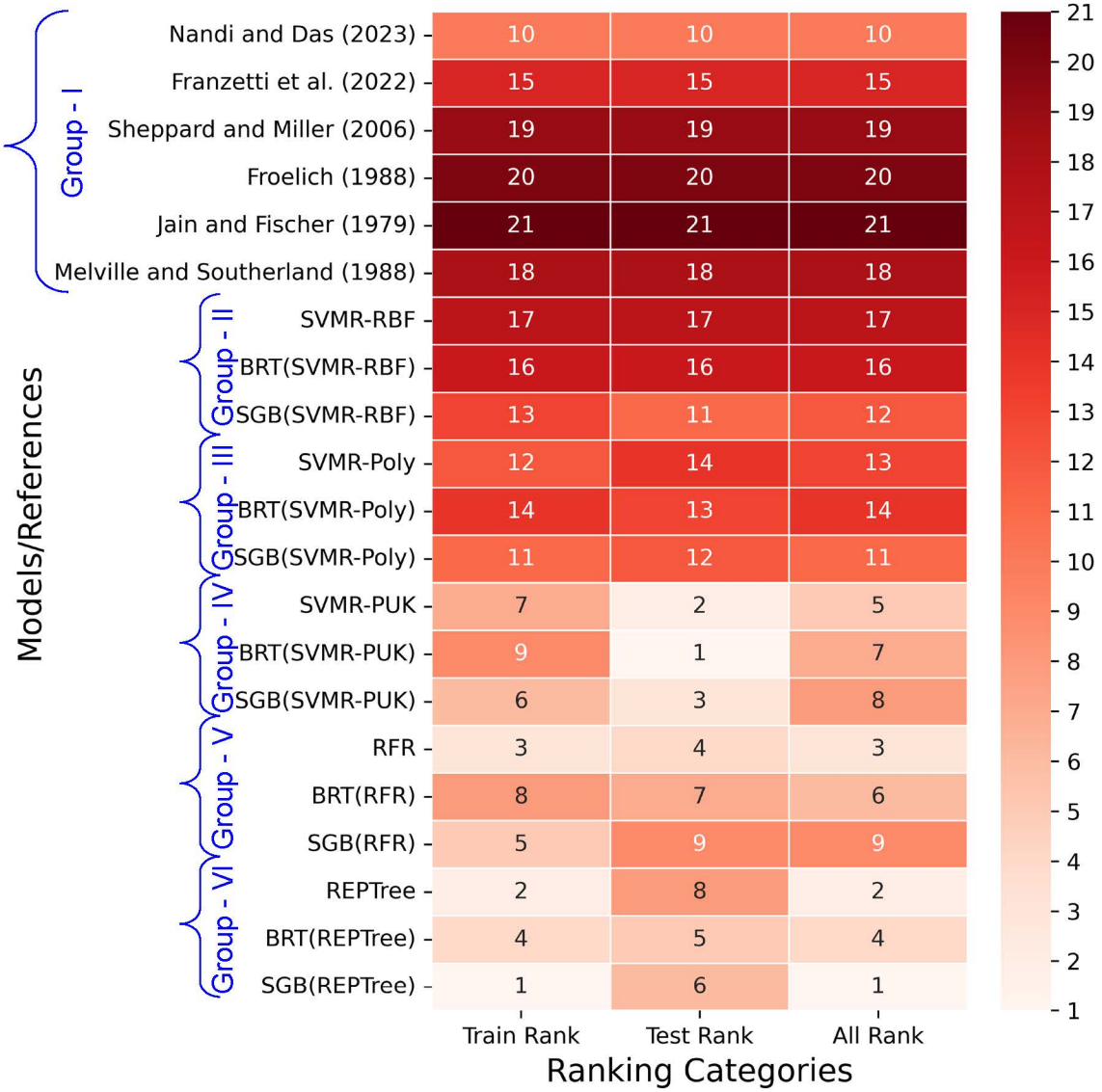

Fig. 4.8. Ranking of the models/references.

4.3.3. Sensitivity analysis of input variable

The sensitivity analysis has been done using BRT(SVMR-PUK), which demonstrated the best model for d_{sm} during the testing. The sensitivity analysis entails systematically removing each dimensionless input variable (u/u_c, h/d, σ, d/d_{50}, $ut/d\Delta^{0.5}$, d/W, Fr) one at a time. For instance, in the first step, u/u_c is removed from the variable set, and the prediction performance of the selected model is evaluated using the remaining input variables. The evaluation is based on four essential model assessment metrics: CC, MKGE, ANMBE, and PI. The results, as presented in Table 4.8, indicate that when σ is removed from the input combination, the model shows the lowest CC, MKGE, and PI values, along with the highest ANMBE values, which indicates the most influential variable in the training stage.

Table 4.8 shows that removing σ results in the lowest CC values, while removing u/u_c leads to the lowest MKGE and PI values and the highest ANMBE values, creating uncertainty in selecting the most important variable during the testing phase. To resolve this, CP is used to rank the key variables for both training and testing stages, showing that σ and u/u_c are the most important variables for predicting d_s in clear water.

Table 4.8. Sensitivity analysis on input variables using BRT(SVM-PUK).

Input variable functions	#	Training				Testing			
		CC	MKGE	ANMBE	PI	CC	MKGE	ANMBE	PI
$D_{sm} = f(u/u_c, h/d, \sigma, d/d_{50}, ut/d\Delta^{0.5}, d/W, \text{Fr})$	–	0.9435	0.8889	0.0118	0.9426	0.8887	0.8251	0.0060	0.8883
$D_{sm} = f(h/d, \sigma, d/d_{50}, ut/d\Delta^{0.5}, d/W, \text{Fr})$	u/u_c	0.8742	0.7816	0.0148	0.8772	0.8297	**0.6804**	**0.0304**	**0.8287**
$D_{sm} = f(u/u_c, \sigma, d/d_{50}, ut/d\Delta^{0.5}, d/W, \text{Fr})$	h/d	0.9297	0.8724	0.0090	0.9295	0.8719	0.8059	0.0048	0.8726
$D_{sm} = f(u/u_c, h/d, d/d_{50}, ut/d\Delta^{0.5}, d/W, \text{Fr})$	σ	**0.8679**	**0.7724**	**0.0341**	**0.8693**	**0.8295**	0.7047	0.0256	0.8319
$D_{sm} = f(u/u_c, h/d, \sigma, ut/d\Delta^{0.5}, d/W, \text{Fr})$	d/d_{50}	0.9356	0.8809	0.0102	0.9353	0.8809	0.8082	0.0012	0.8816
$D_{sm} = f(u/u_c, h/d, \sigma, d/d_{50}, d/W, \text{Fr})$	$ut/d\Delta^{0.5}$	0.9266	0.8617	0.0107	0.9262	0.8722	0.8024	0.0103	0.8724
$D_{sm} = f(u/u_c, h/d, \sigma, d/d_{50}, ut/d\Delta^{0.5}, \text{Fr})$	d/W	0.9279	0.8657	0.0088	0.9276	0.8845	0.8215	0.0044	0.8833
$D_{sm} = f(u/u_c, h/d, \sigma, d/d_{50}, ut/d\Delta^{0.5}, d/W)$	Fr	0.9170	0.8490	0.0059	0.9174	0.8790	0.8054	0.0159	0.8785

Note: # - removed variable

4.3.4. Uncertainty analysis

Prediction errors are calculated, with the mean and standard deviation (SD) used to assess the uncertainty. A negative mean indicates underestimation, while a positive mean suggests overestimation of observed values. Table 4.9 presents the confidence limits at the 5% significance level during the testing phase to evaluate the uncertainty of the models in this study. It shows that the Melville and Southerland (1988) and REPTree models tend to underestimate the d_{sm}/d, while all other models overestimate it. Furthermore, the SGB(RFR) model produces results with the smallest prediction uncertainty (0.0221), while the Jain and Fischer (1979) model has the highest uncertainty (0.1664).

Table 4.9. Statistical attributes of the prediction errors obtained from the models

Model/References	Average	SD	Margin of error	Upper limit	Lower limit	Uncertainty band
Franzetti et al. (2022)	0.0817	0.3432	0.0267	0.1085	0.0550	0.0534
Sheppard and Miller (2006)	0.2519	0.4677	0.0364	0.2883	0.2155	0.0728
Froelich (1988)	0.1726	0.5386	0.0419	0.2145	0.1307	0.0838
Jain and Fischer (1979)	1.0069	1.0688	0.0832	1.0901	0.9237	**0.1664**
Melville and Southerland (1988)	-0.0210	0.5276	0.0411	0.0201	-0.0620	0.0821
Nandi and Das (2023)	0.0346	0.3133	0.0244	0.0590	0.0102	0.0488
SVMR-RBF	0.0133	0.4363	0.0340	0.0473	-0.0206	0.0679
BRT(SVMR-RBF)	0.0001	0.4231	0.0329	0.0331	-0.0328	0.0659
SGB(SVMR-RBF)	0.0043	0.4023	0.0313	0.0356	-0.0270	0.0626
SVMR-Poly	0.0076	0.4085	0.0318	0.0394	-0.0242	0.0636
BRT(SVMR-Poly)	0.0045	0.4050	0.0315	0.0360	-0.0271	0.0631
SGB(SVMR-Poly)	0.0038	0.4088	0.0318	0.0356	-0.0280	0.0636
SVMR-PUK	0.0087	0.2271	0.0177	0.0264	-0.0089	0.0354
BRT(SVMR-PUK)	0.0114	0.2179	0.0170	0.0283	-0.0056	0.0339
SGB(SVMR-PUK)	0.0162	0.2050	0.0160	0.0322	0.0003	0.0319
RFR	0.0079	0.1450	0.0113	0.0192	-0.0034	0.0226
BRT(RFR)	0.0132	0.1739	0.0135	0.0267	-0.0004	0.0271
SGB(RFR)	0.0056	0.1418	0.0110	0.0166	-0.0055	**0.0221**
REPTree	-0.0013	0.2076	0.0162	0.0149	-0.0175	0.0323
BRT(REPTree)	0.0102	0.1911	0.0149	0.0251	-0.0046	0.0297
SGB(REPTree)	0.0010	0.2028	0.0158	0.0168	-0.0148	0.0316

Using a larger dataset can improve the accuracy of results. It helps reduce errors, enhances efficiency, and minimizes bias. Combining meta-learning techniques with fine-tuning of base models further increases predictive accuracy. Including extensive field data strengthens the ability to generalize the model. Physics-informed machine learning models are useful as they provide insights into how independent parameters affect scour. This can help future studies decide which parameters to focus on under specific conditions. For more reliable scour predictions, future research should look beyond clear-water data. It should also include live bed and field data. This will help address real-world complexities and the effects of scale.

4.4. Conclusions

Three base learners (SVMR, RFR, and REPTree) are used, with SVMR tested with three kernels (Poly, RBF, and PUK). Furthermore, two meta-learners (BRT and SGB) are combined with these base learners to improve d_s prediction. A total of 15 standalone and combined methods are tested on 634 datasets from 35 studies, creating a strong predictive model without hyper-variable adjustment. Six empirical formulas from recent studies are

also compared. Performances are evaluated using statistical metrics like CC, MKGE, ANMBE, and PI.

- The best parameters input found using best subset regression followed by KNN are flow intensity (u/u_c), flow shallowness (h/d), sediment gradation (σ), sediment coarseness (d/d_{50}), dimensionless time ($ut/d\Delta^{0.5}$), constriction ration (d/W) and Froude number (Fr) to predict dimensionless d_s (d_{sm}/d).
- The formula of Nandi and Das (2023) gives the best results across all three datasets when compared to the previous five literature formulas.
- It is found that the SGB(REPTree) model shows the best performance, it is ranked 1 using compromise programming, considering the training and all datasets. However, when considering the testing dataset, the BRT(SVMR-PUK) model shows the best.
- After sensitivity analysis during both the training and testing phases, it was found that sediment gradation (σ) and the threshold condition for sediment movement (u/u_c) are the most important variables for predicting d_{sm}/d in clear water.
- The uncertainty analysis shows that the SGB(RFR) model has the lowest prediction uncertainty, while the Jain and Fischer (1979) formula shows the highest uncertainty.

This study provides valuable insights for engineers and bridge designers, enabling more accurate scour estimation using data-driven soft computing techniques. The findings demonstrate that ensemble models for machine learning significantly outperform standalone machine learning methods in predicting scour, offering a more reliable approach for practical applications.

References

Akib, S., Mohammadhassani, M., and Jahangirzadeh, A. (2014). Application of ANFIS and LR in prediction of scour depth in bridges. *Computers & Fluids, 91*, 77–86.

Aksoy, A. O., Bombar, G., Arkis, T., and Guney, M. S. (2017). Study of the time-dependent clear water scour around circular bridge piers. *Journal of Hydrology and Hydromechanics, 65*(1), 26–34.

Alabi, P. D. (2006). *Time development of local scour at a bridge pier fitted with a collar* (M.Sc. thesis). University of Saskatchewan, Department of Civil and Geological Environmental Engineering.

Arneson, L. A., Zevenbergen, L. W., Lagasse, P. F., and Clopper, P. E. (2012). *Evaluating scour at bridges* (Hydraulic Engineering Circular no. 18). Washington, DC: U.S. Department of Transportation, Federal Highway Administration.

Bateni, S. M., Borghei, S. M., and Jeng, D. S. (2007). Neural network and neuro-fuzzy assessments for scour depth around bridge piers. *Engineering Applications of Artificial Intelligence, 20*(3), 401–414.

Beg, M. (2013). Predictive competence of existing bridge pier scour depth predictors. *European International Journal of Science and Technology, 2*(1), 161–178.

Breiman, L. (2001). Random forests. *Machine Learning, 45*, 5–32.

Bui, D. T., Shirzadi, A., Amini, A., Shahabi, H., Al-Ansari, N., Hamidi, S., Singh, S. K., Pham, B. T., Ahmad, B. B., and Ghazvinei, P. T. (2020). A hybrid intelligence approach

to enhance the prediction accuracy of local scour depth at complex bridge piers. *Sustainability, 12*(3), 1063.

Chabert, J., and Engeldinger, P. (1956). *Étude des affouillements autour des piles de ponts*. Technical report. Chatou, France: Laboratoire National d'Hydraulique.

Chang, W. Y., Lai, J. S., and Yen, C. L. (2004). Evolution of scour depth at circular bridge piers. *Journal of Hydraulics Engineering, 130*(9), 905–913.

Cheng, M. Y., Cao, M. T., and Wu, Y. W. (2015). Predicting equilibrium scour depth at bridge piers using evolutionary radial basis function neural network. *Journal of Computing in Civil Engineering, 29*(5), 04014070.

Chiew, Y. M. (1984). *Local scour at bridge piers*. Doctoral dissertation, Department of Civil Engineering, University of Auckland, Auckland, New Zealand.

Chiew, Y. M. (1995). Mechanics of riprap failure at bridge piers. *Journal of Hydraulic Engineering, 121*(9), 635–643.

Choi, S. U., and Choi, S. (2022). Prediction of local scour around bridge piers in the cohesive bed using support vector machines. *KSCE Journal of Civil Engineering, 26*(5), 2174–2182.

Choi, S. U., Choi, B., and Lee, S. (2017). Prediction of local scour around bridge piers using the ANFIS method. *Neural Computing and Applications, 28*(2), 335–344.

Chou, J. S., and Nguyen, N. M. (2022). Scour depth prediction at bridge piers using metaheuristics-optimized stacking system. *Automation in Construction, 140*, 104297.

Dargahi, B. (1990). Controlling mechanism of local scouring. *Journal of Hydraulic Engineering, 116*(10), 1197–1214.

Das, S., and Mazumdar, A. (2018). Evaluation of hydrodynamic consequences for horseshoe vortex system developing around two eccentrically arranged identical piers of diverse shapes. *KSCE Journal of Civil Engineering, 22*, 2300–2314.

Das, S., Das, R., and Mazumdar, A. (2013). Circulation characteristics of horseshoe vortex in the scour region around circular piers. *Water Science and Engineering, 6*(1), 59–77.

Dey, S., Bose, S. K., and Sastry, G. L. (1995). Clear water scour at circular piers: A model. *Journal of Hydraulic Engineering, 121*(12), 869–876.

Diakoulaki, D., Mavrotas, G., and Papayannakis, L. (1995). Determining objective weights in multiple criteria problems: The CRITIC method. *Computers & Operations Research, 22*(7), 763–770.

Ebtehaj, I., Bonakdari, H., Zaji, A. H., and Sharafi, H. (2019). Sensitivity analysis of parameters affecting scour depth around bridge piers based on the non-tuned, rapid extreme learning machine method. *Neural Computing and Applications, 31*, 9145–9156.

Ettema, R., Kirkil, G., and Muste, M. (2006). Similitude of large-scale turbulence in experiments on local scour at cylinders. *Journal of Hydraulic Engineering, 132*(1), 33–40.

Ettmer, B., Orth, F., and Link, O. (2015). Live-bed scour at bridge piers in a lightweight polystyrene bed. *Journal of Hydraulic Engineering, 141*(9), 04015017.

Firat, M., and Gungor, M. (2009). Generalized regression neural networks and feed forward neural networks for prediction of scour depth around bridge piers. *Advances in Engineering Software, 40*(8), 731–737.

Franzetti, S., Larcan, E., and Mignosa, P. (1989). Erosione alla base di pile circolari di ponte: Verifica sperimentale di esistenza di una situazione di equilibrio. [In Italian.] *Idrotecnica, 3*, 135–141.

Franzetti, S., Radice, A., Rebai, D., and Ballio, F. (2022). Clear water scour at circular piers: A new formula fitting laboratory data with less than 25% deviation. *Journal of Hydraulic Engineering, 148*(10), 04022021.

Froehlich, D. C. (1988). Analysis of onsite measurements of scour at piers. In *Proceedings of the ASCE National Conference on Hydraulic Engineering* (pp. 534–539). Colorado Springs, CO.

Gao, D., Posada, G. L., and Nordin, C. F. (1993). Pier scour equations used in the People's Republic of China. Report FHWA-SA-93-076. U.S. Department of Transportation, Federal Highway Administration, Washington, DC.

Graf, W. H. (1995). Load scour around piers. *Annual Report.*

Hancu, S., and Predescu, L. (1989). Experimental results on local scour around bridge piers in free surface water currents and pressurized air currents. In *Proceedings of the 23rd Congress of the IAHR* (pp. Madrid, Spain).

Indian Roads Congress (IRC). (2000). *Standard specifications and code of practice for road bridges* (IRC: 78-2000). New Delhi, India.

Jain, S. C., and Fischer, E. E. (1979). Scour around circular piers at high Froude numbers. Report FHWA-RD-79-104. U.S. Department of Transportation, Federal Highway Administration, Washington, DC.

Khosronejad, A., Kang, S., and Sotiropoulos, F. (2012). Experimental and computational investigation of local scour around bridge piers. *Advances in Water Resources, 37*, 73–85.

Kumbure, M. M., and Luukka, P. (2022). A generalized fuzzy k-nearest neighbor regression model based on Minkowski distance. *Granular Computing, 7*(3), 657–671.

Lança, R. M., Fael, C. S., Maia, R. J., Pêgo, J. P., and Cardoso, A. H. (2013). Clear-water scour at comparatively large cylindrical piers. *Journal of Hydraulic Engineering, 139*(11), 1117–1125.

Lança, R., Fael, C., and Cardoso, A. H. (2010). Assessing equilibrium clear water scour around single cylindrical piers. *River Flow*, 1207–1214.

Lança, R., Simarro, G., Fael, C. M. S., and Cardoso, A. H. (2016). Effect of viscosity on the equilibrium scour depth at single cylindrical piers. *Journal of Hydraulic Engineering, 142*(3), 06015022.

Lee, S. O., and Sturm, T. W. (2009). Effect of sediment size scaling on physical modeling of bridge pier scour. *Journal of Hydraulic Engineering, 135*(10), 793–802.

Link, O., Henríquez, S., and Ettmer, B. (2019). Physical scale modeling of scour around bridge piers. *Journal of Hydraulic Research, 57*(2), 227–237.

Link, O., Pfleger, F., and Zanke, U. (2008). Characteristics of developing scour-holes at a sand-embedded cylinder. *International Journal of Sediment Research, 23*(3), 258–266. https://doi.org/10.1016/S1001-6279(08)60023-X

Manes, C., and Brocchini, M. (2015). Local scour around structures and the phenomenology of turbulence. *Journal of Fluid Mechanics, 779*, 309–324.

Melville, B. W. (1997). Pier and abutment scour: Integrated approach. *Journal of Hydraulic Engineering, 123*(2), 125–136.

Melville, B. W., and Chiew, Y. M. (1999). Time scale for local scour at bridge piers. *Journal of Hydraulic Engineering, 125*(1), 59–65.

Melville, B. W., and Sutherland, A. J. (1988). Design method for local scour at bridge piers. *Journal of Hydraulic Engineering, 114*(10), 1210–1226.

Mia, F., and Nago, H. (2003). Design method of time-dependent local scour at circular bridge piers. *Journal of Hydraulic Engineering, 129*(6), 420–427.

Mignosa, P. (1980). Fenomeni di erosione locale alla base delle pile dei ponti. [In Italian.] *M.Sc. thesis, Politecnico di Milano.*

Nandi, B., and Das, S. (2023). Identify most promising temporal scour depth formula for circular piers proposed over last six decades. *Ocean Engineering, 286*, 115639.

National Cooperative Highway Research Program (NCHRP). (2011). *Scour at wide piers and long skewed piers.* Authored by D. M. Sheppard, H. Demir, and B. Melville. National Academies of Sciences, Engineering, and Medicine. The National Academies Press.

Oliveto, G., and Hager, W. H. (2002). Temporal evolution of clear-water pier and abutment scour. *Journal of Hydraulic Engineering, 128*(9), 811–820.

Quinlan, J. R. (1987). Simplifying decision trees. *International Journal of Man-Machine Studies, 27*, 221–234.

Raikar, R. V., and Dey, S. (2005). Clear-water scour at bridge piers in fine and medium gravel beds. *Canadian Journal of Civil Engineering, 32*(4), 775–781.

Razali, N. M., and Wah, Y. B. (2011). Power comparisons of Shapiro-Wilk, Kolmogorov-Smirnov, Lilliefors, and Anderson-Darling tests. *Journal of Statistical Modeling and Analysis, 2*(1), 21–33.

Shalmani, Y. A., and Hakimzadeh, H. (2015). Experimental investigation of scour around semi-conical piers under steady current action. *European Journal of Environmental and Civil Engineering, 19*(6), 717–732.

Sheppard, D. M., and Miller, W. J. (2006). Live-bed local pier scour experiments. *Journal of Hydraulic Engineering, 132*(7), 635–642.

Sheppard, D. M., Melville, B., and Demir, H. (2014). Evaluation of existing equations for local scour at bridge piers. *Journal of Hydraulic Engineering, 140*(1), 14–23.

Sheppard, D. M., Odeh, M., and Glasser, T. (2004). Large scale clear-water local pier scour experiments. *Journal of Hydraulic Engineering, 130*(10), 957–963.

Singh, U. K., Jamei, M., Karbasi, M., Malik, A., and Pandey, M. (2022). Application of a modern multi-level ensemble approach for the estimation of critical shear stress in cohesive sediment mixture. *Journal of Hydrology, 607*, 127549.

Sumer, B. M. (2007). Mathematical modelling of scour: A review. *Journal of Hydraulic Research, 45*(6), 723–735.

Vapnik, V. (1995). *The nature of statistical learning theory.* Springer.

Yanmaz, A. M., and Altinbilek, H. D. (1991). Study of time-dependent local scour around bridge piers. *Journal of Hydraulic Engineering, 117*(10), 1247–1268.

Chapter 5

Quasi-Equilibrium Scour Time around Isolated Circular Pier

5.1. Introduction

Scour is a critical factor contributing to bridge failure. It refers to the erosion of sediment around bridge piers due to flowing water, which weakens the bridge foundation, leading to collapse (Melville and Coleman 2000). Accurate estimation of scour depth (d_s) is essential for effective bridge design and maintenance. Underestimating the d_s can compromise the stability of bridges, while overestimation leads to unnecessary construction expenses. Different researchers have utilized experimental (Link et al. 2008, Lança et al. 2010, Ansari and Ahmad 2024), numerical (Zhao et al. 2010, Omara and Tawfik 2018), and machine learning techniques (Nandi et al. 2024) to quantify scour for various hydraulic structures and sediment conditions. Meta-analyses of clear-water scour, such as those by Melville and Chiew (1999), Sheppard et al. (2014), and Franzetti et al. (2022), have summarized decades of research on this phenomenon.

Extensive studies have focused on the mechanisms of scour around isolated cylindrical piers (Breusers et al. 1977). Most formulas for calculating equilibrium d_s (d_{se}) assume that time need not be included in dimensional analysis. However, limited studies address the time (t) required to reach a quasi-equilibrium state of d_{se}. While peak flood events in rivers and waterways are typically short-lived, understanding the temporal evolution of d_s (d_{st}) during these periods is crucial for real-world monitoring (Nandi and Das 2023). Different studies have developed formulas to predict d_{st} for such scenarios. This study emphasizes the importance of t to reach quasi-equilibrium (T_e). Few studies (e.g., Melville and Chiew 1999, Choi and Choi 2016) have developed formulas to estimate T_e, defined as the time beyond which the incremental increase in d_s is negligible. Chabert and Engeldinger (1956) noted that equilibrium occurs when d_s ceases to increase over t appreciably. Ettema (1980) defined T_e, as the t at which the incremental d_s is less than 1 mm in 4 hours. Similarly, Melville and Chiew (1999) proposed a threshold of less than 5% of pier diameter (d) in 24 hours, while Grimaldi (2005) suggested a threshold of $0.05W/3$ in 24 hours, where W represents the channel width. Experimental extrapolation of seven-day d_{se} values for circular piers (Lança et al. 2010). These varying definitions highlight the ambiguity surrounding the experimental determination of T_e, which leads to the need for designs focused on T_e.

Sumer et al. (1992) conducted experimental analyses on T_e using 18 laboratory datasets, resulting in overestimated d_{se} values. Melville and Chiew (1999) analyzed d_{st} evolution using 84 isolated datasets and developed formulas for d_{st} and T_e. Kothyari et al. (2007) introduced

a dimensionless time parameter incorporating reference time t_r and the densimetric Froude number (F_d), but their calculated T_e values exceeded observed durations. Sheppard et al. (2014) used a large dataset (569 laboratory and 928 field measurements) to propose a formula for T_e. Choi and Choi (2016) employed 20 datasets from literature studies to predict d_{st}, resulting in underestimations.

Two primary approaches for scour prediction exist: the d_{st} predictor (Melville and Chiew 1999, Choi and Choi 2016) and the d_{st}/d predictor (Franzetti et al. 2022, Nandi et al. 2024). The d_{st}/d_{se} predictors require separate formulas for d_{se}, dependent on T_e, while the d_{st}/d predictors allow d_{st} or d_{se} to be directly calculated without T_e dependence. However, d_{se} is traditionally considered independent of time, assuming dimensionless time factor = 1, which can overestimate T_e (Franzetti et al. 2022). Despite d_{se} being an asymptotic process theoretically requiring infinite t, quasi-equilibrium states can be practically achieved.

The influencing parameters of T_e, including pier slenderness (h/d), flow intensity (u/u_c), sediment coarseness (d/d_{50}), sediment uniformity (σ), and constriction ratio (d/W) are analyzed. Here, h is the approach flow depth, u is the flow velocity, u_c is the critical velocity, d_{50} is the median sediment size, and W is the flume width. By establishing functional relationships among these parameters, a new formula is proposed for T_e. This formula eliminates the need for long-term experiments while providing accurate predictions of d_{se} for pier design. Moreover, it optimizes T_e values to improve d_{st}/d_{se} predictions. The meta-analysis incorporates data from over 35 studies spanning 64 years, including 774 isolated datasets and eight laboratory experiments conducted for this research. By integrating diverse datasets and addressing previous limitations in experimental duration, this study offers a robust method for accurate and economical d_s prediction. The aim is to contribute to advancing d_{st} as well as the quasi-equilibrium state of scour modeling by emphasizing T_e and refining existing predictors.

5.2. Methods

5.2.1. Curation of scour time data

To develop the T_e formula, specific assumptions are set to maintain a general and widely applicable approach. Conditions such as slender piers or sediment without ripples were excluded, and the initial dataset, drawn from over 35 studies, eliminated cases with more than one unknown parameter, leaving over 750 data points.

Now, the initial dataset only underwent the conditions for T_e, $T^* \geq 5\times10^5$, for flow intensity, $0.4 \leq (u/u_c) \leq 1.2$, for flow shallowness, $(h/d) \leq 6$, and for sediment properties, $\Delta > 1$. Multiple factors led to the choice of long-duration tests i.e., $T^* \geq 5\times10^5$, Here, T^* is time scale = uT_e/d. Franzetti et al. (1982) showed that the relative error in scour prediction decreases with increasing T^*, and with a high value of it the scour values are not significantly affected by the experimental procedures. According to many researchers, scour should not happen for $u/u_c < 0.5$, in addition, the depth of the scour should increase as a function of u/u_c, reaching a maximum for $u/u_c = 1$. The experiments that are included in this research were acknowledged as clear-water instances by the researchers. Due to homogenization,

values of u/u_c slightly higher than 1 can be achieved. The maximum value of u/u_c used in this study is 1.2. While this range is sufficient for the analysis, it is too low to allow the formation of large bedforms, meaning the d_s does not vary significantly. Furthermore, organic soil, which usually has a specific gravity below 2, was excluded from the dataset. The final dataset was carefully filtered for developing the formula. The T_e formula introduced in this study is designed to calculate when the d_s tend to reach equilibrium under unidirectional clear-water flow conditions.

A threshold observed quasi-equilibrium time (T_e) of 2 days was selected based on an analysis of available studies. This threshold excluded over 90% of the literature data, as shown in Table 5.1. Researchers have previously defined different criteria for determining equilibrium. For instance, Melville and Chiew (1999) suggested that equilibrium is reached when the increase in d_s over 24 hours is less than 5% of d. Similarly, Grimaldi (2005) proposed that equilibrium occurs when the scour rate is less than $0.05\times W/3$ in 24 hours. These criteria indicate that experiments need to run for more than 24 hours to estimate equilibrium conditions accurately. However, to make the process more practical while still ensuring reliability, a 2-day (48-hour) threshold was adopted in this study to achieve a quasi-state. This timeframe provides a good balance between practicality and accuracy, accommodating variations in experimental setups reported in the literature. Researchers can still adjust this threshold depending on the specific goals of their studies. The chosen approach offers a consistent and practical way to d_s for bridge pier designs and related applications.

Table 5.1. Dataset collected from the literature used to develop a new time scale formula.

Authors	#	u/u_c	h/d	σ	d/d_{50}	$uT_e/d=T^*$	d/W
Ettema (1980)	16	0.97-1.07	0.20-5.91	1.10 - 1.34	13.03- 53.47	7.44×10^5 - 3.36×10^6	0.07 - 0.16
Hancu and Predescu (1989)	5	0.81-0.99	0.77-1.67	1.22 - 1.71	15.00- 65.00	6.51×10^5 - 2.30×10^6	0.03 - 0.13
Chiew (1995)	5	0.98-1.20	2.14	1.25	72.92	1.38×10^6 - 3.95×10^6	0.12
Graf (1995)	2	1.02	1.55-2.31	1.30	47.62- 52.38	1.51×10^6 - 2.27×10^6	0.10 - 0.11
Melville and Chiew (1999)	18	0.59-0.94	0.71-5.26	1.30	39.58- 73.03	7.10×10^5 - 2.32×10^6	0.04 -0.12
Lee and Sturm (2009)	8	0.70-0.82	4.04-5.00	1.25	8.18- 36.91	2.29×10^6 - 3.40×10^6	0.01
Jones from NCHRP (2011)	6	0.58-0.84	1.75-1.76	1.37	30.36- 30.42	9.16×10^5 - 2.68×10^6	0.15
Das et al. (2013)	3	0.79-0.98	1.60	1.80	60.61	1.07×10^6 - 1.33×10^6	0.06
Lança et al. (2016)	6	0.75-0.89	1.00-1.51	1.18 - 1.50	58.14- 58.59	1.76×10^6 - 3.44×10^6	0.01 - 0.04
Data ranges	69	0.58-1.20	0.20-5.91	1.10 - 1.80	08.18 - 73.03	6.51×10^5 - 3.95×10^6	0.01 - 0.16

5.2.2. Dimensionless analysis: Buckingham π theorem

It is assumed that because T_e and d_{se} are fundamentally interdependent, both should have a similar dependence on the same set of parameters (Melville and Chiew 1999). The relation between T_e and its dependent parameters is written in Eq. (5.1). Here, ν is kinematic viscosity.

$$T_e = \varphi_1 \left\{ \begin{matrix} \text{flow}\left(\rho_f, \nu, u, h, g\right), \text{sediment}\left(\rho_s, d_{50}, \sigma, u_c\right), \\ \text{pier and channel } (d, W) \end{matrix} \right\} \tag{5.1}$$

After applying Buckingham π theorem, Eq. (5.1) can be written as Eq. (5.2).

$$\varphi_2\left(\frac{uT_e}{d},\frac{\nu}{du},\frac{\rho_s}{\rho_f},\frac{d_{50}}{d},\frac{u_c}{u},\frac{dg}{u^2},\frac{h}{d},\frac{W}{d},\sigma\right)=0 \tag{5.2}$$

Rearranging the parameters, Eq. (5.2) is represented as Eq. (5.3). Here, Re is Reynolds number, Fr is Froude number,

$$\frac{uT_e}{d}\left(=T^*\right)=\varphi_3\left(\mathrm{Re},\Delta,\frac{d}{d_{50}},\frac{u}{u_c},\mathrm{Fr},\frac{h}{d},\frac{d}{W},\sigma\right) \tag{5.3}$$

5.2.3. Experiment setup and methodology

A total of eight additional experiments are carried out in a recirculating flume. The length of the sand bed was 5 m with 0.81 m width (Fig. 5.1a). The sand bed was located 2.9 m upstream from the flume inlet causing the turbulence to become fully developed (Das et al. 2013). All bridge pier models are constructed using circular Perspex sheets of 5, 7, 9, and 11 cm diameters. The flow is regulated using a control valve installed in the delivery pipeline, while the h is maintained using a tailgate. Before starting each experiment, the sand bed is levelled, and the desired h is set. After each test, the water is carefully drained without disturbing the sand bed, and the d_s is measured using a laser distance sensor with a measurement accuracy of ±1.5 mm.

The mechanism of local scour is given in Fig. 5.1b. The figure shows how scour initiates due to the combined effects of downflow and the horseshoe vortex, which transport sediment downstream of the pier with the help of wake vortices.

The complicated movement around a structure fixed in the sediment bed causes erosion on the bed, and the flow patterns can be classified as *downflow*, *horseshoe vortex*, *wake and cast of vortices*, and a *bow wave* (Fig. 5.1b).

The pressure at the front of the pier is highest just below where the water meets the air and decreases as go deeper. This makes the water flow downward along the pier, creating a *downflow*. The *downflow* is strongest just below the sediment bed when there is a hole in the riverbed. The horseshoe vortex forms because the water separates at the front of the hole and swirls around like a spiral. The horseshoe vortex results from scour rather than causing it, however, it does contribute to the movement of material away from the scour hole.

The stagnation pressure accelerates the flow alongside the pier, leading to flow separation at the sides and the creation of a wake with a cast of vortices at the boundaries with the main flow (see Fig. 5.1b). Scouring starts at the sides of the cylinder, with the holes quickly moving upstream around the perimeter of the cylinder to meet at the centreline. The eroded material is carried around the pier by the combined effect of the accelerating flow and the spiral motion of the horseshoe vortex.

Figure 5.1c shows the scour beds observed after experimental runs 1, 6, and 7, corresponding to d of 11 cm, 9 cm, and 7 cm, respectively.

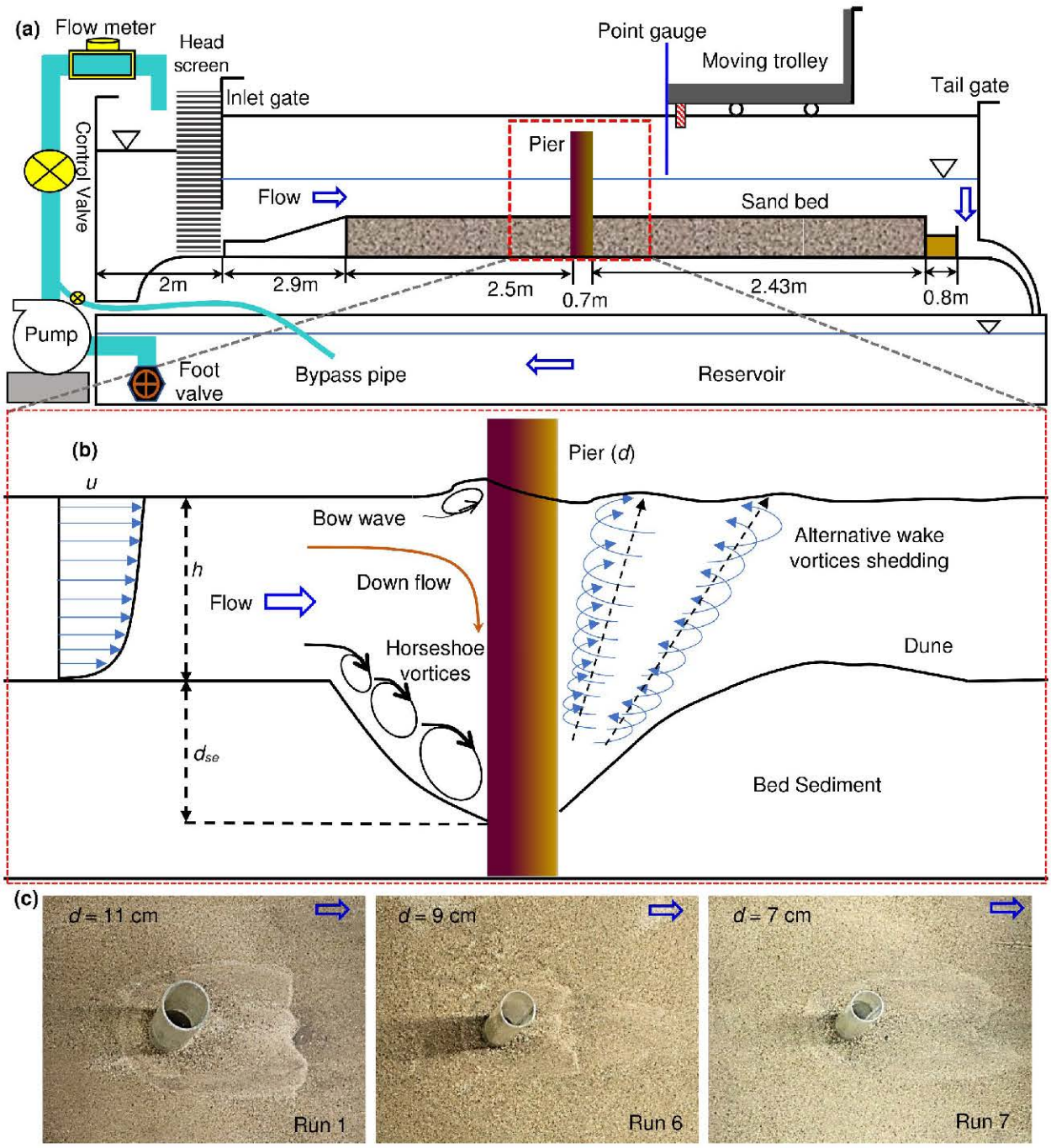

Fig. 5.1. (a) Schematic diagram of the tilting flume showing its different components and 5 m × 0.2 m working section of sand bed, **(b)** Scour bed formed after experimental Run 1, Run 6 and Run 7, respectively, and **(c)** Scour mechanism showing development of vortices and dunes at circular mono-pier.

These alternate vortices create turbulence that disrupts the sediment bed, lifting particles into suspension and carrying them away towards downstream after losing the strength the sediment is deposited and creates dune formation. Based on the grading curve from sieve analysis (Fig. 5.2), sand bed material was used with sizes d_{50} = 0.805 mm, d_{16} = 0.43 mm, d_{84} = 1.32 mm, d_{90} = 1.62 mm, σ_g = 1.75 and Δ = 1.63.

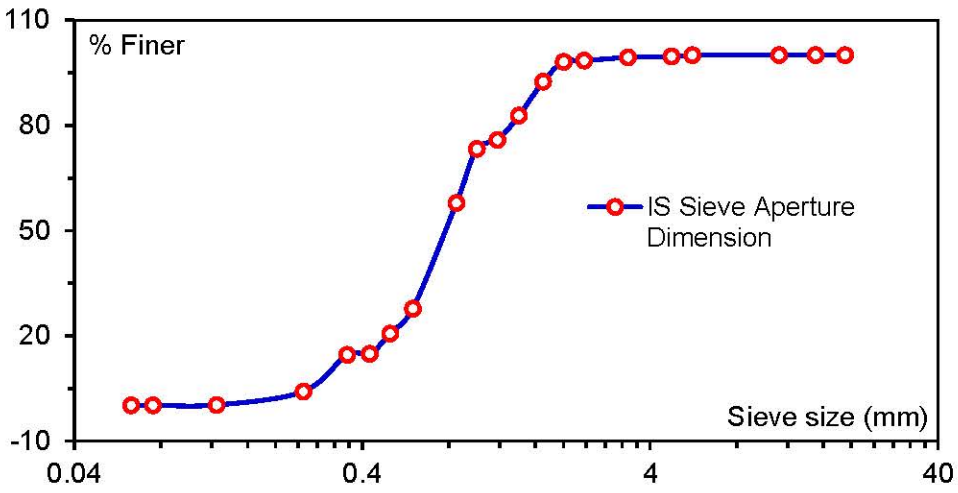

Fig. 5.2. Grading curve of sand.

The bed slope (=1:2400) is kept constant. The critical bed shear stress (τ_{oc}) is determined by using the critical Shields parameter, $\Theta_c = \tau_{oc}/(\rho_w \Delta g d_{50})$. The Θ_c is calculated using the particle parameter (D_*). Here, $D_* = d_{50}(\Delta g/\nu)^{1/3} = 20.062$ as $20 < D_* \leq 150$ and therefore $\Theta_c = 0.013(D_*)^{0.29} = 0.03101$, Then $\tau_{oc} = 0.03101\Delta\rho_w g d_{50} = 0.3861$ N/m^2 and $u_{*c} = (\tau_o/\rho_w)^{1/2} = 0.01966$ m/s. Here, u_c is calculated from the relation: $(u_c/u_{*c}) = 5.75\log(h/2d_{50}) + 6$ where u_{*c}, h, d_{50} are known. The present experimental condition is given in Table 5.2.

Table 5.2. Details of experiments conducted at the fluvial hydraulics laboratory.

Run No	Q (cumec)	h (m)	d (m)	u (m/s)	u_c (m/s)	Fr (-)	u/u_c (%)
1	0.0275	0.145	0.110	0.234	0.339	0.280	69.050
2	0.0275	0.135	0.090	0.251	0.337	0.260	74.165
3	0.0275	0.140	0.070	0.243	0.335	0.230	71.516
4	0.0275	0.125	0.050	0.272	0.332	0.210	80.098
5	0.0255	0.145	0.110	0.217	0.339	0.250	64.028
6	0.0255	0.135	0.090	0.233	0.337	0.230	68.771
7	0.0255	0.140	0.070	0.225	0.335	0.200	66.315
8	0.0255	0.125	0.050	0.252	0.332	0.180	74.272

The validation of the present formula is done by the 24 datasets collected from the previous literature including our eight experimental datasets with relevant ranges given in Table 5.3.

Table 5.3. Experimental dataset used for validating the newly proposed formula.

References	#	u/u_c	h/d	σ	d/d_{50}	$uT_e/d=T^*$	d/W
Chabert and Engeldinger (1956)	1	0.74	3.50	1.08	384.62	1.47×10^6	0.10
Mignosa (1980)	2	0.81-0.86	2.59-2.60	1.32	19.20	2.14×10^6 - 2.26×10^6	0.10

Chiew (1995)	2	0.65-0.98	2.14-2.88	1.25	72.92	9.00×10^5 - 1.39×10^6	0.12
Oliveto and Hager (2002)	3	0.77-1.03	0.35-2.41	1.25-2.35	13.23 - 59.77	1.03×10^6 - 8.93×0^5	0.06
Sheppard et al. (2002, 2004)	1	0.81	0.61	1.21	315.52	8.39×10^5	0.15
Chang et al. (2004)	2	0.77-1.09	1.00-1.50	2.00	100.00 - 142.86	5.64×10^5 - 9.20×10^5	0.10
Raikar and Dey (2005)	2	0.86-0.87	4.17-7.81	1.16-1.10	5.79 - 5.85	1.45×10^6 - 2.25×10^6	0.05-0.10
Alabi (2006)	1	0.79	2.00	1.23	216.98	6.19×10^5	0.09
Lança et al. (2013)	1	0.88	2.78-2.78	1.36	104.65	2.01×10^6	0.05
Link et al. (2019)	1	1.01	1.53	1.45	416.67	6.00×10^5	0.11
Present study	8	0.70-0.82	1.32-2.50	1.75	62.14 - 136.70	5.12×10^5 - 1.17×10^6	0.06 - 0.14
Total	24	0.70-1.09	0.35-7.81	1.08-2.35	13.23 - 416.67	5.12×10^5 - 2.26×10^6	0.05 - 0.26

5.2.4. Statistical performance indicator

The evaluation of the T^* formula is conducted using key performance indicators. These indicators include the Correlation Coefficient (CC), the Sum of Squared Errors (SSE), and the Root Mean Square Error (RMSE) given in Table 3.5. The Coefficient of Determination (R^2), and Mean Absolute Percentage Error (MAPE) are given in Table 5.4. The CC and R^2 assess the strength and accuracy of the relationship between observed and computed values, ensuring that the model captures the trends effectively. On the other hand, SSE, MAPE, and RMSE quantify the prediction errors, with lower values showing better performance. Here, $(T^*)_{oi}$ is the i^{th} observed value, $(\overline{T}^*)_o$ is the mean of the observed, $(T^*)_{ci}$ is the i^{th} computed value, $(\overline{T}^*)_c$ is the mean of the computed values, N is the number data points.

Table 5.4. Performance indicators with their pertinent ranges and ideal values.

Performance indicator	Range	Ideal value
$R^2 = \left\{ \dfrac{N\sum_{i=1}^{N}(T^*)_{oi}\times(T^*)_{ci} - \sum_{i=1}^{N}(T^*)_{oi}\sum_{i=1}^{N}(T^*)_{ci}}{N^2\times SD_c\times SD_o} \right\}$	0 to +1	1
$MAPE = \dfrac{1}{N}\sum_{i=1}^{N}\left\lvert\dfrac{(T^*)_{ci}-(T^*)_{oi}}{(T^*)_{ci}}\right\rvert\times100$	0 to ∞	0

The detailed methodology of this chapter is given in Fig. 5.3.

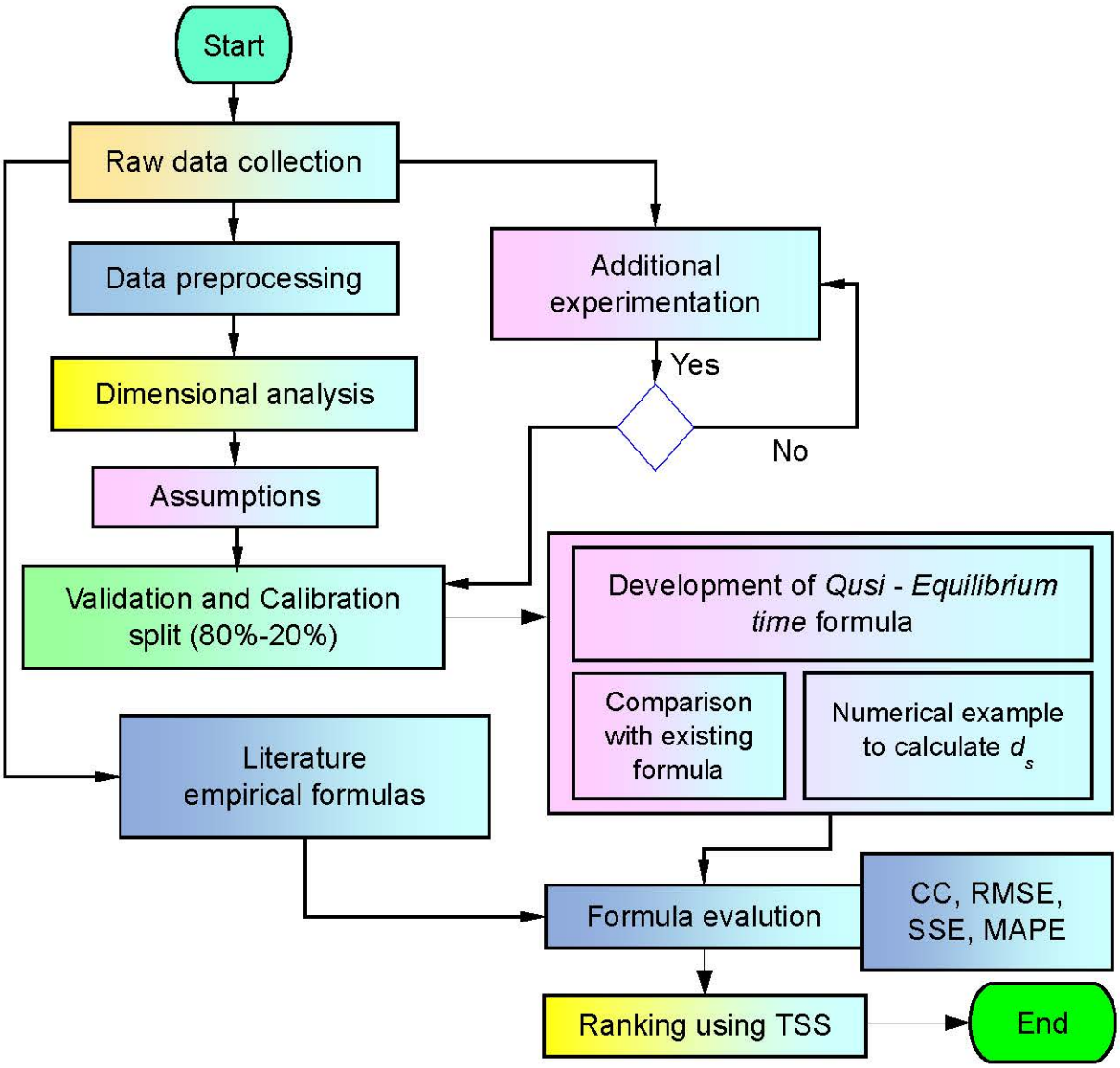

Fig. 5.3. The methodology for the present study.

5.3. Results and discussion

5.3.1. Properties of the time functions

The impact of Re becomes negligible when Re > 7000 (Monti 1994). The parameter Δ remains nearly constant at approximately 1.6, and F_D strongly correlates with u/u_c. Therefore, u/u_c is chosen as the influencing parameter. This decision is based on the long duration of the experiment. Consequently, using the dimensional analysis, Eq. (5.3) simplifies to Eq. (5.4).

$$T^* = \frac{uT_e}{d} = \varphi_4\left(\frac{d}{d_{50}}, \frac{u}{u_c}, \frac{h}{d}, \frac{d}{W}, \sigma\right) \tag{5.4}$$

Several researchers have examined the hypothesis that different parameters independently affect the T_e scale. This study provides calibrated formulas for T^* (time scale = uT_e/d) (Eq. 5.5) or T_e (Eq. 5.6) as shown below.

$$T^* = \frac{uT_e}{d} = \lambda f_1\left(\frac{u}{u_c}\right) f_2\left(\frac{h}{d}\right) f_3(\sigma) f_4\left(\frac{d}{d_{50}}\right) f_5\left(\frac{d}{W}\right) \tag{5.5}$$

$$T_e = \lambda\left(\frac{d}{u}\right) f_1\left(\frac{u}{u_c}\right) f_2\left(\frac{h}{d}\right) f_3(\sigma) f_4\left(\frac{d}{d_{50}}\right) f_5\left(\frac{d}{W}\right) \tag{5.6}$$

T^* depends on each independent parameter in the formula. The resulting time function includes a constant $\lambda = 86.81$ days/sec, and the parameter functions are defined in Eqs. (5.7–5.11) as follows:

$$f_1\left(\frac{u}{u_c}\right) = \begin{cases} 0.85\left(\frac{u}{u_c}\right) & 0.4 \le \frac{u}{u_c} \le 1 \\ 1 & \frac{u}{u_c} > 1 \end{cases} \tag{5.7}$$

$$f_2\left(\frac{h}{d}\right) = 0.64\left(\frac{h}{d}\right)^{0.23} \tag{5.8}$$

$$f_3(\sigma) = 0.97(\sigma)^{-0.88} \tag{5.9}$$

$$f_4\left(\frac{d}{d_{50}}\right) = 1.59\left(\frac{d}{d_{50}}\right)^{-0.2} \tag{5.10}$$

$$f_5\left(\frac{d}{W}\right) = 0.41\left(\frac{d}{W}\right)^{-0.21} \tag{5.11}$$

The effect of each parameter on the T_e scale is as follows Ettema et al. (1998) noted that u/u_c is related to the stage of local scour. When d_{st} reaches d_{sm}, it has a similar effect on the T_e scale (Melville and Chiew 1999) as when u/u_c is close to 1. From Fig. 5.4(a), T^* for clear-water scour increases quickly with u/u_c and reaches its highest value. In this study, the u/u_c value is slightly above the threshold. For clear-water scour, a linear fit best represents the relationship between the T_e scale u/u_c. However, when u/u_c exceeds the threshold, T^* decreases rapidly based on the dataset of literature in Eq. (5.7).

The T_e scale (Fig. 5.4b) increases as the pier h/d increases and reaches its maximum value around $(h/d) \sim 6$. The effect of h/d is significant when $h/d \le 6$, but it becomes less important beyond this point. In previous studies, this increasing trend is often represented using a power law (Melville 1999, NCHRP 2011, Choi et al. 2016), as shown in Eq. (5.8).

The effect of σ on d_s has been examined, and different researchers have proposed formulas for d_s. This indicates that σ significantly impacts the T_e scale shown in Fig. 5.4c, T^* decreases as σ increases. The relationship between the T_e scale and σ under clear-water scour conditions is best described by a power law, as expressed in Eq. (5.9).

Previous researchers (Ettema 1980, Melville and Chiew 1999, NCHRP 2011, Choi and Choi 2016) identified d/d_{50} as a significant factor affecting the T_e scale. As shown in Fig. 5.4d, d/d_{50} negatively influences T^*, meaning that as d/d_{50} increases, T^* decreases. The plot

indicates that T^* continues to decrease with increasing d/d_{50} and finally stabilizes at around 60. The relationship between the T_e scale and d/d_{50} is best described by Eq. (5.10).

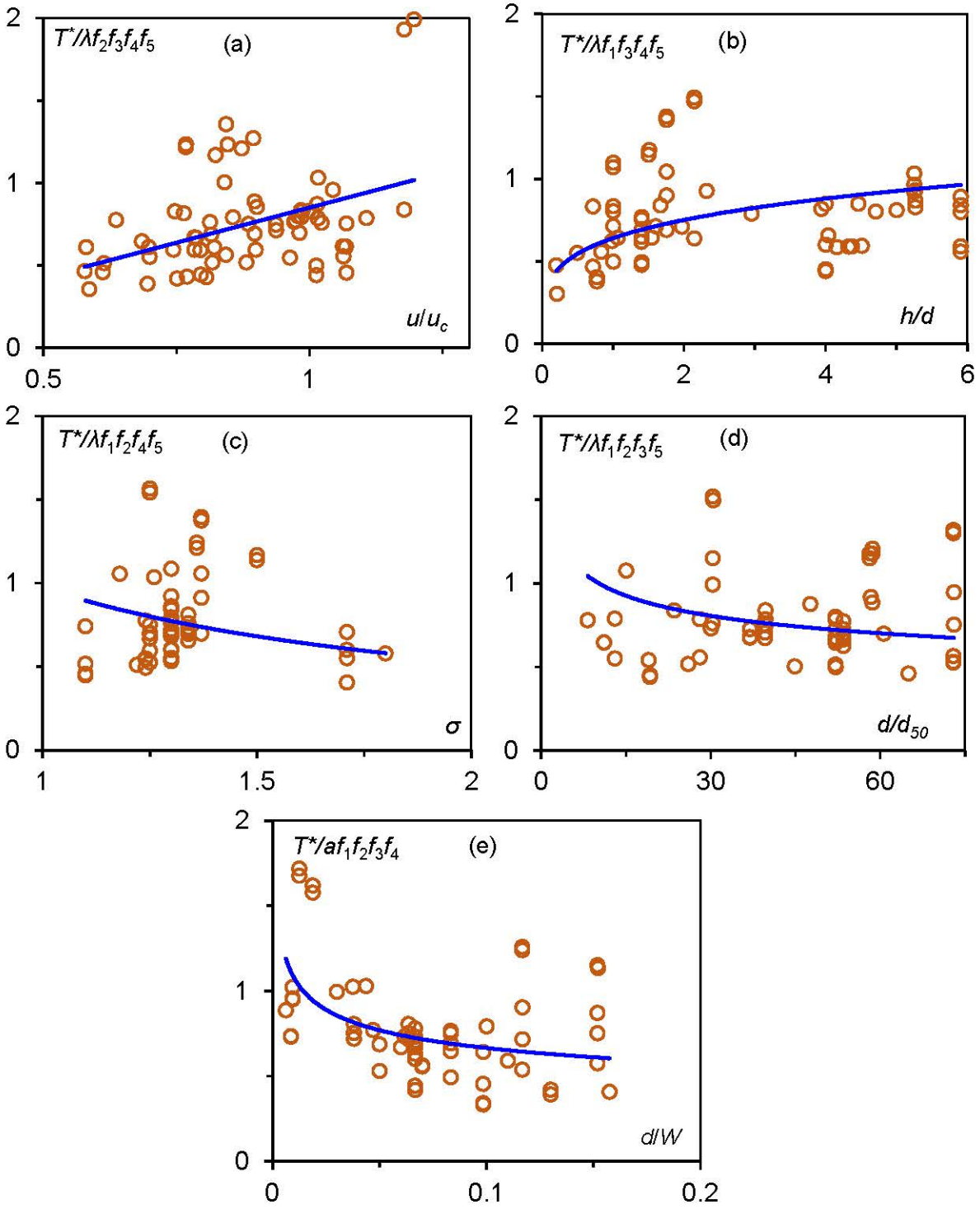

Fig. 5.4. Functions for T^* **(a)** $f_1(u/u_c)$, **(b)** $f_2(h/d)$, **(c)** $f_3(\sigma)$, **(d)** $f_4(d/d_{50})$, and **(e)** $f_5(d/W)$. The blue line represents the parameter function, while the orange circle indicates the normalized T^* using the rest of the parameter functions.

Constriction refers to the influence of the sidewall, commonly measured as the constriction ratio (d/W). If the channel is sufficiently large ($d/W < 10\%$), the impact of d/W

on the scour process is minimal (Chiew 1984). However, when d/W exceeds 10%, the sidewall significantly affects T_e. Sheppard et al. (2004) studied d/W = 15%, and in this study, d/W > 10%, consistent with findings from different researchers (Melville and Chiew 1999, NCHRP 2011) (as shown in Fig. 5.4e). The figure indicates that as d/W increases, T^* decreases and stabilizes around 0.15. The relationship between T^* and d/W under clear-water scour conditions is expressed in Eq. (5.11).

5.3.2. Comparison of computed and observed T^*

A comparison between measured and computed T_e scales using different formulas, including the newly developed formula, is shown in Fig. 5.5(a-f). Here, in these line plots, the T^* values are scaled using Z normalization. However, in the scatter plots, the computed values are shown without Z normalization. Z normalization is defined as: [(value of i^{th} sample - sample mean)/ sample standard deviation].

Nearly 55% of the data points fall within the deviation limits from the perfect agreement line (PAL), represented by solid black lines [shown in Fig. 5.5(a)].

From the line plot, it is evident that the computed values from the present study are closer to the observed values. Figure 5.5(b) shows the variation between observed and computed values, along with the line plot of Melville and Chiew (1999). This formula also shows good agreement, with about 30% of data points falling within the 20% deviation lines.

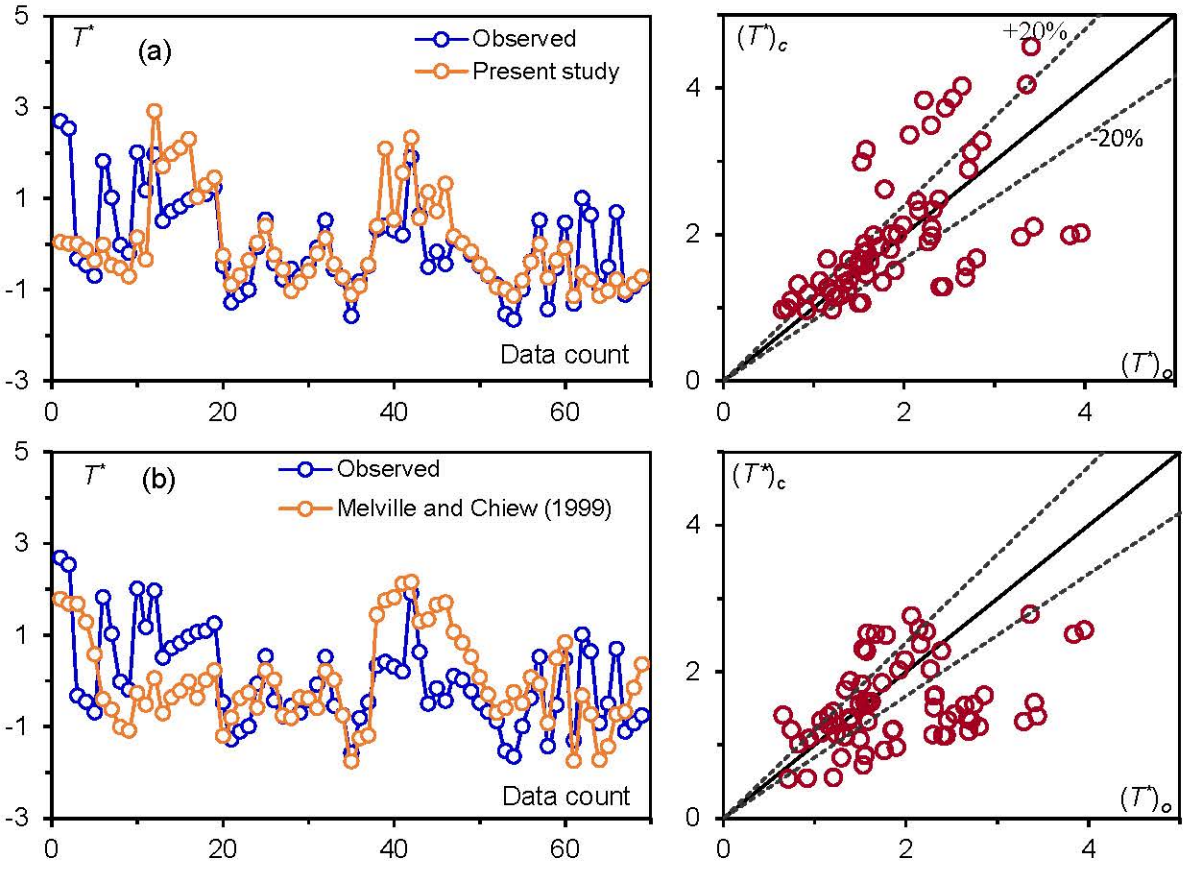

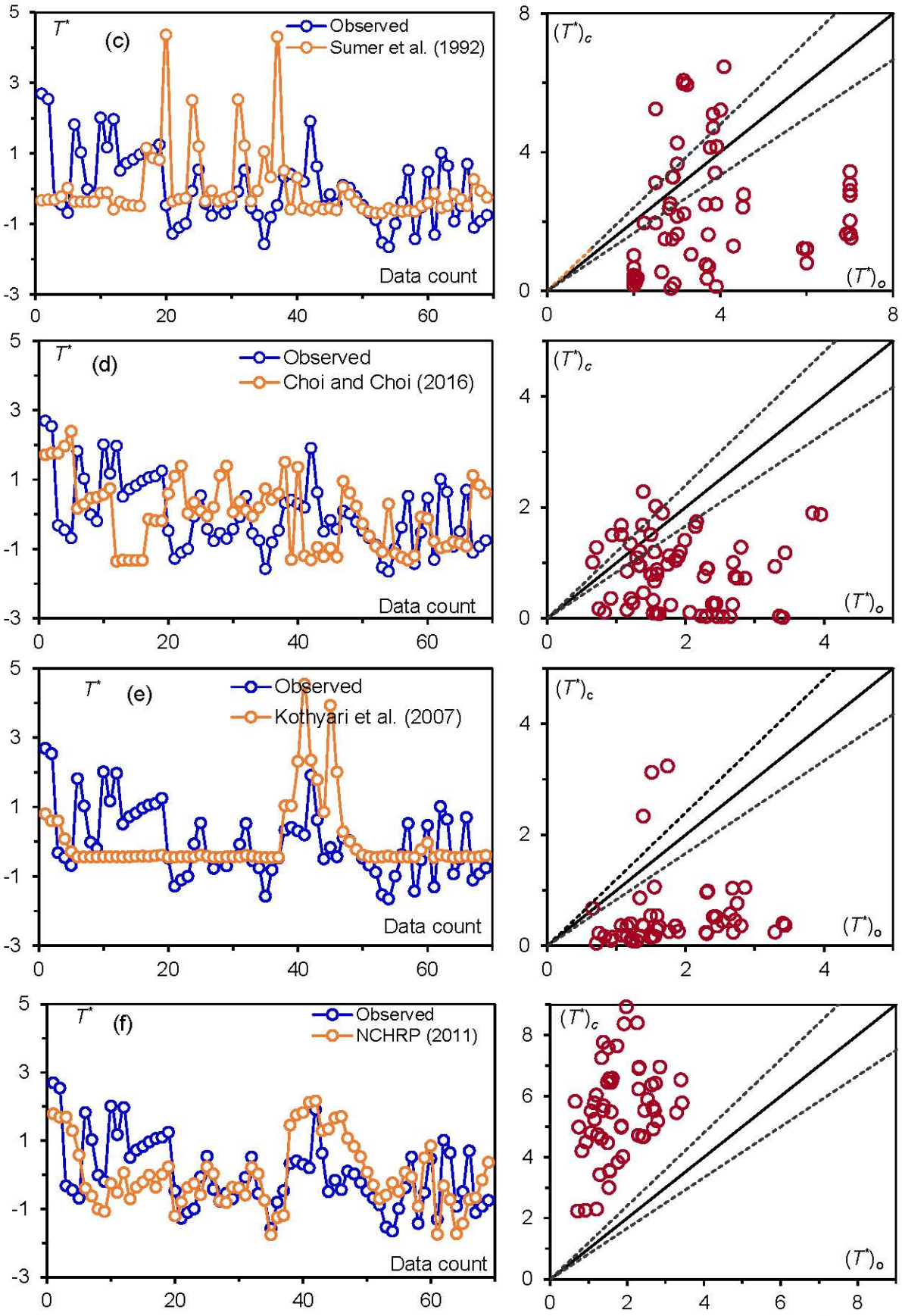

Fig. 5.5. Comparision between measured and computed equilibrium time scale (T^*) using formulas of (**a**) Present study, (**b**) Melville and Chiew (1999), (**c**) Sumer et al. (1992), (**d**) Choi and Choi (2016), (**e**) Kothyari et al. (2007), and (**f**) NCHRP (2011).

For Kothyari et al. (2007), Choi and Choi (2016), and Sumer et al. (1992), less than 2%, 8%, and 12% of the data points, respectively, fall within the 20% deviation lines, as seen in Figs. 5.5(c), 5.5(e), and 5.5(d), respectively.

However, for NCHRP (2011), no computed T^* data fall within the 20% deviation lines (Fig. 5.5f), and the T^* is over-computed in this case. The computed T_e scales by Sumer et al. (1992), Kothyari et al. (2007), and Choi and Choi (2016) tend to underestimate the time scale (T^*) as seen in Figs. 5.5(c), 5.5(e), and 5.5(d), where the data points lie below the PAL. Only a few T^* data points from these studies fall within the 20% deviation lines

The relevant influence factors for training and validation of both the literature and new formulas are presented in Table 5.5. For the present study, the highest CC is observed, along with the lowest values of RMSE, R^2, SSE, and MAPE for the calibrated T^* datasets.

Table 5.5. Performance indicators for different formulas of T^* datasets.

References	Data set	CC	RMSE	R^2	SSE	MAPE	% P_{out}
Sumer et al. (1992)	Training	-0.03	2.45	0.00	414.53	162.70	88.41
	Validation	0.16	8.06	0.03	1249.32	466.87	100.00
Melville and Chiew (1999)	Training	0.39	0.83	0.16	47.15	65.00	69.57
	Validation	0.59	0.49	0.35	5.44	47.91	62.50
Kothyari et al. (2007)	Training	0.19	14.09	0.04	13705.66	640.08	98.55
	Validation	0.07	124.64	0.01	372730.35	7068.62	100.00
Sheppard et al. (2011)	Training	0.39	4.99	0.16	1716.17	449.05	100.00
	Validation	0.59	4.41	0.35	384.54	468.03	100.00
Choi and Choi (2016)	Training	-0.07	1.46	0.00	147.77	120.63	91.30
	Validation	0.36	124.12	0.13	369752.52	4808.35	95.83
Present Study	Training	0.59	0.75	0.35	38.60	52.16	44.93
	Validation	0.72	0.65	0.52	10.07	53.06	45.83

The, 24 T^* data points from the literature, including eight experimental T^* data conducted by the authors (which are not used for the calibration of the present formula), but are used for the validation set. The prediction capability of the literature formulas is also tested for the present experimental conditions and validation set, as shown in Fig. 5.6(a-b). In Fig. 5.6(a), the line plot of T^* versus data count for observed and literature studies, including the present study, shows that the computed T^* values from the present study are closer to the observed values. The T^* values in the line plot are normalized using Z normalization to present the data on a homogeneous scale.

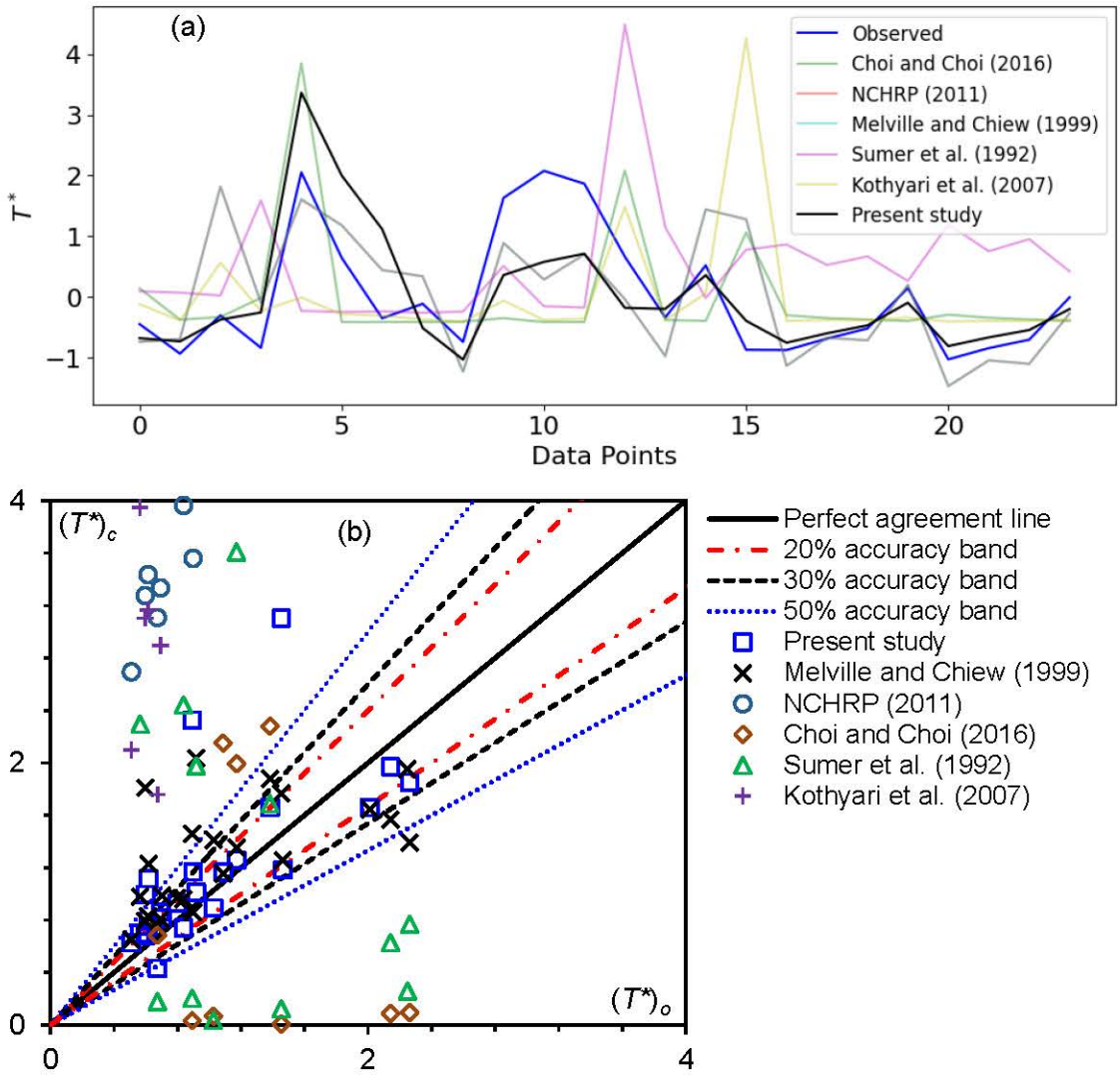

Fig. 5.6. Shows **(a)** the observed and computed T^* values for the validation dataset, and **(b)** a comparison of the percentage deviation of T^* within different accuracy bands, as obtained using formulas from the literature and the present study.

In Fig. 5.6(b), the 20%, 30%, and 50% data deviation percentages are shown. It is found that for the present study, 54.17%, 75%, and 79.17% of the data lie within the 20%, 30%, and 50% deviation lines, respectively. The formula of Melville and Chiew (1999), 37.5%, 54.17%, and 79.17% of the data fall within the same deviation ranges. These values are quite similar to the present formula. However, in the case of the other three formulas, the data points within the 20% deviation line are minimal.

For the validation dataset, the MAPE for this study is found to be 53.06%, and the CC value for the validation set is 72%, which is the highest among all models tested. The SSE value is particularly high for Kothyari et al. (2007) and Choi and Choi (2016). Overall, the statistical performance indicators for the validation T^* dataset show that the formula of the present study performs better than the literature.

5.3.3. A numerical example to calculate d_{se}/d and d_{st}/d_{se} using T_e

This approach outlines a refined methodology for determining d_{se} based on the d_{sm} formula proposed by Franzetti et al. (2022). The problem statement and the observed and computed values are listed in Table 5.6. The procedures are detailed below:

Step 1: Determination of T_e

[1] Calculate the parameter functions f_1, f_2 f_3 f_4, and f_5 using the relationships defined in Eqs. (5.7–5.11). These functions capture the influence of key hydraulic and sediment parameters.

[2] Calculate T_e through Eq. (5.6) by combining these parameter functions with the ratio d/u and a time constant λ = 86.81 days/sec, ensuring consistency in dimensional analysis.

Step 2: Estimation of d_{se}/d

[1] Employ the computed T_e from Step 1 to evaluate the time factor given in Franzetti et al. (2022) as $uT_e/\Delta d$.

[2] Integrate the parameter functions to derive the non-dimensional d_s ratio for quasi-state d_{se}/d, following the formulation presented in the study.

Step 3: Prediction of d_{st}/d_{se}

[1] Using the problem data (The problem statements are (1) u=0.330 m/s, h=0.375 m, d= 0.075 m, d_{50}=0.00086 m, σ =1.360, Δ=1.65, W= 2.00 m, d_{se} = 0.161 m. (2) u=0.310 m/s, h=0.200 m, d= 0.050 m, d_{50}=0.00086 m, σ =1.360, Δ=1.65, W= 2.00 m, d_{sm} = 0.165 m for computing d_{st}.), compute the non-dimensional time factor t/t_e. Here, te can be replaced by T_e.

[2] Apply the derived t/T_e to compute d_{st}/d_{se} using Sumer et al. (1992), Melville and Chiew (1999), NCHRP (2011), and Choi and Choi (2016) to generate time-series calculations.

The application of this method to 38 case examples show superior accuracy in the derived T_e and its subsequent use in calculating d_{se} (Fig. 5.7). Time-series plots demonstrate that calculations using this approach show good agreement with the perfect agreement line (PAL) compared to literature formula (Fig. 5.8). This method gives the best way to estimate d_{se}.

Table 5.6. Numerical problems, observations, and solutions

Problem numbers	Problems statements							Observations		Results	
	u (m/s)	h (m)	d (m)	σ	d_{50} (m)	Δ	B (m)	$(T_e)_o$ (days)	$(d_{se}/d)_o$	$(T_e)_c$ (days)	$(d_{se}/d)_c$
1	0.31	1.20	0.31	1.51	0.00022	1.65	6.10	6.79	0.83	11.54	0.85
2	0.39	0.87	0.92	1.29	0.00080	1.65	6.10	5.96	0.67	18.04	0.78
3	0.76	1.22	0.92	1.21	0.00290	1.65	6.10	7.83	1.34	13.05	1.31
4	0.65	0.56	0.92	1.21	0.00290	1.65	6.10	13.75	1.11	12.13	1.00
5	0.55	0.29	0.92	1.21	0.00290	1.65	6.10	18.67	0.96	11.51	0.76
6	0.49	0.17	0.92	1.21	0.00290	1.65	6.10	25.67	0.67	11.12	0.62
7	0.29	0.16	0.08	1.40	0.00086	1.65	0.83	34.90	2.24	3.69	1.81
8	0.31	0.16	0.08	1.40	0.00086	1.65	0.83	45.60	2.45	3.78	1.82
9	0.35	0.16	0.08	1.46	0.00128	1.65	0.83	29.70	1.63	3.24	1.79
10	0.35	0.15	0.08	1.46	0.00128	1.65	0.83	24.90	1.85	3.15	1.80
11	0.34	0.13	0.06	1.46	0.00128	1.65	0.83	29.00	2.05	2.92	1.80
12	1.11	0.60	0.03	1.24	0.00535	1.66	1.52	2.01	1.17	2.48	1.49
13	1.28	0.60	0.03	1.10	0.00780	1.66	1.52	1.49	0.82	2.59	1.42
14	1.17	0.60	0.03	1.24	0.00535	1.66	1.52	1.56	1.40	2.35	1.49
15	1.35	0.60	0.03	1.10	0.00780	1.66	1.52	2.06	1.03	2.45	1.42
16	0.99	0.60	0.05	1.07	0.00380	1.66	0.46	3.01	1.62	2.72	1.90
17	0.48	0.60	0.05	1.17	0.00084	1.66	0.46	5.66	2.30	3.80	2.32
18	1.11	0.60	0.05	1.24	0.00535	1.66	1.52	4.16	1.62	3.06	1.71
19	0.48	0.60	0.05	1.17	0.00084	1.65	1.52	7.94	2.41	5.11	2.32
20	0.46	0.60	0.15	1.17	0.00084	1.65	1.52	20.66	2.07	7.95	1.89
21	0.48	0.60	0.15	1.17	0.00084	1.65	1.52	26.32	2.32	7.54	1.89
22	0.83	0.10	0.03	1.24	0.00535	1.66	1.52	2.13	0.96	2.20	1.46
23	0.68	0.60	0.10	2.64	0.00190	1.65	1.52	10.40	0.76	2.65	0.79
24	0.68	0.60	0.10	2.00	0.00190	1.65	1.52	12.43	1.01	3.39	1.34
25	0.68	0.60	0.10	1.84	0.00190	1.65	1.52	10.09	1.32	3.64	1.55
26	0.68	0.60	0.10	1.32	0.00190	1.65	1.52	10.09	1.69	4.88	2.16
27	0.68	0.60	0.10	1.16	0.00190	1.65	1.52	15.32	2.09	5.47	2.29
28	0.96	0.60	0.10	1.59	0.00410	1.65	1.52	19.05	1.74	2.91	1.73
29	0.96	0.60	0.10	1.34	0.00410	1.65	1.52	16.75	2.00	3.39	1.98
30	0.96	0.60	0.10	1.17	0.00410	1.65	1.52	17.08	2.19	3.82	2.11
31	0.15	0.14	0.05	1.32	0.00250	0.18	0.50	58.16	1.67	7.32	1.91
32	0.29	0.11	0.11	1.00	0.00330	0.42	1.00	46.88	1.94	8.40	1.92
33	0.33	0.25	0.05	1.36	0.00086	1.65	2.00	9.87	1.98	4.10	2.05
34	0.27	0.16	0.08	1.36	0.00086	1.65	0.82	34.90	2.23	3.78	1.78
35	0.30	0.16	0.08	1.36	0.00086	1.65	0.82	45.60	2.45	3.87	1.83
36	0.34	0.16	0.08	1.46	0.00128	1.65	0.82	29.73	1.63	3.23	1.76
37	0.34	0.15	0.08	1.46	0.00128	1.65	0.82	24.85	1.80	3.14	1.77
38	0.34	0.13	0.06	1.46	0.00128	1.65	0.82	28.99	2.02	2.92	1.80

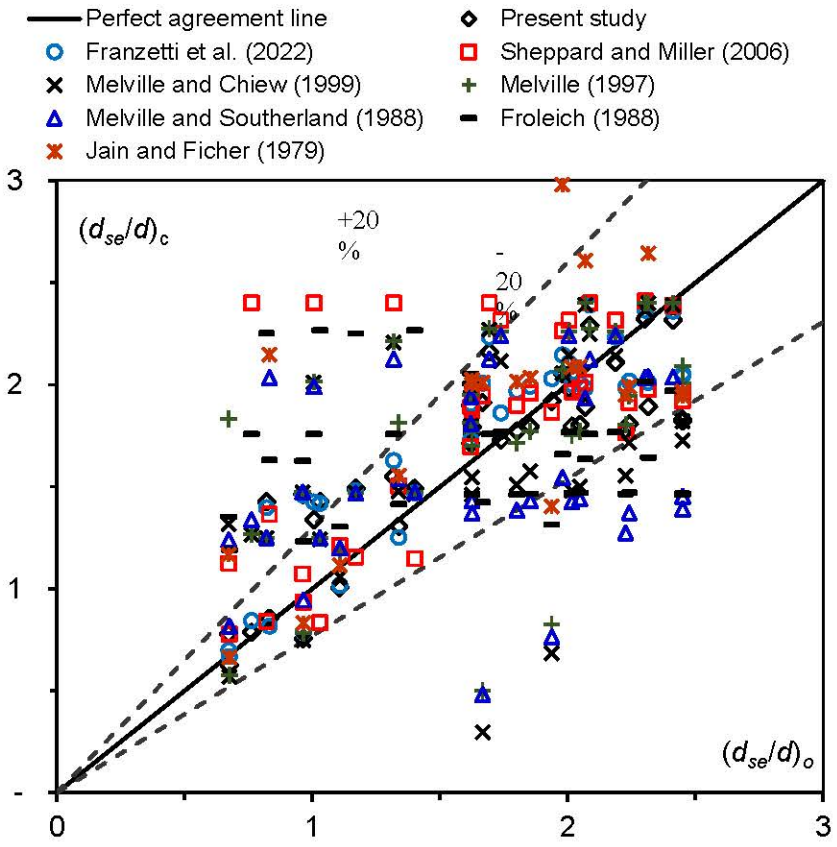

Fig. 5.7. Comparison of observed and computed scour depths.

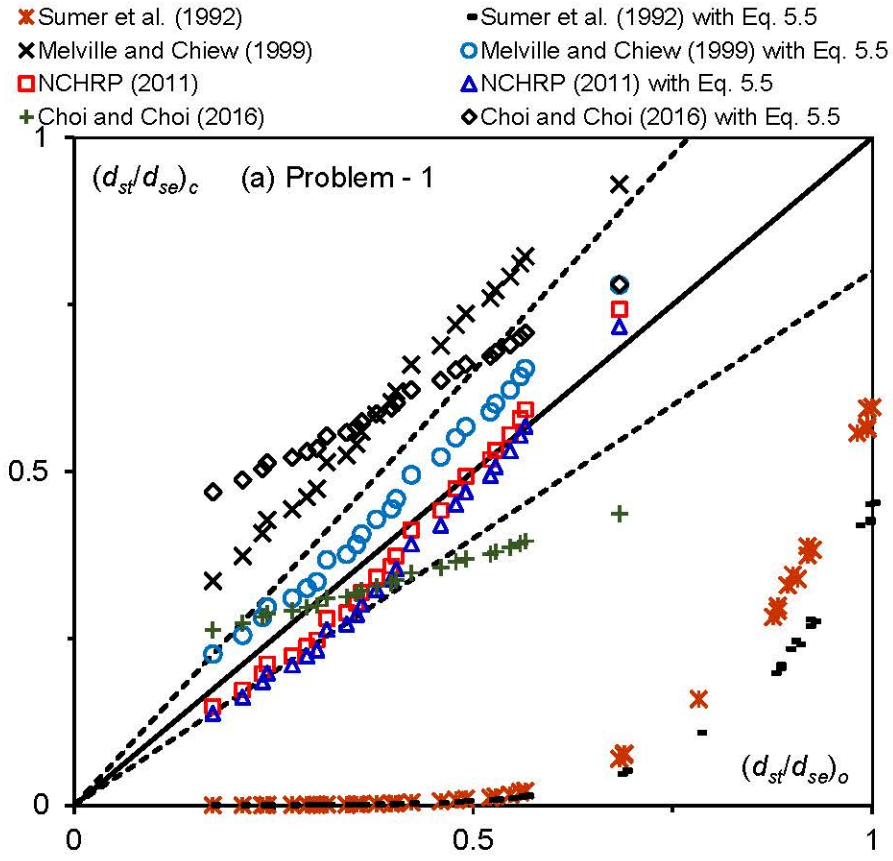

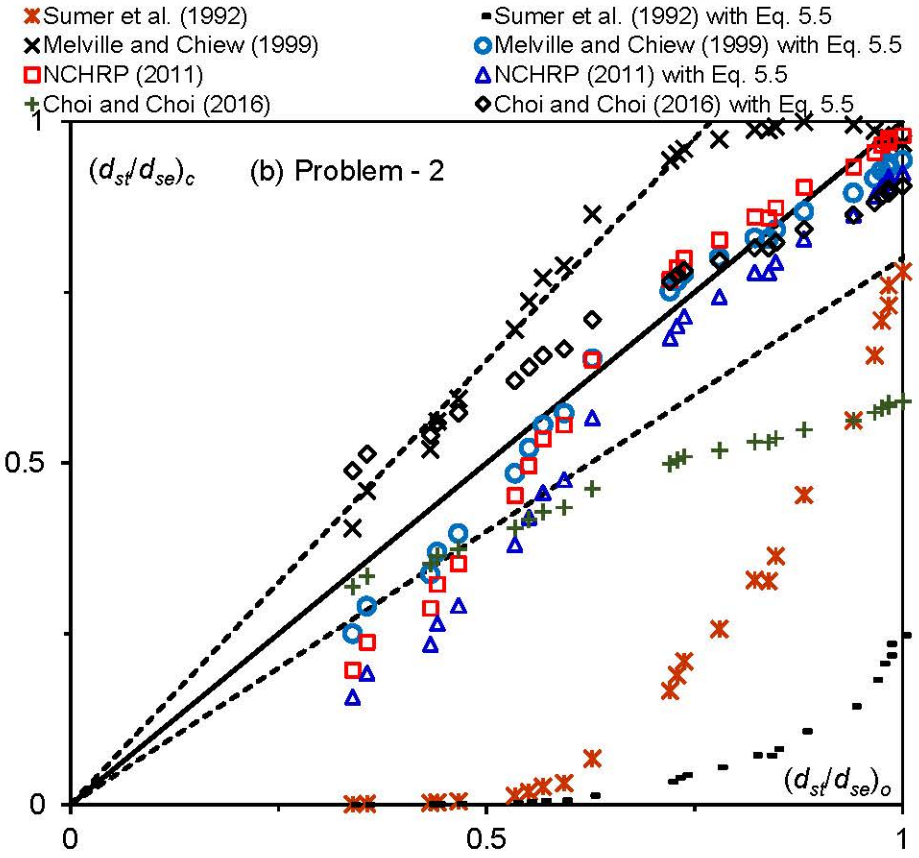

Fig. 5.8. Comparison of observed and computed d_{st} for **(a)** Problem- 1, and **(b)** Problem- 2.

5.3.4. Comparison of the formula using statistical attribute

This part of the study compares the new formula with existing ones to check how accurately they calculate T^*. The average and SD of errors indicate that when the mean error is positive, the observed values are overestimated, and when it is negative, they are underestimated (Table 5.7). The results show that the new formula performs better than literature. This study confirms that the new formula has the smallest prediction uncertainty band (0.61), while the formula by Kothyari et al. (2007) has the widest band (7.74), at a 5% significance level. The second-best formula is Melville and Chiew (1999).

Table 5.7. The uncertainty in the current study in comparison to the literature review

Authors	Average	Standard deviation	Margin of error	Upper limit	Lower limit	Uncertainty band
Present study	-0.29	1.36	0.30	0.01	-0.60	0.61
Melville and Chiew (1999)	-0.79	1.48	0.33	-0.46	-1.12	0.66
Choi and Choi (2016)	-1.10	2.82	0.63	-0.47	-1.73	1.26
Sheppard et al. (2011)	7.64	4.32	0.97	8.61	6.68	1.93
Sumer et al. (1992)	-0.01	4.43	0.99	0.98	-1.00	1.98
Kothyari et al. (2007)	5.13	17.32	3.87	9.00	1.26	7.74

Figure 5.9 uses Taylor diagrams to compare the performance of the new formula with existing formulas across overall data. The distance between the points from the observed point, especially when closer to the higher correlation line, reflects the strength of each formula. The new formula shows points that are closely aligned with the observations, indicating better performance compared to the other models.

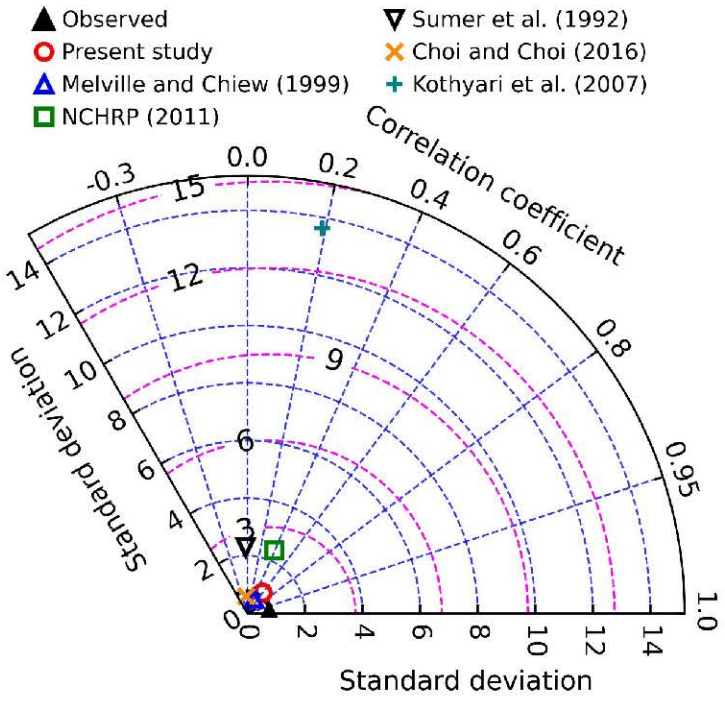

Fig. 5.9. The Taylor diagram shows how well different formulas perform compared to the training dataset.

5.4. Conclusions

This study conducts a meta-analysis of data from the literature on local scour around circular piers under clear-water conditions. The dimensionless parameters influencing the quasi-equilibrium time scale (T_e) are calibrated using 69 datasets. Furthermore, 24 datasets, including eight additional experimental datasets, are used for validating the new formula. The key findings are summarized as follows:

- The main factors influencing the T_e are flow shallowness (h/d), flow intensity (u/u_c), sediment coarseness (d/d_{50}), sediment uniformity (σ), and constriction ratio (d/W).
- The parameters of the new formula showed better performance than literature formulas, with improvements in CC and MAPE by approximately 51% and 20%, respectively.
- The new formula outperforms the literature formula, with 35.5% more calibration data and 26.7% more validation data falling within ±80% accuracy compared to the previous best formula.
- A numerical example demonstrated how to use the new formula to calculate T_e for 38 problem statements from the literature, achieving 89.47% of calculation within ±20% deviation.

- The new formula has the smallest uncertainty band (0.61) compared to other formulas, and Taylor diagrams show its better performance.

The new T_e formula is highly effective for predicting when d_s stabilize under unidirectional clear-water flow. However, a key limitation is the observed equilibrium time for the threshold is set at two days, which excludes 90% of the datasets from the literature.

References

Alabi, P. D. (2006). *Time development of local scour at a bridge pier fitted with a collar* (M.Sc. thesis). Department of Civil and Geological Environmental Engineering, University of Saskatchewan.

Ansari, M. F., and Ahmad, Z. (2024). Scour pattern at zero-degree confluent channels. *Acta Geophysica, 72*, 3547–356.

Breusers, H. N. C., Nicollet, G., and Shen, H. W. (1977). Local scour around cylindrical pier. *Journal of Hydraulic Research, 15*(3), 211–252.

Chabert, J., and Engeldinger, P. (1956). *Étude des affouillements autour des piles de ponts* [Study of scour around bridge piers]. Technical Report, Laboratoire National d'Hydraulique, Chatou, France.

Chang, W. Y., Lai, J. S., and Yen, C. L. (2004). Evolution of scour depth at circular bridge piers. *Journal of Hydraulic Engineering, 130*(9), 905–913.

Chiew, Y. M. (1984). *Local scour at bridge piers*. Doctoral dissertation, Department of Civil Engineering, University of Auckland, Auckland, New Zealand.

Chiew, Y. M. (1995). Mechanics of riprap failure at bridge piers. *Journal of Hydraulic Engineering, 121*(9), 635–643.

Choi, S. U., and Choi, B. (2016). Prediction of time-dependent local scour around bridge piers. *Water and Environment Journal, 30*(1–2), 14–21.

Das, S., Das, R., and Mazumdar, A. (2013). Circulation characteristics of horseshoe vortex in the scour region around circular piers. *Water Science and Engineering, 6*(1), 59–77.

Ettema, R. (1980). *Scour at bridge piers*. Ph.D. thesis. University of Auckland.

Franzetti, S., Radice, A., Rebai, D., and Ballio, F. (2022). Clear water scour at circular piers: A new formula fitting laboratory data with less than 25% deviation. *Journal of Hydraulic Engineering, 148*(10), 04022021.

Graf, W. H. (1995). Load scour around piers. *Annual Report*, Iowa Highway Research Board, Ames, IA.

Kothyari, U. C., Hager, W. H., and Oliveto, G. (2007). Generalized approach for clear-water scour at bridge foundation elements. *Journal of Hydraulic Engineering, 133*(11), 1229–1240.

Lança, R., Fael, C., and Cardoso, A. H. (2010). Assessing equilibrium clear water scour around single cylindrical piers. *River Flow 2010*, 1207–1214.

Lança, R. M., Fael, C. S., Maia, R. J., Pêgo, J. P., and Cardoso, A. H. (2013). Clear-water scour at comparatively large cylindrical piers. *Journal of Hydraulic Engineering, 139*(11), 1117–1125.

Lança, R., Simarro, G., Fael, C. M. S., and Cardoso, A. H. (2016). Effect of viscosity on the equilibrium scour depth at single cylindrical piers. *Journal of Hydraulic Engineering, 142*(3), 06015022.

Lee, S. O., and Sturm, T. W. (2009). Effect of sediment size scaling on physical modeling of bridge pier scour. *Journal of Hydraulic Engineering, 135*(10), 793–802.

Link, O., Henríquez, S., and Ettmer, B. (2019). Physical scale modeling of scour around bridge piers. *Journal of Hydraulic Research, 57*(2), 227–237.

Link, O., Pfleger, F., and Zanke, U. (2008). Characteristics of developing scour-holes at a sand-embedded cylinder. *International Journal of Sediment Research, 23*(3), 258–266.

Melville, B. W., and Chiew, Y. M. (1999). Time scale for local scour at bridge piers. *Journal of Hydraulic Engineering, 125*(1), 59–65.

Mignosa, P. (1980). *Fenomeni di erosione locale alla base delle pile dei ponti* (M.Sc. thesis). Politecnico di Milano.

Monti, R. (1994). *Indagine sperimentale sulle caratteristiche fluido-dinamiche del campo di moto intorno ad una pila circolare.* Ph.D. thesis. Politecnico di Milano, Italy.

Nandi, B., and Das, S. (2023). Identify most promising temporal scour depth formula for circular piers proposed over the last six decades. *Ocean Engineering, 286*, 115639.

Nandi, B., Patel, G., and Das, S. (2024). Prediction of maximum scour depth at clear water conditions: Multivariate and robust comparative analysis between empirical equations and machine learning approaches using extensive reference metadata. *Journal of Environmental Management, 354*, 120349.

National Cooperative Highway Research Program (NCHRP). (2011). *Scour at Wide Piers and Long Skewed Piers* (D. M. Sheppard, H. Demir, and B. Melville, Eds.). National Academies of Sciences, Engineering, and Medicine. The National Academies Press.

Oliveto, G., and Hager, W. H. (2002). Temporal evolution of clear-water pier and abutment scour. *Journal of Hydraulic Engineering, 128*(9), 811–820.

Sheppard, D. M., Melville, B., and Demir, H. (2014). Evaluation of existing equations for local scour at bridge piers. *Journal of Hydraulic Engineering, 140*(1), 14–23.

Sheppard, D. M., Odeh, M., and Glasser, T. (2002). *Clearwater local sediment scour experiments* (Coastal Engineering Technical Report No. 131). Department of Civil and Coastal Engineering, University of Florida.

Sheppard, D. M., Odeh, M., and Glasser, T. (2004). Large scale clear-water local pier scour experiments. *Journal of Hydraulic Engineering, 130*(10), 957–963.

Sumer, B. M., Christiansen, N., and Fredsoe, J. (1992). Time scale of scour around a vertical pile. In *Second International Offshore and Polar Engineering Conference.* International Society of Offshore and Polar Engineers.

Chapter 6

Maximum Scour around Two Piers Semi-empirical

6.1. Introduction

The growing traffic in rapidly expanding metropolitan areas has led to the construction of new bridges alongside existing ones to meet the rising demand for transportation infrastructure. These modern parallel bridges are often wide and supported by two closely spaced piers arranged side-by-side (SBS), tandem (TAN), or eccentrically (ECC), sometimes aligned differently to handle structural loads (Coleman 2005, Beg and Beg 2015, Das et al. 2019). Building these new bridges creates complex water flow patterns that engineers must carefully consider. Accurately estimating scour depth (d_s) is crucial for designing strong and reliable bridge foundations.

Research on isolated (ISO) bridge piers has been ongoing for over a century, starting with the regime theory of Lacey and advancing to recent works like Franzetti et al. (2022) and Nandi and Das (2023), which analyze experimental data. Moreover, studies by Oliveto and Hager (2002) and Tang et al. (2023) have established design criteria for hydraulic processes of scour. This field has also developed different soft computing models for predicting d_s (e.g., Choi and Choi 2022, Kumar et al. 2023, Pandey et al. 202, Nandi et al. 2024). Over the years, researchers have derived more than 80 formulas addressing equilibrium, maximum, or temporal d_s evaluation, with significant contributions from Melville (1997), Sheppard and Miller (2006), Lança et al. (2013), and many others.

Hannah (1978) conducted experiments on pier groups to study d_s and observed that 80% of d_s developed within the first seven hours (Raudkivi 1998). Research by Asthiani and Kordakandi (2012), Hamidi and Siadatmousavi (2018), and Namaee and Sui (2019) focused on analyzing flow patterns around SBS piers. Movahedi et al. (2013) explored the equivalent pier diameter (d_{eq}) to study the time evolution of scour around such piers. They proposed a formula based on experimental data and linked d_{eq} to the center-to-center pier spacing (r). Furthermore, they analyzed the maximum d_s (d_{sm}) around SBS piers and developed a formula to estimate d_{sm} as a function of r. The accuracy of their model was compared with the d_{sm} formula proposed by Devi and Kumar (2022*a*).

Different researchers have conducted experiments to study the mutual interference effects between TAN piers (Beg and Beg 2015, Wang et al. 2016, Liu 2018, Memar et al. 2020). These studies examined the flow patterns around TAN piers, focusing on the complex flow behavior near the downstream pier (Asthiani and Kordakandi 2013, Garg et al. 2022). Keshavarzi et al. (2018) analyzed the influence of r on d_{sm}, while Memar et al. (2020) investigated how the size and position of collars affect d_s around two TAN circular piers.

However, Yilmaz et al. (2017) and Devi and Kumar (2022*b*) studied the temporal evolution of clearwater d_s (d_{st}) for two TAN circular piers.

Das et al. (2014, 2016) studied how varying longitudinal spacing between piers influences these effects. Other studies have examined turbulent flow hydrodynamics around multiple piers with various shapes and arrangements (Das et al. 2016, Jaman et al. 2017, Das and Mazumdar 2017, Das et al. 2019). Khaple et al. (2017) highlighted how upstream pier interference affects the scour of the downstream pier. Qi et al. (2019) modeled d_s around twin piers under combined waves and currents based on r. Nandi and Das (2024) investigated different pier shapes and arrangements, validating results against established formulas and experimental data. Research on clearwater scour around ECC multiple piers is limited.

This study aims to analyze the research on scouring around SBS, TAN, and ECC piers. The study identifies key factors affecting d_{sm}, including pier arrangement, spacing, sediment properties, flow conditions, geometry, and time. By reviewing methodologies, experimental setups, and modeling approaches in the literature, the study highlights the strengths and limitations of existing research. New formulas have been developed to calculate d_{sm}, incorporating parameters such as flow intensity (u/u_c), flow shallowness (h/d), sediment coarseness (d/d_{50}), time (t), r, and flow skew angle (φ), d is pier diameter. Statistical performance indicators Correlation Coefficient (CC), Nash Sutcliffe Efficiency (NSE), Normalize Root Mean Squared Error (NRMSE), and Index Agreement (IA) are used to evaluate the reliability of these formulas. This study provides a detailed overview of current knowledge and outlines future research directions in this field.

6.2. Methods

6.2.1. Curation of scour data and pre-processing

To examine the influence of pier position and r on d_{sm}, 486 datasets are gathered from 12 literature sources. Table 6.1 outlines the experimental and flume conditions for these datasets, including parameters such as flume dimensions (L×W×H: length×width×height), flow depth (h), and flow velocity (u). After a thorough screening process focusing on key factors affecting scour development, 430 datasets are selected for analysis.

Descriptive statistics for the three pier arrangements are summarized in Table 6.2. Key metrics include the arrangement of piers (A), standard deviation (SD), sum of squared errors (SS), interquartile range (IQR), skewness (Skew), kurtosis (Kurt), and results from the Anderson-Darling normality test (AD). The p-value from this test indicates whether the data follows a normal distribution ($p > 0.05$ suggests normality).

Table 6.1. Relevant experimental conditions in 12 literatures

References	Flume size (L×B×H) (m×m×m)	d_{50} (mm)	h (cm)	u (m/s)	d (cm)	t (min)
Das et al. (2014)	10×0.81×0.6	0.37	6.0–8.0	0.213–0.262	5.0	1440–1800

Malik and Setia (2014)	12×0.60×0.7	0.18	12.9–13.4	0.250–0.260	5.0	300
Das et al. (2016)	11×0.81×0.6	0.73	12.5	0.247	5.0–7.0	2160–5400
Wang et al. (2016)	12×0.42×0.7	0.70	12.0–15.0	0.147–0.281	6.0	300
Khaple et al. (2017)	15×0.91×0.7	0.96–1.80	16.0	0.346–0.472	6.0–8.2	2160
Keshavarzi et al. (2018)	19×0.61×0.6	0.85	11.5–16.0	0.264–0.344	5.5	4500
Liu et al. (2018)	12×0.42×0.7	0.70	12.0	0.132–0.276	3.0	300
Das et al. (2019)	11×0.81×0.6	0.83	12.5	0.247	7.0	3900
Malik and Setia (2020)	15×0.40×0.6	0.30	11.8–15.0	0.250–0.260	4.2	3000
Malik and Setia (2021)	12×0.60×0.7	0.23	15.5–17.7	0.250–0.260	6.2	300
Devi and Kumar (2022*a*)	14×1.10×0.8	0.60	12.0–16.3	0.224–0.300	5.0	480
Devi and Kumar (2022*b*)	14×1.10×0.8	1.75	12.0–16.4	0.224–0.400	5.0	480

Table 6.2. The descriptive statistics of the variables are considered for the different arrangements.

A.	Var.	Mean	SD	SS	Median	Range	IQR	Skew.	Kurt.	AD	*p*
SBS	d_{sm1}/d	1.58	0.16	80.78	1.62	0.73	0.27	0.55	1.05	0.82	0.03
	d_{sm2}/d	1.58	0.16	80.44	1.6	0.72	0.24	0.83	1.37	0.62	0.1
	u/u_c	0.88	0.08	24.72	0.89	0.23	0.19	-0.44	-1.33	1.99	<0.005
	h/d	2.85	0.33	263.39	2.98	0.86	0.78	-0.18	-1.39	1.42	<0.005
	d/d_{50}	125.8	77.9	694924.5	83.3	186.2	42.5	1.38	-0.06	7.42	<0.005
	ut/d	1.64E+05	1.77E+05	1.83E+12	1.51E+05	1.04E+06	4.38E+04	5.27	29.11	7.32	<0.005
	r/d	3.11	1.23	357.18	3	4	2	-0.01	-1.09	0.44	0.27
TAN	d_{sm1}/d	0.94	0.53	310.96	0.95	1.96	0.82	0.05	-0.94	1.93	<0.005
	d_{sm2}/d	0.79	0.44	218.12	0.77	1.71	0.67	0.19	-0.83	1.5	<0.005
	u/u_c	0.72	0.17	146.22	0.72	0.61	0.3	-0.07	-1.21	3.51	<0.005
	h/d	2.79	0.84	2270.57	2.5	2.8	2	0.52	-1.24	23.52	<0.005
	d/d_{50}	85.72	56.89	2833524	85.71	249.21	42.86	2.32	5.31	32.86	<0.005
	ut/d	1.91E+05	2.91E+05	3.25E+13	8.37E+04	1.26E+06	6.56E+04	2.72	6.29	57.17	<0.005
	r/d	7.61	4.79	21639.48	7	16	9	0.36	-1.13	6.17	<0.005
ECC	d_{sm1}/d	1.42	0.53	114.63	1.35	1.66	1.09	0.35	-1.43	2.17	<0.005
	d_{sm2}/d	1.52	0.54	129.21	1.5	1.87	1.05	0.22	-1.23	0.96	0.01
	u/u_c	0.89	0.1	40.22	0.9	0.33	0.18	-0.42	-0.9	2.41	<0.005
	h/d	2.24	0.73	277.1	1.79	2.37	0.93	0.29	-1.2	2.32	<0.005
	d/d_{50}	92.94	44.52	529017.87	95.89	106.67	103.65	-0.29	-1.56	4.03	<0.005
	ut/d	8.83E+05	2.31E+05	4.16E+13	1.02E+06	6.83E+05	2.60E+05	-0.77	-0.95	3.93	<0.005
	φ	36.29	13.74	75076.75	34.77	55.27	22.15	0.21	-0.7	0.85	0.03
	r/d	5.25	2.3	1634.87	5.26	10.4	2.1	0.86	1.13	1.2	<0.005

The correlation heatmap in Fig. 6.1a shows the relationships between parameters for different pier arrangements, highlighting which factors are more or less influential in predicting d_{sm}. Violin plots confirm these distribution characteristics (Fig. 6.1b). For instance, the ratio r/d shows a negative correlation with d_{sm1}/d and d_{sm2}/d where d_{sm1} and d_{sm2} represent the d_{sm} at Pier-1 and Pier-2, respectively (Fig. 6.2). This indicates when r/d increases, both d_{sm1}/d and d_{sm2}/d decrease, which makes r/d a critical parameter. Moreover,

parameters like ut/d and d/d_{50} have minimal influence on predictions, which shows their lesser importance.

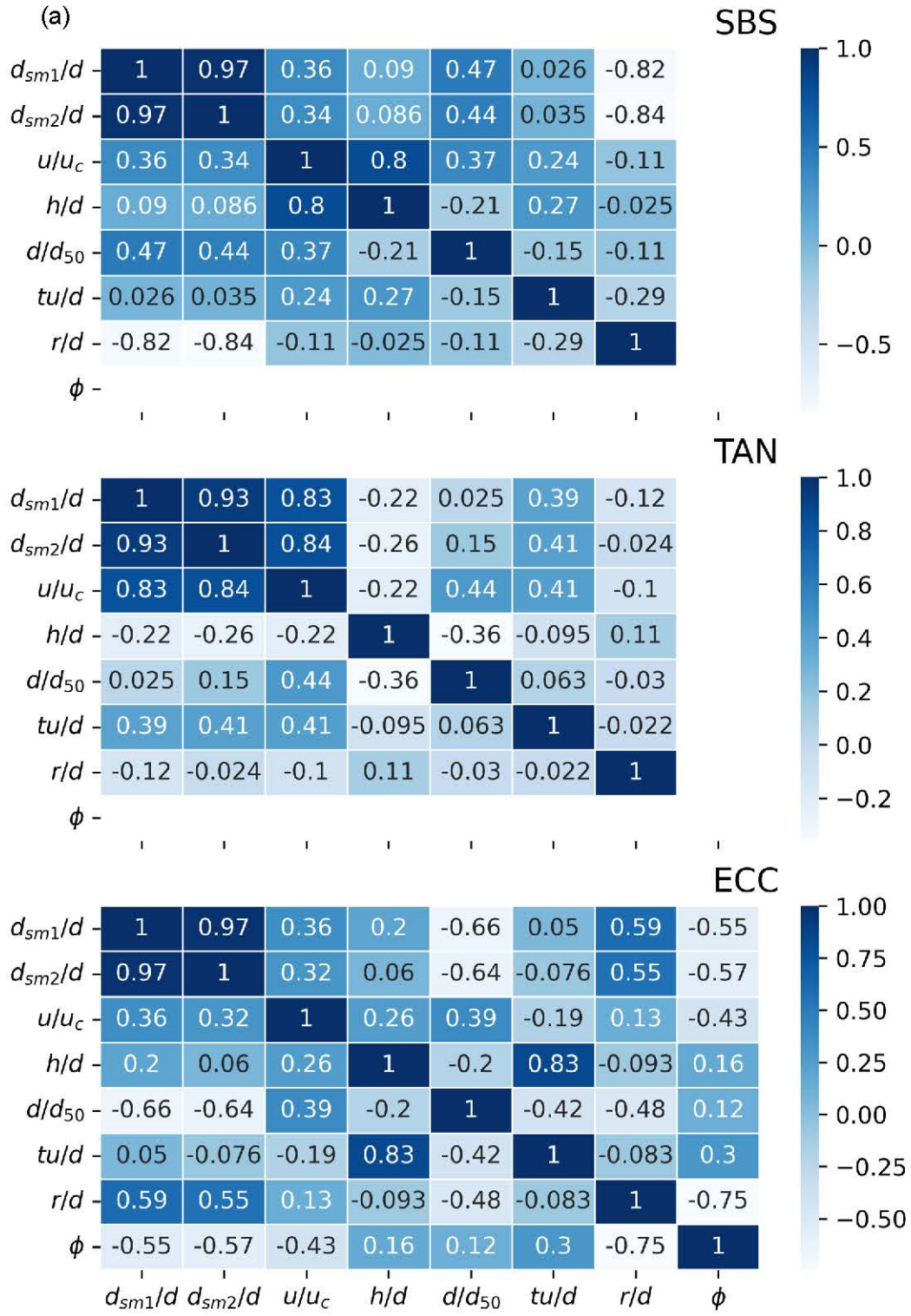

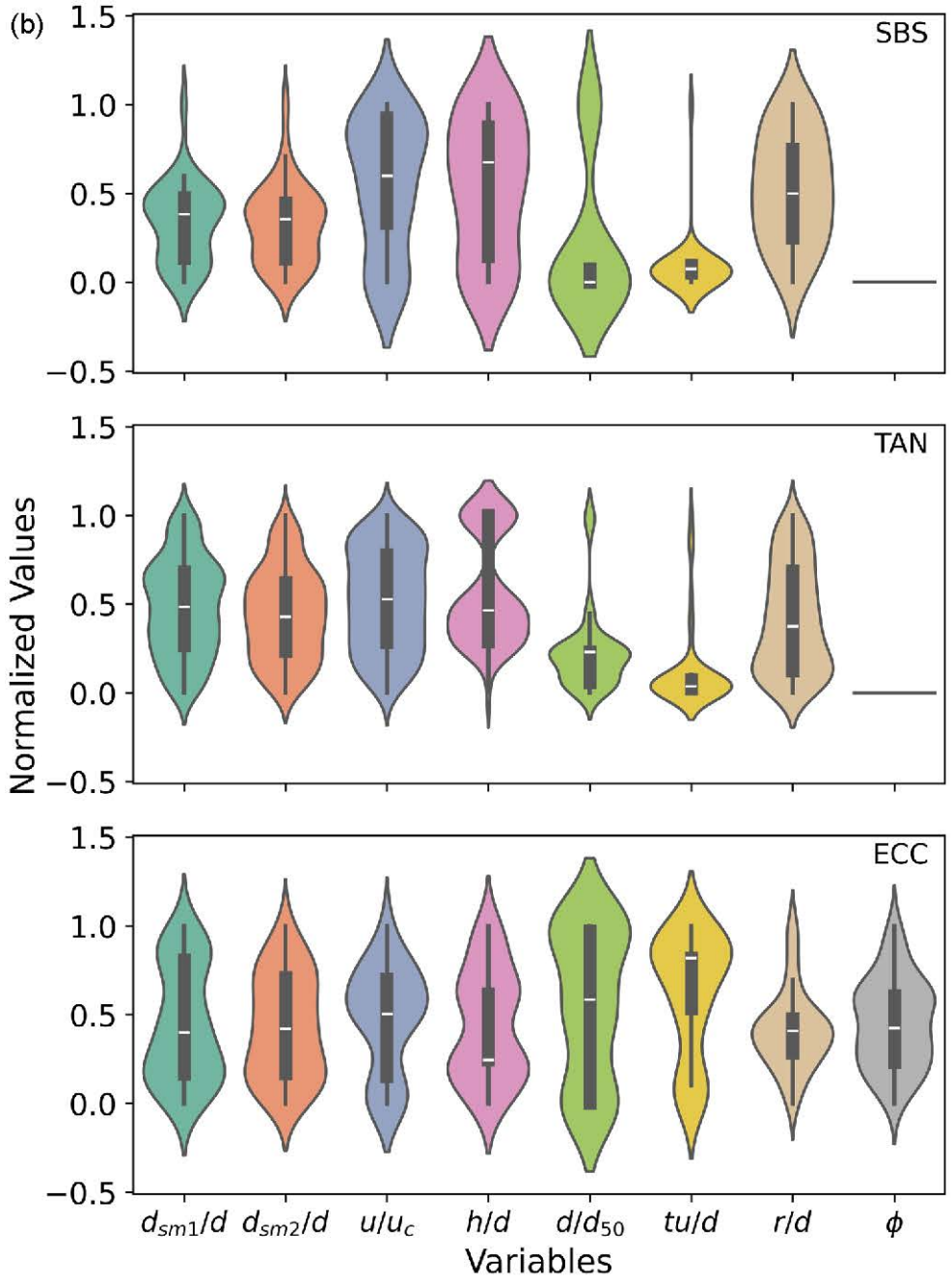

Fig. 6.1. (a) Correlation heatmap for different arrangements of piers, and **(b)** Violin plots for different arrangements of piers

For the SBS arrangement, most variables have low skewness values between -0.44 and 1.38, except for ut/d (=5.27), which suggests symmetrical distributions for most variables. Similarly, kurtosis values are low, which indicates broad and flat distributions, except for ut/d, which has a high kurtosis of 29.11, which suggests a sharp-peaked (leptokurtic) distribution. The Anderson-Darling (AD) test indicates that r/d and d_{sm2}/d are normally distributed ($p > 0.05$), while most variables deviate from normality ($p < 0.005$).

In the TAN arrangement, parameters like d/d_{50} and ut/d, show higher skewness and kurtosis, which indicates asymmetrical and sharply peaked distributions, respectively. Other

variables show skewness values between -0.07 and 0.52 (suggesting near-symmetry) and kurtosis values between -0.83 and -1.24, which reflect platykurtic (broad and flat) distributions. Violin plots suggest outliers for d/d_{50} and ut/d (Fig. 6.1b). Here, all variables fail the AD test ($p < 0.005$), confirming they do not follow normal distributions.

In the ECC arrangement, most variables show moderate skewness and kurtosis, with slight skewness observed for d_{sm1}/d and ut/d. However, the AD test shows that most variables do not follow a normal distribution, except for the skew angle φ ($p = 0.03$), which, while not fully normal, shows a tendency toward normality.

The analysis of Table 6.1 and Fig. 6.1 underscores the complexity and heterogeneity of the data distributions across different arrangements. This highlights the necessity of using nonlinear techniques to effectively capture and interpret these complicated relationships for accuracy. The schematic diagram of two pier combination is given in Fig. 6.2.

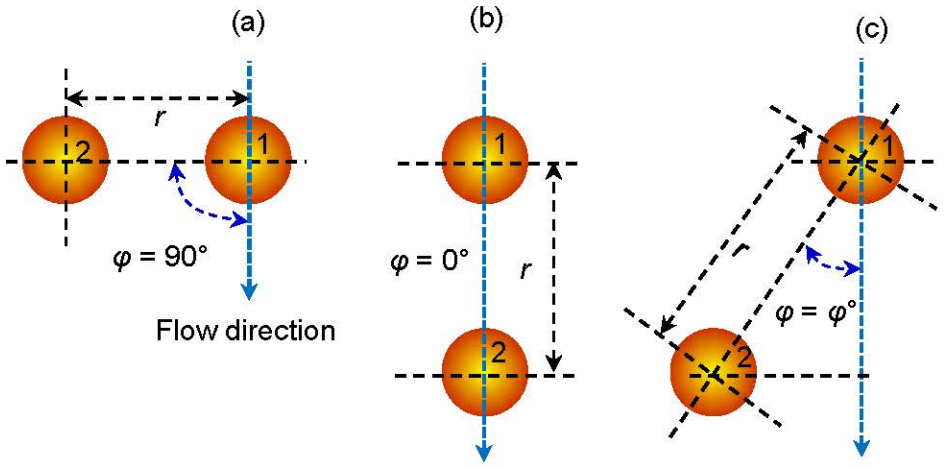

Fig. 6.2. Schematic diagrams of piers in **(a)** SBS, **(b)** TAN, and **(c)** ECC arrangements ("1" denotes Pier-1 and "2" denotes Pier-2).

6.2.2. Dimensional analysis: Buckingham π theorem

The d_{sm} for two circular piers placed in different r and φ is evaluated using the different parameters given in Eq. (6.1). Here, u_c is critical velocity, σ is sediment gradation, ρ_f is water density, ρ_s is sediment density, g is gravitational acceleration, μ is dynamic viscosity.

$$d_{sm} = f\left(h, d, u, u_c, d_{50}, r, \varphi, \rho_f, \rho_s, \sigma, t, g, W, \mu\right) \tag{6.1}$$

Using Buckingham π theorem Eq. (6.1) has been converted into Eq. (6.2). Here, $\Delta = (\rho_s/\rho_f)-1$, Δ is sediment density ratio, d/W is constriction ratio, r/d is dimensionless spacing, Re is Reynolds number, Fr is Froude number, ut/d is dimensionless time.

$$\frac{d_{sm}}{d} = f_2\left(\frac{h}{d}, \frac{u}{u_c}, \frac{d}{d_{50}}, \frac{r}{d}, \varphi, \frac{\rho_f u h}{\mu} = \mathrm{Re}, \frac{u}{\sqrt{gh}} = \mathrm{Fr}, \sigma, \frac{ut}{d}, \Delta, \frac{d}{W}\right) \tag{6.2}$$

6.2.3. Promising maximum scour depth formulas

Most existing literature focuses on determining the equilibrium d_s (d_{se}) under clearwater conditions, often neglecting the time factor, which depends on sediment properties, flow parameters, and pier geometry. Here, s is the clear spacing between Pier-1 and Pier-2, P_f is the pier position factor, which ranges from 0 to 2 (Das et al. 2019), e denotes the ECC spacing between piers, l is the flow wise spacing between piers, and T is the time scale (Khaple et al. 2017). The functional form of each model from the literature is provided in Table 6.3.

Table 6.3. Different functions used to develop scour depth formulas in literature.

Arrangement	Literature	Functions
ISO	Nandi and Das (2023)	$d_{sm}/d = f(u/u_c, h/d, \sigma, d/d_{50}, ut/d\Delta^{0.5}, d/w)$
	Franzetti et al. (2022)	$d_{sm}/d = f(u/u_c, h/d, \sigma, d/d_{50}, ut/d\Delta^{0.5})$
	Sheppard and Miller (2006)	$d_{sm}/d = f(u/u_c, h/d, d/d_{50})$
SBS	Devi and Kumar (2022a)	$d_{sm1\|2}/d = f(r,d)$
	Malik and Setia (2020)	$d_{sm1\|2}/d = f(e/d)$
	Malik and Setia (2020)	$d_{sm1\|2}/d = f(l/d)$
TAN	Keshavarzi et al. (2018)	$d_{sm1}/d = f(d_{se}/d)$; $d_{sm2}/d = f(d_{se}/d, l)$
	Liu et al. (2018)	$d_{sm1}/d = f(u/u_c)$; $d_{sm2}/d = f(u/u_c, r/d)$
	Khaple et al. (2017)	$d_{sm2}/d = f(d_{se}/d, u/u_c, t/T, l/d, e/d)$
	Wang et al. (2016)	$d_{sm1}/d = f(u/u_c)$; $d_{sm2}/d = f(u/u_c, r/d)$
	Nandi and Das (2024)	$d_{sm1\|2}/d = f(d_{se}/d, d_{50}/d, h/d, r/d, l/d, t/T)$
ECC	Das et al. (2019)	$d_{sm1}/d = f(l/d, P_f)$; $d_{sm2}/d = f(l/d, P_f)$
	Malik and Setia (2020)	$d_{sm1\|2}/d = f(s/d)$; $d_{sm3}/d = f(s/d)$
	Khaple et al. (2017)	$d_{sm2}/d = f(d_{se}/d, u/u_c, t/T, l/d, e/d)$
	Das et al. (2016)	$d_{sm1\|2}/d = f(l/d)$

The researchers have proposed formulas for d_s around TAN piers (Wang et al. 2016, Liu et al. 2018, Keshavarzi et al. 2018, Malik and Setia 2020), while formulas for SBS piers have been provided by two other groups (Malik and Setia 2020, Devi and Kumar 2022*a*). For ECC, TAN, and symmetrical staggered piers, Khaple et al. (2017) presented formulas for the d_{st} based on e and l. Nandi and Das (2024) also developed another d_{st} formula for ECC piers of various shapes, based on r and l.

For ISO piers, three formulas for ds from Sheppard and Miller (2006), Franzetti et al. (2022), and Nandi and Das (2023) are included in this study to compare ds values around SBS piers. This comparison focuses only on the d_{sm} of SBS. The results indicate that using formulas for ISO piers alone is inadequate to explain the interference and sheltering effects observed in groups of piers. This highlights the need for robust formulas for d_{sm} that account for pier spacings and positions (l, e or r, φ) as important factors. Fig. 6.2 presents schematic diagrams of SBS, TAN, and ECC pier arrangements.

6.2.3. Challenges in data curation

The challenges faced during data collection and homogenization are addressed through specific assumptions adopted in this study, as given below:

***Velocity* (u):** To ensure dataset homogeneity, it has chosen to utilize the original u data provided by researchers whether it represents the bulk or depth-averaged u. If any u is unavailable, but discharge (Q=uWh) is given, it is converted to the u. Similarly, if other parameters like Fr, and F_D are available then suitable conversions are applied as applied for Das et al. (2014). Malik and Setia (2021) set the u within the ranges of 0.25-0.26 and 0.24-0.26 m/s, for TAN and SBS arrangement respectively. As the one-decimal-place difference between the TAN ranges rounds off to the same value, it has opted to represent the data by averaging the values for TAN and SBS arrangments.

***Critical velocity* (u_c):** Various research groups presented their experimental findings using shear velocity (u_*) or critical shear velocity (u_{*c}) instead of u_c, introducing challenges for comprehensive analysis. However, this ambiguity can be resolved by converting u_{*c} to u_c by using logarithmic formulas (Melville 1997), specifically u_c/u_{*c} = 5.75 log(h/2d_{50})+6.

***Sediment gradation* (σ):** The utilization of σ directly depends on provided data, otherwise, it is determined using relationships such as $(d_{84.1}/d_{15.9})^{1/2} \sim (d_{84}/d_{16})^{1/2}$, ($d_{84}/d_{50}$) and ($d_{50}/d_{16}$) based on available particle diameter information. Literature-specific formulas are applied when accessible for σ determination. In cases of incomplete data but with information on σ (e.g., if researchers report uniform sediment), σ <1.4 is assigned, commonly selected as 1.3 as in the case of Malik and Setia (2014, 2019). Instances where researchers specified σ < 1.2 as in Wang et al. (2016) and Liu et al. (2018) considered σ = 1.19~1.2. The chosen σ range for this research is 1.18 to 1.8, which indicates uniformly graded sediment in all cases.

***Relative density of sediments* (ρ_s/ρ_f):** The provided ρ_s/ρ_f from the literature is used directly. When ρ_s/ρ_f is not explicitly given, it is calculated as ρ_s/ρ_f with ρ_f assuming 998.2 kg/m³ at 20°C if the temperature is unspecified. If both ρ_s and ρ_f are unspecified, a default value of ρ_s/ρ_f = 2.65 is assumed, which indicates coarse sand. Studies lacking clarity on sediment type are excluded.

***Constriction ratio* (d/W):** It is directly utilized if W is specified. Where, flume specifications, especially W, are not provided, W is derived from Q if available otherwise the data points can be excluded.

***Incipient motion condition* (u/u_c):** While values of u/u_c slightly exceed 1 when estimated using the same formulas. However, this magnitude is insufficient for the formation of significant bed forms and subsequent fluctuations in d_s. Based on the observations, bedforms typically begin to develop at u/u_c greater than 1.2–1.3 (Franzetti et al. 2022). In the present study, u/u_c is calculated using the logarithmic formula. It is found that values of u/u_c are slightly higher 1.01 and 1.07 in the case of Malik and Setia (2014) and Das et al. (2014), respectively. There is a lot of variation in the measurements using the shear Reynolds number (R_*) and the critical Shields parameter (Θ_c), making it difficult to compare results from different research groups. The R_* is important because it helps define the flow conditions. In this study, R_* ranges from 2.08 to 54.90. Figure 6.3 shows that almost all the

data collected in this study fall under the clear-water condition. This classification is based on Θ_c, which is calculated using van Rijn's empirical formula with R_*

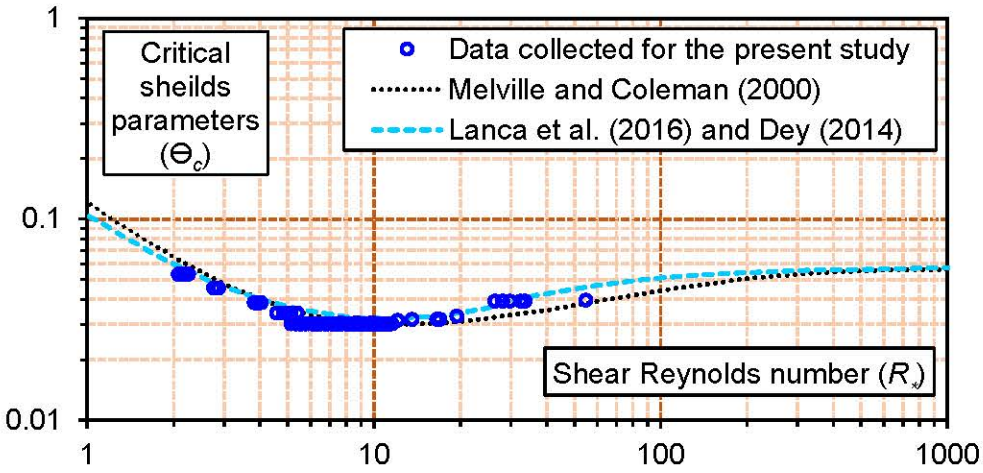

Fig. 6.3. Shields diagram plotted for illustrating incipient motion condition.

Table 6.4 outlines the assumptions made regarding sidewall effects, sediment size, uniformity, and viscosity by various studies, along with the parameter ranges used to evaluate their relevance. The methodology for this study is detailed in Fig. 6.4.

Table 6.4. Flow conditions adopted by different research groups to run their experiments.

Effects	Conditions applied by researchers	References	Ranges of data collected
Negligible sidewall effect	$W/d \geq 6.25$	Raudkivi and Ettema (1983)	4.5–14.3
	$W/d \geq 10$	Chiew and Melville (1987)	
	$W/d \geq 3$	Ballio et al. (2009)	
	$W/d \geq 5$	Lança et al. (2013)	
Negligible sediment size effect	$d/d_{50} > 25$	Breusers and Raudkivi (1991)	28.57–277.78
	$d/d_{50} > 50$	Melville and Chiew (1999)	
	$d/d_{50} \sim 25$–130	Tafarojnoruz et al. (2012)	
Uniform sediment	$\sigma < 1.4$	Dey et al. (1995)	1.18–1.80
Negligible flow viscosity	R>7000	Monti (1994)	9599–55873
Threshold for sediment movement	$u/u_c = 0.4$	Chiew (1995)	0.40–1.07
	$u/u_c = 0.5$	Breusers (1977)	
	$u/u_c = 0.3$	Jones and Sheppard (2000)	
Negligible effect of flow shallowness	$h/d > 3$	Breusers (1977)	1.2–4.0
	$h/d > 1$–3	Ettema (1980)	
	$h/d > 2.6$	Melville and Southerland (1988)	
	$h/d > 4$	Whitehouse (1998)	
	$h/d \geq 4$	Nandi and Das (2023)	

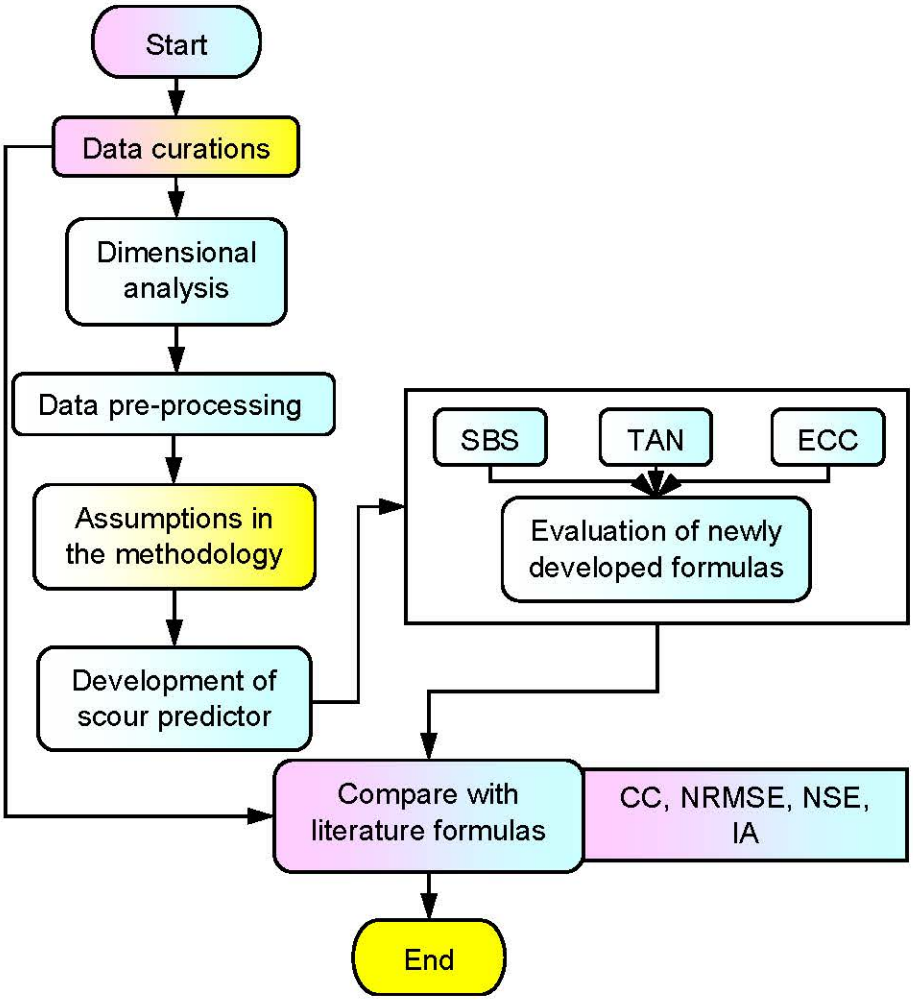

Fig. 6.4. Methodology set to perform the present study.

6.2.4. Statistical performance indicator

This study uses five performance indicators to assess the formula. These are standard deviation (SD), Correlation Coefficient (CC), and Index of Agreement (IA) given in Table 3.5, and Nash-Sutcliffe Efficiency (NSE), Normalized Root Mean Squared Error (NRMSE) (Table 6.5).

Table 6.5. Performance indicators with their pertinent ranges and ideal values.

Performance indicators	Range	Ideal value
$\mathrm{NRMSE} = \dfrac{\sqrt{\frac{1}{N}\sum_{i=1}^{N}\left\{\left(\frac{d_{sm}}{d}\right)_{ci} - \left(\frac{d_{sm}}{d}\right)_{oi}\right\}^2}}{\left(\frac{d_{sm}}{d}\right)_{o}}$	0 to ∞	0

$\mathrm{NSE}=1-\dfrac{\sum_{i=1}^{N}\left\{\left(\frac{d_{sm}}{d}\right)_{oi}-\left(\frac{d_{sm}}{d}\right)_{ci}\right\}^2}{\sum_{i=1}^{N}\left\{\left(\frac{d_{sm}}{d}\right)_{oi}-\overline{\left(\frac{d_{sm}}{d}\right)_{o}}\right\}^2}$	$-\infty$ to 1	0

They measure the variability, the alignment between computed and observed values, the degree of fit, and the overall error in the predictions.

6.3. Results and discussion

6.3.1. Local scour around SBS piers

The assumptions made by various research groups, as given in Table 6.4. The dimensional analysis presented in Eq. (6.2) can be reduced to the simplified form shown in Eq. (6.3). Given the strong correlation between Fr and u/u_c, among them, one parameter can be considered. Furthermore, the effects of the constriction ratio (d/W) and Reynolds number (Re) are disregarded, as indicated by the information in Table 6.4. Furthermore, since σ has a constant value of 1.3, its impact is negligible.

$$\frac{d_{sm}}{d}=f_3\left(\frac{h}{d},\frac{u}{u_c},\frac{d}{d_{50}},\frac{r}{d},\frac{ut}{d}\right) \tag{6.3}$$

In this context, the parameter φ is maintained at a fixed value of 90°, while the variation in Δ is confined to the range of 1.62–1.65, which is approximately constant. As a result, Eq. (6.3) incorporates the essential influential parameters required for estimating d_{sm}. The ranges for further analysis related to SBS piers, to develop the new formula, are detailed in Table 6.5.

Table 6.5. Relevant experimental ranges adopted for SBS, TAN and ECC piers.

References	# *available* /# *taken*	u/u_c	h/d	d/d_{50}	r/d	ut/d
			SBS piers			
Malik and Setia (2020)	9/1	0.94–0.98	3.10–3.50	140.00	1.0–5.0	1.07×10^{6}–1.12×10^{6}
Malik and Setia (2021)	7/7	0.93–0.93	2.57–2.79	269.57	1.0–5.0	7.26×10^{4}–5.08×10^{5}
Devi and Kumar (2022*a*)	24/24	0.75–0.96	2.40–3.26	83.33	1.5–5.0	1.29×10^{5}–1.73×10^{5}
Total	40/32	0.75–0.99	2.57–3.50	83.33–277.78	1.0–5.0	7.26×10^{4}–1.12×10^{6}
			TAN piers			
Das et al. (2014)	4/4	0.90–0.96	1.20	136.99	5.0–7.8	3.69×10^{5}–9.92×10^{5}
Malik and Setia (2014)	8/8	0.97–1.01	2.62–2.68	277.78	1.0–17.0	9.00×10^{4}–9.36×10^{4}
Wang et al. (2016)	126/126	0.40–0.90	2.00–2.50	85.71	1.0–16.0	3.77×10^{4}–8.76×10^{4}

Khaple et al. (2017)	27/13	0.90	1.95–2.667	3.33–85.41	2.0–12.0	5.47×10^5–1.02×10^6
Keshavarzi et al. (2018)	27/21	0.77–0.96	2.09–2.91	64.71	1.0–12.0	1.30×10^6–1.69×10^6
Liu et al. (2018)	79/79	0.40–0.88	4.00	42.86	2.0–16.0	7.81×10^4–1.65×10^5
Malik and Setia (2020)	12/12	0.94–0.99	2.81–3.31	140.00	1.0–17.0	1.07×10^6–1.12×10^6
Malik and Setia (2021)	10/10	0.95–0.96	2.5–2.581	269.565	1.0–17.0	7.40×10^4
Devi and Kumar (2022*b*)	40/9	0.45–0.58	2.4–3.26	28.57	1.5–5.0	1.29×10^5–1.73×10^5
Total	333/268	0.40–1.01	1.20–4.00	3.33–277.78	1.0–16.0	3.77×10^4–1.69×10^6
			ECC piers			
Das et al. (2014)	12/12	0.90–1.07	1.2–1.6	136.99	5.39–6.00	4.60×10^5–5.60×10^5
Das et al. (2016)	5/5	0.78	1.79	95.89	3.46–5.99	1.02×10^6–1.14×10^6
Khaple et al. (2017)	15/15	0.90	2.67	33.33	2.83–11.40	1.02×10^6
Das et al. (2019)	9/9	0.73	1.79	84.85	3.12–5.26	8.24×10^5
Malik and Setia (2020)	9/9	0.96–0.96	2.74–2.86	269.57	1.00–6.00	7.50×10^4
Malik and Setia (2021)	7/0	0.96–0.98	3.10–3.57	140.00	1.00–5.00	1.12×10^6
Total	57/50	0.73–1.07	1.2–3.57	33.33–140.00	1.00–11.40	7.50×10^4–1.14×10^6

Note: # – number of datasets (available/considered for this study)

Equation (6.3) includes five parameters, but the effect of d/d_{50} is excluded in Eq. (6.4). The individual influence of d/d_{50} on estimating d_{sm}, has no such variation and remains constant due to limited variation of the data available in the literature.

The scour function in Eq. (6.4) is formulated as a product of functions corresponding to individual parameters and the ratio d_{sm}/d. This method, which evaluates the separate contributions of various dimensionless parameters, has been widely adopted by researchers (e.g., Melville and Coleman 2000, Franzetti et al. 2022, Nandi and Das 2023). The scour function includes a constant η, with the parameter functions defined in Eqs. (6.5-6.8). These functions are derived through nonlinear curve fitting using data from each parameter while accounting for the combined effects of all other parameter functions on d_{sm}/d.

The effect on both sides of the pier is symmetrical (Breusers and Raudkivi 1991). Hence, the relationship can be expressed using a single formula, as shown below:

$$\frac{d_{m1|2}}{d}=\eta\alpha_1\left(\frac{u}{u_c}\right)\alpha_2\left(\frac{h}{d}\right)\alpha_3\left(\frac{ut}{d}\right)\alpha_4\left(\frac{r}{d}\right) \tag{6.4}$$

where,

$$\alpha_1\left(\frac{u}{u_c}\right)=1-\exp\left\{-\exp\left(0.42+0.50\frac{u}{u_c}\right)\right\} \tag{6.5}$$

and

$$\alpha_2\left(\frac{h}{d}\right)=1-\exp\left\{-2356.68+0.50\left(\frac{h}{d}\right)^{-4.88}\right\} \tag{6.6}$$

and $$\alpha_3\left(\frac{r}{d}\right)=1-\exp\left\{-6.66\left(\frac{r}{d}\right)^{-0.97}\right\} \quad (6.7)$$

and $$\alpha_4\left(\frac{ut}{d}\right)=1-\exp\left\{-0.09\left(\frac{ut}{d}\right)^{-0.30}\right\} \quad (6.8)$$

where all the individual function peak value = 1, and η = 2.06, representing its maximum value of $(d_{sm1|2}/d)_o$.

The trend observed in Fig. 6.5(a) indicates that as u/u_c increases, $d_{sm1|2}/d$ also increases, which align with the physical phenomenon of scour. Similarly, Fig. 6.5(b) shows that h/d influences $d_{sm1|2}/d$.

The most critical parameter is r/d, as $d_{sm1|2}/d$ shows a decreasing trend modeled by a 1-parameter sigmoid function [Fig. 6.5(c)]. Initially, d_{sm} increases due to the larger effective d when r is near zero but decreases rapidly around r=1.5d as pier interference reduces the effects of scour, it keeps declining until r=6d.

For ut/d, an increasing trend in $d_{sm1|2}/d$ can be seen, using a 1-parameter sigmoid function [Fig. 6.5(d)]. The d_{sm} increases with t and stabilizes once equilibrium is reached.

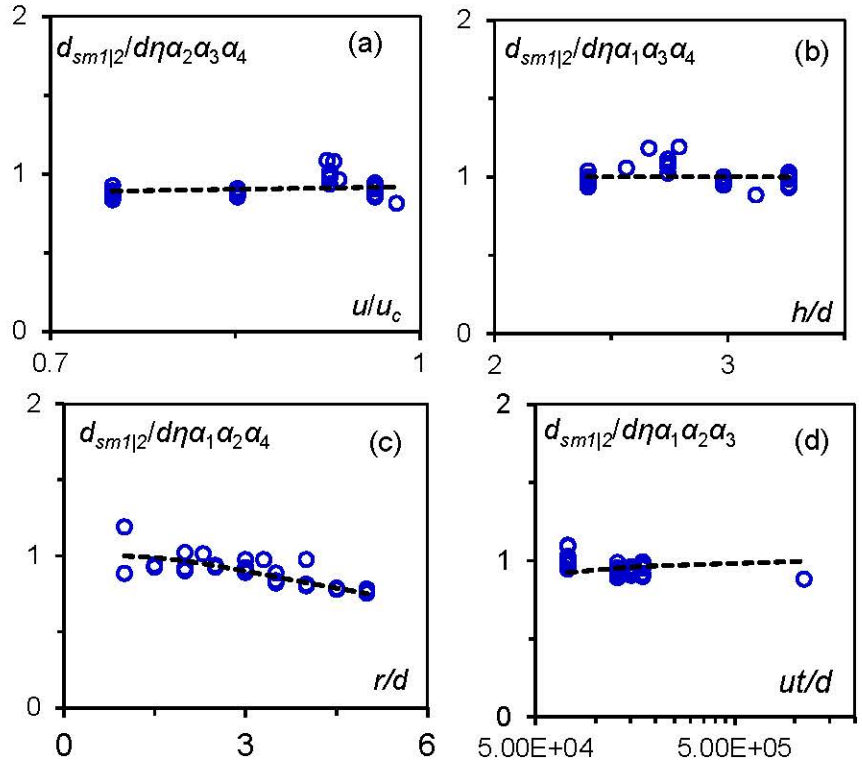

Fig. 6.5. Scour functions (a) $\alpha_1(u/u_c)$, (b) $\alpha_2(h/d)$, (c) $\alpha_3(r/d)$, and (d) $\alpha_4(ut/d)$ for SBS piers. Thick dashed lines represent scour functions

Comparison plot for $(d_{sm1|2}/d)_c$ and $(d_{sm1|2}/d)_o$ from Eq. (6.4) and with the literature formulas shown in Fig. 6.6. It is clear from the figure that this formula shows better results as compared to the other literature formulas from ISO pier (Nandi and Das 2023, Franzetti

et al. 2022, Wang et al. 2016, and Sheppard and Miller 2006) and a dedicated formula for SBS piers developed by Malik and Setia (2020).

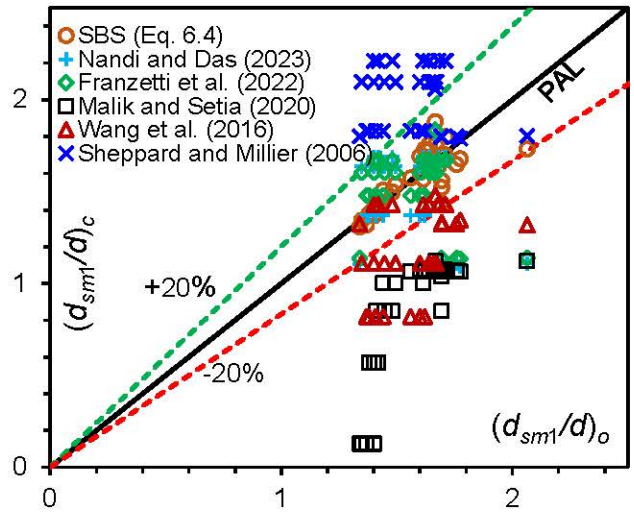

Fig. 6.6. Comparison between measured and computed d_{sm} values for the present study and reference literature.

Table 6.6 shows the performance indicators for the SBS pier arrangement and previous literature. The percentage of datasets within the error band P_{in} the observed versus computed d_{sm} comparison plot.

Table 6.6. Performance indicators for SBS, TAN (Pier-1|2) and ECC piers arrangement.

Pier	Literature	CC	NSE	NRMSE	IA	P_{in} (%)
SBS	Newly developed Eq. (6.4)	0.76	0.53	0.07	0.87	100.00
ISO	Nandi and Das (2023)	-0.27	-3.49	0.21	0.29	75.00
ISO	Franzetti et al. (2022)	-0.33	-2.88	0.20	0.25	81.25
SBS	Malik and Setia (2020)	0.74	-21.41	0.47	0.34	0.00
TAN Pier -1	Wang et al. (2016)	0.36	-7.86	0.30	0.36	34.38
ISO	Sheppard and Miller (2006)	-0.13	-8.28	0.30	0.28	31.25
TAN Pier-1	Newly proposed Eq. (6.10)	0.91	0.83	0.23	0.95	66.79
	Malik and Setia (2020)	0.07	-0.09	0.59	0.36	24.25
	Wang et al. (2016)	0.60	-0.05	0.58	0.77	62.69
TAN Pier-2	Newly proposed Eq. (6.10)	0.83	0.69	0.31	0.90	52.61
	Malik and Setia (2020)	-0.01	-0.11	0.58	0.29	23.88
	Wang et al. (2016)	0.62	-1.89	0.94	0.60	13.43
ECC Pier-1	Newly developed Eq. (6.18)	0.75	0.55	0.25	0.81	68.00
	Das et al. (2016)	0.32	-1.13	0.54	0.50	24.00
	Malik and Setia (2020)	0.41	-0.50	0.45	0.59	48.00
ECC Pier-2	Newly developed Eq. (6.18)	0.65	0.41	0.27	0.74	66.00
	Das et al. (2016)	0.35	-1.19	0.52	0.49	26.00
	Malik and Setia (2020)	0.35	-0.86	0.48	0.56	38.00

Note: - P_{in} (%) = (Number of data within the interval/ number of total data)×100

When comparing the SBS piers, the ISO pier formula performs the poorest. This indicates the need to develop a new formula based on the influential parameter like (r/d). Earlier, Malik and Setia (2020) developed a formula for SBS, which does not agree well with the measured and computed values of $d_{sm1|2}/d$ for this extensive dataset. The highest CC = 0.76, NSE = 0.53, IA= 0.87, and P_{in} = 100% are found for Eq. (6.4). The lowest NRMSE = 0.07 shows the superior performance of Eq. (6.4) than the formulas from other literature (Fig. 6.7).

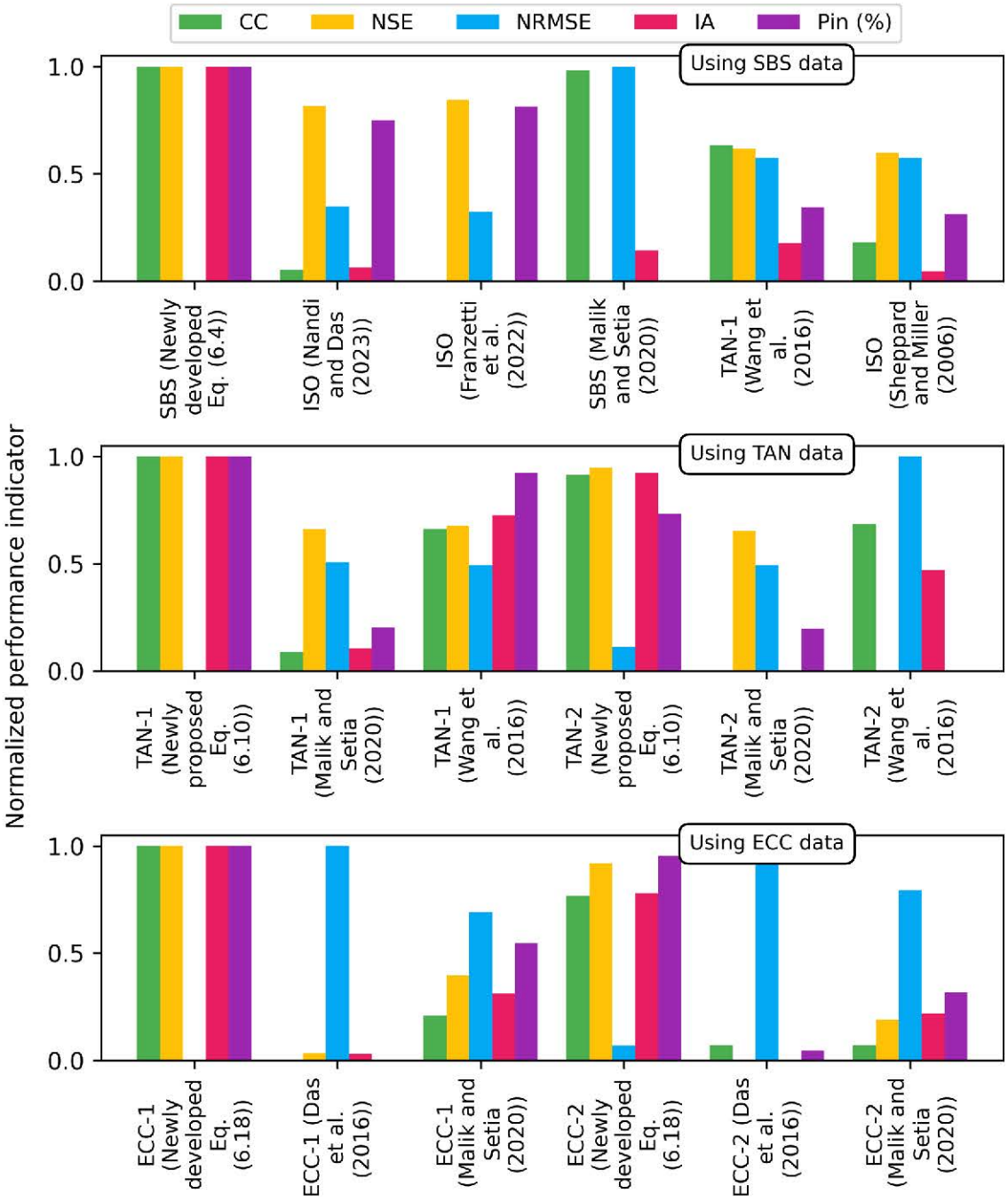

Fig. 6.7. Comparison of performance indicators for the present study and literature formulas using three different sets of data.

The present formula (Eq. 6.4) outperforms Malik and Setia (2020) by 2.7% in terms of CC, which makes it the best formula. The other formulas show negative NSE values. However, Eq. (6.4) gives a positive NSE value, that indicates better goodness of fit. This new formula shows a 65% improvement in NRMSE compared to Franzetti et al. (2022), the best performer. Furthermore, it outperforms Wang et al. (2016) by an impressive 141.7% improvement in IA. Moreover, it contains 23.1% more datasets within the accuracy band compared to Franzetti et al. (2022).

6.3.2. Local scour around TAN piers

The dimensional analysis is given in Eq. (6.2) and can be simplified to Eq. (6.9).

$$\frac{d_m}{d} = f_4\left(\frac{h}{d}, \frac{u}{u_c}, \frac{d}{d_{50}}, \frac{r}{d}, \frac{ut}{d}\right) \tag{6.9}$$

In this analysis, the parameter φ is maintained at a constant value of 0°, while Δ remains within the narrow range of 1.58–1.65, showing a nearly constant value. The σ = 1.18–1.3 from most of the literature data, its influence on the results is negligible. Only four experiments were conducted by Das et al. (2014) with σ = 1.7, the effect of this σ can be neglected when considering the entire dataset. As a result, Eq. (6.10) incorporates the critical parameters required for accurately computing d_{sm}.

The relevant ranges of parameters for further analysis in developing a new formula for SBS piers are provided in Table 6.6. Equation (6.10) considers five normalized scour parameters influencing $d_{sm1|2}$ in TAN arrangements. A dataset of more than 330 data points is collected and, after initial assessment 268 unique datasets are considered for further evaluation. Here, d/d_{50} is a significant parameter affecting scour. The parameter functions are detailed in Eqs. (6.11–6.16).

$$\frac{d_{m1|2}}{d} = \lambda_{1|2}\beta_{1|2}\left(\frac{u}{u_c}\right)\beta_3\left(\frac{h}{d}\right)\beta_4\left(\frac{d}{d_{50}}\right)\beta_5\left(\frac{tu}{d}\right)\beta_6\left(\frac{r}{d}\right) \tag{6.10}$$

where,

$$\beta_1\left(\frac{u}{u_c}\right) = 1 - \exp\left\{-\exp\left(-5.72 + 9.29\frac{u}{u_c}\right)\right\} \tag{6.11}$$

$$\beta_2\left(\frac{u}{u_c}\right) = 1 - \exp\left\{-\exp\left(-5.72 + 9.69\frac{u}{u_c}\right)\right\} \tag{6.12}$$

and

$$\beta_3\left(\frac{h}{d}\right) = 1 - \exp\left\{-2356.68\left(\frac{h}{d}\right)^{-4.88}\right\} \tag{6.13}$$

and

$$\beta_4\left(\frac{d}{d_{50}}\right) = 0.84\left[\left(\frac{d}{d_{50}}\right)^{1.85}\exp\left\{-2.98\left(\frac{d}{d_{50}}\right)^{0.24}\right\} + 0.50\right] \tag{6.14}$$

and
$$\beta_5\left(\frac{tu}{d}\right)=\frac{1.03\left(\frac{tu}{d}\right)}{\left\{31216+\left(\frac{tu}{d}\right)\right\}} \tag{6.15}$$

and
$$\beta_6\left(\frac{r}{d}\right)=0.44+(0.7-0.44)\exp\left\{-0.004\left(\frac{r}{d}-2.84\right)^2\right\} \tag{6.16}$$

where, the peak values of all individual functions are considered equal to 1, and λ_1 = 2.53 and λ_2 = 2.06 which is the maximum value of $(d_{sm1|2}/d)_o$ for TAN Pier-1 and Pier-2 respectively.

An increasing trend of u/u_c is observed as a 2-parameter sigmoid function, with d_{sm1}/d increasing gradually as u/u_c increases. This is due to the increase of intensity of horseshoe vortices as u grows. d_{sm1}/d peaks at u/u_c =1, as shown in Fig. 6.8(a).

Now, for h/d, the effect on d_{sm1}/d is negligible up to h/d ≈3.5, after which a decreasing trend is seen in Fig. 6.8(b). A significant impact of d/d_{50} is observed, with d_{sm1}/d initially increasing up to around 60, and then decreasing and represented by an exponential function, as shown in Fig. 6.8(c).

The ut/d versus d_{sm1}/d relationship shows an increasing trend, represented by the "Michaelis-Menten" function in Fig. 6.8(d). The most influential parameter, r/d, shows an initial increase in d_{sm1}/d up to r/d≈3, followed by a decrease represented using "Bragg formula" [Fig. 6.8(e)].

However, when there is no gap, the upstream scour at Pier-1 looks like that of a single pier. As the spacing increases, a reinforcing effect enhances d_{sm1}/d. Beyond a certain gap, interference effects reduce, resulting in a decrease of d_{sm1}/d , like an ISO pier.

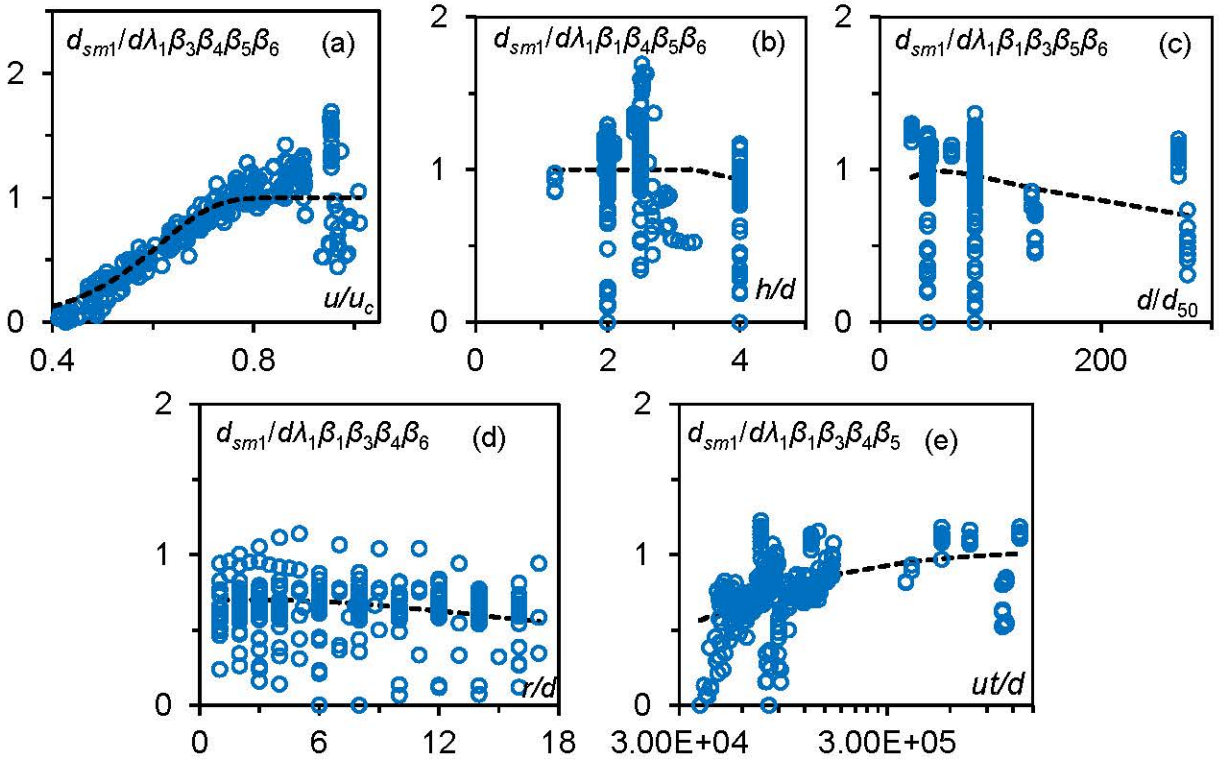

Fig. 6.8. Scour functions **(a)** $\beta_1(u/u_c)$, **(b)** $\beta_2(h/d)$, **(c)** $\beta_3(d/d_{50})$, **(d)** $\beta_4(r/d)$, and **(e)** $\beta_5(ut/d)$ for TAN Pier-1. Thick dashed lines represent the scour function.

A similar trend is observed for all five scour parameter functions for Pier-2, with the primary difference being for the constant parameter for u/u_c function to achieve the best fit, as this is the critical parameter near the upstream of Pier-2 [Fig. 6.9(a)]. As u increases, d_{sm1}/d behaves like that of a single pier, irrespective of the pier spacing. However, for d_{sm2}/d, the relationship between d_{sm} and u is divided into four separate regions based on u_c, a key characteristic of local scour in TAN pier arrangements (Liu et al. 2018).

For Pier-2, only the function of u/u_c changes to predict d_{sm2}/d, while all other parameter functions remain same [Fig. 6.9(b-e)]. The rear pier experiences a sheltering effect from Pier-1, which reduces d_{sm}. However, the overall behavior of d_{sm} for Pier-2 is similar to that of Pier-1, with d_{sm} values is always lower for Pier-2 than Pier-1.

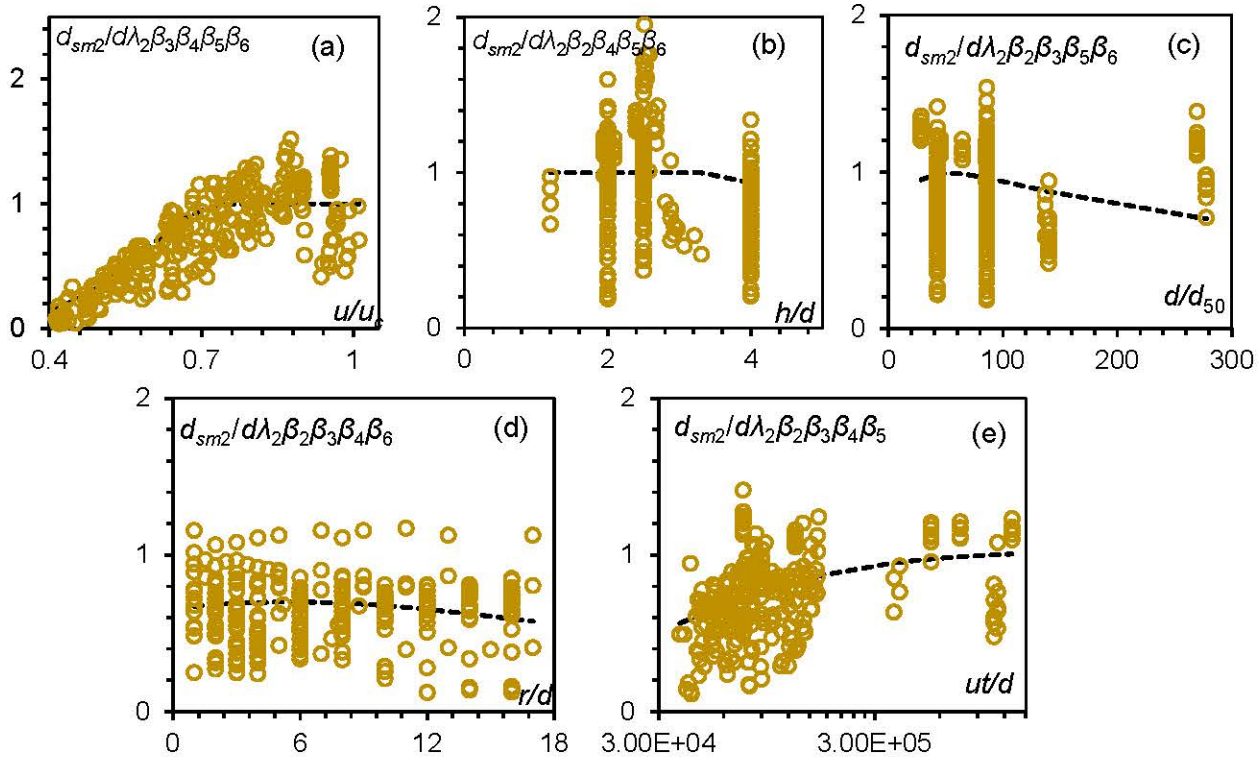

Fig. 6.9. Scour functions **(a)** δ_1 (u/u_c), **(b)** δ_2 (h/d), **(c)** δ_3 (d/d_{50}), **(d)** δ_4 (r/d), and **(e)** δ_5 (ut/d) for TAN pier-2. Thick dashed lines represent the scour functions.

Figure 6.10 shows that present formula is better compared to literature formulas (Eq. 6.10). The formula by Wang et al. (2016) is found in good agreement as shown in Fig. 6.10(c-d). Figure 6.10(e-f) shows that Malik and Setia's (2020) formula has lower agreement but it shows good agreement for selected data sets from where these regression models initially developed.

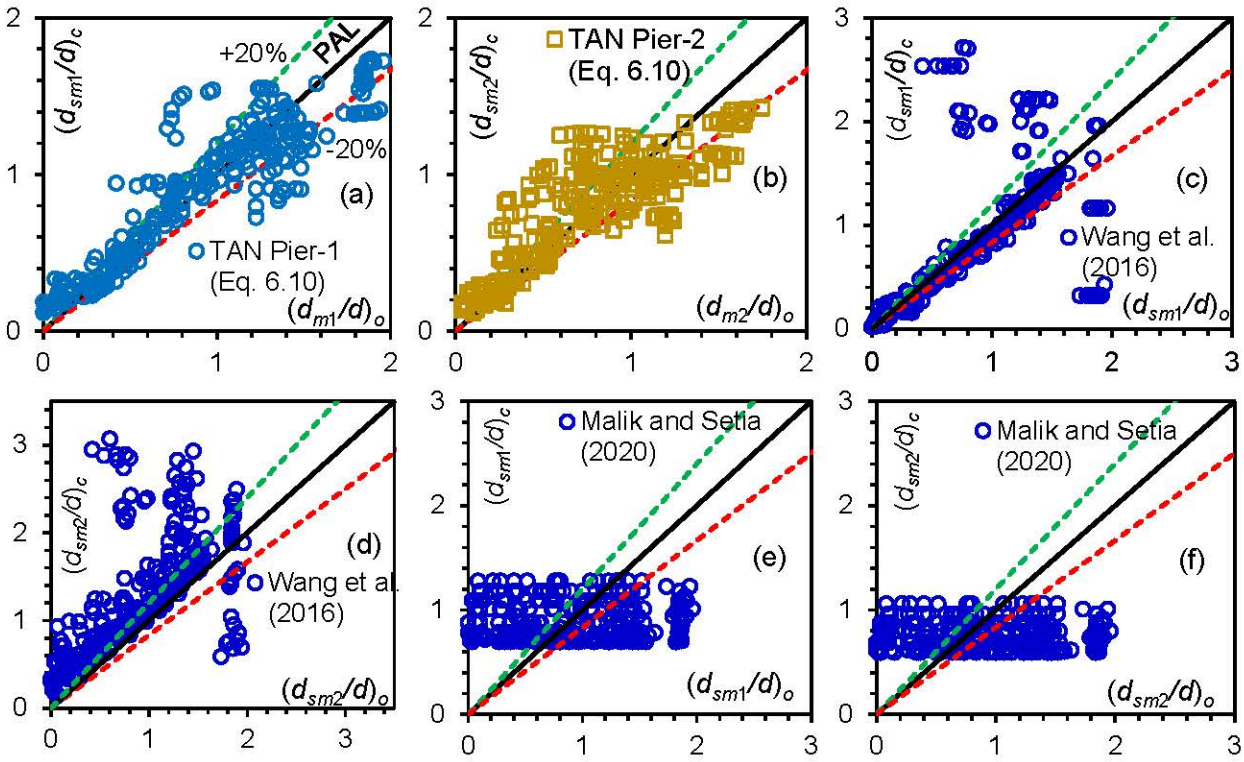

Fig. 6.10. Comparison between measured and computed d_{sm} values for reference literature for TAN **(a, c, e)** Pier-1, and **(b, d, f)** Pier-2.

The performance indicators for TAN pier arrangements are shown in Fig. 6.7, For Pier-1, Eq. (6.10) achieves the highest values of CC = 0.91, NSE = 0.83, and IA = 0.95, showcasing its superior predictive performance. The lowest NRMSE = 0.23 for Pier-1 further emphasizes its accuracy compared to other literature formulas.

For Pier-2, Eq. (6.10) shows the highest values of CC = 0.83, NSE = 0.69, and IA = 0.90. Furthermore, the lowest NRMSE = 0.31 for Pier-2 indicates its strong performance in terms of error minimization relative to other formulas. These results highlight the robustness and reliability of Eq. (6.10) for predicting scour in TAN pier arrangements.

The new formula outperforms the formula by Wang et al. (2016) by 51.7% for Pier-1 and 33.9% for Pier-2 in terms of the CC. Equation (6.10), however, gives a positive NSE close to 1, indicating better goodness of fit for both piers.

Furthermore, the new formula shows significant improvements in NRMSE compared to Malik and Setia (2020), for Pier-1 and Pier-2. It improves NRMSE by 67.9% for Pier-1 and 46.6% for Pier-2. Furthermore, Eq. 6.10 shows a 23.4% and 50% improvement in IA over Wang et al. (2016) for Pier-1 and Pier-2, respectively.

Moreover, Eq. (6.10) includes 6.54% more datasets within the accuracy band compared to Wang et al. (2016) for Pier-1, and 120.3% more datasets within the accuracy band for Malik and Setia (2020) for Pier-2.

6.3.3. Local scour around ECC piers

The dimensional analysis provided in Eq. (6.2) can be simplified to Eq. (6.17) by applying the assumptions adopted by various research groups, as given in Table 6.2.

$$\frac{d_{sm}}{d} = f_3\left(\frac{h}{d}, \frac{u}{u_c}, \frac{d}{d_{50}}, \frac{r}{d}, \frac{ut}{d}, \varphi\right) \tag{6.17}$$

Here, the parameter φ does not remain constant but varies between 11.3° and 74.0°, significantly impacting d_{sm} near the upstream of Pier-2 due to the reinforcement effect, shed vortices, or due to the compressed horseshoe vortex phenomena. The variation is 1.58–1.65, showing almost constant value as for most experiments σ = 1.18–1.8, the influence can be neglected. The relevant ranges for further analysis of SBS piers to develop a new formula are provided in Table 6.4.

Equation (6.18) includes six normalized parameters that influence d_{sm} for Pier-1 and Pier-2 in ECC arrangements. Six parameter functions are used for evaluation, as given in Eqs. (6.19–6.25).

$$\frac{d_{m1|2}}{d} = \xi_{1|2}\gamma_{1|2}\left(\frac{u}{u_c}\right)\gamma_3\left(\frac{h}{d}\right)\gamma_4\left(\frac{d}{d_{50}}\right)\gamma_5\left(\frac{tu}{d}\right)\gamma_6\left(\frac{r}{d}\right)\gamma_7(\varphi) \tag{6.18}$$

$$\gamma_1\left(\frac{u}{u_c}\right) = 1 - \exp\left\{-\exp\left(-7.39 + 10.11\frac{u}{u_c}\right)\right\} \tag{6.19}$$

$$\gamma_2\left(\frac{u}{u_c}\right) = 1 - \exp\left\{-\exp\left(-7.39 + 10.52\frac{u}{u_c}\right)\right\} \tag{6.20}$$

$$\gamma_3\left(\frac{h}{d}\right) = 1 - \exp\left\{-2356.68\left(\frac{h}{d}\right)^{-4.88}\right\} \tag{6.21}$$

$$\gamma_4\left(\frac{d}{d_{50}}\right) = 0.84\left[\left(\frac{d}{d_{50}}\right)^{1.85}\exp\left\{-2.98\left(\frac{d}{d_{50}}\right)^{0.24}\right\} + 0.50\right] \tag{6.22}$$

$$\gamma_5\left(\frac{tu}{d}\right) = \frac{1.05\left(\frac{tu}{d}\right)}{\left\{52335.00 + \left(\frac{tu}{d}\right)\right\}} \tag{6.23}$$

$$\gamma_6\left(\frac{r}{d}\right) = \frac{1.02\left(\frac{r}{d}\right)}{2.05 + \left(\frac{r}{d}\right)} \tag{6.24}$$

$$\gamma_7(\varphi) = 1 - \exp\left\{-2356.68\left(\sin\varphi + \cos\varphi\right)^{-4.88}\right\} \tag{6.25}$$

Here, individual function peak values are considered equal to 1, and $\xi_1 = 2.35$ and $\xi_2 = 2.58$ which are the maximum values of $(d_{sm1|2}/d)_o$ for Pier-1 and Pier-2.

The parameter u/u_c shows an increasing trend represented by the 2-parameter sigmoid function in Fig. 6.11(a). As u/u_c increases, the strength of the downward flow and horseshoe vortex also increases, resulting in a subsequent rise in d_{sm}. The effect of h/d is negligible, as shown in Fig. 6.11(b), due to the small range of datasets within specific h/d values. Initially, the range of d/d_{50} is around 30 to 80, with no clear trend can be seen. However, after 80, a decreasing trend is observed, as shown in Fig. 6.11(c).

The parameter r/d is found to be the most significant to compute d_{sm} for this dataset, showing a continuously increasing trend against the normalized d_s, as shown in Fig. 6.11(d). The parameter ut/d also shows an increasing trend in Fig. 6.11(e). There is no clear trend is seen for φ [Fig. 6.11(f)], due to the limited variation in φ in the dataset.

A similar trend is observed for all six scour parameter functions for Pier-2. The only difference is that the constant parameter is used for u/u_c. This is adjusted to best fit the parameter function, as u/u_c is critical parameter near the upstream of Pier-2, shown in Fig. 6.12(a). The parameter functions are presented for d_{sm2}/d in Figs. 6.12(b-f) for all the other parameters.

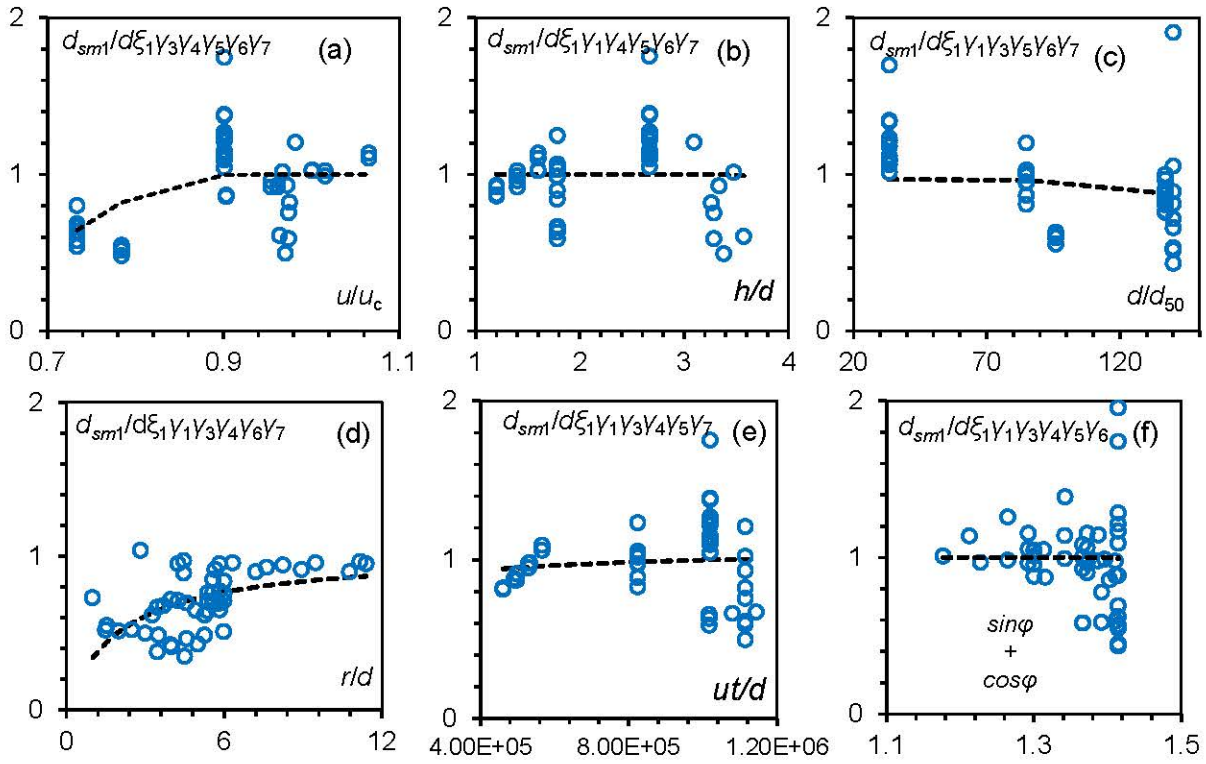

Fig. 6.11. Scour functions **(a)** $\gamma_1(u/u_c)$, **(b)** $\gamma_3(h/d)$, **(c)** $\gamma_4(d/d_{50})$, **(d)** $\gamma_5(r/d)$, **(e)** $\gamma_6(tv/d)$, and **(f)** $\gamma_7(\varphi)$ for ECC Pier-1. Thick dashed lines represent scour functions.

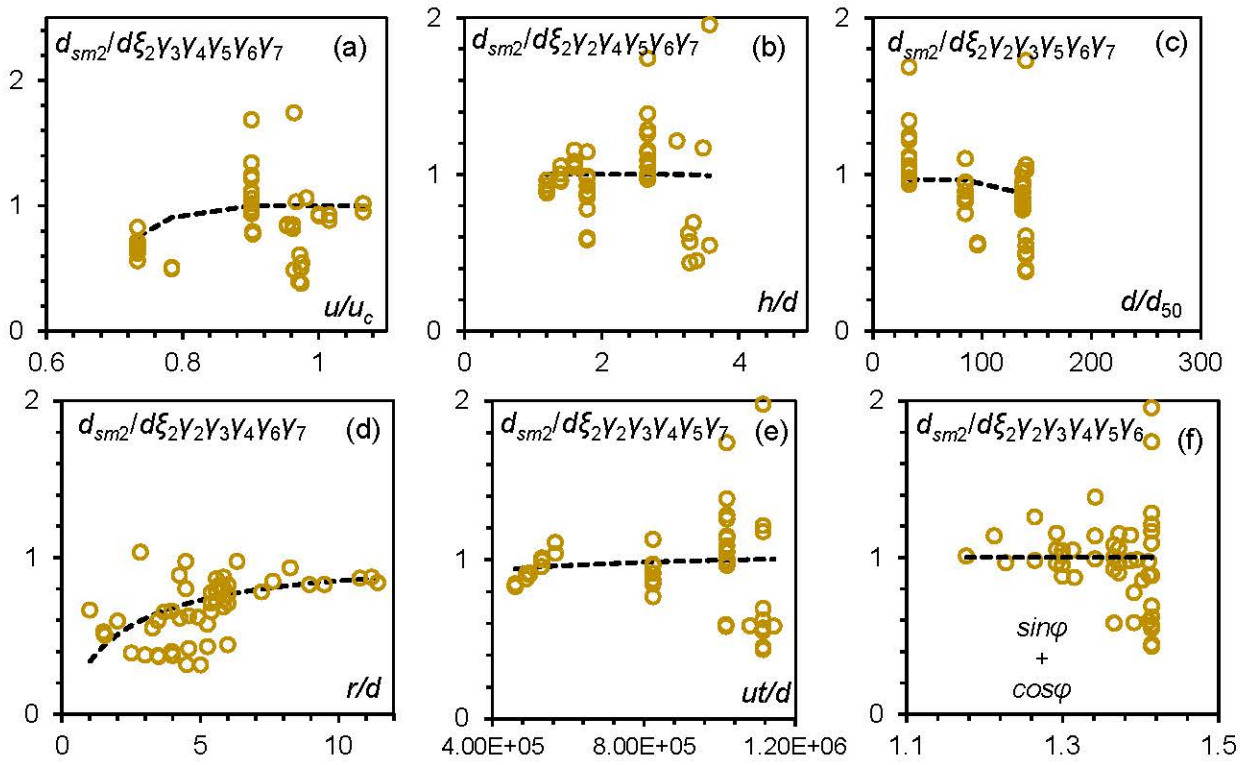

Fig. 6.12. Scour functions **(a)** $\gamma_2(u/u_c)$, **(b)** $\gamma_3(h/d)$, **(c)** $\gamma_4(d/d_{50})$, **(d)** $\gamma_5(r/d)$, **(e)** $\gamma_6(tv/d)$, and **(f)** $\gamma_7(\varphi)$ for ECC Pier-2. Thick dashed lines represent scour functions.

From Figs 6.13(a-b) it is clearly seen that the present formula outperforms the literature formulas. The formulas from Das et al. (2016) and Malik and Setia (2020) show good agreement only with selective datasets used to develop the regression models, highlighting that the new formula provides more consistent and superior results across a broader dataset.

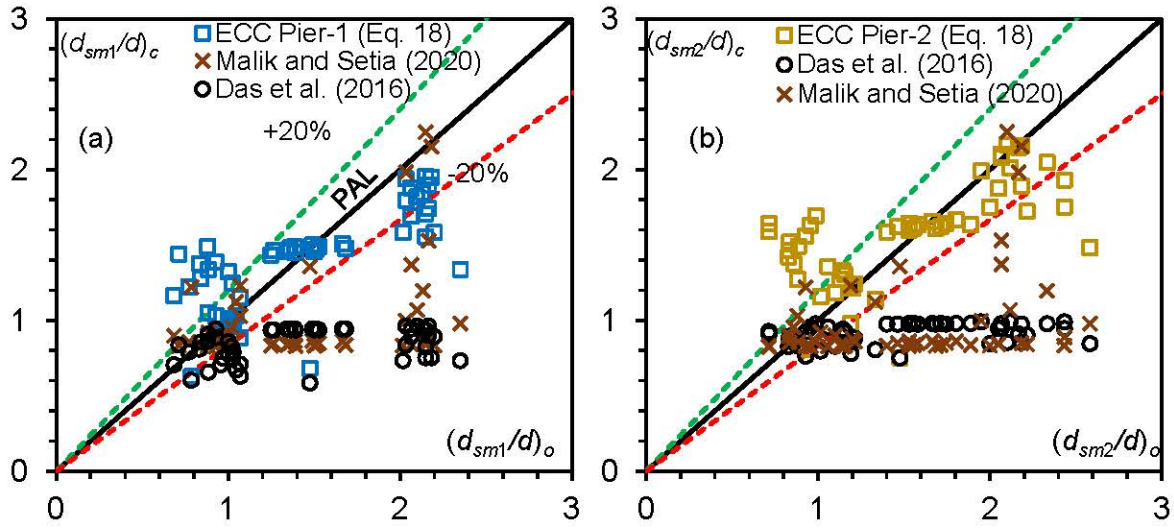

Fig. 6.13. Comparison between measured and computed d_{sm} values near ECC arrangements for the present study and with reference literature **(a)** Pier-1, and **(b)** Pier-2.

It is observed that the present formula (Eq. 6.18) performs better across all performance indicators. For Pier-1 in the ECC arrangement, the highest values of CC = 0.75, NSE = 0.55, and IA = 0.81 are found for Eq. (6.18), along with the lowest NRMSE = 0.25. For Pier-2, the highest values of CC = 0.65, NSE = 0.41, and IA = 0.56, with the lowest NRMSE = 0.27, again showing better results than the literature (Fig. 6.7).

The newly proposed Eq. (6.18) outperforms Malik and Setia (2020) by approximately 85.8% in terms of CC, making it the most successful. The other formulas, except for Eq. (6.18), result in negative NSE values and show lower results. Equation (6.10) shows a good improvement in NRMSE, with 44.4% and 43.8% compared to Malik and Setia (2020) for Pier-1 and Pier-2, respectively. Furthermore, the formula (Eq. 6.18) shows an impressive 37.8% and 34.1% improvement in IA for Pier-1 and Pier-2, respectively. Furthermore, it includes 41.7% and 73.7% more datasets within the accuracy band compared to Malik and Setia (2020) for Pier-1 and Pier-2, respectively.

However, for the TAN arrangement, the front pier reaches the highest accuracy, with CC = 0.91, NSE = 0.83, NRMSE = 0.23, and IA = 0.95. On the other hand, Pier-2 in the ECC arrangement shows the lowest accuracy, with CC = 0.65, NSE = 0.41, NRMSE = 0.27, and IA = 0.74 (Fig. 6.14). The limited availability of data significantly impacts the accuracy of the d_{sm} formula in SBS and ECC arrangements.

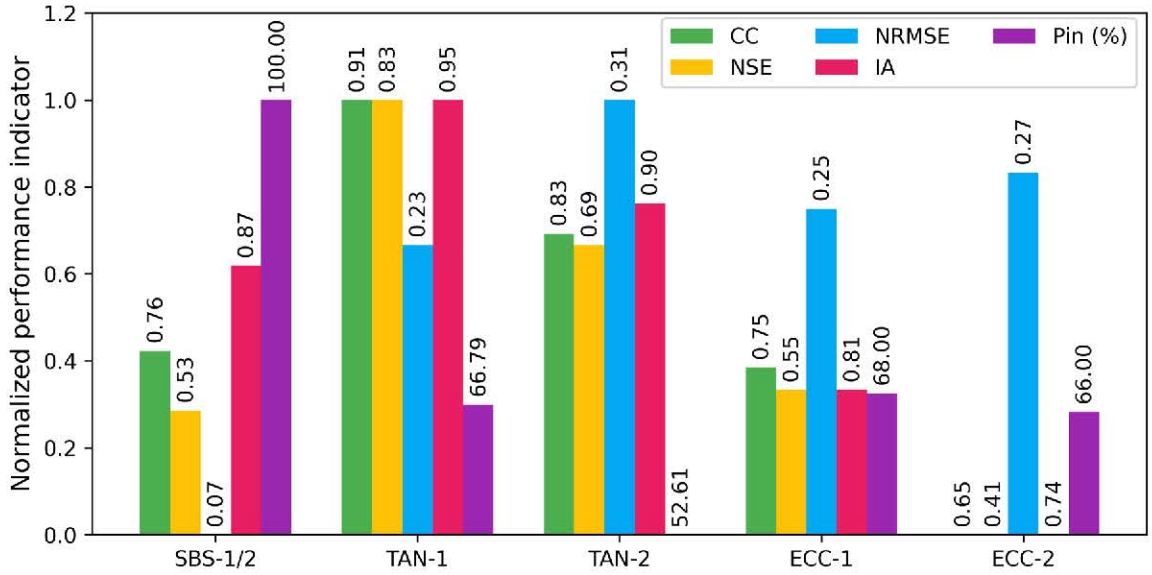

Fig. 6.14. Comparison of performance indicators for three types of twin pier arrangements.

6.3.4. Overall discussion

The dynamics of flow, especially the contracted flow and the interference of horseshoe vortices referred to as the "compressed horseshoe vortex" phenomenon, is crucial in determining and changing d_s between two piers placed in SBS. When piers are positioned perpendicular to the flow in a SBS arrangement, each pier creates horseshoe vortices, which can merge when the spacing between them is very small. Reducing the space between the piers compresses the inner parts of these vortices, increasing their u and resulting in deeper

d_s, as shown in this study (Hannah 1978, Hosseini and Amini 2015). The effective diameter (Breusers and Raudkivi 1991, Salim and Jones 1996) also plays an important role in increasing d_s. These flow patterns are significantly different from those around ISO piers. To improve the accuracy of predicting d_s around SBS piers, this study adds a pier spacing factor. This factor accounts for the unique flow characteristics of SBS configurations, improving the accuracy of d_s predictions.

In TAN pier arrangements, flow dynamics are affected by additional factors such as reinforcement and sheltering (Khaple et al. 2017, Das et al. 2019). When the rear pier is close to the front pier, their scour hole merges, increasing d_s around Pier-1, a phenomenon called reinforcement (Raudkivi 1991). Reverse flow is generally seen between the piers, except near the bed in front of Pier-2, where u decreases due to the sheltering effect of Pier-1. Behind Pier-2, a narrow downflow area and recirculation zone may form, with a smaller and weaker wake compared to Pier-1. The d_s around Pier-1 is influenced by downflow and horseshoe vortices, while for Pier-2, sediment transport, and upstream sheltering are more important (Devi and Kumar 2022*b*). Initially, d_s may rise quickly due to sediment transport and sheltering effects, then decrease as sediment from upstream fills the scour holes, before increasing again. These fluctuations in d_s are a result of the sheltering effect around both piers. To address these issues, the study introduces the pier spacing factor to simulate the sheltering effect, allowing for more accurate d_{sm} predictions in the developed formula.

The sheltering effect occurs as the front pier reduces flow near Pier-2. This effect is particularly strong when φ is small or near zero, which can reduce d_s (Wang et al. 2016, Liu et al. 2018). However, as φ increases and the r widens, the interaction between the wake vortices of the front pier and the horseshoe vortices, along with the downflow from Pier-2, strengthens, leading to an increase in d_s at the upstream face of Pier-2. However, if the pier spacing is increased further, the piers may behave independently, and neither sheltering nor reinforcement will have a major effect on d_s. The d_{sm} at Pier-2 may exceed that of Pier-1, and the d_s at Pier-1 may also exceed that of an ISO pier under the same conditions. This can be attributed to the reinforcing effect of scouring. Furthermore, the arrangement of the piers and the interaction between the horseshoe vortices of the rear pier and the wake vortices of the front pier likely contribute to the increased d_s at ECC rear piers.

A limitation of this study is the lack of sufficient data for various pier arrangements, and other limitations are discussed below. The total dataset includes 350 calibrated data points, with 30 and 50 relevant to SBS and ECC pier combinations, respectively, while the rest are for TAN arrangements. The limited dataset available in the literature is used to develop the formulas to the best of our knowledge. All preprocessed data are used to derive formulas for each arrangement. However, separate calibration and validation sets could improve prediction accuracy.

The correlation analysis shows that u/u_c is the most important predictor, with a positive correlation of around 80%, leading to clearer trends and less scatter in the data. For other predictors, low correlations indicate more scatter, which shows that these variables contribute less to predicting d_s, and may not align well with the central trend of the data.

Although the choice of the appropriate formula for calculating u_c has been discussed in previous studies for both single and twin piers, we have used the widely accepted Melville (1997) logarithmic formula for consistency, which could be a limitation.

There is a lack of comprehensive studies on the effects of ECC spacing between piers, this gap in the literature of this review can be an important area for future research. Future research could explore scour mechanisms in complex pier arrangements to better understand the interference effects between adjacent piers, the influence of neighboring piers, and the impact of flow patterns on d_{st}. Field and live-bed data from flume studies can help develop more robust formulas for computing d_s. Understanding the spacing for d_{sm} in each scenario can provide useful insights for creating guidelines on the maximum and minimum d_s related to pier positions. These guidelines can help designers and engineers strategically place piers in areas of minimum scour, improving the durability and lifespan of bridges. While considerable attention has been given to pier spacing in SBS and TAN arrangements, research on longitudinal and ECC gaps in ECC pier arrangements is still limited.

6.4. Conclusions

The rapid growth of urban areas generates more traffic which requires new bridges near the existing ones. This leads to different bridge designs like side-by-side, tandem, and eccentric piers. To analyze the interference effect in such cases, the data collected is grouped into these three types, and formulas are developed to estimate scour. Different statistical methods are used to test how well these formulas work. The study led to the following conclusions:

- The proposed formula for side-by-side piers achieves a maximum scour function value of 2.06, influenced mainly by flow intensity (u/u_c), flow shallowness (h/d), pier spacing (r/d), and dimensionless time (ut/d). This formula outperforms the existing formulas based on performance indicators.
- For tandem and eccentric pier arrangements, different hydraulic parameters, especially centre-to-centre pier spacing (r) help to predict d_{sm}, assessing the *reinforcing* and *sheltering* effect. The Pier-1 and Pier-2 d_{sm} differ due to interference and sheltering effects, two separate formulas for each pier have been established.
- Proposed formulas for tandem piers achieved maximum scour function values of 2.53 for Pier-1 and 2.06 for Pier-2. Key factors for tandem piers include u/u_c, h/d, sediment coarseness (d/d_{50}), r/d, and ut/d. The developed formula shows better results than the formulas reported in the literature.
- In the case of eccentric piers, the newly developed formula has maximum scour function values of 2.35 for Pier-1 and 2.58 for Pier-2. Key influential parameters are u/u_c, h/d, d/d_{50}, r/d, flow skew angle (φ) and ut/d. This formula shows better results in terms of performance indicators.
- The performance was measured as a percentage of the experimental data within a ± 20% error band. In the side-by-side, tandem, and eccentric cases, 100%, more than 50%, and more than 65% of the data fell within this band, respectively. In the statistical evaluation of parameters, the highest accuracy is attained for the tandem front pier, while the eccentric rear pier showed the lowest accuracy. Limited data affects the accuracy of the maximum d_s formulas for side-by-side and eccentric configurations.

This study improves d_s prediction for different pier arrangements (side-by-side, tandem and eccentric), helping engineers design safer bridges. It applies a pier spacing factor to make

the calculation more accurate. The findings can guide better pier placement, which can reduce scour risks and may increase the durability of the bridge pier.

References

Ataie-Ashtiani, B., and Aslani-Kordkandi, A. (2012). Flow field around side-by-side piers with and without a scour hole. *European Journal of Mechanics-B/Fluids, 36*, 152–166.

Ataie-Ashtiani, B., and Aslani-Kordkandi, A. (2013). Flow field around single, tandem piers. *Flow Turbulence and Combustion, 90*, 471–490.

Ballio, F., Teruzzi, A., and Radice, A. (2009). Constriction effects in clear-water scour at abutments. *Journal of Hydraulic Engineering, 135*(2), 140–145.

Beg, M., and Beg, S. (2015). Scour hole characteristics of two unequal size bridge piers in tandem arrangement. *ISH Journal of Hydraulic Engineering, 21*(1), 85–96.

Breusers, H. N. C., and Raudkivi, A. J. (1991). *Scouring*. Hydraulic Structures Design Manual 723 Series, Vol. 2. Rotterdam: Balkema.

Breusers, H. N. C., Nicollet, G., and Shen, H. W. (1977). Local scour around cylindrical pier. *Journal of Hydraulic Research, 15*(3), 211–252.

Chiew, Y. M. (1995). Mechanics of riprap failure at bridge piers. *Journal of Hydraulic Engineering, 121*(9), 635–643.

Chiew, Y. M., and Melville, B. W. (1987). Local scour around bridge piers. *Journal of Hydraulic Research, 25*(1), 15–26.

Choi, S. U., and Choi, S. (2022). Prediction of local scour around bridge piers in the cohesive bed using support vector machines. *KSCE Journal of Civil Engineering, 26*(5), 2174–2182.

Coleman, S. E. (2005). Clearwater local scour at complex piers. *Journal of Hydraulic Engineering, 131*(4), 330–334.

Das, R., Das, S., Jaman, H., and Mazumdar, A. (2019). Impact of upstream bridge pier on the scouring around adjacent downstream bridge pier. *Arabian Journal for Science and Engineering, 44*, 4359–4372.

Das, R., Khwairakpam, P., Das, S., and Mazumdar, A. (2014). Clear water local scour around eccentric multiple piers to shift the line of sediment deposition. *Asian Journal of Water, Environment and Pollution, 11*(3), 47–54

Das, S., and Mazumdar, A. (2015). Turbulence flow field around two eccentric circular piers in scour hole. *International Journal of River Basin Management, 13*(3), 343–361.

Das, S., Das, R., and Mazumdar, A. (2016). Comparison of local scour characteristics around two eccentric piers of different shapes. *Arabian Journal for Science and Engineering, 41*, 1199–1213.

Devi, G., and Kumar, M. (2022*a*). Characteristics assessment of local scour encircling twin bridge piers positioned side by side (SbS). *Sādhanā, 47*(3), 109.

Devi, G., and Kumar, M. (2022*b*). Experimental study of the local scour around the two piers in the tandem arrangement using ultrasonic ranging transducers. *Ocean Engineering, 266*, 112838.

Dey, S., Bose, S. K., and Sastry, G. L. (1995). Clear water scour at circular piers: a model. *Journal of Hydraulic Engineering, 121*(12), 869–876.

Ettema, R. (1980). *Scour at bridge piers*. Ph.D. thesis, Department of Civil Engineering, University of Auckland.

Franzetti, S., Radice, A., Rebai, D., and Ballio, F. (2022). Clear water scour at circular piers: a new formula fitting laboratory data with less than 25% deviation. *Journal of Hydraulic Engineering, 148*(10), 04022021.

Garg, V., Setia, B., Singh, V., and Kumar, A. (2022). Scour protection around bridge pier and two-piers-in-tandem arrangement. *ISH Journal of Hydraulic Engineering, 28*(3), 251–263.

Hamidi, A., and Siadatmousavi, S. M. (2018). Numerical simulation of scour and flow field for different arrangements of two piers using SSIIM model. *Ain Shams Engineering Journal, 9*(4), 2415–2426.

Hannah, C. R. (1978). *Scour at pile groups*. Research Report No. 28–3, Civil Engineering Dept., University of Canterbury, Christchurch, New Zealand.

Hosseini, R., and Amini, A. (2015). Scour depth estimation methods around pile groups. *KSCE Journal of Civil Engineering, 19*, 2144–2156.

Jaman, H., Das, S., Das, R., and Mazumdar, A. (2017). Hydrodynamics of flow obstructed by inline and eccentrically-arranged circular piers on a horizontal bed surface. *Journal of The Institution of Engineers (India): Series A, 98*, 77-83.

Jones, J. S., and Sheppard, D. M. (2000). Local scour at complex pier geometries. In *Building Partnerships*, Joint Conference on Water Resource Engineering and Water Resources Planning and Management 2000. ASCE. Minnesota, United States. 1-9.

Keshavarzi, A., Shrestha, C. K., Melville, B., Khabbaz, H., Ranjbar-Zahedani, M., and Ball, J. (2018). Estimation of maximum scour depths at upstream of front and rear piers for two in-line circular columns. *Environmental Fluid Mechanics, 18*, 537–550.

Khaple, S., Hanmaiahgari, P. R., Gaudio, R., and Dey, S. (2017). Interference of an upstream pier on local scour at downstream piers. *Acta Geophysica, 65*, 29–46.

Kumar, S., Goyal, M. K., Deshpande, V., and Agarwal, M. (2023). Estimation of time dependent scour depth around circular bridge piers: Application of ensemble machine learning methods. *Ocean Engineering, 270*, 113611.

Lança, R. M., Fael, C. S., Maia, R. J., Pêgo, J. P., and Cardoso, A. H. (2013). Clear-water scour at comparatively large cylindrical piers. *Journal of Hydraulic Engineering, 139*(11), 1117–1125.

Liu, Q. S., Tang, H. W., Wang, H., and Xiao, J. F. (2018). Critical velocities for local scour around twin piers in tandem. *Journal of Hydrodynamics, 30*, 1165–1173.

Malik, R., and Setia, B. (2014). Experimental study on behaviour of closely placed bridge pier models. In Proceedings of the National Conference on Current Advances in Hydraulic and Hydropower Engineering and Water Conservation (CAHHEWC-2013), Kurukshetra, India.

Malik, R., and Setia, B. (2020). Interference between pier models and its effects on scour depth. *SN Applied Sciences, 2*, 68.

Malik, R., and Setia, B. (2021). Local scour around closely placed bridge piers. *ISH Journal of Hydraulic Engineering, 27*(4), 396–403.

Melville, B. W. (1997). Pier and abutment scour: Integrated approach. *Journal of Hydraulic Engineering, 123*(2), 125–136.

Melville, B. W., and Chiew, Y. M. (1999). Time scale for local scour at bridge piers. *Journal of Hydraulic Engineering, 125*(1), 59–65.

Melville, B. W., and Coleman, S. E. (2000). *Bridge scour*. Highlands Ranch, CO: Water Resources Publications.

Melville, B. W., and Sutherland, A. J. (1988). Design method for local scour at bridge piers. *Journal of Hydraulic Engineering, 114*(10), 1210–1226.

Memar, S., Zounemat-Kermani, M., Beheshti, A., Rahimpour, M., Cesare, G. D., and Schleiss, A. J. (2020). Influence of collars on reduction in scour depth at two piers in a tandem configuration. *Acta Geophysica, 68*, 229–242.

Monti, R. (1994). Indagine sperimentale delle caratteristiche fluidodinamiche del campo di moto intorno ad una pila circolare. Tesi di Dottorato di Ricerca. Politecnico di Milano, Milan, Italy (in Italian).

Movahedi, N., Dehghani, A. A., Zahiri, A. R., Aarabi, M. J., and Esmaeili, T. (2013). Reduction of local scour around side-by-side piers using bed sill. In: 12th Int. Symp. on River Sedimentation 2013.

Namaee, M. R., and Sui, J. (2020). Velocity profiles and turbulence intensities around side-by-side bridge piers under ice-covered flow condition. *Journal of Hydrology and Hydromechanics, 68*(1), 70–82.

Namaee, M., and Sui, J. (2019). Local scour around two side-by-side cylindrical bridge piers under ice-covered conditions. *International Journal of Sediment Research, 34*(4), 355–367.

Nandi, B., and Das, S. (2023). Identify most promising temporal scour depth formula for circular piers proposed over last six decades. *Ocean Engineering, 286*(2), 115639.

Nandi, B., and Das, S. (2024). Equation for time-dependent local scour at pier-like structures with eccentric in-line arrangements. In Proceedings of the Institution of Civil Engineers-Water Management, *177*(6), 361–374.

Nandi, B., Patel, G., and Das, S. (2024). Prediction of maximum scour depth at clear water conditions: Multivariate and robust comparative analysis between empirical formulas and machine learning approaches using extensive reference metadata. *Journal of Environmental Management, 354*, 120349.

Oliveto, G., and Hager, W. H. (2002). Temporal evolution of clear-water pier and abutment scour. *Journal of Hydraulic Engineering, 128*(9), 811–820.

Pandey, M., Karbasi, M., Jamei, M., Malik, A., and Pu, J. H. (2023). A comprehensive experimental and computational investigation on estimation of scour depth at bridge abutment: Emerging ensemble intelligent systems. *Water Resources Management, 37*(9), 3745–3767.

Qi, W. G., Li, Y. X., Xu, K., and Gao, F. P. (2019). Physical modelling of local scour at twin piles under combined waves and current. *Coastal Engineering, 143*, 63–75.

Raudkivi, A. J. (1998). *Loose Boundary Hydraulics*. Rotterdam, Netherlands: A. A. Balkema.

Raudkivi, A. J., and Ettema, R. (1983). Clear-water scour at cylindrical piers. *Journal of Hydraulic Engineering, 109*(3), 338–350.

Salim, M., and Jones, J. S. (1996). Scour around exposed pile foundations. *North American Water and Environment Congress*, 2202–2211. Anaheim, CA: ASCE.

Sheppard, D. M., and Miller, J. W. (2006). Live-bed local pier scour experiments. *Journal of Hydraulic Engineering, 132*(7), 635–642.

Tafarojnoruz, A., Gaudio, R., and Calomino, F. (2012). Evaluation of flow-altering countermeasures against bridge pier scour. *Journal of Hydraulic Engineering, 138*(3), 297–305.

Tang, H., Liu, Q., Zhou, J., Guan, D., Yuan, S., Tang, L., and Zhang, H. (2023). Process-based design method for pier local scour depth under clear-water condition. *Journal of Hydraulic Engineering, 149*(12), 06023009.

Wang, C., Yu, X., and Liang, F. (2017). A review of bridge scour: Mechanism, estimation, monitoring and countermeasures. *Natural Hazards, 87*, 1881–1906.

Wang, H., Tang, H., Liu, Q., and Wang, Y. (2016). Local scouring around twin bridge piers in open-channel flows. *Journal of Hydraulic Engineering, 142*(9), 06016008.

Whitehouse, R. (1998). *Scour at marine structures: A manual for practical applications.* Thomas Telford.

Yilmaz, M., Yanmaz, A. M., and Koken, M. (2017). Clear-water scour evolution at dual bridge piers. *Canadian Journal of Civil Engineering, 44*(4), 298–307.

Chapter 7

Maximum Scour around Two Piers: Machine Learning Approach

7.1. Introduction

Scouring at bridge piers occurs when changes in flow patterns increase local shear stress, causing sediment particles from the riverbed to be displaced. This erosion around bridge piers is a threat to bridge stability, with flood-induced scour accounting for 53% of bridge failures (Wardhana and Hadipriono 2003). The development of scour holes and the relationship between scour depth (d_s) and flow velocity (u) depend on the scour either clear-water or live-bed scour (Chabert and Engeldinger 1956). Understanding the flow patterns and structures around piers is essential to understanding how scour develops (Das et al. 2013). Local scour around multiple piers, along with flow patterns such as reinforcement, sheltering, and vortices, play a key role in determining d_s (Hannah 1978, Ataie-Ashtiani and Beheshti 2013, Das et al. 2016).

Recent studies have applied machine learning (ML) techniques to predict d_s near hydraulic structures like bridge pier groups (Bateni et al. 2007). Lee et al. (2008) employed Back-Propagation Neural Networks (BPN) for bridge piers. Firat and Gungor (2009) applied Generalized Regression Neural Networks (GRNN) for circular piers. Guven et al. (2009) used linear genetic programming (LGP) for circular piers. Firat (2009) and Akib et al. (2014) developed an Adaptive Neuro-Fuzzy Inference System (ANFIS) for circular piers. Pal et al. (2012) estimated d_s using an M5 model tree. Cheng et al. (2014) introduced the Evolutionary Radial Basis Function Neural Network (ERBFNN). Choi et al. (2017) used ANFIS to estimate d_s. Ebtehaj et al. (2019) applied Extreme Learning Machines (ELM) while Choi and Choi (2022) used Support Vector Machines (SVMs) to estimate d_s. Kumar et al. (2023) predicted time-varying d_s with the ensemble and standalone ML methods like Bagging Regressor (BR), AdaBoost Regressor (ABR), and Support Vector Regression (SVR). Eini et al. (2023) used hybrid ML methods, including XGBoost, for predicting d_s near isolated piers and employed Shapley additive explanations (SHAP) to evaluate contributing parameters. Nandi et al. (2024) combined the Bagging Regression Tree (BRT) and Stochastic Gradient Boosting (SGB) to analyze isolated pier d_s, comparing these ML mdoels with six existing formulas.

Malik and Setia (2020*b*) used ML techniques, including M5 and ANN regression models, to predict d_s around tandem piers. Hannah (1978) studied d_s at cylindrical pier groups. The side-by-side pier research focused on flow dynamics (Ataie-Ashtiani and Aslani-Kordkandi 2013, Namaee and Sui 2019, Sahu et al. 2023). Computational fluid

dynamics (CFD) simulations are now commonly used to study scour patterns around pier groups (Bordbar et al. 2022, Puspasari and Tang 2023). Hamidi and Siadatmousavi (2018) and Ahmad et al. (2018) conducted recent numerical studies on side-by-side piers. The effects of sheltering and reinforcing in tandem pier arrangements were explored by researchers like Kim et al. (2014), Amini and Parto (2017), and Okhravi et al. (2023). Liang et al. (2017) conducted flume experiments on scour around pier groups, testing different arrangements like single, tandem, and side-by-side piers. Devi and Kumar (2022*a*) developed and compared formulas for maximum d_s (d_{sm}) around twin piers. Studies on tandem piers analyzed mutual interference effects (Beg and Beg 2015, Wang et al. 2016, Liu 2018), spacing effects on scour (Keshavarzi et al. 2018), and collar size impact on d_s (Memar et al. 2020). Yilmaz et al. (2017) and Devi and Kumar (2022*b*) explored the temporal d_s (d_{st}) around tandem piers. Research on eccentric multiple piers focused on sediment deposition and interference effects (Das et al. 2014, 2016). Studies on turbulent flow around multiple identical piers were done by Das and Mazumdar (2015), Jaman et al. (2017), and Das et al. (2019). Khaple et al. (2017) examined upstream interference effects on downstream pier scour, while Qi et al. (2019) modeled scour around twin piers under waves and currents. Nandi and Das (2024) validated experimental studies on various pier shapes and eccentric tandem arrangements using literature data and formulas.

While significant research has been conducted on scour around single piers, the understanding of scour around pier groups, especially in side-by-side, tandem, and eccentric arrangements, is still limited. Existing d_s formulas for multiple piers, mainly developed through regression analysis for individual pier arrangements, often fail to account for the nonlinearities in data across different flow conditions and various influencing parameters. Pier arrangements like side-by-side, tandem, and eccentric configurations have been studied through experimental, numerical, and CFD simulations. However, there is a lack of ML models for predicting d_s around two-pier groups. Therefore, this study proposes a robust model for predicting d_s that integrates multiple pier arrangements into a unified method. Two ensemble methods, Random Forest (RF) and Extreme Gradient Boosting (XGBoost), which use bagging and boosting algorithms, are applied to accurately estimate d_s upstream of such piers. Feature selection is performed using Sequential Forward Selection (SFS) with RF and XGBoost. Visualization techniques like SHAP and Partial Dependence Plot (PDP) are used to highlight the importance of features and their effects on predicting d_s. The performance of models is evaluated using R^2, MAE, and MSE.

7.2. Methods

7.2.1. Data description

More than 12 studies are selected for the initial data collection. During the screening process, over 450 data samples are gathered for side-by-side, tandem, and eccentric piers. After screening the data based on the parameters influencing scour development, the sample size was reduced to 431 data samples, as shown in Table 7.1.

Table 7.1. Sources for relevant experimental data ranges

References	#	u/u_c	h/d	d/d_{50}	φ (°)	r/d	$ut/d\Delta^{0.5}$
Malik and Setia (2014)	16	0.93-1.01	2.58-2.84	277.78	0-90	1.0-17.0	6.8×10^4-7.3×10^4
Das et al. (2014)	16	0.90-1.07	1.20-1.60	136.99	0-31	5.0-7.8	2.9×10^5-4.5×10^5
Das et al. (2016)	5	0.78	1.79	95.89	30.-60	3.5-6.0	8.1×10^5-9.1×10^5
Wang et al. (2016)	126	0.40-0.90	2.00-2.50	85.71	0	1.0-16.0	2.9×10^4-6.8×10^4
Khaple et al. (2017)	42	0.90	1.95-2.67	33.33-85.42	0-63.4	2.0-12.0	4.3×10^5-7.9×10^5
Keshavarzi et al. (2018)	27	0.77-0.96	2.09-2.91	64.71	0	1.0-12.0	1.0×10^6-1.3×10^6
Liu et al. (2018)	79	0.41-0.88	4.00	42.86	0	2.0-16.0	6.1×10^4-1.3×10^5
Das et al. (2019)	9	0.73	1.79	84.85	34.8-74	3.1-5.3	6.6×10^5
Malik and Setia (2020)	30	0.94-0.99	2.81-3.57	140.00	0	1.0-17.0	8.3×10^5-8.7×10^5
Malik and Setia (2021)	17	0.92-0.96	2.50-2.85	269.57	0-90	1.0-17.0	5.7×10^4
Devi and Kumar (2022*a*)	24	0.75-0.96	2.40-3.26	83.33	90	1.5-5.0	1.0×10^5-1.4×10^5
Devi and Kumar (2022*b*)	40	0.45-0.58	2.40-3.26	28.57	0	1.50	8.3×10^5-8.7×10^5
Total	431	0.41-1.07	1.20-4.00	28.57-277.78	0-90	1.0-17.0	2.9×10^4-1.3×10^6

Experiments conducted

7.2.2. Dimensionless analysis: Buckingham π theorem

This research evaluates the d_{sm} for two circular piers positioned at various r using depends on parameters defined in Eq. (7.1). Here, ρ_f is water density, ρ_s is sediment density, g is gravitational acceleration, μ is the dynamic viscosity of water, d is pier diameter.

$$d_{sm} = f\left(h, d, u, u_c, d_{50}, r, \varphi, \rho_f, \rho_s, \sigma, t, g, W, \mu\right) \tag{7.1}$$

The Buckingham π theorem simplifies physical interactions by reducing the number of variables and identifying dimensionless parameters (Eq. 7.2).

$$\frac{d_{sm}}{d} = f_2\left(\frac{h}{d}, \frac{u}{u_c}, \frac{d}{d_{50}}, \frac{r}{d}, \varphi, \frac{\rho_f u h}{\mu} = \mathrm{Re}, \frac{u}{\sqrt{gh}} = \mathrm{Fr}, \sigma, \frac{ut}{d}, \Delta, \frac{d}{W}\right) \tag{7.2}$$

Moreover, Δ has been combined with the dimensionless time, while the effects of σ, d/W, Fr, and Re are considered negligible based on the assumptions from previous studies (Table 7.2) simplified to Eq. (7.3).

$$\frac{d_{sm}}{d} = f_2\left(\frac{h}{d}, \frac{u}{u_c}, \frac{d}{d_{50}}, \frac{r}{d}, \varphi, \frac{ut}{d\Delta^{0.5}}\right) \tag{7.3}$$

Table 7.2 shows the assumptions made by various research groups about the sidewall effect, sediment size effect, sediment uniformity (σ), and viscous effects.

Table 7.2. Assumptions adopted by different research groups.

Effects	Conditions applied by researchers	References	Ranges of data collected for this study
Negligible side-wall effect	$W/d \geq 3$	Ballio et al. (2009)	4.5–14.3
Negligible sediment size effect	$d/d_{50} > 50$	Melville and Chiew (1999)	28.57–277.78
Uniform sediment	$\sigma < 1.4$	Dey et al. (1995)	1.18–1.80
Negligible flow viscosity	Re>7000	Monti (1994)	9599–55873
Threshold for sediment movement	$u/u_c = 0.4$	Chiew (1995)	0.40–1.07
Negligible effect of flow shallowness	$h/d \geq 4$	Nandi and Das (2023)	1.2–4.0

7.2.3. Promising maximum scour depth formulas

Most of the existing studies emphasize identifying the $d_{sm1|2}/d$ around bridge piers under clear-water conditions, often overlooking the temporal aspects to estimate d_s (Table 7.3).

Table 7.3. Functions used to develop scour depth formulas in literature.

Arrang-ement	References	Functions	Schematic arrangements
Side-by-side	Malik and Setia (2020)	$d_{sm1\|2}/d = f(e/d)$	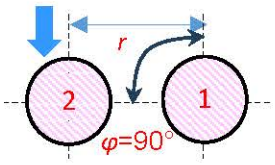
	Devi and Kumar (2022*a*)	$d_{sm1\|2}/d = f(r, d)$	
Tandem	Khaple et al. (2017)	$d_{sm2}/d = f(d_{se}/d, u/u_c, t/T, l/d)$	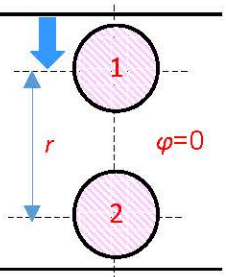
	Wang et al. (2016)	$d_{sm1}/d = f(u/u_c)$, $d_{sm2}/d = f(u/u_c, r/d)$	
	Liu et al. (2018)	$d_{sm1}/d = f(u/u_c)$, $d_{sm2}/d = f(u/u_c, r/d)$	
	Keshavarzi et al. (2018)	$d_{sm1}/d = f(d_{se}/d)$, $d_{sm2}/d = f(d_{se}/d, l)$	
	Malik and Setia (2020)	$d_{sm1\|2}/d = f(l/d)$	
Eccentric	Khaple et al. (2017)	$d_{sm2}/d = f(d_{se}/d, u/u_c, t/T, l/d, e/d)$	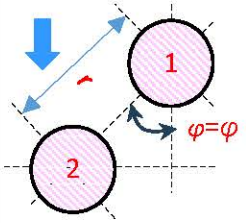
	Das et al. (2016)	$d_{sm1\|2}/d = f(l/d)$	
	Das et al. (2019)	$d_{sm1\|2}/d = f(l/d, \mathrm{P})$	
	Malik and Setia (2020)	$d_{sm1\|2}/d = f(s/d)$	
	Nandi and Das (2024)	$d_{sm1\|2}/d = f(d_{se}/d, d_{50}/d, h/d, r/d, l/d, t/T)$	

Here, parameters include e (center-to-center eccentricity or transverse distance between piers), l (center-to-center longitudinal distance between piers), s (shortest distance between Pier-1 and Pier-2), P (pier position factor, ranging from 0 to 2 based on pier positioning), and r (clear distance between two eccentric piers).

For this study, formulas proposed by Wang et al. (2016) for estimating d_s around side-by-side piers and by Das et al. (2016) for eccentric multiple piers are selected for comparison. These formulas are chosen because they offer valuable insights into the complex scour processes associated with different pier arrangements. Formulas by Liu et al. (2018) and Khaple et al. (2017) are found to have limitations in their application due to the narrow range of experimental conditions. Similarly, formulas by Devi and Kumar (2022*a*) and Nandi and Das (2024) relied on single-pier experiments, which are not available for all the literature to compare.

7.2.4. Challenges in data curation

We have faced several challenges in collecting the literature data are listed below:

***Velocity* (u):** Various methods in the literature are used to calculate u, including bulk and depth-averaged u. To ensure consistency, this study uses the original u data provided by the researchers, regardless of the calculation method.

***Critical velocity* (u_c):** The u_c is often presented as shear velocity (u_*) or critical shear velocity (u_{*c}) leading to analytical challenges. This doubt is solved by converting u_{*c} to u_c using a logarithmic formula (Melville 1997).

***Sediment gradation* (σ):** Literature-specific formulas are applied to determine σ. For incomplete data but with reports of uniform sediment, σ is assigned a value <1.4, commonly set as 1.3, as done by Malik and Setia (2014, 2020). When σ <1.2 is specified, such as in Wang et al. (2016) and Liu et al. (2018), σ is considered as 1.19–1.2.

***Relative density of sediments*:** This is taken directly from the literature. If not provided in the literature, it is calculated using ρ_s/ρ_f, where ρ_f is assumed to be 998.2 kg/m^3 at 20°C unless otherwise specified. A default value relative density of sand 2.65, which represents coarse sand, is used for unspecified sediment densities. Literature without clear information on sediment type is excluded from the analysis.

***Incipient Motion Condition* (u/u_c):** To maintain uniformity, this study uses a single method to calculate flow intensity (u/u_c). The logarithmic formula is used for conversion among threshold shear velocity (u_{*c}) and u_c. Slightly higher u/u_c values (u/u_c >1.2–1.3) are taken as indicators of bedform initiation. The u/u_c values for Malik and Setia (2014), and Das et al. (2014) are calculated as 1.01 and 1.07, respectively.

The analysis of incipient motion conditions in this study includes Shields curves derived from literature data (Fig. 7.1). The area below the dashed and dotted lines represents conditions where no sediment movement occurs. However, some data points in this study lie above this region, however in the literature clearwater condition was mentioned in the relevant literature.

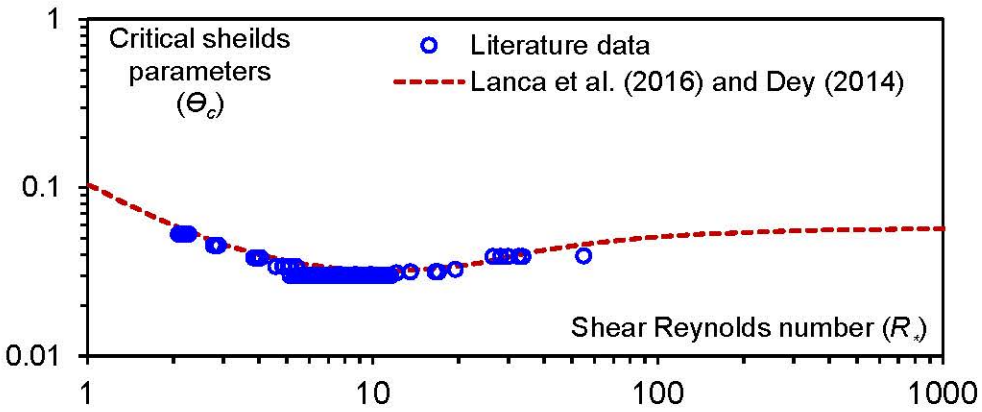

Fig. 7.1. Shields diagram to show incipient motion condition.

7.2.5. Pre-processing of curated data

During the data processing, raw data are converted into independent dimensionless variables u/u_c, h/d, h/d, d/d_{50}, $ut/d\Delta^{0.5}$, φ, and r/d, which serve as input variables. The normalized d_s ($d_{sm1|2}/d$) is taken as the response variable. Descriptive statistical measures for these dimensionless variables are given in Table 7.4.

Furthermore, variable d/d_{50} showed the highest skewness of 1.95, which shows a significant deviation from a normal distribution. Furthermore, d/d_{50} showed a kurtosis of 3.5, which suggests a heavy-tailed distribution. Kolmogorov-Smirnov (KS) goodness-of-fit test is conducted to check the distribution of data.

The null hypothesis (H_o) stated that the data follow a normal distribution, while the alternative hypothesis (H_a) argued otherwise. At a significance level (α) of 0.05, H_o was rejected for all variables, as the p-values are less than 0.01. This strongly supports H_a, showing that these variables do not conform to a normal distribution.

Moreover, with all variables in Table 7.4 showing KS statistics greater than 0.01, Therefore, none of the variables in this data set are likely to follow a normal distribution based on the results of the KS test.

Table 7.4. Descriptive statistics of variable considered for the different arrangements where P <0.01.

Variable	Mean	SD	Minimum	Maximum	Range	IQR	Skewness	Kurtosis	KS
d_{sm1}/d	1.23	0.65	0	2.53	2.53	1.04	0.02	-0.95	0.07
d_{sm2}/d	1.1	0.58	0.03	2.58	2.55	0.94	0.06	-0.96	0.07
u/u_c	0.79	0.17	0.4	1.07	0.67	0.3	-0.61	-0.87	0.17
h/d	2.75	0.74	1.2	4	2.8	1.21	0.38	-0.65	0.14
d/d_{50}	87.94	61.92	28.57	277.78	249.21	42.86	**1.95**	**3.5**	0.32
$ut/d\Delta^{0.5}$	290265	360945	29447	1314672	1285226	368023	1.42	0.76	0.37
φ	14.23	29.59	0	90	90	0	1.9	2.02	0.46
r/d	6.36	4.35	1	17	16	7	0.84	-0.41	0.17

A matrix correlation shows the links between independent and dependent variables for the interdependencies to predict the $d_{sm1|2}/d$ in Fig. 7.2.

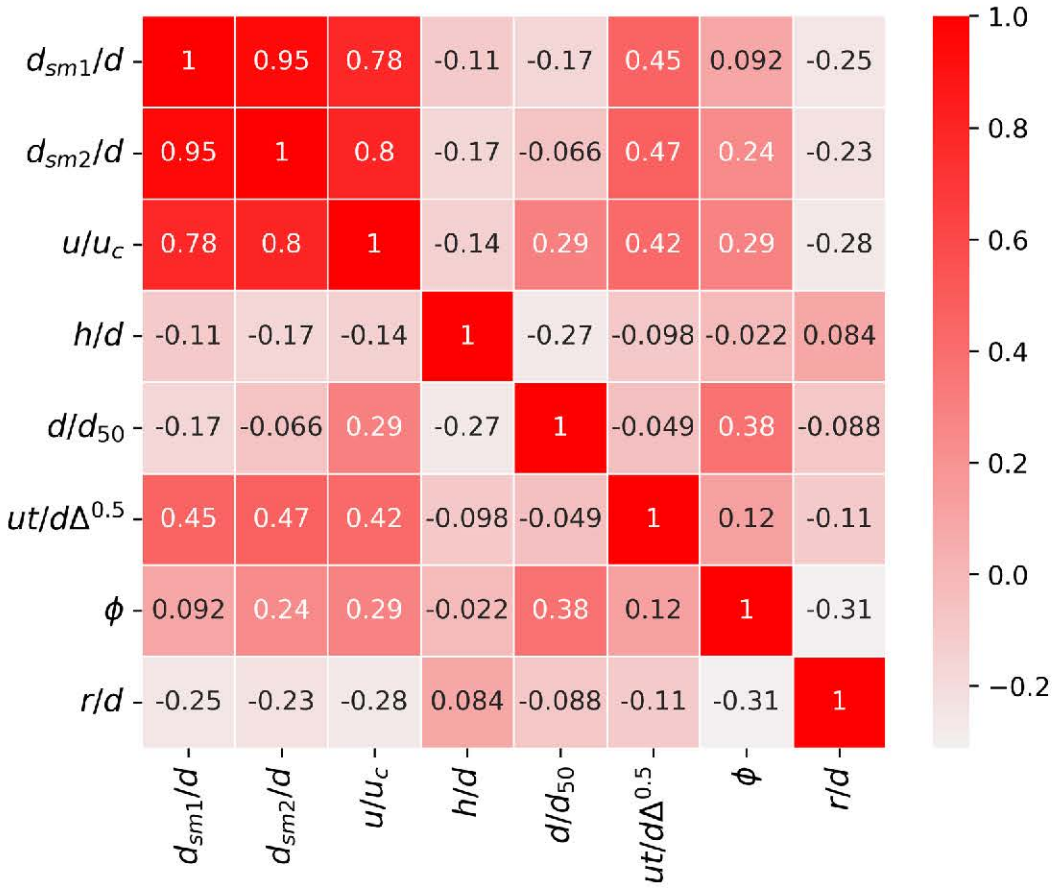

Fig. 7.2. Correlation plot for all features of the selected literature.

7.2.6. Description of machine learning models

(a) Random forest (RF)

Bagging, or bootstrap aggregating, improves ML by creating multiple models from different samples of the dataset and combining their predictions through averaging or voting (Fig. 7.3). This boosts accuracy and stability, especially with decision trees, by reducing variance and overfitting. RF is an advanced bagging method used for regression and classification. It builds multiple decision trees using random subsets of data and features, ensuring diverse models. RF is reliable, handles non-linear relationships well, works efficiently with large datasets, and requires less hyperparameter adjustment (Breiman 2001).

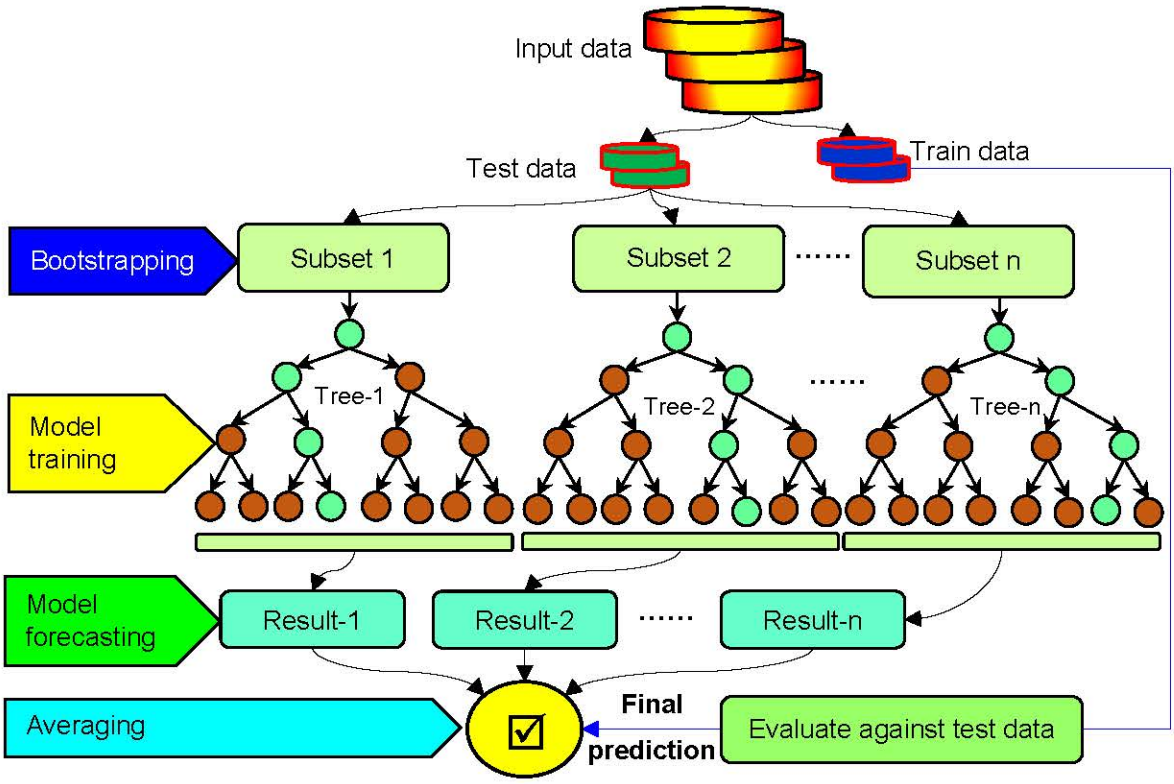

Fig. 7.3. Ensemble tree-based bagging model algorithm (RF).

(b) Extreme Gradient Boosting (XGBoost)

Boosting, similar to bagging, combines models to increase performance in an adaptive, sequential manner (Friedman 2001). It fits weak learners one after another, focusing on the observations that are hardest to predict. This iterative process creates a strong model with minimal bias, often using small decision trees to maintain efficiency and effectiveness. XGBoost, a type of ensemble learning, follows this adaptive fitting method, setting it apart from bagging (Chen and Guestrin 2016). XGBoost applies boosting principles effectively, leading to better performance in a wide range of ML tasks (Fig. 7.4).

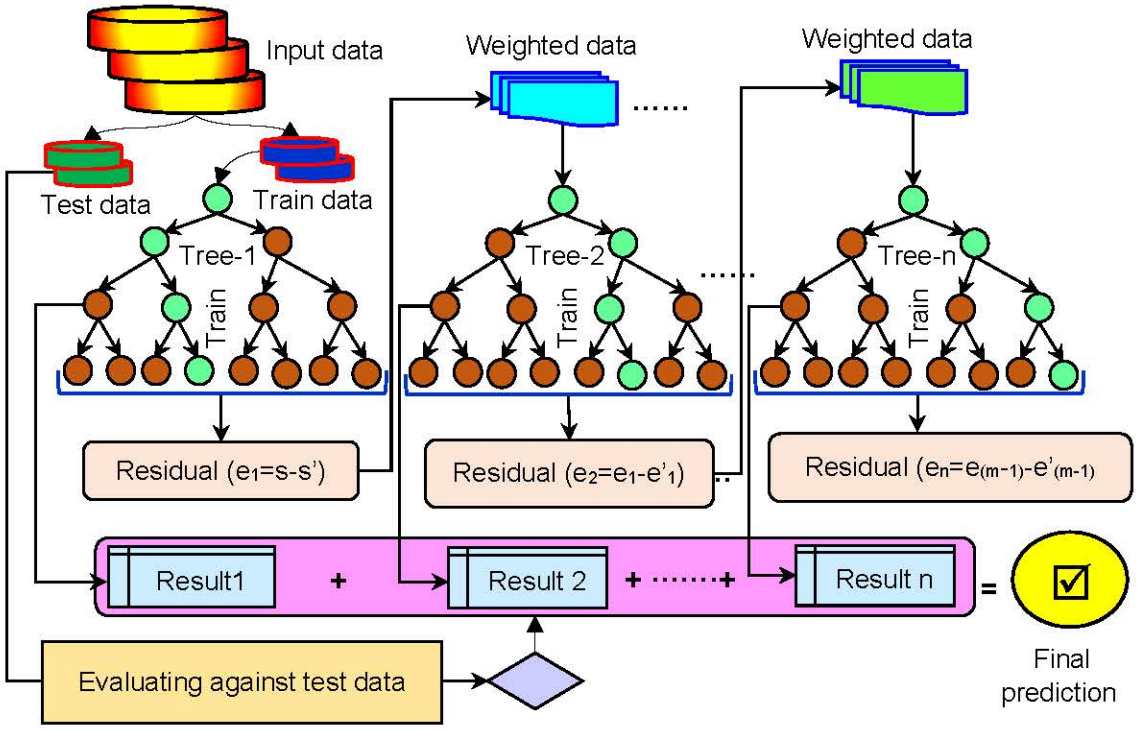

Fig. 7.4. Boosting model algorithm (XGBoost).

The entire methodology of the present study including the feature selection, training and testing of the selected model, PDP and SHAP analysis along with the performance metric evaluation given in Fig. 7.4.

7.2.7. Sequential feature selection (SFS)

Sequential feature selection (SFS) is a method to choose the most important features for a model by adding or removing them one at a time. It measures how each feature affects the accuracy of model, helping to simplify the model and make it better by focusing on the key features (Rückstieß et al. 2011). For regression tasks, this process often uses a measure called negative mean squared error (neg-MSE), where the goal is to minimize error. When SFS is applied to models like Random Forest (RF) and XGBoost, the models are trained with different combinations of features, and their performance is checked using cross-validation. The negative sign in neg-MSE helps the algorithm aim for the best accuracy. Features are added one by one, and the process stops when adding more features doesn't improve performance or when a set limit is reached. This ensures the model uses only the most useful features, improving accuracy and reducing the risk of overfitting.

7.2.8. Partial dependence plot (PDP)

With the growth in computing power, modern supervised learning algorithms can quickly process complex datasets, leading to highly accurate models. However, a trade-off often exists between accuracy and interpretability. While models such as RF and XGBoost provide precise predictions, they are not easily interpretable, unlike traditional linear models that have clear prediction formulas. To overcome this challenge, partial dependence plots (PDPs) are used. PDPs help visualize the relationship between individual predictors and the outcome in complex models like RFs and XGBoost. By displaying how subsets of features affect the response variable while accounting for the average effects of other predictors, PDPs enhance understanding of these "black-box" models. They also support ranking and scoring predictors based on their impact on the predicted outcome (Greenwell et al. 2018).

Let, a set of features denoted by $w = \{w_1, w_2, \ldots, w_k\}$ representing a model with a prediction function is $y(w)$. If we divide the set of feature w into an interest set, G_s, and its complement will be denoted as, $G_c = w \backslash G_s$, then the "partial dependence" of the response (y_w) on G_s is defined as follows (Eq. 7.4).

$$y_s(G_s) = E_{R_c}\left\{\hat{y}(G_s, G_c)\right\} = \int \hat{y}(G_s, G_c) P_c(G_c)\, dG_c \tag{7.4}$$

where the marginal probability density of G_c is denoted by $P_c(G_c)$ and it can be calculated using the expression: $P_c(G_c) = \int P(w)\, dG_s$. Equation (7.4) can be estimated from a set of training data by adapting the formulation mentioned in Eq. (7.5).

$$\overline{y}_s(G_s) = \frac{1}{N}\sum_{i=1}^{N} \hat{y}\left(G_s, G_{i,c}\right) \tag{7.5}$$

Here, $G_{i,c}$ (where, $i = 1, 2, \ldots, N$) represents the values of G_c observed in the training sample. This averaging process accounts for the influence of all other predictors.

7.2.9. Shapley additive explanations (SHAP)

The SHAP helps evaluate the influence of each input variable on the prediction of a model. Lundberg and Lee (2017) introduced SHAP plots, based on concepts from game theory. Inspired by Shapley values (Shapley 1953), originally used to determine fair contributions of players in cooperative games, SHAP explains whether each of the input effects on the prediction is positive or negative. Recently, SHAP interpretations have been applied to scour prediction problems using various ML models to highlight the impact of parameters on isolated pier d_s prediction (Eini et al. 2023).

SHAP values are computed and utilized as feature attributions, representing a weighted average of all conceivable differences (Eq. 7.8).

$$\chi_i = \sum_{w \subseteq A \setminus \{i\}} \frac{|w|!(|J|-|w|-1)!}{|J|!} \left[y_{w \cup \{i\}} \left(x_{w \cup \{i\}} \right) - y_w \left(x_w \right) \right] \tag{7.8}$$

χ_i, indicates the contribution of the i^{th} feature in terms of SHAP values. J is the collection of all features. $|J|$ and $|w|$ denote the number of features in J and w respectively, and $w \subseteq J$, $y_{w \cup \{i\}}$ and y_w denote models output with and without the i^{th} feature, respectively. Variable x_a denotes the values of the input features in set J. Following this, the model output can be expressed as a linear sum of a constant base value and SHAP values (Eq. 7.9).

$$g\left(x'\right) = \chi_0 + \sum_{i=1}^{|J|} \chi_i x_i' \tag{7.9}$$

Here, χ_0 is a base value, $x' \in \{0, 1\}^{|J|}$, where, $x' = 1$, when a feature is present and $x' = 0$, when the feature is not present.

7.2.10. Statistical performance indicator

This study evaluates model performance using multiple metrics, including R^2, MAE (see Table 3.5), and MSE (Table 7.5), each offering a unique perspective. R^2 assesses how well the model predictions align with actual observations, focusing on linear relationships. MAE measures the average error magnitude, ignoring direction, and provides an overall accuracy assessment. MSE, emphasizing larger errors through squaring, captures predictive accuracy while being sensitive to outliers. Together, these metrics ensure a detailed evaluation of the predictive capabilities of models, covering different aspects of performance and robustness. Mean Bias Error is used for bias estimation in the prediction.

Table 7.5. Performance indicators with their pertinent ranges and ideal values.

Performance indicators	Range	Ideal value
$\text{MSE} = \frac{1}{N} \sum_{i=1}^{N} \left\{ \left(\frac{d_{sm}}{d} \right)_{ci} - \left(\frac{d_{sm}}{d} \right)_{oi} \right\}^2$	0 to ∞	0
$\text{MBE} = \frac{1}{N} \sum_{i=1}^{N} \left(\frac{d_{sm}}{d} \right)_{ci} - \left(\frac{d_{sm}}{d} \right)_{oi}$	$-\infty$ to ∞	

The detailed methodology for the present study is given in the flow diagram below with each method adopted in this chapter in detail (Fig. 7.5).

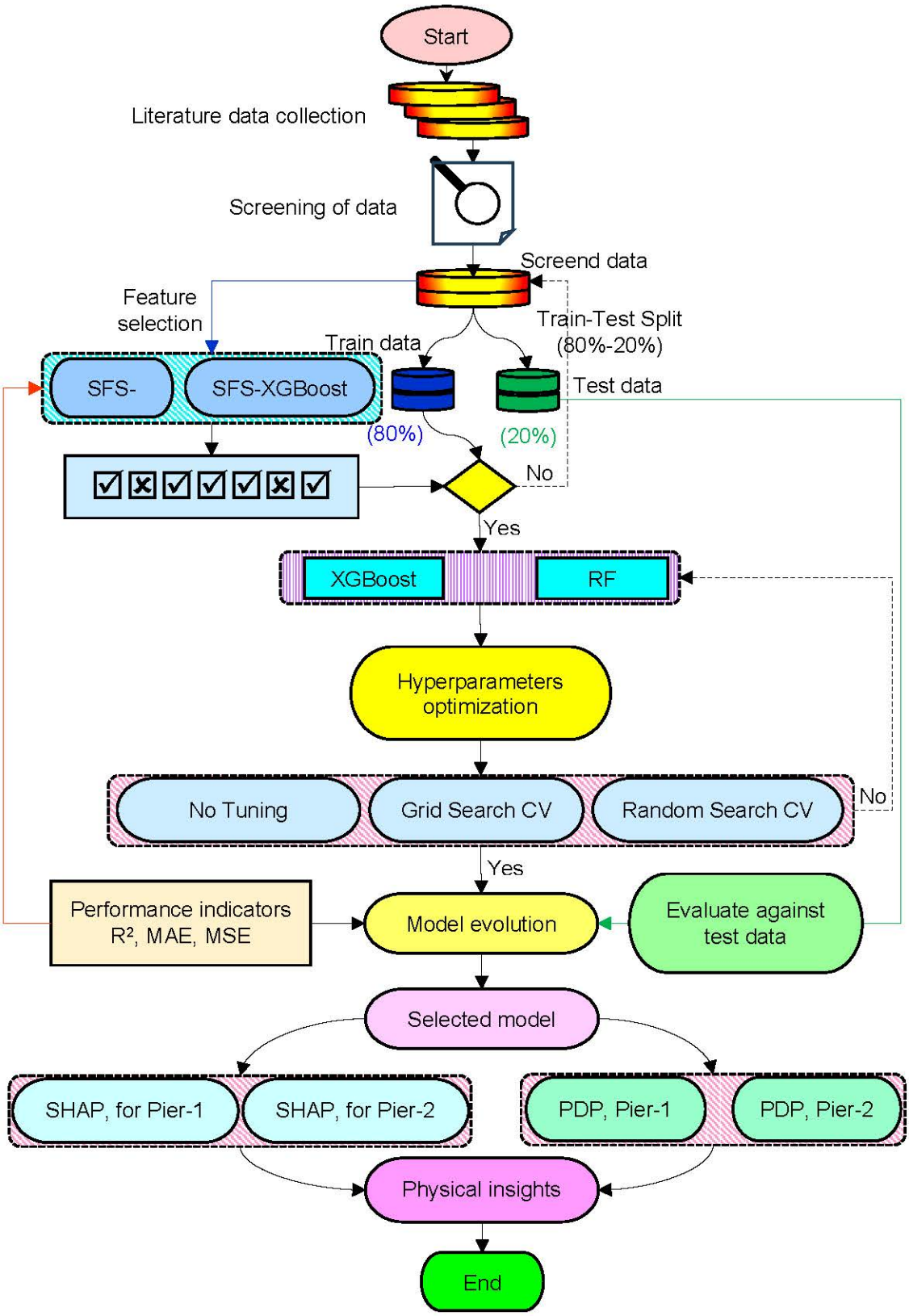

Fig. 7.5. Methodology developed for this study.

7.3. Results and discussion

This study focuses on ensemble ML techniques to estimate d_{sm} around two-pier arrangements. Using the scikit-learn (version 1.3.1) Application Programming Interface (API), the research applies a unified interface for implementing algorithms in tasks like classification, regression, clustering, and dimensionality reduction. Two key methods, RF and XGBoost, represent the bagging and boosting approaches, respectively. The dataset is organized to estimate d_s around side-by-side, tandem, and eccentric circular piers. Model performance is evaluated using R^2, MAE, and MSE metrics. For SFS-RF and SFS-XGBoost, five input parameters for Pier-1 and five to six for Pier-2 are systematically selected.

7.3.1. Feature selection for model building

SFS is a technique used to improve model performance by identifying the most important features and eliminating redundant ones (Table 7.6).

Table 7.6. Selection of best input combination using SFS.

Model	Pier-1, Scoring: neg-MSE		Pier-2, Scoring: neg-MSE	
	Selected features	(MSE) min	Selected features	(MSE) min
SFS-RF	u/u_c, h/d, d/d_{50}, $ut/d\Delta^{0.5}$, r/d	0.0102	u/u_c, d/d_{50}, $ut/d\Delta^{0.5}$, φ, r/d	0.0158
SFS-XGBoost	u/u_c, d/d_{50}, $ut/d\Delta^{0.5}$, φ, r/d	0.0105	u/u_c, h/d, d/d_{50}, $ut/d\Delta^{0.5}$, φ, r/d	0.0129

The study assessed four optimal input combinations derived through SFS using RF and XGBoost, with results presented in Table 7.6. These combinations include influential factors identified based on the neg-MSE scoring method for Pier-1 (Fig. 7.6) and Pier-2 (Fig. 7.7), respectively.

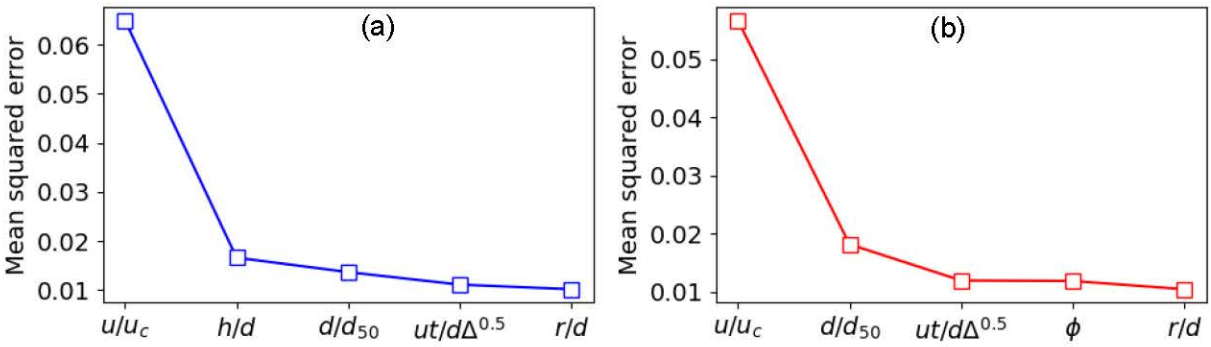

Fig. 7.6. Best input parameters for Pier-1 using **(a)** RF, and **(b)** XGBoost.

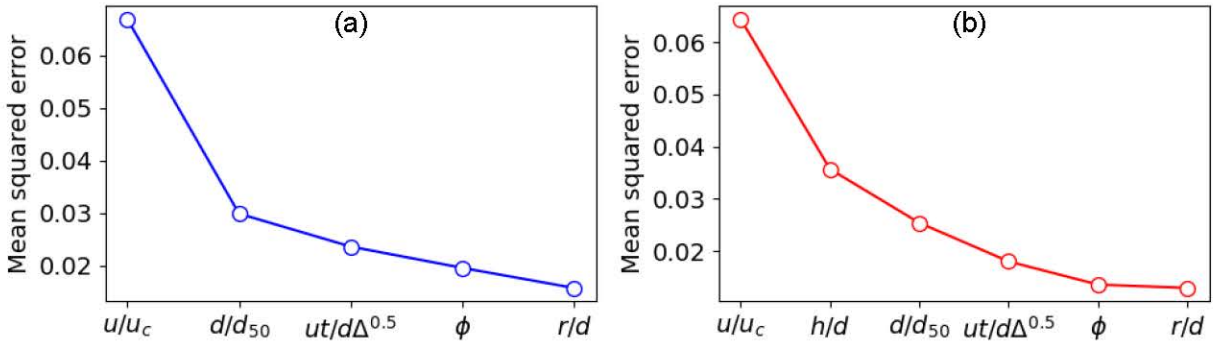

Fig. 7.7. Best input parameters for Pier-2 using **(a)** RF, and **(b)** XGBoost.

It is observed that the u/u_c is the most significant parameter across all combinations, while r/d has the least significance. For Pier-1, the φ is not selected as an influential parameter in SFS-RF, and the h/d is excluded in SFS-XGBoost. For Pier-2, the h/d is not chosen in SFS using r/d, whereas all parameters are included in SFS-XGBoost.

7.3.2. Tuning of machine learning models

The ML models in this study are optimized using Grid Search CV (GSCV) and Random Search CV (RSCV). These tuned models are compared against non-tuned models, which use default parameters provided by the scikit-learn library. The tuning parameters for the ML models are detailed in Table 7.7. By exploring both tuned and default configurations, the study aims to evaluate and compare the effectiveness of different approaches in predicting d_s.

Table 7.7. Selected hyperparameters for ML models.

Model	Tuning Method	Hyperparameters for Pier-1	Hyperparameters for Pier-2
RF	No Tuning	Default parameters	Default parameters
	GSCV	bootstrap: True, max_depth: 20, min_samples_leaf: 1, min_samples_split: 2, n_estimators: 200	bootstrap: False, max_depth: 20, min_samples_leaf: 1, min_samples_split: 2, n_estimators: 50
	RSCV	bootstrap: True, max_depth: 20, min_samples_leaf: 1, min_samples_split: 2, n_estimators: 76	bootstrap: True, max_depth: 20, min_samples_leaf: 1, min_samples_split: 4, n_estimators: 137

XGBoost	No Tuning	Default parameters	Default parameters
	GSCV	colsample_bytree: 1.0, gamma: 0, learning_rate: 0.1, max_depth: 4, min_child_weight: 1, n_estimators: 200, subsample: 0.9	colsample_bytree: 0.9, gamma: 0, learning_rate: 0.2, max_depth: 4, min_child_weight: 5, n_estimators: 300, subsample: 0.9
	RSCV	colsample_bytree: 1.0, gamma: 0, learning_rate: 0.1, max_depth: 4, min_child_weight: 1, n_estimators: 106, subsample: 0.9	colsample_bytree: 1.0, gamma: 0, learning_rate: 0.2, max_depth: 3, min_child_weight: 5, n_estimators: 204, subsample: 0.9

7.3.3. Evaluation of machine learning models

The performance indicators for the evolution of R^2, MAE, and MSE are derived from the training and testing datasets, as shown in Table 7.8. This table shows two machine learning models, each utilizing three different parameter optimization techniques. The corresponding performance metrics for these models are provided in Table 7.8.

Table 7.8. Performance indicators of pier scour models for training, testing, and overall data.

Model	Tuning Status	Performance metrics	Pier-1		Pier-2	
			Training	Testing	Training	Testing
RF	No Tuning	R^2	0.996	0.967	0.992	0.947
		MAE	0.027	0.078	0.034	0.097
		MSE	0.002	0.013	0.003	0.018
	GSCV	R^2	0.997	0.968	0.995	0.963
		MAE	0.023	0.074	0.028	0.082
		MSE	0.001	0.013	0.002	0.013
	RSCV	R^2	0.997	0.979	0.992	0.972
		MAE	0.025	0.063	0.038	0.068
		MSE	0.001	0.008	0.003	0.009
XGBoost	No Tuning	R^2	0.989	0.958	0.984	0.961
		MAE	0.052	0.092	0.057	0.09
		MSE	0.004	0.017	0.005	0.014
	GSCV	R^2	0.989	0.962	0.999	0.961
		MAE	0.052	0.075	0.011	0.08
		MSE	0.004	0.015	0.000	0.014
	RSCV	R^2	0.997	0.960	0.997	0.968
		MAE	0.029	0.078	0.026	0.076
		MSE	0.001	0.015	0.001	0.011

(a) Random forest (RF)

Significant accuracy in predicting $d_{sm1|2}/d$ is achieved with a non-tuned model, yielding nearly identical results to the tuned models (GSCV and RSCV) for RF, when rounded to two decimal places. However, when evaluated with three decimal places, the RF model for Pier-1, using GSCV, shows the highest performance in the training phase with $R^2 = 0.997$, MAE = 0.023, and MSE = 0.001. In the testing phase, RSCV delivers the best results for predicting d_{sm1}/d with $R^2 = 0.979$, MAE = 0.063, and MSE = 0.008.

For RF on Pier-2, GSCV in the training phase shows the best results, with $R^2 = 0.995$, MAE = 0.028, and MSE = 0.002. In the testing phase, RSCV performs best for predicting d_{sm2}/d with $R^2 = 0.972$, MAE = 0.068, and MSE = 0.009.

Therefore, the best-performing model for RF in predicting $d_{sm1|2}/d$ is optimized using RSCV, as it yields the highest performance in the testing dataset.

(b) Extreme gradient boosting (XGBoost)

Using a non-tuned model to predict $d_{sm1|2}/d$, the XGBoost ML model achieves considerable accuracy. For Pier-1, XGBoost-RSCV provides the highest accuracy in the training phase, with $R^2 = 0.997$, MAE = 0.029, and MSE = 0.001. In the testing phase, both XGBoost-GSCV delivers the highest accuracy, with $R^2 = 0.962$, MAE = 0.075, and MSE = 0.015, when rounded to three decimal places.

For Pier-2, XGBoost-GSCV achieves the highest accuracy in the training phase with $R^2 = 0.999$, MAE = 0.011, and MSE = 0.000, showing over fittings. In the testing phase, XGBoost-RSCV shows the highest performance, with $R^2 = 0.968$, MAE = 0.076, and MSE = 0.011, when considering three decimal places.

Therefore, both RF-RSCV models for Pier-1 and Pier-2 are recommended for model evaluation.

7.3.4. Comparison of $(d_{sm1|2}/d)_o$ with $(d_{sm1|2}/d)_p$

The scatter plots between $(d_{sm1|2}/d)_o$ and $(d_{sm1|2}/d)_p$, for both the training and testing datasets, are shown in Figs. 7.8-7.11 for all models, including RF-non tuned, RF-GSCV, RF-RSCV, XGBoost-non tuned, XGBoost-GSCV, and RF-RSCV for both the training and testing phases. In these figures, the d_s predictions from all models are concentrated around the Perfect Agreement Line (PAL), represented by a solid line. The dashed lines around the PAL represent the ±20% deviation, and the concentration of data points near the PAL indicates satisfactory model accuracy in predicting d_s.

In the case of RF-RSCV for both training and testing phases, the predictions for d_{sm1}/d (as shown in Fig. 7.8) are closely aligned with the PAL, showing the best performance in this scenario. When predicting d_{sm2}/d, RF-RSCV shows the best performance in both the training and testing phases (as seen in Fig. 7.10).

For XGBoost-RSCV and XGBoost-GSCV in predicting d_{sm1}/d, the predictions also align closely with the PAL, demonstrating the models' effectiveness, as shown in Fig. 7.9. In the case of d_{sm2}/d, XGBoost-RSCV shows the best performance in both the training and testing phases, with predictions again concentrated around the PAL, as seen in Fig. 7.11.

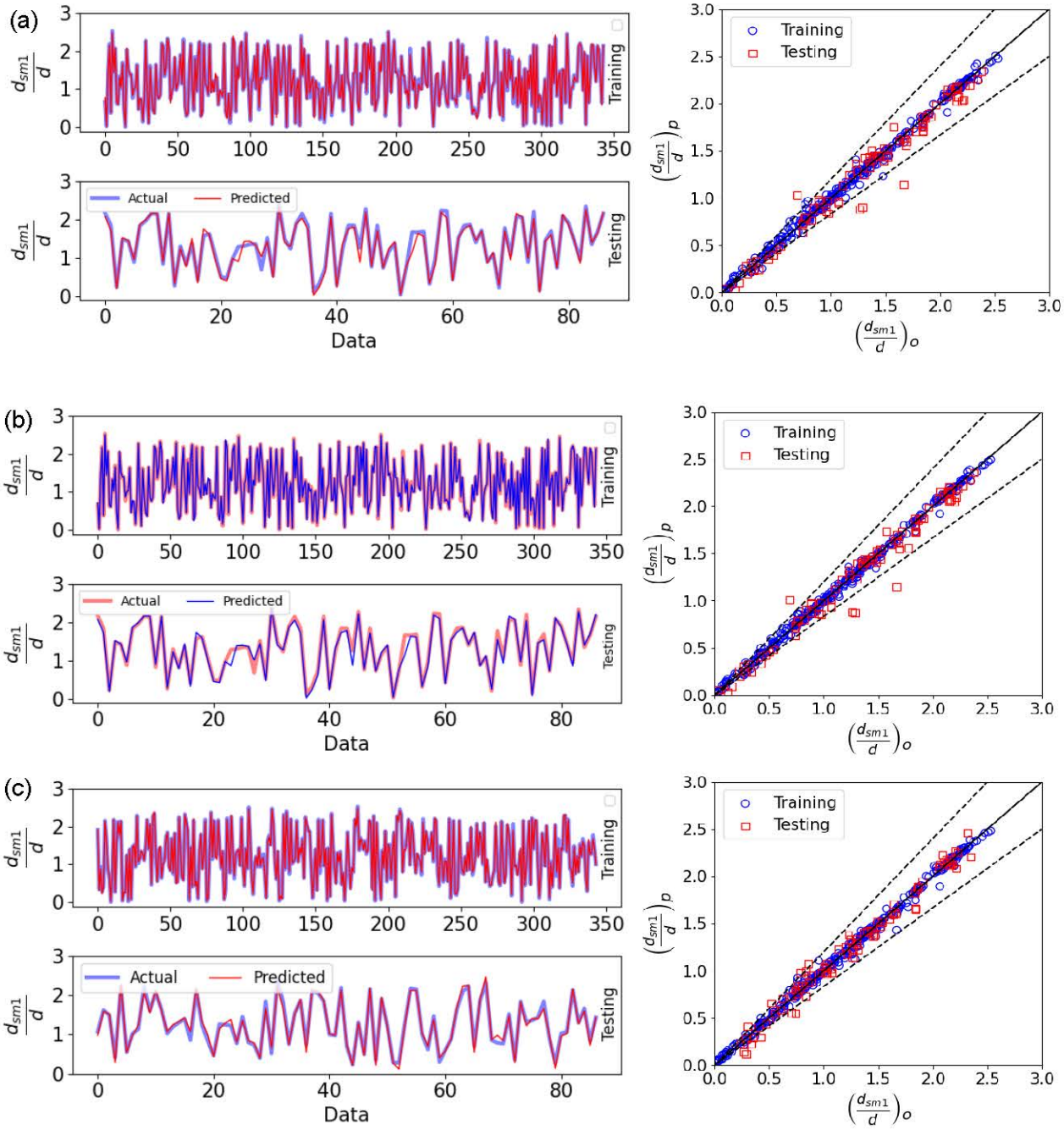

Fig. 7.8. Line graphs of predicted versus observed d_{sm1}/d with scatter plots using RF **(a)** non-tuned, **(b)** GSCV, and **(c)** RSCV.

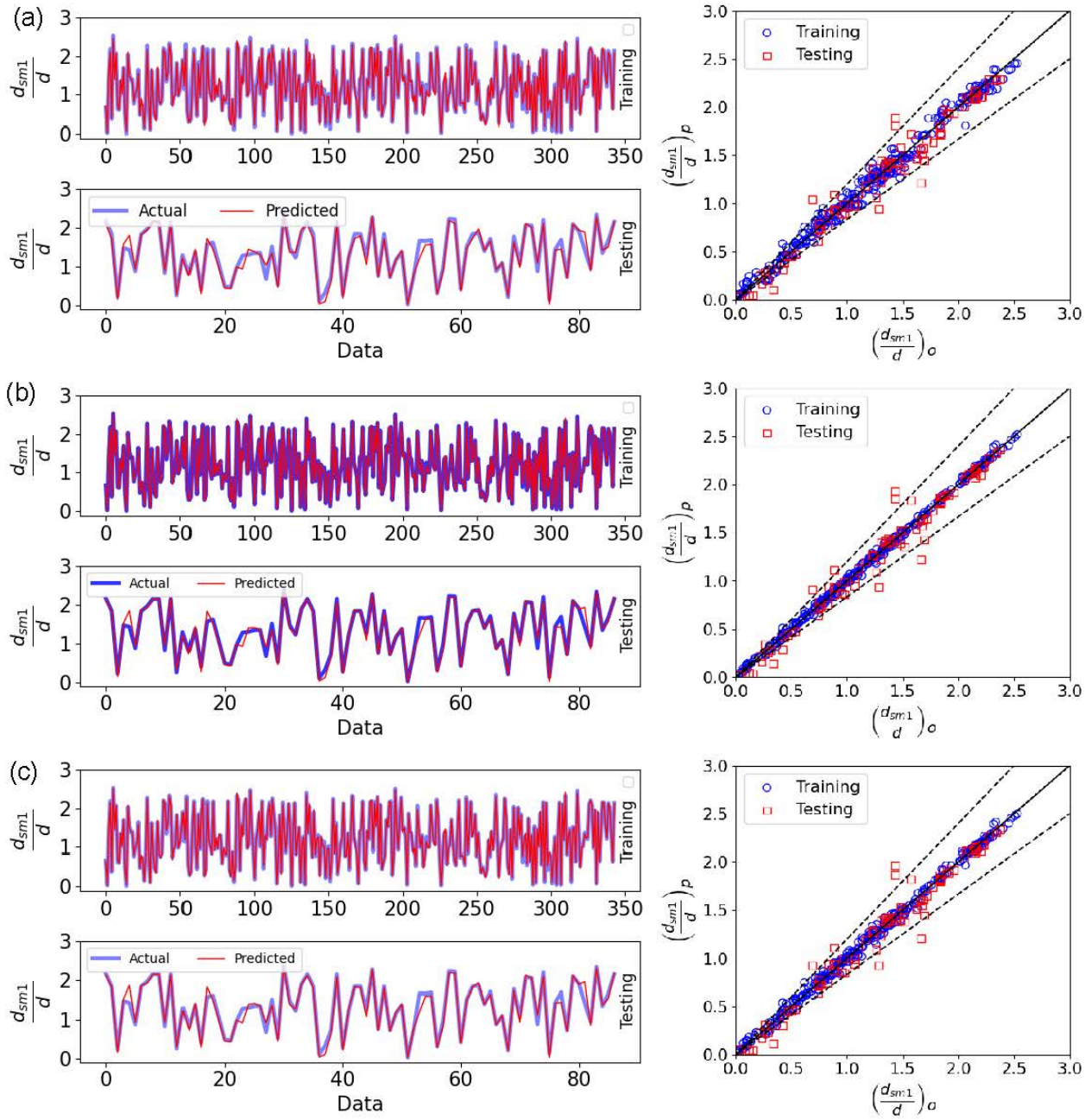

Fig. 7.9. Line graphs of predicted versus observed d_{sm1}/d with scatter plots using XGBoost **(a)** non-tuned, **(b)** GSCV, and **(c)** RSCV.

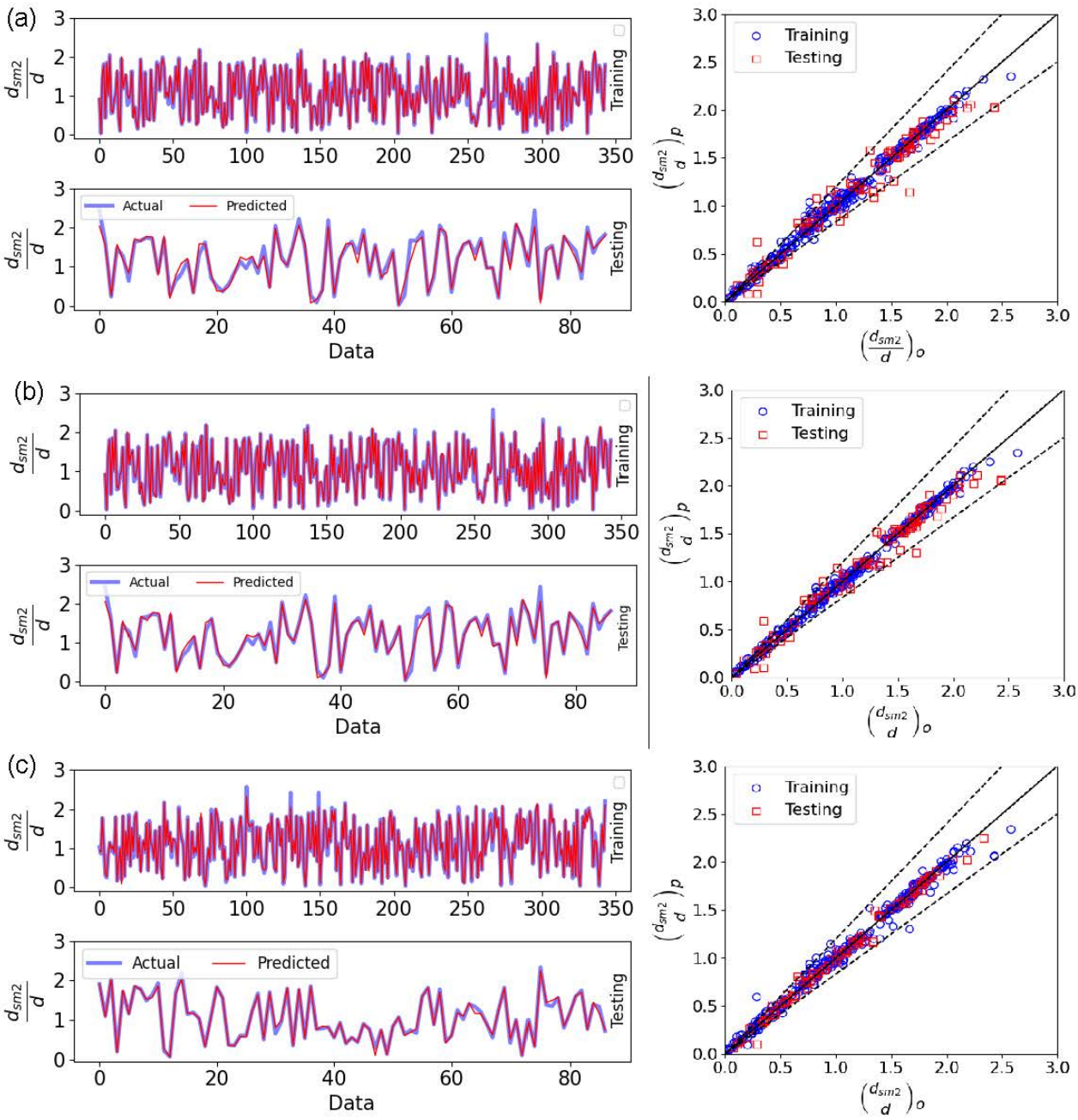

Fig. 7.10. Line graphs of predicted versus observed d_{sm2}/d with scatter plots using RF **(a)** non-tuned, **(b)** GSCV, and **(c)** RSCV.

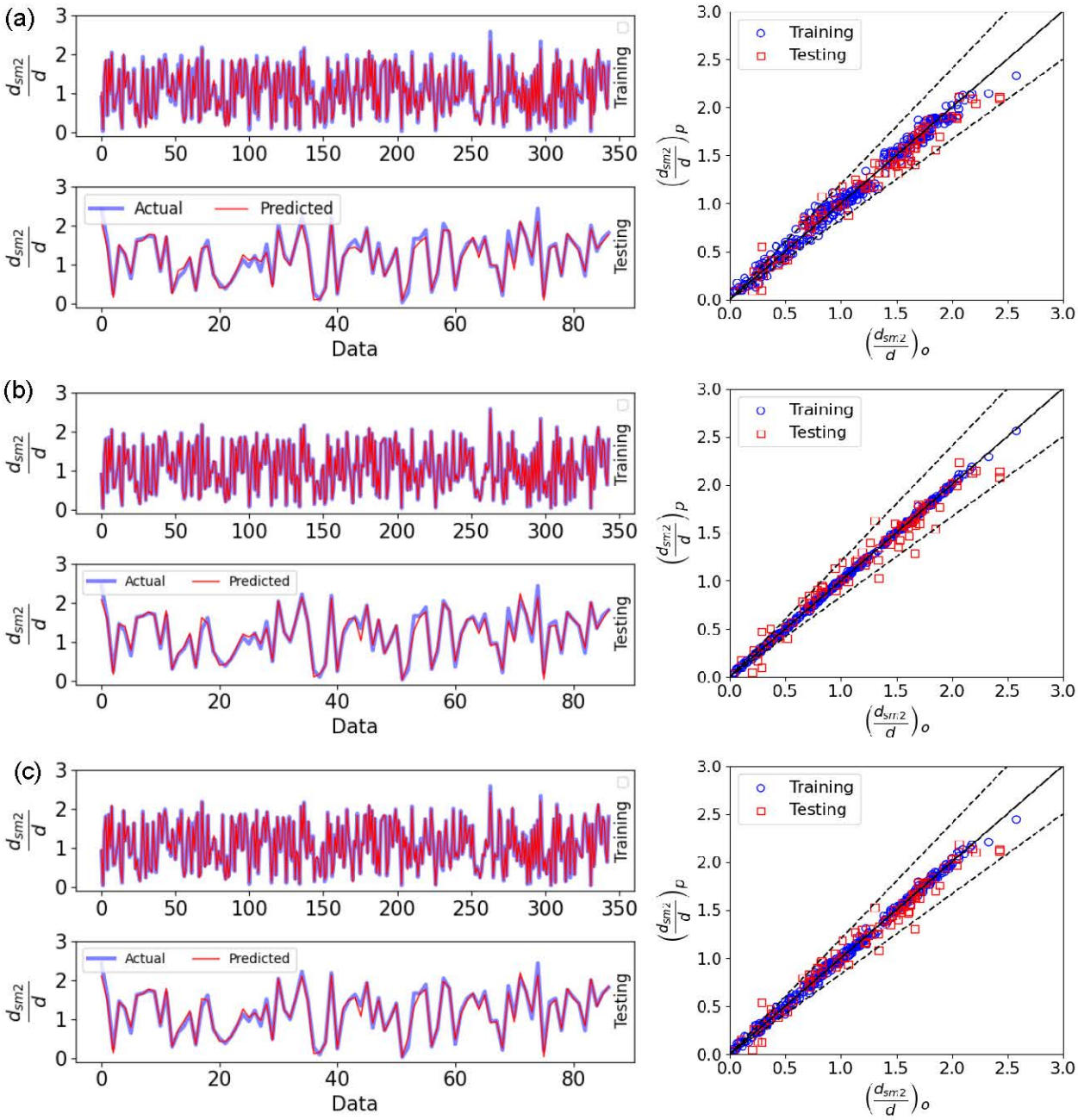

Fig. 7.11. Line graphs of predicted versus observed d_{sm2}/d with scatter plots using XGBoost **(a)** non-tuned, **(b)** GSCV, and **(c)** RSCV.

7.3.5. Analysis of relative error (RE) for $d_{sm1|2}/d$

The relative error (RE) in percentages for both empirical and machine learning (ML) models is shown in Figs. 7.12-7.15. A higher concentration of data points near the zero line is preferred, as it indicates reduced prediction errors across training, testing, and validation phases. This

clustering signifies the effectiveness of the model in minimizing differences, making it a critical metric for evaluating the optimal prediction models.

The RE% values are divided into negative and positive categories, represented by a horizontal dashed line at 0. Analyzing the distribution of data points around this line offers valuable insights into how effectively each model minimizes prediction errors. This comparative assessment plays a crucial role in determining the most reliable ML-based methodology for predicting $(d_{sm1|2}/d)_o$.

In the training dataset, the graph shows that for RF-GSCV (Pier-1) in predicting d_{sm1}/d, the residuals are primarily concentrated around the zero line, highlighting the effectiveness of model during training. When compared with the testing dataset for the RF model, the RF-RSCV model is identified as the best performer. Most residuals in the testing dataset are closely clustered near the zero line, with the scatter of data confined within the ±20% error band, as shown in Fig. 7.12.

During the training stage of XGBoost models for predicting d_{sm1}/d, particularly XGBoost-RSCV (Pier-1), the residuals progressively converge around the zero line in the later stages, showing improved accuracy over time. However, in the initial stages of d_{sm1}/d, prediction, the residuals show a higher level of spreading, as illustrated in Fig. 7.13. When comparing the testing dataset, both XGBoost-GSCV and XGBoost-RSCV demonstrate a strong concentration of residuals near the zero line, with the dispersion of data appearing nearly identical throughout the figure.

For the prediction of d_{sm2}/d, an analysis of the RE in percentage shows that the RF-RSCV model shows superior performance during both the testing and training phases, as shown in Fig. 7.14. However, the RF-RSCV model for the training phase shows signs of overfitting, which limits its reliability despite the minimal deviation in RE across the training and testing datasets. Addressing this issue could involve utilizing a larger training dataset or employing advanced optimization techniques to enhance model generalizability.

The prediction of d_{sm2}/d using XGBoost-RSCV and GSCV shows that the residuals are largely concentrated around the zero line, which indicates a high level of accuracy in minimizing errors. This pattern is consistently observed across both the training and testing phases, as shown in Fig. 7.15. The clustering of residuals near the zero line underscores the robustness of model and reliability in predicting d_{sm2}/d.

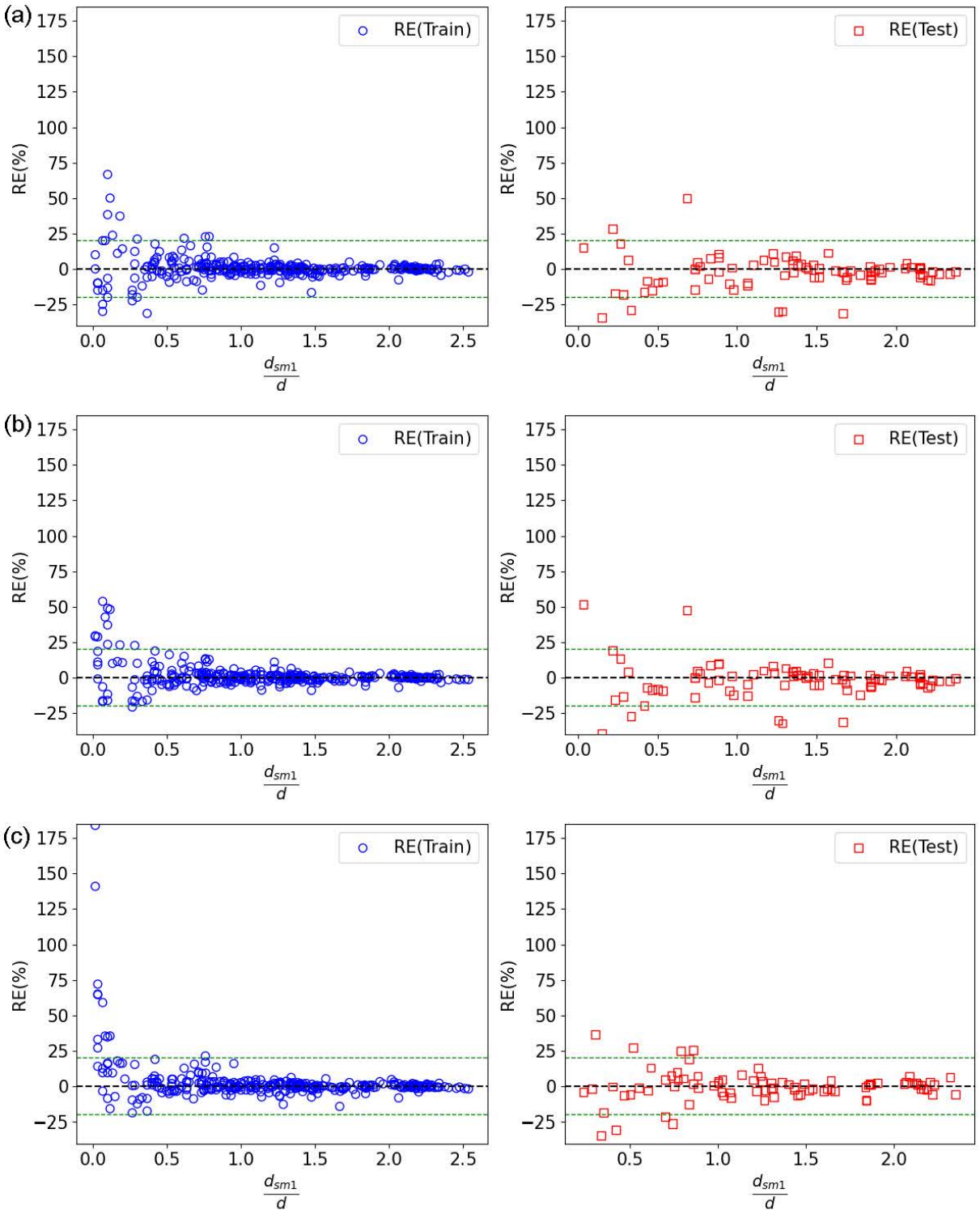

Fig. 7.12. The relative error (RE in %) to predict d_{sm1}/d for the training and testing datasets using RF **(a)** non-tuned, **(b)** GSCV, and **(c)** RSCV.

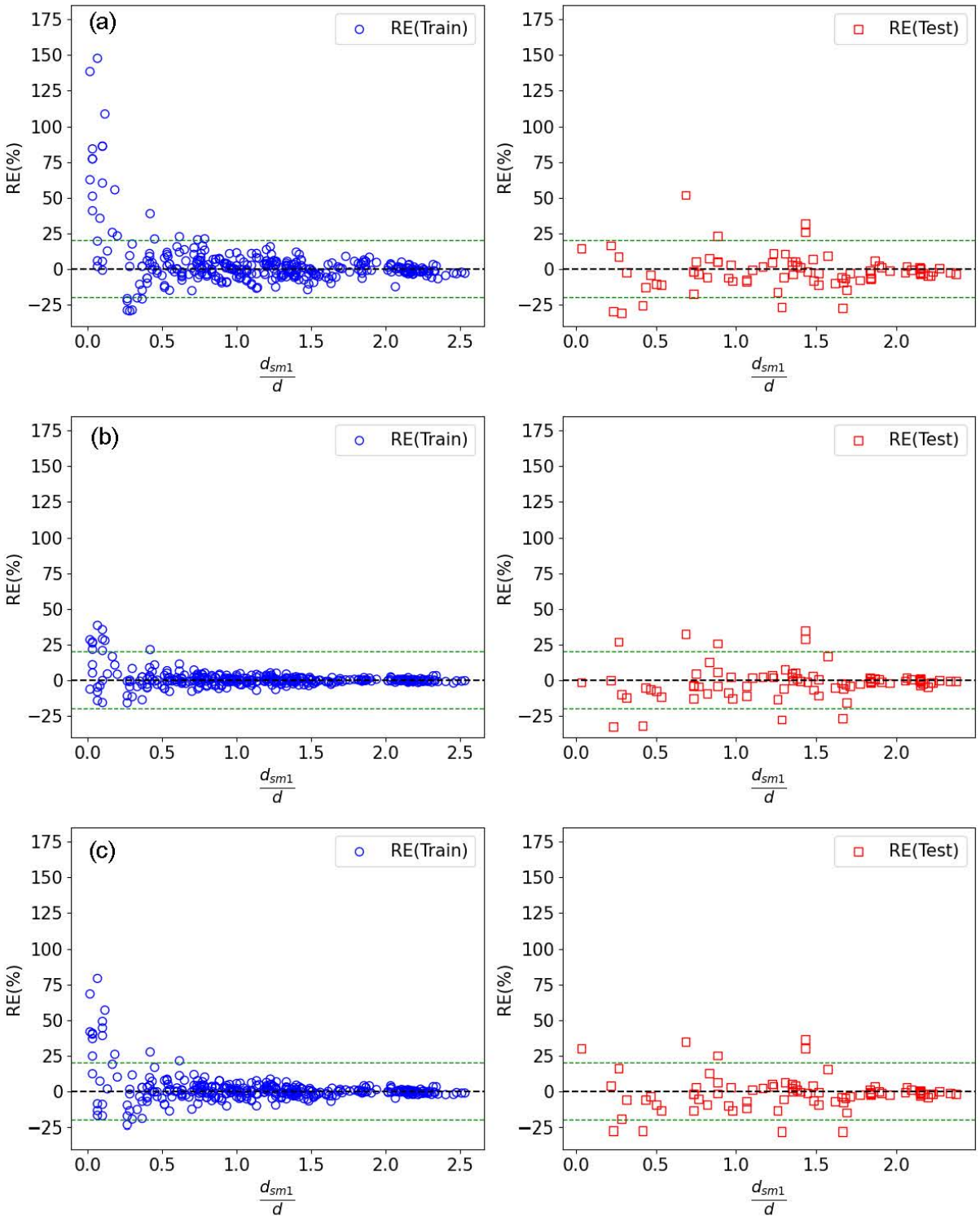

Fig. 7.13. The RE of d_{sm1}/d for the training and testing datasets using XGBoost **(a)** non-tuned, **(b)** GSCV, and (c) RSCV.

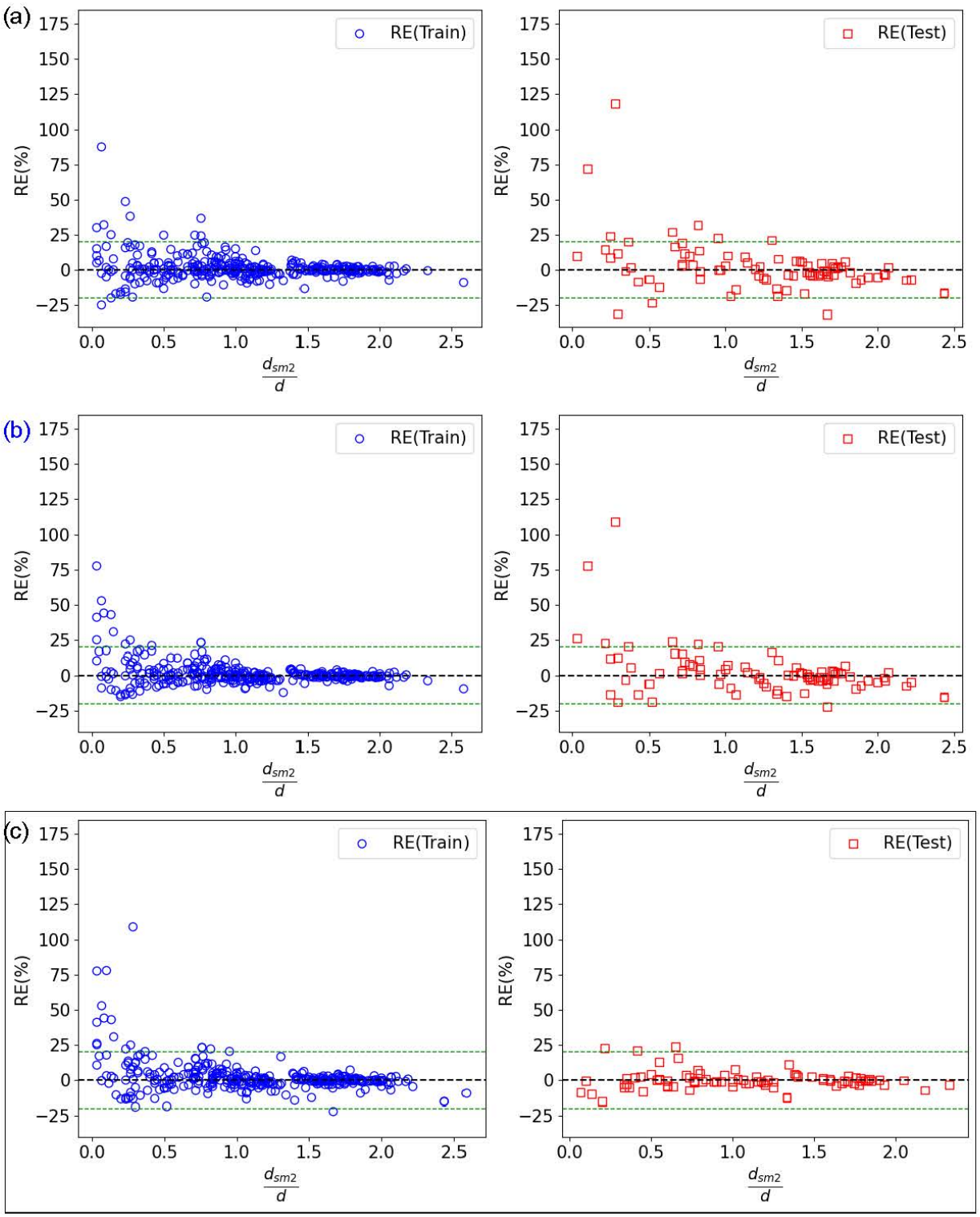

Fig. 7.14. The RE of d_{sm2}/d for the training and testing datasets using RF **(a)** non-tuned, **(b)** GSCV, and **(c)** RSCV.

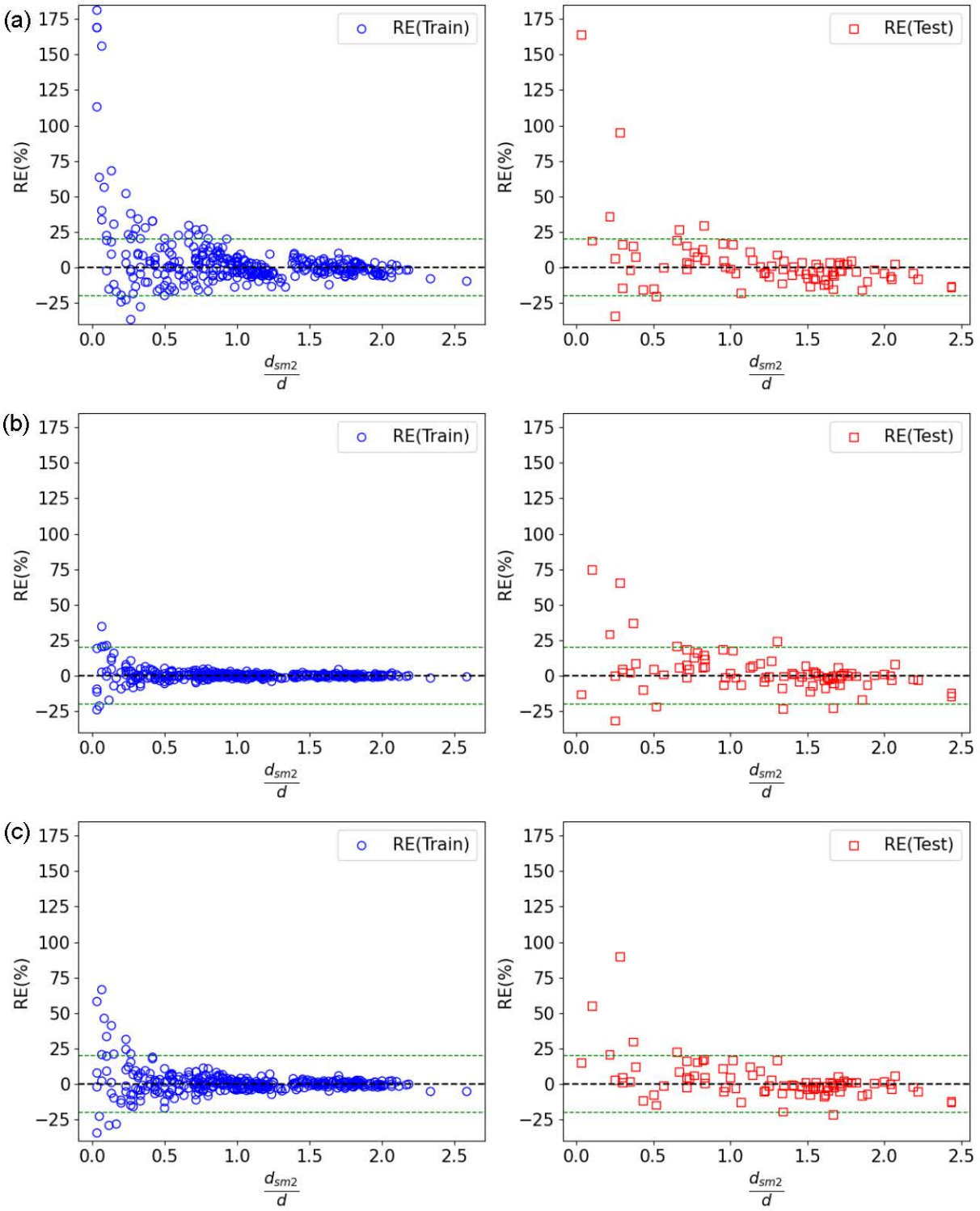

Fig. 7.15. The RE of d_{sm2}/d for the training and testing datasets using XGBoost **(a)** non-tuned, **(b)** GSCV, and **(c)** RSCV.

The RMSE values for $d_{sm1|2}/d$ predictions generated by RF and XGBoost models across three optimization techniques, with varying numbers of iterations are shown in Figs. 7.16-7.19.

As the iterations increase, the RMSE values for $d_{sm1|2}/d$ predictions decrease sharply, eventually stabilizing at asymptotic values. The learning curve of a model is considered well-fitted when the RMSE in the training phase stabilizes at a final value and the RMSE in the validation phase follows a similar trend with minimal deviation.

In this analysis, the focus is placed on the testing phase iterations, where the graphs show stable asymptotic behavior across nearly all ML models. Based on observations from Figs. 7.16-7.19, the learning behavior of the proposed RF-GSCV during training and RF-RSCV for testing has great learning behavior for Pier-1 and Pier-2. In the case of XGBoost-GSCV and XGBoost-RSCV during testing for predicting d_{sm1}/d, as well as the XGBoost-RSCV model for predicting d_{sm2}/d, aligns with these criteria. This suggests their reliability and suitability as predictive models.

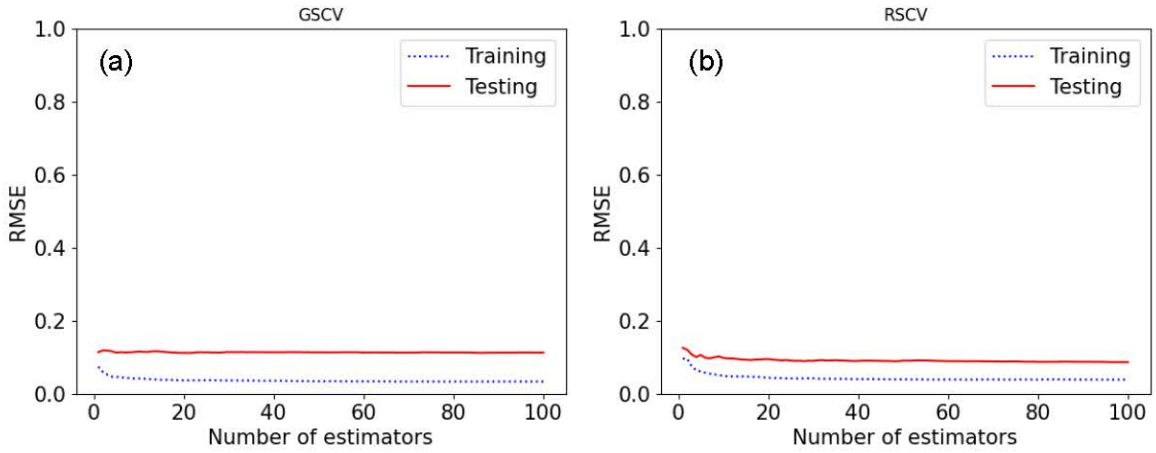

Fig. 7.16. Differences in RMSE, in d_{sm1}/d predictions for RF, and the number of iterations during both training and testing stages, **(a)** GSCV, and **(b)** RSCV.

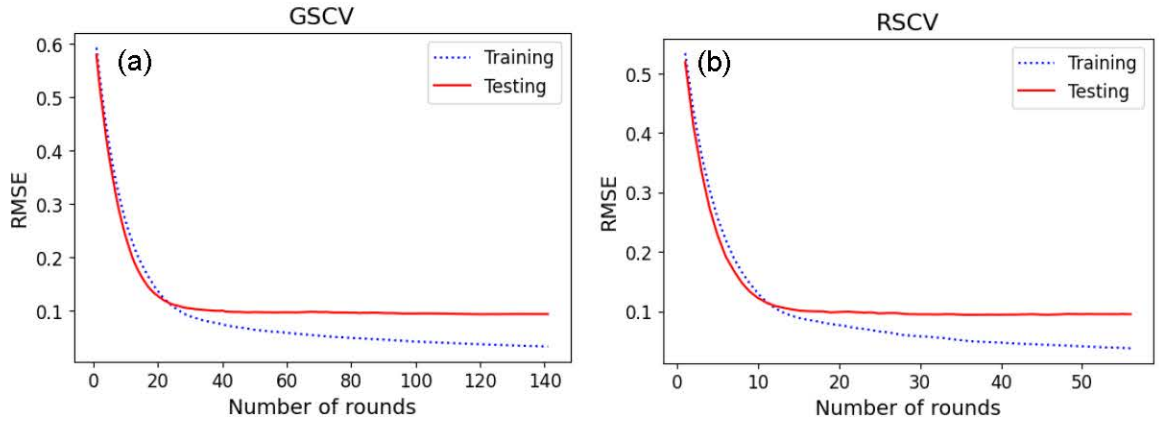

Fig. 7.17. Differences in RMSE, in d_{sm1}/d predictions for XGBoost, and the number of iterations during both training and testing stages, **(a)** GSCV, and **(b)** RSCV.

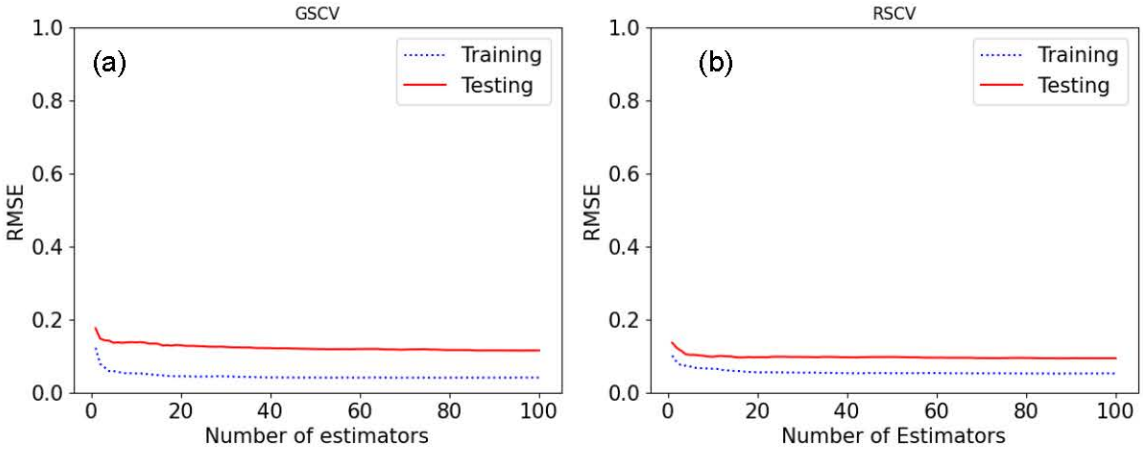

Fig. 7.18. Differences in RMSE, in d_{sm2}/d predictions for RF, and the number of iterations during both training and testing stages, **(a)** GSCV, and **(b)** RSCV.

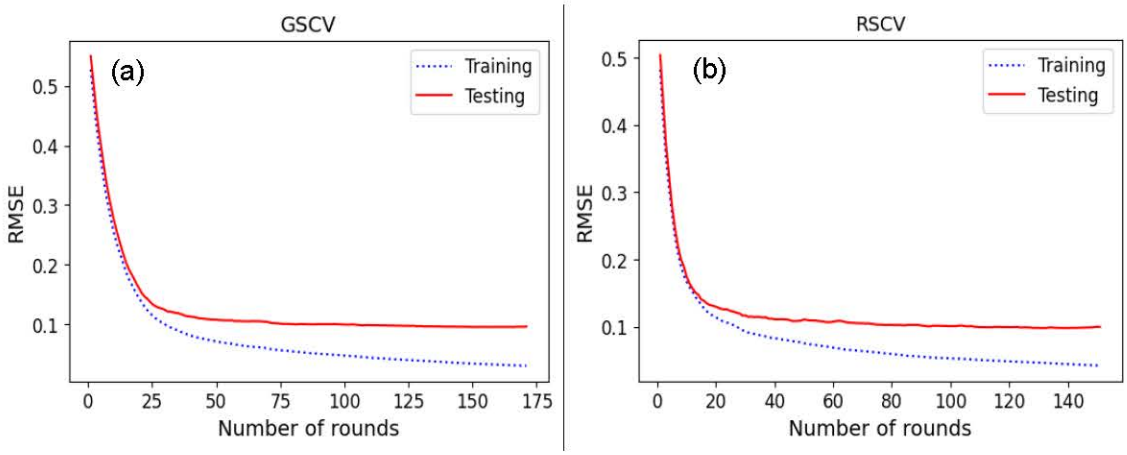

Fig. 7.19. Differences in RMSE, in d_{sm2}/d predictions for XGBoost, and the number of iterations during both training and testing stages, **(a)** GSCV, and **(b)** RSCV.

7.3.6. Effect of parameters to predict $d_{sm1|2}/d$, using PDPs

Figures 7.20-7.21 depict the partial dependence of $d_{sm1|2}/d$, on each influential parameter using single-variable PDPs based on the trained model described by Eq. (7.4), Hash marks at the bottom of each plot indicate the deciles ("Deciles" divide a dataset into ten equal parts, with each part representing 10% of the data.) of the predictor variable distribution, providing a visual representation of the data density for each parameter.

From Figs. 7.20(a-b), it can be seen that RF-RSCV and XGBoost-RSCV are the best-performing models for d_{sm1}/d prediction. The partial dependence of u/u_c for both models shows a similar increasing trend, peaking at $u/u_c = 1$. For the features d/d_{50} and r/d, the dependence on prediction appears quite consistent across the two models.

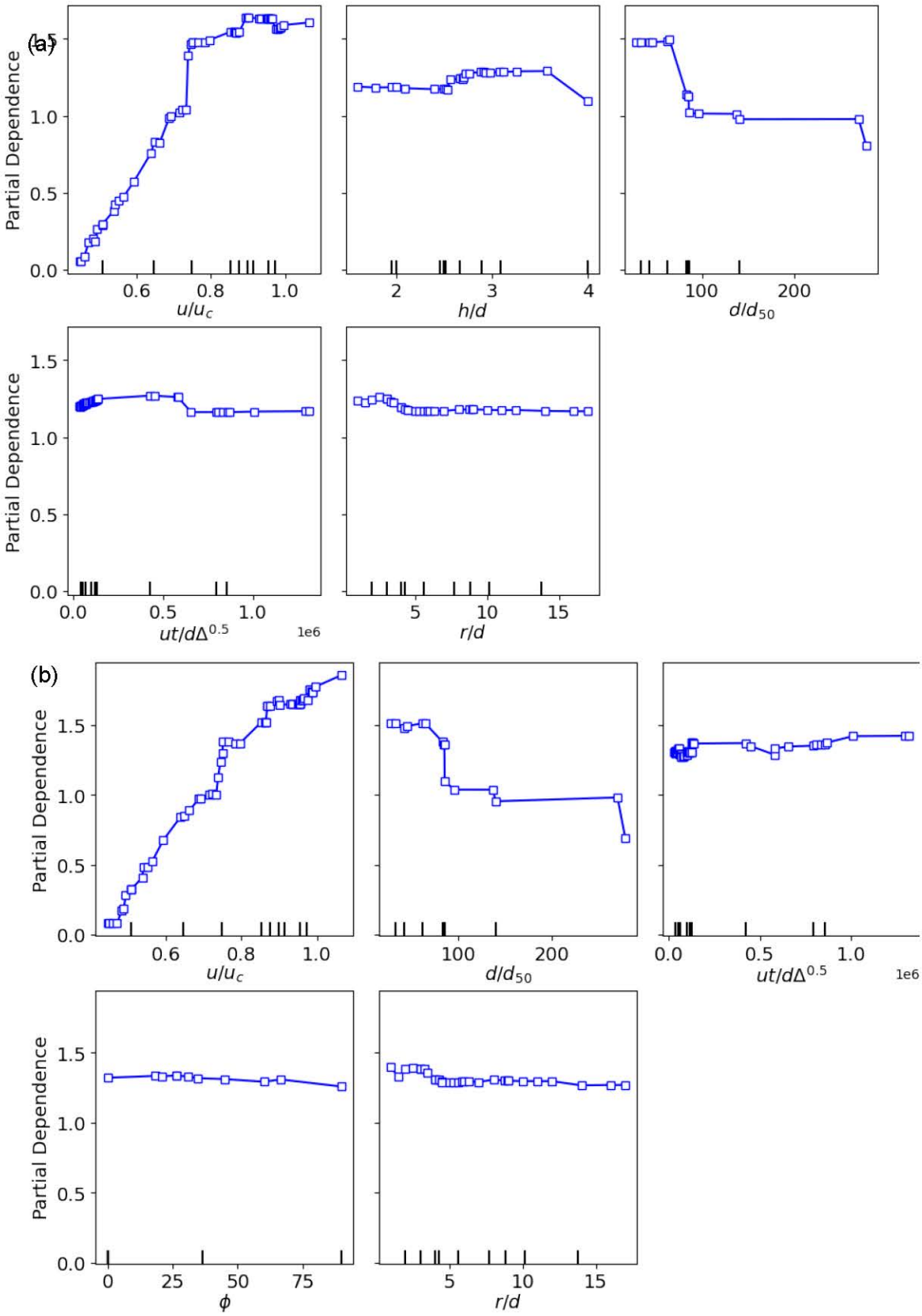

Fig. 7.20. PDPs to predict d_{sm1}/d using **(a)** RF-RSCV, and **(b)** XGBoost-RSCV.

The RF model shows that the feature h/d initially shows no significant trend, but after a value of 2.5, it shows an increasing trend, peaking around 3.5, before showing a decreasing trend afterwards. Similarly, the feature $ut/d\Delta^{0.5}$ shows an initial increasing trend, stabilizing at a constant value after approximately 0.8×10^6, which indicates no further dependence.
Whereas, the XGBoost model shows a continuously decreasing trend in the dependence of φ on d_{sm1}/d prediction. These observations highlight the distinct feature interactions captured by the two models and their implications for predicting d_{sm1}/d.

Figures 7.21(a-b) show the PDPs for predicting d_{sm2}/d using the RF and XGBoost models, both optimized using RSCV during the training stage. The effects of the parameters u/u_c, d/d_{50}, φ, $ut/d\Delta^{0.5}$, and r/d are quite similar in both models, although some differences are observed in the plots.

For both models, the effect of u/u_c shows a strictly increasing partial dependence on the prediction of d_{sm2}/d. Regarding d/d_{50}, both models show an initial decreasing trend, but after reaching a value around 130, no further dependence is observed, as shown in the figure. The effect of r/d initially shows a decreasing trend, but after a value of 5, it changes to an increasing trend for predicting d_{sm2}/d in both models.

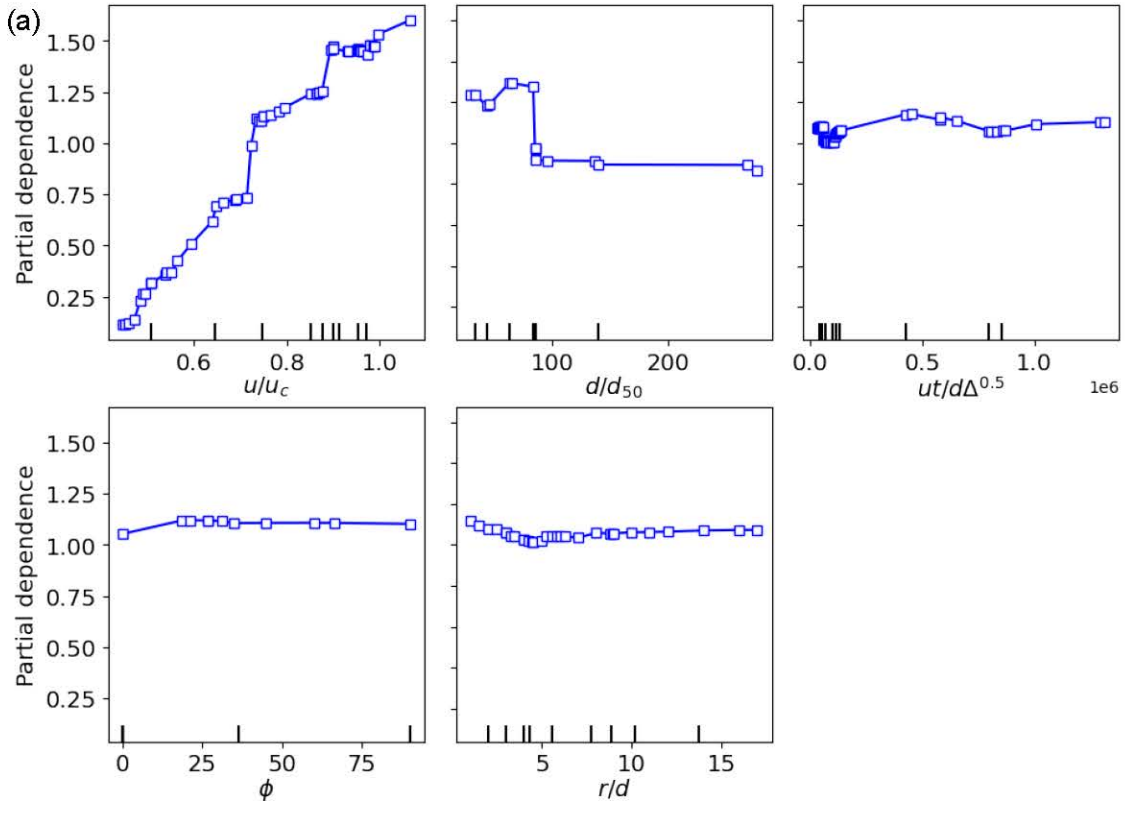

(b)

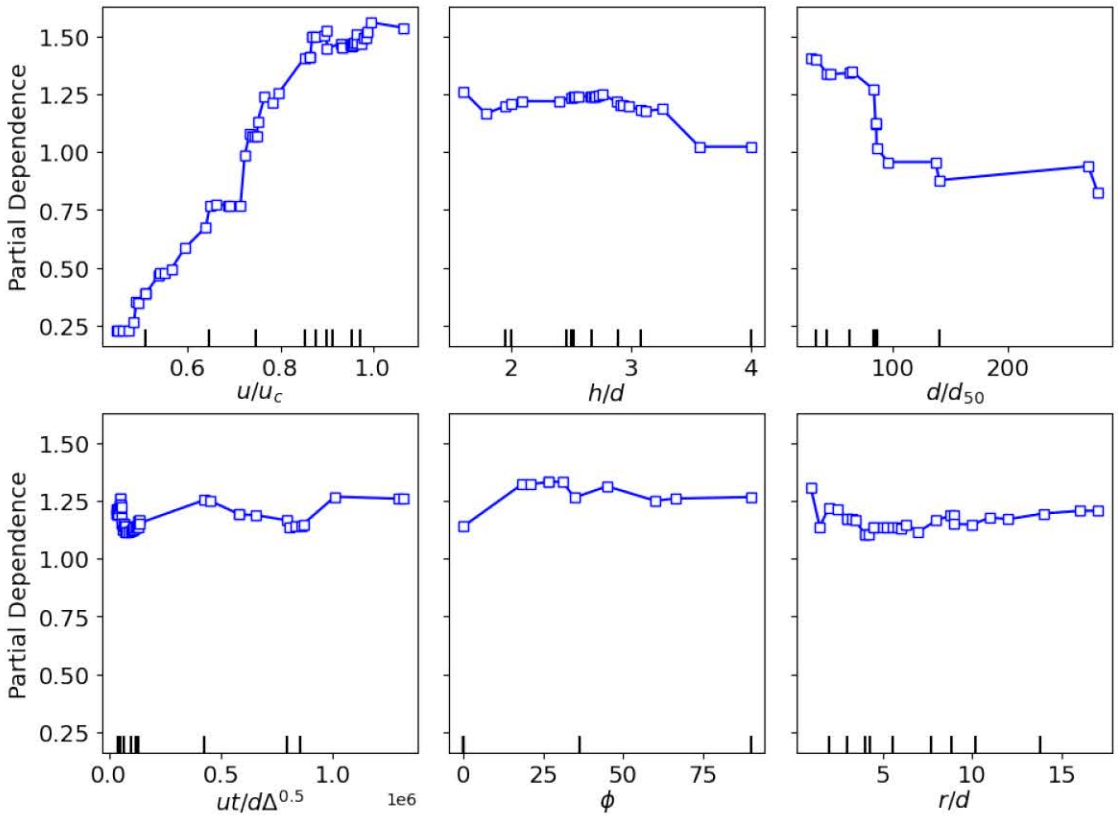

Fig. 7.21. PDPs to predict d_{sm2}/d using **(a)** RF-RSCV, and **(b)** XGBoost-RSCV.

The parameter φ shows an increasing trend initially up to about 40°, followed by a decreasing partial dependence up to 70°, after which no further dependence is observed in both models. For $ut/d\Delta^{0.5}$, there is an increasing trend in its effect on predicting d_{sm2}/d, but after a value of 1×106, the dependence stabilizes, and shows no further effect on the prediction of d_{sm2}/d. Lastly, in the XGBoost model, the effect of h/d shows a decreasing trend in predicting d_{sm2}/d.

These observations provide insight into how different features influence the prediction of d_{sm2}/d in the two models, highlighting the varying relationships between the features and the target variable.

7.3.7. Sensitivity analysis using SHAP

Figures 7.22 and 7.23 display the beeswarm plots based on the RF and XGBoost models (best models in the testing phase) for predicting $d_{sm1|2}/d$, using the feature variables obtained from the SFS-RF and SFS-XGBoost methods, respectively. In these plots, the variables are ordered on the y-axis according to their importance. The x-axis represents the mean SHAP value, which can be either positive or negative, showing the contribution of each feature to the prediction. Each point on the beeswarm plot represents a prediction, and the color of the points indicates

the actual value of the feature being plotted, not the SHAP value. The thicker areas of the beeswarm plot signify regions where there is a higher density of predictions and show a greater concentration of data points in those regions. This visualization helps in understanding the influence and distribution of different features on the prediction of model for $d_{sm1|2}/d$.

Figures 7.22(a) and 7.22(b) show the SHAP plots for RF and XGBoost models predicting d_{sm1}/d, respectively. These plots show that the parameter u/u_c has the greatest influence on the prediction of d_{sm1}/d for both models. The second most influential parameter is d/d_{50} for both RF and XGBoost. In terms of the sensitivity ranking of parameters, for the RF model, the order of importance is u/u_c, d/d_{50}, h/d, $ut/d\Delta^{0.5}$, and r/d, in both the training and testing phases. For the XGBoost model, the ranking of influential parameters is u/u_c, d/d_{50}, h/d, $ut/d\Delta^{0.5}$, and r/d, again in both the training and testing stages. These rankings provide valuable insights into the relative significance of each feature in the predictions of model.

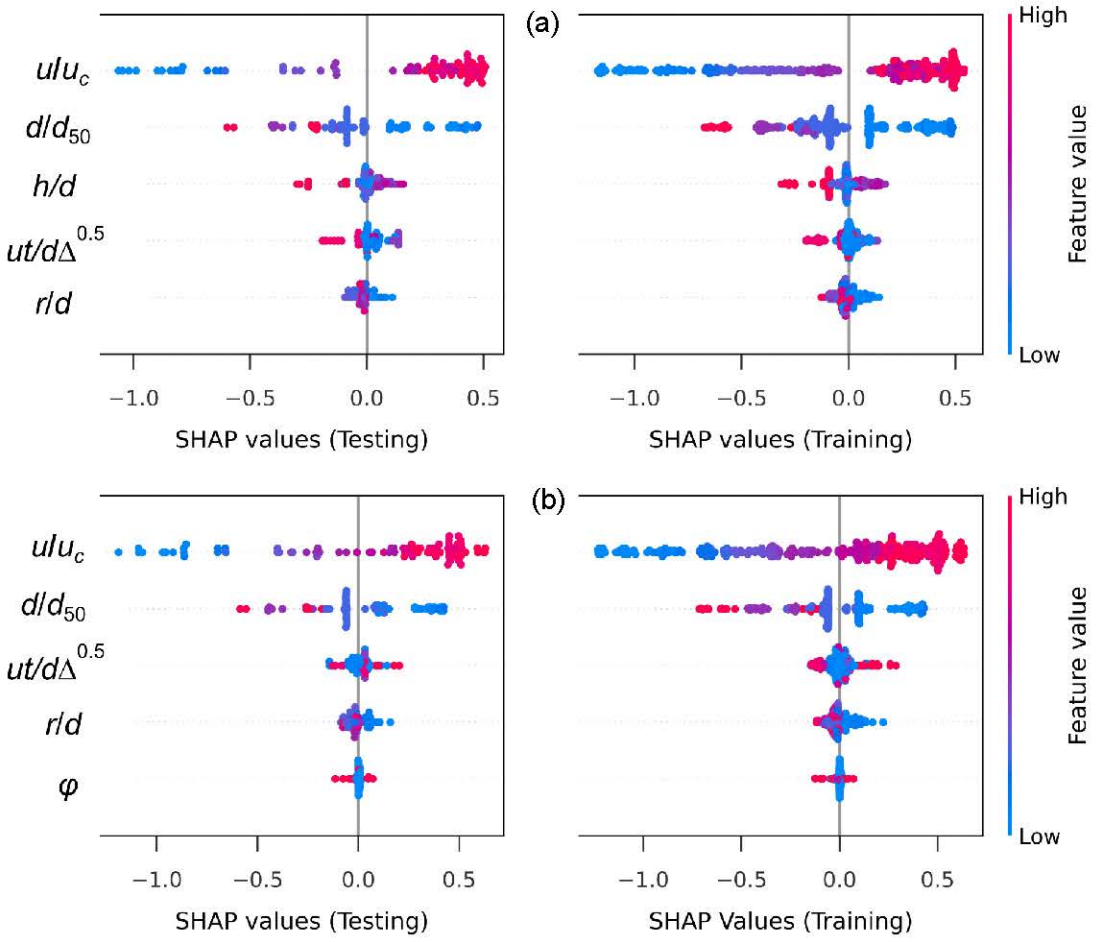

Fig. 7.22. SHAP summary plots are utilized to rank the significance of each feature in estimating d_{sm1}/d predictions, employing both **(a)** RF, and **(b)** XGBoost (best models).

The larger values of the u/u_c parameter correspond to higher SHAP values, which lead to higher d_{sm1}/d estimates. Similarly, a negative relationship is observed for d/d_{50} in both models,

as d/d_{50} increases, d_{sm1}/d decreases, which aligns with the trend seen in the PDPs. These relationships are consistent with the physical nature of the scouring process, where an increase in d/d_{50} (a larger particle size) typically reduces the d_s.

When compared to other parameters, the SHAP values for variables such as h/d, $ut/d\Delta^{0.5}$, and r/d are more uniformly distributed around the zero line, which shows a moderate influence on the d_{sm1}/d prediction. Although the SHAP plot provides insights into the relative importance of each feature, it does not directly indicate whether the influence is positive or negative for each specific value. However, this limitation can be addressed by using the PDPs, which provide a clearer understanding of the nature and direction of the influence of each parameter on the predictions of model.

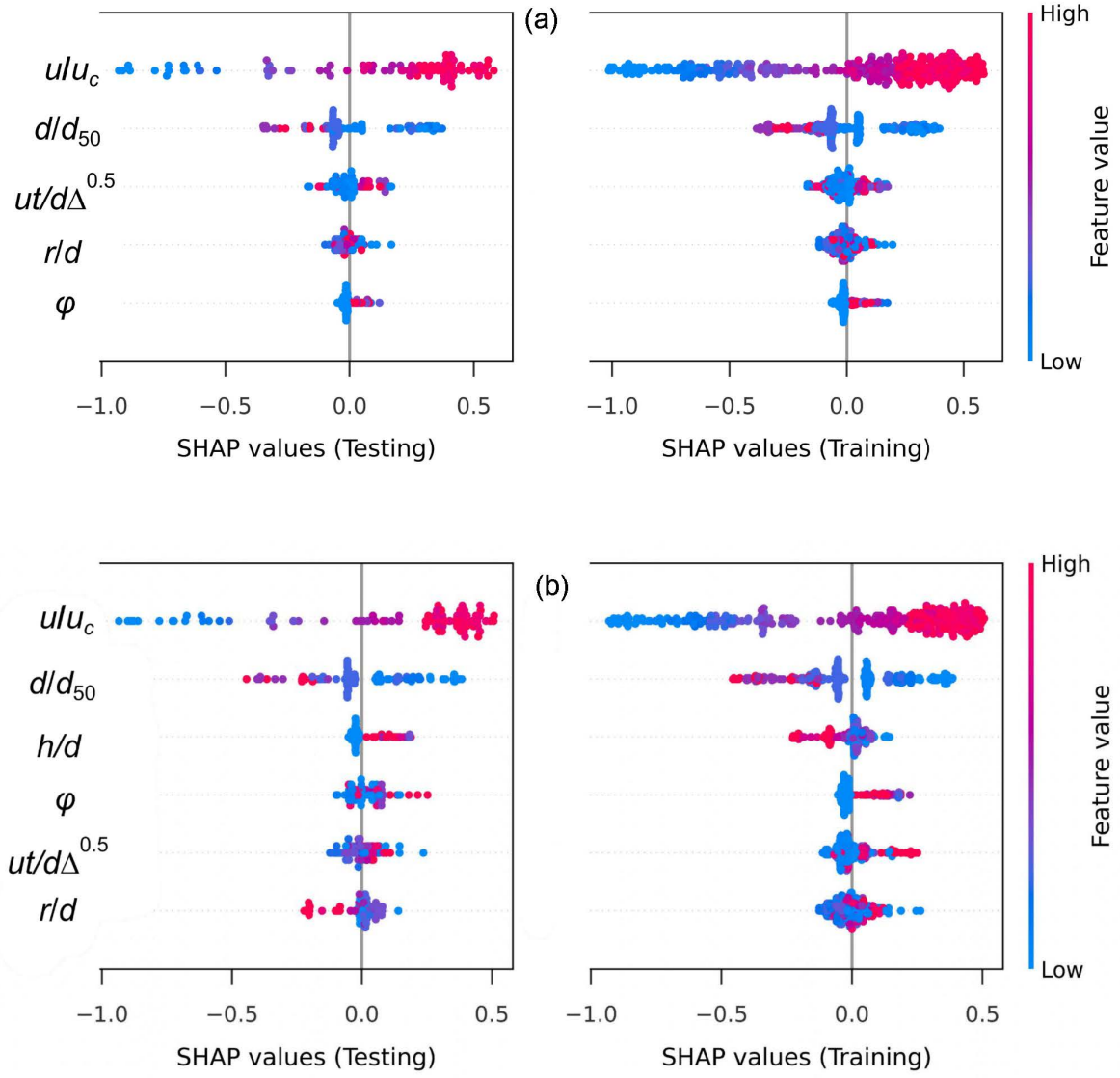

Fig. 7.23. SHAP summary plots are utilized to rank the significance of each feature in estimating d_{sm2}/d predictions, employing both **(a)** RF, and **(b)** XGBoost (best models).

Figures 7.23(a-b) show the SHAP plots for RF and XGBoost models used to predict d_{sm2}/d. Both plots show that the u/u_c parameter has the most significant influence on the d_{sm2}/d prediction for both models, followed by d/d_{50} as the second most influential parameter. In terms of sensitivity ranking for RF, the order of importance in both the training and testing phases is as follows: u/u_c, d/d_{50}, $ut/d\Delta^{0.5}$, r/d, and φ. For XGBoost, the ranking in the training phase is: u/u_c, d/d_{50}, $ut/d\Delta^{0.5}$, r/d, and φ, while in the testing phase, the order shifts slightly to u/u_c, d/d_{50}, $ut/d\Delta^{0.5}$, r/d and φ.

The accurate quantitative influence of each parameter on d_{sm2}/d can be better understood through the corresponding PDPs, which clearly show how each feature affects the d_s predictions, providing a clearer and more direct interpretation than the SHAP plots alone.

7.3.8. Ranking of ML models using Taylor diagram

The Taylor Diagram compares the performance of various models, including RF and XGBoost, under different conditions such as GSCV, RSCV, and without tuning. The key metrics analyzed CC, SD, and RMSE. Among the models, RF-RSCV shows the best performance for both d_{sm1}/d and d_{sm2}/d compared to the correlation but the deviation is high for RF-RSCV, while RF-GSCV performs better in the case of d_{sm1}/d (Fig. 7.24a). The models without tuning perform the closest to RF-GSCV for d_{sm1}/d, while for d_{sm2}/d it does not perform well (Fig. 7.24b).

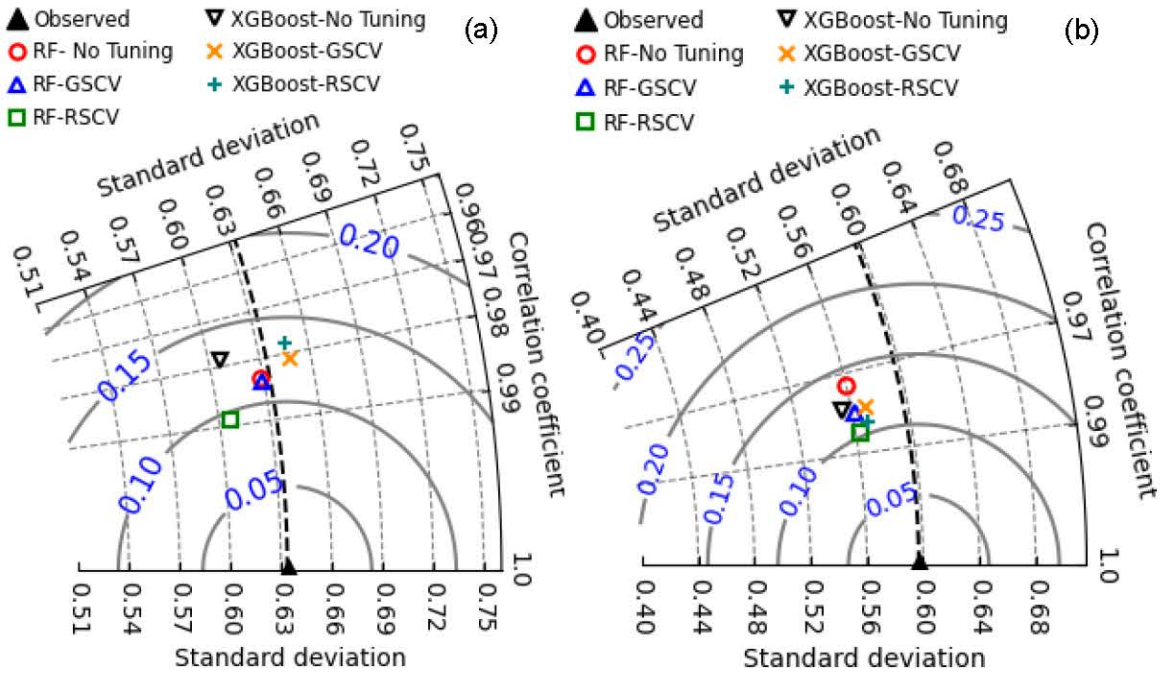

Fig. 7.24. Taylor diagram to rank the models in $d_{sm1|2}/d$ predictions using testing data **(a)** for d_{sm1}/d, and **(b)** for d_{sm2}/d.

7.3.9. Comparison with literature formula using RF-RSCV

The comparison with the best model which is RF-RSCV with the literature formula with individual arrangements are compared and given in Table 7.9.

Table 7.9. Comparison with the existing model for two pier arrangements.

Arrangement	Literature formula/ best model	Performance metrics	Pier-1	Pier-2
Side by side	RF-RSCV	R^2	0.973	0.924
		MAE	0.003	0.009
		MSE	0.039	0.056
	Malik and Setia (2020*a*)	R^2	0.127	0.131
		MAE	0.396	0.515
		MSE	0.538	0.610
Tandem	RF-RSCV	R^2	0.995	0.992
		MAE	0.003	0.003
		MSE	0.033	0.035
	Malik and Setia (2020*a*)	R^2	0.048	0.012
		MAE	0.529	0.379
		MSE	0.602	0.507
	Liu et al. (2018)	R2	0.230	0.214
		MAE	0.502	0.493
		MSE	0.429	0.483
	Wang et al. (2016)	R^2	0.230	0.225
		MAE	0.502	0.489
		MSE	0.429	0.487
Eccentric	RF-RSCV	R^2	0.986	0.967
		MAE	0.004	0.011
		MSE	0.039	0.075
	Malik and Setia (2020*a*)	R^2	0.172	0.121
		MAE	0.411	0.531
		MSE	0.465	0.555
	Das et al. (2016)	R^2	0.100	0.121
		MAE	0.583	0.626
		MSE	0.587	0.621

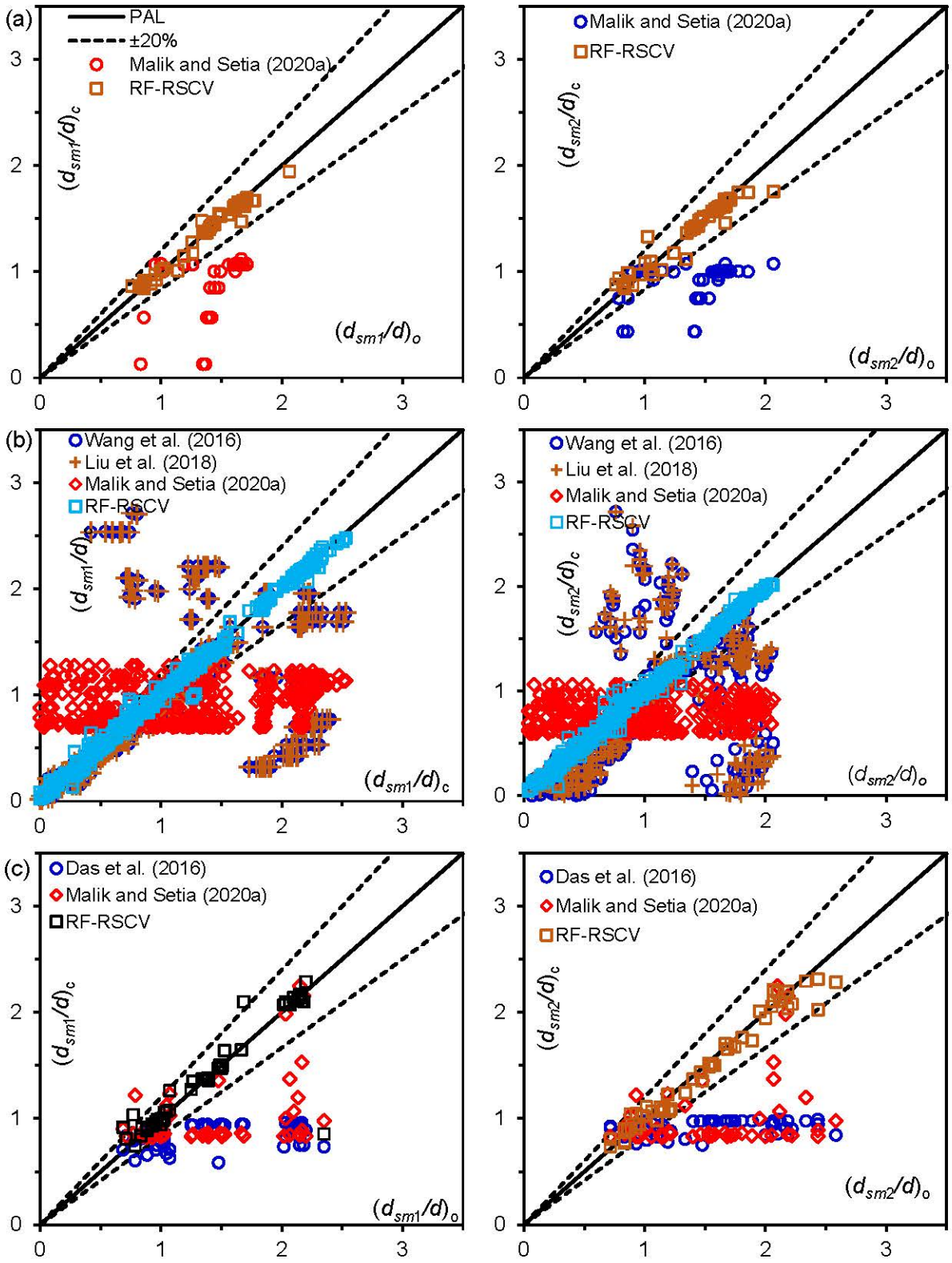

Fig. 7.25. Comparison of the predicted and observed scatter plots of d_{sm1}/d and d_{sm2}/d for the existing model with the ML model (RF-RSCV) for **(a)** side-by-side, **(b)** tandem, and **(c)** eccentric piers. (Here it has chosen only one model RF-RSCV which is the best model in case of testing data).

7.3.10. Parameter interdependence to compute scour at Pier -2

We have chosen XGBoost-GSCV, since all the influential parameters are selected through SFS, we acknowledge that the effect of each parameter is influenced by the other hydraulic parameters. This extensive analysis of parameter interdependence on d_{sm2}/d gives deep insights into flow phenomena. We believe this approach effectively captures the complex interactions and provides a more comprehensive understanding of the factors affecting to estimate d_{sm2}/d.

(a) Scour at Pier-2 with sediment coarseness and flow skew angle

An increasing trend of d_{sm2}/d is observed in the coarse sediment limb, while an opposite trend is noted in the fine sediment region. The d_s reaches a maximum at d/d_{50} around 60 (Franzetti et al. 2022). The rise in the coarse-sediment limb is consistent with many literature descriptions. However, the decrease after the maximum is more debated. Some literature, such as Melville (1997), shows d_{sm2}/d for values of d/d_{50} exceeding a certain threshold, while others (Sheppard et al. 2006, Lança et al. 2013) suggested a decrease in d_s.

In the present study, the coarse sediment data has not been found significantly, while the fine sediment experiment dominated ($d/d_{50} > 60$ for most of the literature). The Partial Dependence Plot (PDP) shows a recession limb for fine sediment that consistently decreases, aligning with the research findings of previous studies. The nature of d_{sm2}/d vs. d/d_{50} against some fixed value u/u_c =1, h/d =10, r/d =10, and $ut/d\Delta^{0.5}$ = its maximum value, showing the effect for different φ values (Fig. 7.26a).

(b) Analysis of the effect of flow intensity on scour at pier-2 with time

This analysis focuses on the maximum scour condition, which is achieved at a specific t referred to as the maximum t for a given experiment. It can be seen that the d_s increases with higher u/u_c, as illustrated in the figure below (Fig. 7.26b). During this maximum t, the d_s for each experiment reaches a quasi-equilibrium stage, reflecting the conditions of that particular experiment. If we consider the temporal evolution of a specific experiment, we can observe an increasing trend in d_s. However, since the abscissa in the figure represents discrete maximum t plotted against d_s on the ordinate, no general trend is immediately apparent. The nature of d_{sm2}/d vs. $ut/d\Delta^{0.5}$ against some fixed value h/d =10, u/u_c =1, d/d_{50} =100, and for r/d = 10, showing the effect for different u/u_c.

(c) The effect of skew angle and pier spacings on scour at Pier-2

The d_{sm2}/d decreases with the increase of r/d, which aligns with the literature studies. Also, the d_{sm2}/d increases for small $\varphi°$ for the eccentric pier as evidenced by the model in Fig. 7.26c. The nature of d_{sm2}/d plotted against u/u_c =1, h/d =10, d/d_{50} =100, and $ut/d\Delta^{0.5}$ = its maximum value.

(d) The Effect of pier spacings on scour at Pier-2 against flow skew angles

The effect of the parameter r/d on d_{sm2}/d was analyzed against various values of φ, and a similar physical trend was observed as reported by Qi et al. (2019). In their study, they normalized the d_s using the d_s of a single pier. This dimensionless approach yielded consistent trends for both cases. However, for angles of 0° and 90°, most studies and available data focus on side-by-side and tandem pier configurations, as there is more data available for these arrangements. Our results showed similar trends to those found in the literature for these configurations. Whereas, there is limited data available for eccentric pier configurations, so the trends for such arrangements may differ. We acknowledge the data limitations in our study for eccentric pier configurations. The nature of d_{sm2}/d vs. r/d against some fixed value u/u_c =1, h/d =10, d/d_{50} =100, and $ut/d\Delta^{0.5}$ = its maximum value, with different φ (Fig. 7.26d).

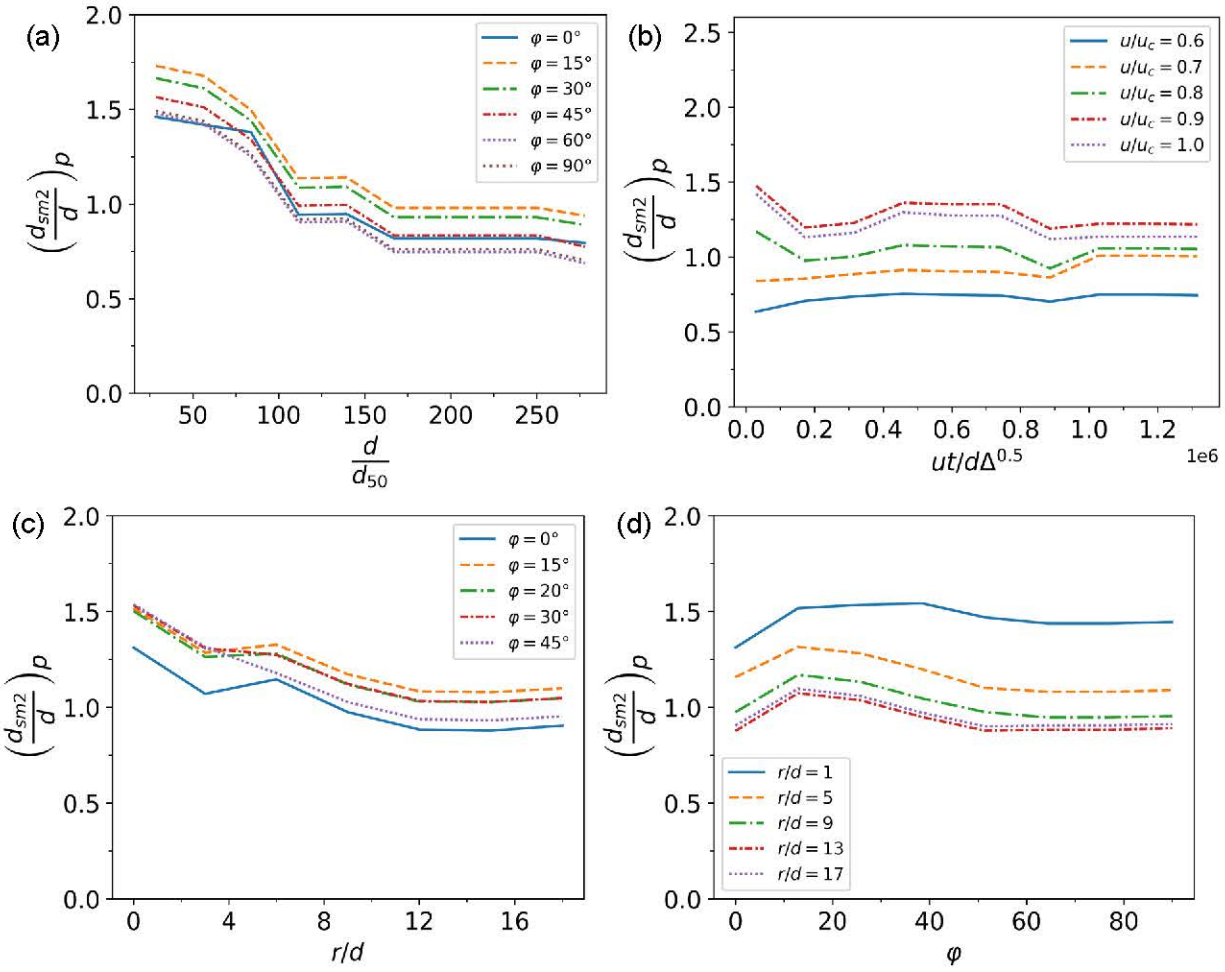

Fig. 7.26. The effect of **(a)** d/d_{50} on d_{sm2}/d against different φ, **(b)** $ut/d\Delta^{0.5}$ on d_{sm2}/d against different u/u_c, **(c)** $ut/d\Delta^{0.5}$ on d_{sm2}/d against different r/d, and **(d)** r/d on d_{sm2}/d against different φ.

7.4. Conclusions

In real life, complex flow occurs with multiple bridge piers like side-by-side, tandem, or eccentric arrangements. Predicting maximum socur depth (d_{sm}) near these piers is a major challenge. However, literature includes research that used only either CFD tools or numerically solved problems to compute such d_s. Some research used lab data to empirically compute d_s for such complex arrangements. Therefore, in this study, the impact of pier spacing and placement on estimating d_{sm} are analyzed using ensemble ML methods like Random Forest (RF) and Extreme Gradient Boosting (XGBoost). The aim is to predict both front and rear pier d_{sm} effectively. The Partial Dependence Plots (PDPs) and SHapley Additive exPlanations (SHAP) are used to demonstrate the importance of features. The effectiveness of the ensemble ML model performance is evaluated using R^2, MAE and MSE metrics.

- For the feature selection sequential forward selection with RF and XGBoost applied and the set selected feature for Pier-1 are [u/u_c, h/d, d/d_{50}, $ut/d\Delta^{0.5}$, R], [u/u_c, d/d_{50}, $ut/d\Delta^{0.5}$, φ, R] and for Pier-2 are [u/u_c, d/d_{50}, $ut/d\Delta^{0.5}$, φ, R], [u/u_c, h/d, d/d_{50}, $ut/d\Delta^{0.5}$, φ, r/d].
- RF-GSCV (Pier-1) showed the highest performance in training with R^2 = 0.997, MAE = 0.023 and MSE = 0.001, and when compared to testing RF-RSCV (Pier-1) showed the highest performance in predicting d_{sm1}/d with R^2 = 0.979, MAE = 0.063 and MSE = 0.008.
- RF-GSCV (Pier-2) in the training phase showed results with the highest R^2 = 0.995, MAE = 0.028 and MSE = 0.002. In the case of the testing phase the RF-RSCV (Pier-2) is best best-performing model, with R^2 = 0.972, MAE = 0.068, and MSE = 0.009.
- XGBoost-RSCV (Pier-1) gives the highest accuracy in the training phase to predict d_{sm1}/d, with R^2 = 0.997, MAE = 0.029 and MSE = 0.001. In the testing phase, XGBoost-GSCV (Pier-1) both give the highest accuracy with identical values considering three decimal places, with R^2 = 0.962, MAE = 0.075 and MSE = 0.015.
- XGBoost-GSCV (Pier-2) gives the highest accuracy in the training phase with R^2 = 0.999, MAE = 0.011 and MSE = 0.000. In the testing phase, XGBoost-RSCV gives the highest accuracy with identical values considering three decimal places, with R^2 = 0.968, MAE = 0.076 and MSE = 0.011.
- The SHAP plot shows u/u_c as the most influential parameter for all models, followed by d/d_{50}. In RF and h/d, φ is the least influential, while r/d is the least important in the XGBoost model.
- PDPs quantitatively depict each parameter. The u/u_c shows increasing trends in all plots, while d/d_{50}, decreases across models. Other parameters show moderate dependence.

To prevent overfitting, we avoided adding extra data through data augmentation in training when experimental data was lacking. However, it is not recommended for sensitive cases due to associated risks. Due to data scarcity on certain pier combinations, the model showing overfitting in the current scenario is used only for comparison, which shows that it should be ignored. Further experiments are vital to enhance understanding of complex phenomena.

Employing more advanced ML models and parameter optimization techniques will improve predictive capabilities.

References

Ahmad, N., Bihs, H., Myrhaug, D., Kamath, A., and Arntsen, Ø.A. (2018). Three-dimensional numerical modelling of wave-induced scour around piles in a side-by-side arrangement. *Coastal Engineering, 138*, 132–151.

Amini, A., and Parto, A.A. (2017). 3D numerical simulation of flow field around twin piles. *Acta Geophysica, 65*(6), 1243–1251.

Ataie-Ashtiani, B., and Aslani-Kordkandi, A. (2013). Flow field around single, tandem piers. *Flow, Turbulence and Combustion, 90*, 471–490.

Ballio, F., Teruzzi, A., and Radice, A. (2009). Constriction effects in clear-water scour at abutments. *Journal of Hydraulic Engineering, 135*(2), 140–145.

Bateni, S.M., Borghei, S.M., and Jeng, D.S. (2007). Neural network and neuro-fuzzy assessments for scour depth around bridge piers. *Engineering Applications of Artificial Intelligence, 20*(3), 401–414.

Beg, M., and Beg, S. (2015). Scour hole characteristics of two unequal size bridge piers in tandem arrangement. *ISH Journal of Hydraulic Engineering, 21*(1), 85–96.

Bordbar, A., Sharifi, S., Guo, Z., and Hemida, H. (2022). Estimating the equilibrium scour depth around two side-by-side piers with different spacing ratios in live-bed conditions. *Ocean Engineering, 257*, 111641.

Breiman, L. (2001). Random forests. *Machine Learning, 45*(1), 5–32.

Chabert, J., and Engeldinger, P. (1956). Étude des affouillements autour des piles de ponts. [In French.] Technical Report, Laboratoire National d'Hydraulique, Chatou, France.

Chen, T., and Guestrin, C. (2016). XGBoost: A scalable tree boosting system. *KDD '16 Proceedings of the 22nd ACM SIGKDD Conference on Knowledge Discovery and Data Mining*, 785–794.

Chiew, Y.M. (1995). Mechanics of riprap failure at bridge piers. *Journal of Hydraulic Engineering, 121*(9), 635–643.

Choi, S.U., Choi, B., and Lee, S. (2017). Prediction of local scour around bridge piers using the ANFIS method. *Neural Computing and Applications, 28*(2), 335–344.

Choi, S.U., and Choi, S. (2022). Prediction of local scour around bridge piers in the cohesive bed using support vector machines. *KSCE Journal of Civil Engineering, 26*(5), 2174–2182.

Das, R., Das, S., Jaman, H., and Mazumdar, A. (2019). Impact of upstream bridge pier on the scouring around adjacent downstream bridge pier. *Arabian Journal for Science and Engineering, 44*, 4359–4372.

Das, R., Khwairakpam, P., Das, S., and Mazumdar, A. (2014). Clear water local scour around eccentric multiple piers to shift the line of sediment deposition. *Asian Journal of Water, Environment and Pollution, 11*(3), 47–54.

Das, S., Das, R., and Mazumdar, A. (2013). Circulation characteristics of horseshoe vortex in the scour region around circular piers. *Water Science and Engineering, 6*(1), 59–77.

Das, S., Das, R., and Mazumdar, A. (2016). Comparison of local scour characteristics around two eccentric piers of different shapes. *Arabian Journal for Science and Engineering, 41*, 1199–1213.

Das, S., and Mazumdar, A. (2015). Turbulence flow field around two eccentric circular piers in scour hole. *International Journal of River Basin Management, 13*(3), 343–361.

Devi, G., and Kumar, M. (2022*a*). Characteristics assessment of local scour encircling twin bridge piers positioned side by side (SbS). *Sādhanā, 47*(3), 109.

Devi, G., and Kumar, M. (2022*b*). Experimental study of the local scour around the two piers in the tandem arrangement using ultrasonic ranging transducers. *Ocean Engineering, 266*, 112838.

Ebtehaj, I., Bonakdari, H., Zaji, A. H., and Sharafi, H. (2019). Sensitivity analysis of parameters affecting scour depth around bridge piers based on the non-tuned, rapid extreme learning machine method. *Neural Computing and Applications, 31*, 9145–9156.

Eini, N., Bateni, S. M., Jun, C., Heggy, E., and Band, S. S. (2023). Estimation and interpretation of equilibrium scour depth around circular bridge piers by using optimized XGBoost and SHAP. *Engineering Applications of Computational Fluid Mechanics, 17*(1), 2244558.

Firat, M. (2009). Scour depth prediction at bridge piers by ANFIS approach. *Proceedings of ICE-Water Management, 162*(4), 279–288.

Firat, M., and Gungor, M. (2009). Generalized regression neural networks and feed forward neural networks for prediction of scour depth around bridge piers. *Advances in Engineering Software, 40*(8), 731–737.

Franzetti, S., Radice, A., Rebai, D., and Ballio, F. (2022). Clear water scour at circular piers: a new formula fitting laboratory data with less than 25% deviation. *Journal of Hydraulic Engineering, 148*(10), 04022021.

Friedman, J.H. (2001). Greedy function approximation: A gradient boosting machine. *Annals of Statistics, 29*(5), 1189–1232.

Greenwell, B. M., Boehmke, B. C., and McCarthy, A. J. (2018). A simple and effective model-based variable importance measure. *arXiv preprint arXiv:1805.04755*.

Guven, A., Azamathulla, H. M., and Zakaria, N. (2009). Linear genetic programming for prediction of circular pile scour. *Ocean Engineering, 36*(12–13), 985–991.

Hamidi, A., and Siadatmousavi, S. M. (2018). Numerical simulation of scour and flow field for different arrangements of two piers using SSIIM model. *Ain Shams Engineering Journal, 9*(4), 2415–2426.

Hannah, C. R. (1978). *Scour at pile groups*. Research Report No. 28–3, Civil Engineering Dept., University of Canterbury, Christchurch, New Zealand.

Jaman, H., Das, S., Das, R., and Mazumdar, A. (2017). Hydrodynamics of flow obstructed by inline and eccentrically-arranged circular piers on a horizontal bed surface. *Journal of the Institution of Engineers (India): Series A, 98*, 77–83.

Keshavarzi, A., Shrestha, C.K., Melville, B., Khabbaz, H., Ranjbar-Zahedani, M., and Ball, J. (2018). Estimation of maximum scour depths at upstream of front and rear piers for two in-line circular columns. *Environmental Fluid Mechanics, 18*, 537–550.

Khaple, S., Hanmaiahgari, P. R., Gaudio, R., and Dey, S. (2017). Interference of an upstream pier on local scour at downstream piers. *Acta Geophysica, 65*, 29–46.

Kim, H. S., Nabi, M., Kimura, I., and Shimizu, Y. (2014). Numerical investigation of local scour at two adjacent cylinders. *Advances in Water Resources, 70*, 131–147.

Kumar, S., Goyal, M.K., Deshpande, V., and Agarwal, M. (2023). Estimation of time dependent scour depth around circular bridge piers: Application of ensemble machine learning methods. *Ocean Engineering, 270*, 113611.

Liang, F., Wang, C., Huang, M., and Wang, Y. (2017). Experimental observations and evaluations of formulae for local scour at pile groups in steady currents. *Marine Georesources & Geotechnology, 35*(2), 245–255.

Liu, Q.S., Tang, H.W., Wang, H., and Xiao, J.F. (2018). Critical velocities for local scour around twin piers in tandem. *Journal of Hydrodynamics, 30*, 1165–1173.

Lundberg, S. M., and Lee, S.I. (2017). A unified approach to interpreting model predictions. *Advances in Neural Information Processing Systems, 30*, 4765–4774

Malik, R., and Setia, B. (2014). Experimental study on behavior of closely placed bridge pier models. In Proceedings of the National Conference in Department of Civil Engineering, National Institute of Technology Kurukshetra, Kurukshetra, India.

Malik, R., and Setia, B. (2020*a*). Interference between pier models and its effects on scour depth. *SN Applied Sciences, 2*, 68.

Malik, R., and Setia, S. (2020b). Prediction of scour depth around bridge piers in tandem arrangement using M5 and ANN regression models. *Archives of Materials Science and Engineering, 102*(2).

Malik, R., and Setia, B. (2021). Local scour around closely placed bridge piers. *ISH Journal of Hydraulic Engineering, 27*(4), 396–403.

Melville, B.W. (1997). Pier and abutment scour: Integrated approach. *Journal of Hydraulic Engineering, 123*(2), 125–136.

Melville, B.W., and Chiew, Y.M. (1999). Time scale for local scour at bridge piers. *Journal of Hydraulic Engineering, 125*(1), 59–65.

Memar, S., Zounemat-Kermani, M., Beheshti, A., Rahimpour, M., Cesare, G.D., and Schleiss, A.J. (2020). Influence of collars on reduction in scour depth at two piers in a tandem configuration. *Acta Geophysica, 68*, 229–242.

Monti, R. (1994). Indagine sperimentale delle caratteristiche fluidodinamiche del campo di moto intorno ad una pila circolare. Tesi di Dottorato di Ricerca. Politecnico di Milano, Milan, Italy (in Italian).

Namaee, M., and Sui, J. (2019). Local scour around two side-by-side cylindrical bridge piers under ice-covered conditions. *International Journal of Sediment Research, 34*(4), 355–367.

Nandi, B., and Das, S. (2023). Identify most promising temporal scour depth formula for circular piers proposed over last six decades. *Ocean Engineering, 286*(2), 115639.

Nandi, B., and Das, S. (2024). Equation for time-dependent local scour at pier-like structures with eccentric in-line arrangements. *Proceedings of the Institution of Civil Engineers - Water Management, 177*(6), 361–374.

Nandi, B., Patel, G., and Das, S. (2024). Prediction of maximum scour depth at clear water conditions: Multivariate and robust comparative analysis between empirical equations and machine learning approaches using extensive reference metadata. *Journal of Environmental Management, 354*, 120349.

Okhravi, S., Gohari, S., Alemi, M., and Maia, R. (2023). Numerical modeling of local scour of non-uniform graded sediment for two arrangements of pile groups. *International Journal of Sediment Research, 38*(4), 597–614.

Pal, M., Singh, N., and Tiwari, N. (2012). M5 model tree for pier scour prediction using field dataset. *KSCE Journal of Civil Engineering, 16*(6), 1079–1084.

Puspasari, A. D., and Tang, J. H. (2023). Numerical simulation of scouring around groups of six cylinders with different flow directions. *Journal of the Chinese Institute of Engineers, 46*(4), 420–430.

Qi, W.G., Li, Y.X., Xu, K., and Gao, F.P. (2019). Physical modelling of local scour at twin piles under combined waves and current. *Coastal Engineering, 143*, 63–75.

Rückstieß, T., Osendorfer, C., and van der Smagt, P. (2011). Sequential feature selection for classification. In D. Wang and M. Reynolds (Eds.), *AI 2011: Advances in Artificial Intelligence. AI 2011* (Lecture Notes in Computer Science, vol 7106, pp. 209–221). Springer, Berlin, Heidelberg.

Sahu, C., Eldho, T. I., and Mazumder, B. S. (2023). Experimental study of flow hydrodynamics around circular cylinder arrangements using particle image velocimetry. *Journal of Fluids Engineering, 145*(1), 011302.

Shapley, L. S. (1953). A value for n-person games. *Contributions to the Theory of Games II*, 307–317.

Wang, H., Tang, H., Liu, Q., and Wang, Y. (2016). Local scouring around twin bridge piers in open-channel flows. *Journal of Hydraulic Engineering, 142*(9), 06016008. Wardhana, K., and Hadipriono, F. C. (2003). Analysis of recent bridge failures in the United States. *Journal of Performance of Constructed Facilities, 17*(3), 144–150.

Yilmaz, M., Yanmaz, A.M., and Koken, M. (2017). Clear-water scour evolution at dual bridge piers. *Canadian Journal of Civil Engineering, 44*(4), 298–307.

Chapter 8

Temporal Scour around Eccentric Piers: Experimental Study

8.1. Introduction

Local scour occurs when sediment around a bridge pier is washed away by flowing water called scour depth (d_s). This sediment removal is the main cause of bridge failure. Research shows that hydraulic issues led to 55% of bridge failures in the USA (Xiong et al. 2023). Scour at a pier occurs under clear-water or live-bed conditions, depending on whether the flow carries sediment. Chabert and Engeldinger (1956) first explained how scour at a circular pier develops over time (t) and with flow velocity (u).

In clear-water equilibrium d_s (d_{se}) is gradually increased and achieved when the rate of scour is very low (Sheppard et al. 2023). Scour is also affected by pier shape and alignment with the flow (Fael et al. 2016). In laboratory experiments, scaled-down bridge pier models, often circular, are used in sediment beds. Circular piers are a standard reference that allows for variability adjustments using correction factors (Franzetti et al. 2022). Over time, researchers have developed many formulas to estimate d_{se} for bridge piers, mainly for isolated piers (see Chapters 3, and 4). However, formulas for eccentric pier arrangements are still scarce (Nandi and Das 2024).

Urban growth and increased traffic often require building new bridges near older ones. This setup looks like two piers that may be aligned, eccentrically in some cases for example Nivedita and Vivekananda bridges in Kolkata (Das et al. 2019). The scour mechanism for such two pier groups creates complex interference. This makes maximum d_s (d_{sm}) predictions much more difficult. Four scour mechanisms occur around pier groups are reinforcing, sheltering, shed vortices, and compressed horseshoe vortices (Hannah 1978). When the rear pier is close to the front pier, the scour hole is overlapped, increasing d_s through reinforcing. However, the front pier reduces the effectiveness of the rear pier approach u, which creates a sheltering effect.

Semi-empirical formulas are developed to predict d_{sm} for pier groups by combining pier positioning factor with isolated pier formulas (*HEC-18:* Richardson and Davis 2001, *New Zealand formula*: Melville and Coleman 2000, *Chinese formulas 65-1*: Gao 1993 and *65-2*: Hoang 2015) by different researchers. These formulas are often compared to predictions for single piers however for complex pier scenarios these can be used by adding factors for pier

positions (e.g., Amini et al. 2012, Liang et al. 2017), these formulas are sometimes used for real-world data (Liang et al. 2019).

After different studies on pier groups (Sumer et al. 2005, Sheppard et al. 2023), a complete understanding of scour geometry piers with eccentric arrangements is still limited. Most studies on pier groups have focused on tandem (Beg and Beg 2015, Wang et al. 2016, Liu et al., 2018) or side-by-side (Malik and Setia 2014, Devi and Kumar 2022) arrangements to study the effect of pier spacing on d_s. Some studies examined the impact of longitudinal spacing (l) variations (Das et al. 2016, Khaple et al. 2017), but fewer have studied variations in transverse spacing (Beg 2004, Malik and Setia 2020).

Based on previous research on scouring, this study focuses on experimentally minimizing the scour around bridge piers arranged eccentrically at varying eccentricity (e). The fixed l = 5.2d (Das et al. 2016) is considered to deal with the worst-case scenario for d_{sm}, d is pier diameter. The goal is to find the minimum scour position for eccentric piers with different e. Clear-water scour conditions are considered in this study because the d_{se} is about 10% greater than the mean d_{se} in live beds (Shen et al. 1969). The effects of flow shallowness (h/d), flow intensity (u/u_c), and e are studied to evaluate mutual interference based on single pier d_s (d_{ss}) as a basis for comparison Here, h is flow depth, u_c is critical velocity. The study analyzes the scour area, size of scour holes, d_{sm}, and d_{st} for various e. The accuracy of the newly developed regression formula is assessed by comparing predictions with experimental data from this study and data from the literature. The newly developed formula is compared with the literature formula and assessed using different performance indicators.

8.2. Methods

8.2.1. Experimental setup

The experimental setup, data acquisition system, and measured variables in this study are thoroughly explained here. The development of d_{st} around eccentric bridge pier models is investigated through 24 experiments and four isolated pier experiments. All experiments are conducted in the Fluvial Hydraulics Laboratory at the School of Water Resources Engineering, Jadavpur University, Kolkata, West Bengal, India. Each element is given in Fig. 8.1.

(a) Experimental flume

In this study, all experiments are conducted in a large recirculating rectangular flume measuring 11 m in length, 0.81 m in width (internal), and 0.60 m in depth (Fig. 8.1a). The flume is divided into three sections: inlet, outlet, and a working section in the middle. At the inlet, a stilling basin with a perforated baffle wall and two vertical steel screens spans the entire cross-section to reduce flow turbulences. The working section, 5 m long and located 3 m from the inlet gate, ensures fully developed turbulence. It features a steel bottom and Plexiglas side walls for visual

observation. The water level is monitored over time to confirm steady and uniform flow. Water discharge (Q) is measured by a flowmeter connected to the delivery pipe and maintained at 20 lps through adjustments to the outlet and bypass valves. The h is controlled by a tailgate at the downstream end. A movable trolley with a Laser Distance Meter (LDS) and Vernier point gauge is used to measure water level, initial bed level, and d_s.

(b) Pump

The recirculating flow system is powered by a 10-hp variable-speed centrifugal pump (Fig. 8.1b) with a maximum Q capacity of 30 lps. The pump operates at a rotational speed of 1430 rpm and has a power output of 7.5 kW. Water is supplied through a 20 cm diameter pipeline that leads directly to the flume. The pump allows precise control of flow rates, ensuring constant water Q and stable experimental conditions. It has high efficiency and reliability which are crucial for maintaining steady flow and minimizing fluctuations that could affect the accuracy of scour measurements. Two pumps are used alternately, ensuring backup and reducing downtime, so operations can continue even if one pump needs maintenance.

(c) Flowmeter

A flowmeter is a device designed to monitor and measure the Q, and pressure of fluids. It serves a crucial role in various applications across industries, ensuring precise management and control of fluid dynamics. In our experiments, we have used a DASMESH model flowmeter (Fig. 8.1c) for these measurements, ensuring the application of precise and dependable data for this analysis.

(d) Laser distance sensor

The Leica DISTO^{TM} D110 Laser Distance Sensor (LDS) (Fig. 8.1d) is used to measure the bed surface and scour profiles around the pier, both lengthwise and widthwise. It can measure up to 70 meters (about 230 feet) with an accuracy of ±1.5 mm. The sensor works at a frequency of 2402–2480 MHz and operates in temperatures ranging from –25 °C to 70 °C. The main advantage of the sensor is that it provides fast and precise measurements.

(e) Sediment bed

The Shields diagram is commonly used to determine the threshold conditions for uniform sediments. By using the fluid density (ρ_f), viscosity (ν), and sediment density (ρ_s), the diagram helps plot the critical shear velocity (u_{*c}) against the median particle size (d_{50}). However, for non-uniform sediments, determining threshold conditions is more complex. The particle size distribution plays a role, so the u_{*c} depends on both the median d_{50} and the geometric standard deviation of sand (σ).

The mobile bed zone, which is about 5 meters long, is filled with sand to a depth of 0.2 meters. This section is located around 3 meters downstream from the flume inlet gate to ensure the flow is fully developed. A sieve analysis is performed to describe the sand used in the study. The results show that the d_{50} of the sand is 0.777 mm. The σ is 1.93, meaning the sand has a nearly uniform size distribution (Raudkivi 1998). This allows the d_s to reach their maximum clear-water value during the experiments. The bed slope is set to 1:2400 for each experiment, and the relative density of sand is 2.63.

Fig. 8.1 Shows **(a)** tilting flume, **(b)** centrifugal pump, **(c)** flowmeter, and **(d)** laser distance meter.

The grain size distribution analysis is shown in Fig. 8.2. The d is carefully selected so that the d_{50} has little effect on the d_s. According to Melville (1997), the sediment size does not significantly impact the d_s when the ratio of d/d_{50} sediment size exceeds 25. In this study, the ratio is 96.69 for a 7 cm pier.

Ripples are small triangular sand waves with a gradual upstream slope (around 6°) and a steep downstream slope (around 32°). They form in fine sediments ($d_{50} < 0.7$ mm), while coarse sediments usually form dunes. Ripples form when the viscous sub-layer is present and threshold

shear stress is nearly reached, while dunes form when the bed is rough. The length of ripples depends on d_{50} and u but is not influenced by h.

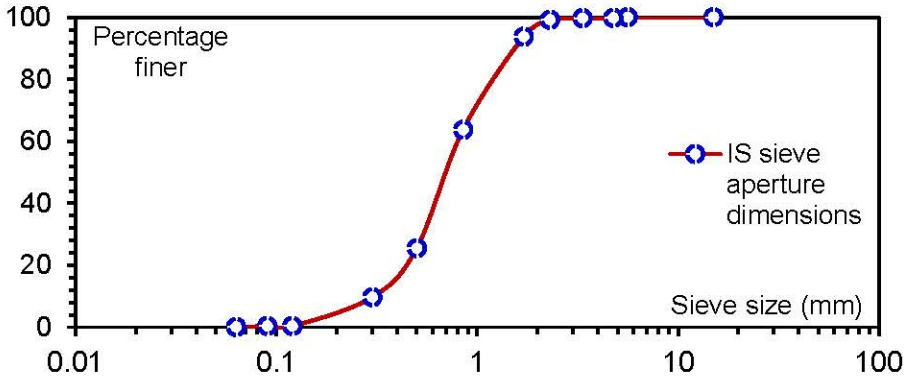

Fig. 8.2. Grain size distribution curve.

Dunes are larger bed forms with a triangular shape, featuring a mild upstream slope and a steep downstream slope. Dunes form in coarser sediments (d_{50} > 0.6 mm). In areas of high turbulence, sediment particles are transported by turbulence, even when local τ_o is below the threshold. On the upstream side of dunes, sediment is driven by τ_o, passes over the crest, and is suppressed in the bed. As sediment moves from the upstream side to the lee side, dunes slowly migrate downstream. The dry sand bed for both single pier and eccentric arrangement is given in Fig. 8.3.

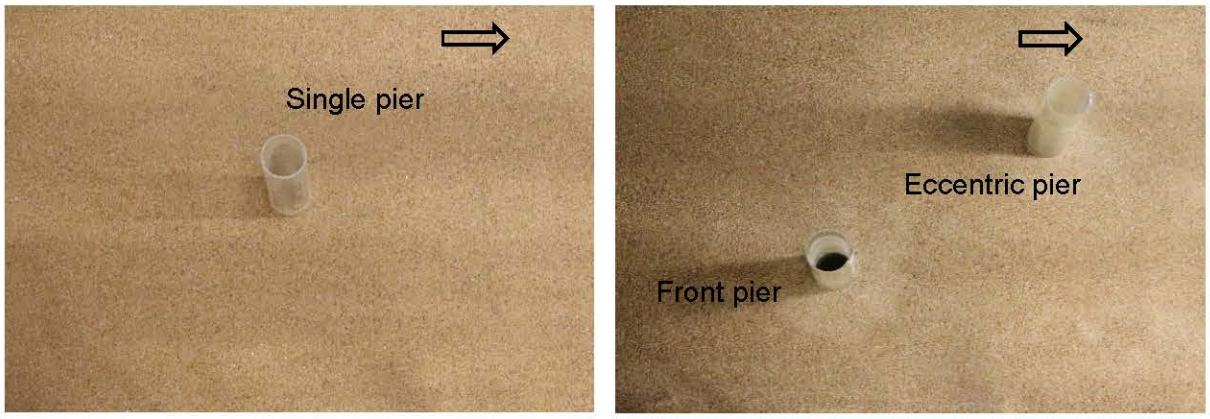

Fig. 8.3. Dry flume bed without water before performing **(a)** single pier experiment, and **(b)** eccentric pier experiment.

After placing the piers in the proper position with correct alignment, a flat sand bed is prepared. The flatness of the sand bed is checked with a spirit level. The sand bed preparation is done for every new eccentric-pier arrangement setup after evenly mixing up the sand.

8.2.2. Experimental procedure

The following procedure is adopted for all experiments. The experiments are conducted under steady, subcritical and clear water flow conditions and in a plain bed. The procedure is as follows:

- The pier models are fixed vertically in the middle of the working section with different e for each experiment.
- The filled sand bed is leveled with a trowel. Bed level is checked using a spirit level and LDS.
- The flume is slowly filled with water to the required depth, ensuring no sediment movement occurs.
- The working area is filled with water, and air bubbles are allowed to escape to avoid disturbances in the bed.
- Water Q is maintained at 20 lps using a flowmeter and adjusted with valves.
- The h (0.116 m, 0.105 m, 0.095 m, 0.084 m) are set using a tailgate at the downstream end of the flume. A movable trolley with an LDS along with a point gauge is used to measure d_s validation with the point gauge.
- Each experiment lasts up to a maximum of 12 hours. After each experiment, the flow is stopped, and d_s is recorded using the LDS.
- The flume is drained slowly, and the sand bed is allowed to dry and d_{sm} measurements along with the scour profile are taken.
- The sand bed is re-leveled, and the process is repeated with different e between the front and eccentric piers (3.5d, 3d, 2.75d, 2.5d, 2.25d, 2d).

The schematic diagram of the flume and the experiments on the flow structure interaction are given in Fig. 8.4(a-c) The length×width×height of the flume is 11×0.81×0.60 m^3, the relative density of sand is 2.63, the d is 7 cm, transverse spacings between eccentric piers, e was 2d–3.5d, longitudinal spacing between eccentric piers l was 5.2d (Das et al. 2016), Q is 20 lps, u was 0.213–0.293 m/s, h was 84-116 mm. The parameters which are kept constant are d, d_{50}, Q, constriction ratio W/d, sediment coarseness d/d_{50}, l/d, and the varied parameters are u/u_c, h/d, Fr, e/d, dimensionless time ut/d.

In eccentric pier arrangements, different flow phenomena interact with each other to influence scour. Mainly down flow and the horseshoe vortex forms around each pier, creating a turbulent flow that increases shear stress on the bed, leading to scour. The wake vortex forms downstream of the piers, causing lower pressure and contributing to sediment removal and transport downstream. The bow wave forms at the leading edge of the upstream pier, obstructing the flow and adding to the turbulence. The reinforcing effect occurs when the flow from the upstream pier increases the turbulence around the downstream pier, which increases scour. Furthermore, the compressed horseshoe vortex squeezes the flow near the piers, further accelerating sediment erosion. Finally, the sheltering effect occurs when the downstream pier partially shields the bed from the flow disturbance caused by the upstream pier, reducing scour

in certain areas. These combined effects of the wake of the front and the horseshoe of the downstream pier result in deeper d_s (Fig. 8.4b).

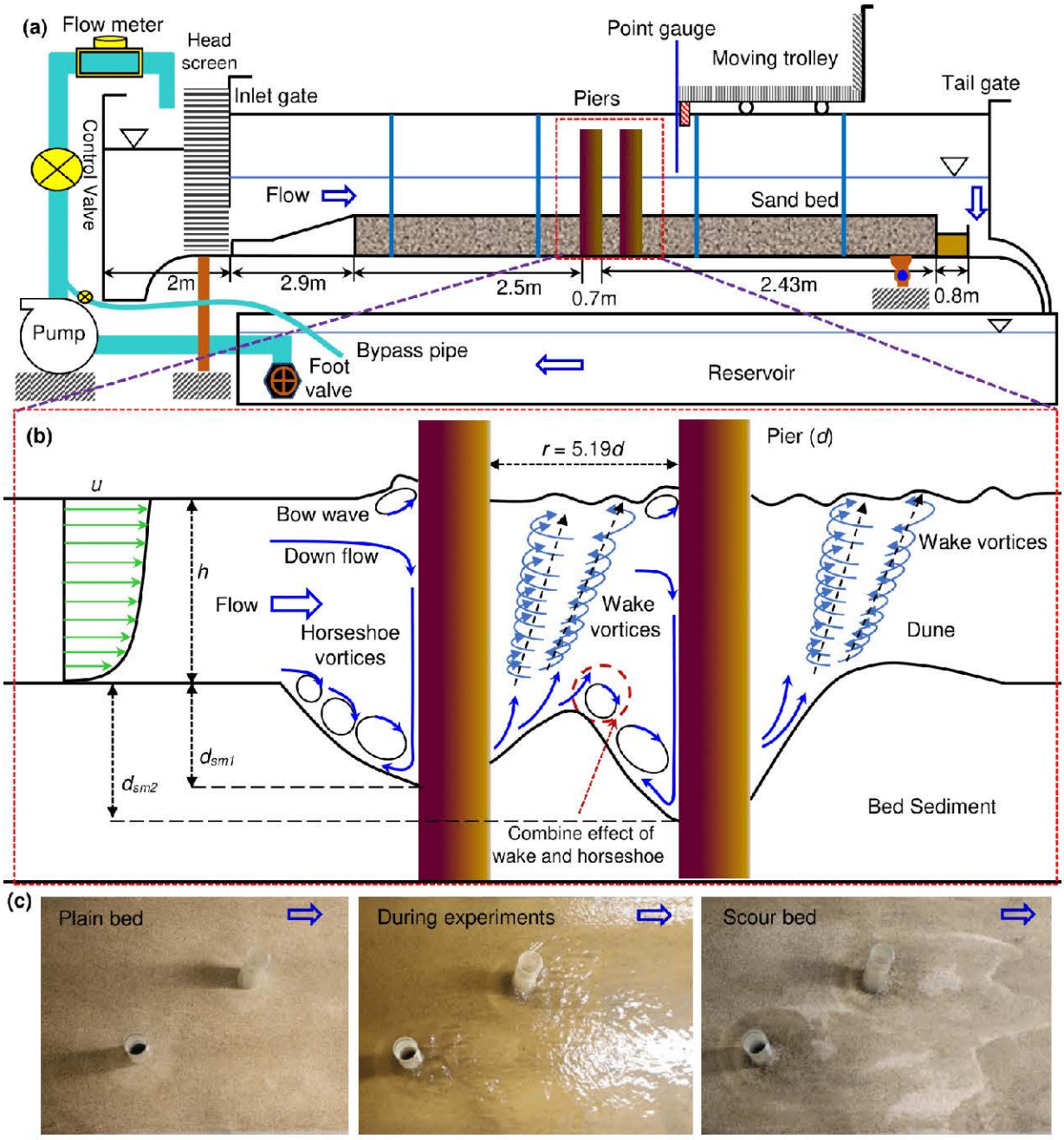

Fig. 8.4. Schematic diagrams of **(a)** tilting flume, **(b)** schematic of flow around the eccentric pier, **(c)** scour evaluation around eccentric arrangements.

In Fig. 8.5, l_R and l_L represent the maximum length, w_R and w_L represent the maximum width right and left respectively, A_{pL} and A_{pR} represent the maximum planar area left and right,

and $\forall_R$ and $\forall_L$ represent the maximum volume of right and left. A_{pM} and $\forall_M$ refer to the maximum planar area and volume of the middle section of the scour.

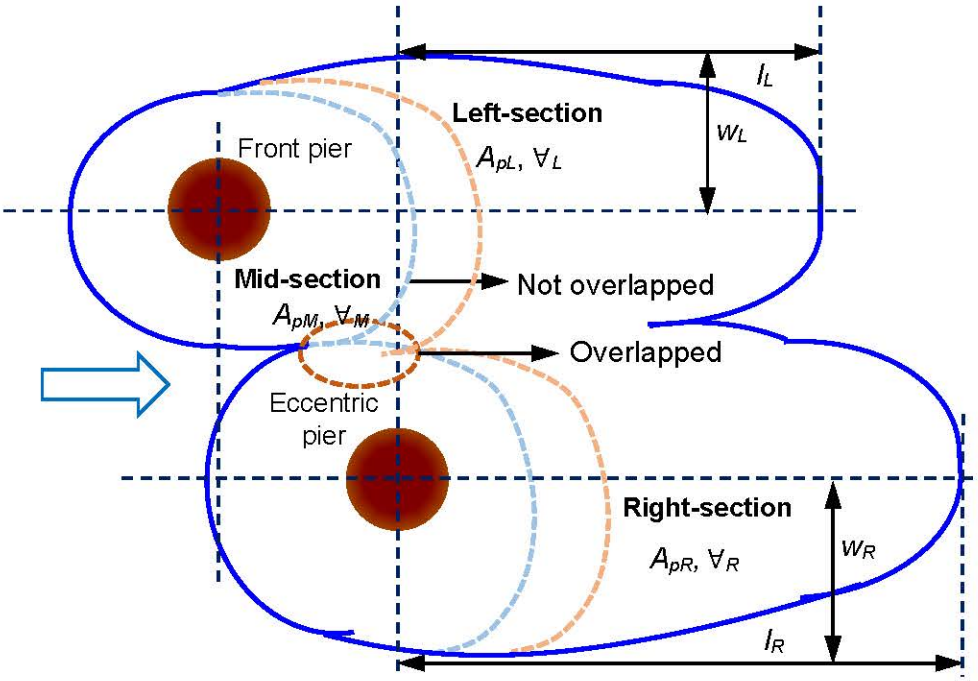

Fig. 8.5. The schematic diagram of scour morphological study.

8.2.3. Dimensional analysis: Buckingham π theorem

The d_{sm} depends on the time t and can be a function of several parameters (Eq. 8.1). Here, K_s is the pier shape factor, β is the correction factor for the alignment of the pier, and S is the channel bed slope.

$$f_1\left(d_{sm},\rho_f,\nu,g,h,u,d_{50},\rho_s,u_c,S,d,\alpha,e,\sigma,W,t,l,K_S,\beta\right)=0 \tag{8.1}$$

Using the Buckingham π theorem makes complex processes easier to comprehend and optimize process parameters (Eq. 8.2).

$$f_3\left(\frac{d_{sm}}{d},\frac{\nu}{hu},\frac{hg}{u^2},\frac{h}{d},\frac{d_{50}}{d},\frac{\rho_f}{\rho_s},\frac{u_c}{u},S,\alpha,\frac{e}{d},\sigma_g,\frac{W}{d},\frac{ut}{d},\frac{l}{d},K_S,\beta\right)=0 \tag{8.2}$$

In this study, the parameters kept constants are d/d_{50}, W/d, S, density ratio ρ_f/ρ_s, l = 5.2d, σ, β, K_s [= 1 for the circular pier (Shukur and Obeid 2016)], Reynolds number Re (= uh/ν), [viscosity becomes negligible when Re > 7000 (Monti 1994)]. The angle of approach flow to the axis (α = 0) is also negligible as in this study, α is not considered. After eliminating the aforementioned non-dimensional π terms, Eq. 8.2 can be written as Eq. 8.3.

$$f_4\left(\frac{d_{sm}}{d},\mathrm{Fr},\frac{h}{d},\frac{u}{u_c},\frac{e}{d},\frac{ut}{d}\right)=0 \tag{8.3}$$

Here, the term u^2/gh is called flow Froude number (Fr). The d_{50} is 0.777 mm, and σ $(=d_{84}/d_{16})^{0.5}$ is 1.93 ($\sigma_g < 2$, Raudkivi 1998). It implies that the sand is of a uniform size distribution (Raudkivi 1998). Melville (1997) stated that if the d/d_{50} is greater than about 25, the bed material grain size does not affect d_s. This condition is met in the current investigation ($d/d_{50} = 90.09$). To reduce contraction scours and prevent wall friction, the piers are fixed ($W/d = 11.57$) ($W/d \geq 6.5$, Ashtiani (2012) for negligible contraction effect). Flow shallowness has no influence if $h/d > 0.6$ (Raudkivi 1983). The sediment incipient motion is reached when $u/u_c \geq 0.4$, as defined by Chiew (1995). The experimental outcomes of the present study are given in Table 8.1. Here, d_{ss}, d_{sm1}, and d_{sm2} represent d_s for the single pier, eccentric pier, and front pier, respectively. The dimensionless time is represented by ut/d.

Table 8.1. Experimental outcomes for the present study.

Exp.	e/d	u/u_c	h/d	Fr	t (min)	ut/d	d_{ss}/d	d_{sm1}/d	d_{sm2}/d
1	–	0.67	1.65	0.20	360	98948.67	0.22	–	–
2	3.5	0.67	1.65	0.20	660	120937.30	–	0.36	0.45
3	3	0.67	1.65	0.20	600	109943.00	–	0.41	0.45
4	2.75	0.67	1.65	0.20	660	120937.30	–	0.42	0.46
5	2.5	0.67	1.65	0.20	600	109943.00	–	0.36	0.48
6	2.25	0.67	1.65	0.20	540	98948.67	–	0.45	0.55
7	2	0.67	1.65	0.20	600	109943.00	–	0.36	0.42
8	–	0.75	1.50	0.23	480	133030.99	0.39	–	–
9	3.5	0.75	1.50	0.23	660	133031.00	–	0.40	0.51
10	3	0.75	1.50	0.23	720	145124.70	–	0.49	0.59
11	2.75	0.75	1.50	0.23	660	133031.00	–	0.54	0.66
12	2.5	0.75	1.50	0.23	600	120937.30	–	0.46	0.57
13	2.25	0.75	1.50	0.23	600	120937.30	–	0.59	0.69
14	2	0.75	1.50	0.23	540	108843.50	–	0.52	0.62
15	–	0.85	1.35	0.27	360	120937.26	0.83	–	–
16	3.5	0.85	1.35	0.27	420	94062.32	–	0.91	0.96
17	3	0.85	1.35	0.27	720	161249.70	–	0.87	0.97
18	2.75	0.85	1.35	0.27	420	94062.32	–	0.92	0.95
19	2.5	0.85	1.35	0.27	600	134374.70	–	0.89	0.92
20	2.25	0.85	1.35	0.27	600	134374.70	–	0.89	1.02
21	2	0.85	1.35	0.27	540	120937.30	–	0.87	0.97
22	–	0.97	1.20	0.32	120	52910.05	0.89	–	–
23	3.5	0.97	1.20	0.32	120	30234.32	–	0.95	1.08
24	3	0.97	1.20	0.32	420	105820.10	–	1.02	1.10
25	2.75	0.97	1.20	0.32	80	20156.21	–	0.95	1.08
26	2.5	0.97	1.20	0.32	80	20156.21	–	0.91	0.99
27	2.25	0.97	1.20	0.32	300	75585.79	–	0.95	1.13
28	2	0.97	1.20	0.32	180	45351.47	–	0.96	1.07

8.2.4. Data description and literature formulas

Table 8.2 presents the detailed experimental ranges collected from the literature along with new experiments from the present study only for the eccentric pier arrangements. Here, φ° is flow skew angle or eccentric angle from the centre line of the front pier.

Table 8.2. Range of experimental conditions used in literature.

Literature	u/u_c (–)	h/d (–)	d/d_{50} (–)	W/d (–)	Fr (–)	e/d (–)	l/d (–)	φ (°)
Beg (2004)	1.0	4.2	33.0	22.9	0.3	1.2-6.4	6.36-8.92	7.5-45.0
Das et al. (2016)	0.8	1.8	95.9	11.6	0.2	3.0	1.73-5.19	30.1-60.1
Khaple et al. (2017)	0.9	2.7	33.3	15.2	0.4	2.00-4.00	2.0-11.0	11.3-63.4
Das et al. (2019)	0.7	1.8	84.8	11.6	0.2	3.0	0.86-4.32	34.8-66.6
Nandi and Das (2024)	0.7	1.8	84.8	11.6	0.2	3.0	5.20	30.0
Present study	0.67-0.96	1.20-1.65	90.1	11.6	0.20-0.32	2-3.5	5.20	21.1-34

8.2.5. Methodology

The critical condition for bed material movement is checked before each experiment using the following steps:

- The flume h is controlled by a tailgate, set at 0.116 m, 0.105 m, 0.095 m, and 0.084 m for the experiments. The bed slope is kept constant at 1:2400.
- The u is set at 67-96% of the u_c of the uniform sand bed, accounting for side-wall effects to ensure clear water scour conditions. This research focuses on clear water flow conditions with a threshold Froude number of $0.67 \leq (\mathrm{Fr_t} = u/u_c) \leq 0.97$ (Dey and Raikar, 2007).
- The ratio between the h and d is varied across four sets of experiments, ranging from 1.2 to 1.65.
- In steady uniform flow within a rectangular flume, τ_o is calculated using the formula $\tau_o = \rho_f g R_h \sin\theta$. Here, ρ_f represents the mass density of water, R_h is the hydraulic radius, and θ is the angle between the sloping bed and the horizontal. For very small bed slope, $\sin\theta$ is approximated as $\tan\theta$ = bed slope, and the resistance at the water-air interface is considered negligible.
- The critical bed shear stress (τ_{oc}) is calculated using the formula $\tau_{oc} = \Theta_c \Delta \rho_f g d_{50}$, where Δ is the relative density of sediment ($\rho_f/\rho s - 1$), Θ_c is the critical Shields parameter. The Θ_c is determined using the empirical formulas of van Rijn for the Shields curve (Eq. 8.4).

$$\Theta_c = \begin{cases} 0.24/D_* & D_* \le 4 \\ 0.14/D_*^{0.64} & 4 \le D_* \le 10 \\ 0.04/D_*^{0.10} & 10 \le D_* \le 20 \\ 0.04D_*^{0.29} & 20 \le D_* \le 150 \\ 0.55 & 150 < D_* \end{cases} \quad (8.4)$$

where D_* is the dimensionless particle parameter, expressed as $D_* = d_{50}(\Delta g/\nu^2)^{1/3}$.

- The u_c is calculated using the formula $u_c = u_{*c}[5.75\log\{h/(2d_{50})\} + 6]$, where $u_{*c} = (\tau_o/\rho_f)^{0.5}$. The critical shear flow Reynolds number (R_{*c}) is calculated as $R_{*c} = (u_{*c}d_{50})/\nu$, at a water temperature of 20°C. The relationship between Θ_c and R_{*c}, as shown in Shields' diagram, indicates that sediment motion begins when $\Theta > \Theta_c$ or $\tau_o > \tau_{oc}$ or $u_* > u_{*c}$.
- During the experiment, a maximum scour stage of the scour hole is considered reached when the difference in d_s is 1 mm or less over an hour, up to a total run time of up to 12 hours. This duration is deemed sufficient for the assessment of maximum scour conditions. After stopping the experiment, d_{sm} is measured at the upstream base of the in-line front and eccentric rear piers using an LDS.
- The contour lines of scour holes and sand deposits around the circular piers are plotted using Surfer software.

8.2.6. Statistical analysis

The total collected data from the literature along with present experimental data are used for computations of scour near the eccentric arrangements. The earlier studies predicted the d_{sm} using multi-linear regression (MLR) (Das et al. 2019), using least-squares methods to minimize the error between calculated and observed values linearly (Eq. 8.5) whereas MNLR analysis based on nonlinear relations (Beg 2004, Liang et al. 2016) given in Eq. (8.6). Some researchers have used this method for analyzing the d_{sm} around the piers. Here, m_1 to m_7 and o_1 to o_7 are arbitrary coefficients.

$$\frac{d_{sm}}{d} = m_1 + m_2\left(\frac{u}{u_c}\right) + m_3\left(\frac{h}{d}\right) + m_4(\mathrm{Fr}) + m_5\left(\frac{e}{d}\right) + m_6\left(\frac{l}{d}\right) + m_7\left(\frac{ut}{d}\right) \quad (8.5)$$

$$\frac{d_s}{d} = o_1\left(\frac{u}{u_c}\right)^{o_2}\left(\frac{h}{d}\right)^{o_3}\mathrm{Fr}^{b_4}\left(\frac{e}{d}\right)^{o_5}\left(\frac{l}{d}\right)^{o_6}\left(\frac{ut}{d}\right)^{o_7} \quad (8.6)$$

Different statistical parameters are chosen to analyze the efficiency of Eqs. (8.5-8.6), using different performance indicators, Mean Squared Error (MSE) (see Table 5.4), Correlation Coefficient (CC) and Root Mean Squared Error (RMSE) (see Table 3.5), Mean Bias Error (MBE) (see Table 7.5). Figure 8.6 presents a flowchart outlining the methodology used in this study.

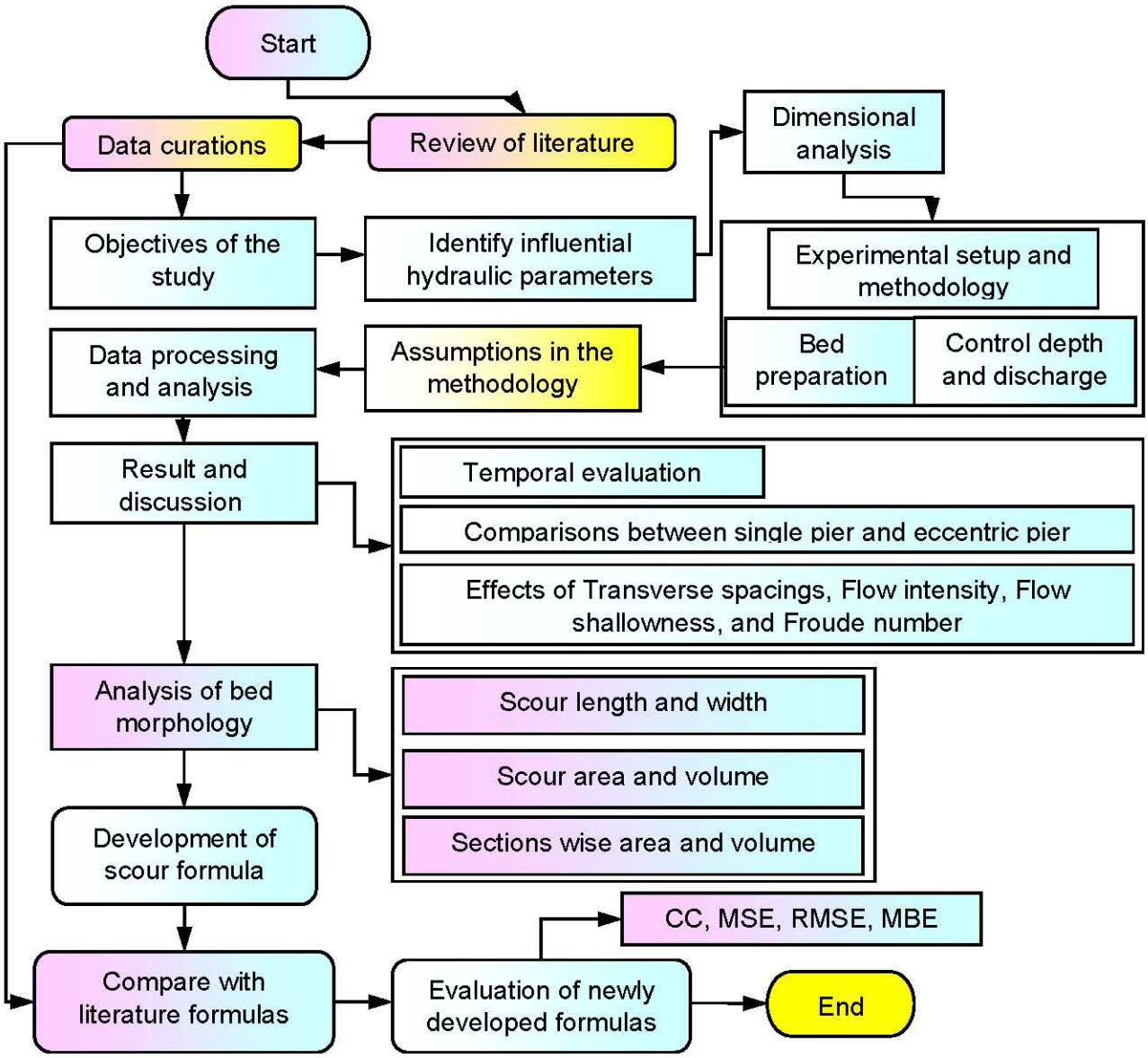

Fig 8.6. Flowchart showing the methodology set for the present study.

8.3. Results and discussion

A total of 24 new experiments with eccentric pier arrangements and four experiments with isolated piers are conducted, maintaining constant experimental conditions across all four sets for each case. The study focused on the variation d_{st}, and to compute d_{sm}. Total four $u/u_c = 0.67$, 0.75, 0.85, and 0.97, $h/d = 1.65$, 1.5, 1.35, and 1.2, and $e/d = 3.5$, 3, 2.75, 2.5, 2.25, and 2 are considered. The bed morphology is also discussed. The spline line connects the observed data in the all graphs given below.

8.3.1. Time dependent variations of d_s

In four single-pier experiments, d_{st} increases with reduced h/d. However, the rapid changes can be seen in the d_{st} from u/u_c = 0.75 to 0.85 (Fig. 8.7a). The parameter influence on single pier maximum d_s (d_{ss}) is given in Fig. 8.7(b-d). The d_{ss}/d increases with the increase in u/u_c, meanwhile, it decreases with the increase of h/d as the u/u_c reduces and the sudden changes can be seen from h/d = 1.35 to 1.5. When the h increases while keeping the same discharge, the approach u slows down. This slower u reduces the bed shear, meaning there is less for scouring or erosion around the structure. This can be explained using the Fr = $u/\sqrt{gh}$, which compares the u to the h. When h increases, Fr decreases, which indicates slower flow conditions with less energy to move sediment. The h/d also affects how the water flows around the structure. When h/d is smaller, the flow is more likely to create strong currents that cause more erosion. As h/d increases, the flow becomes smoother and less likely to cause scouring. Therefore, a greater h reduces u and the τ_o, leading to less erosion around the structure.

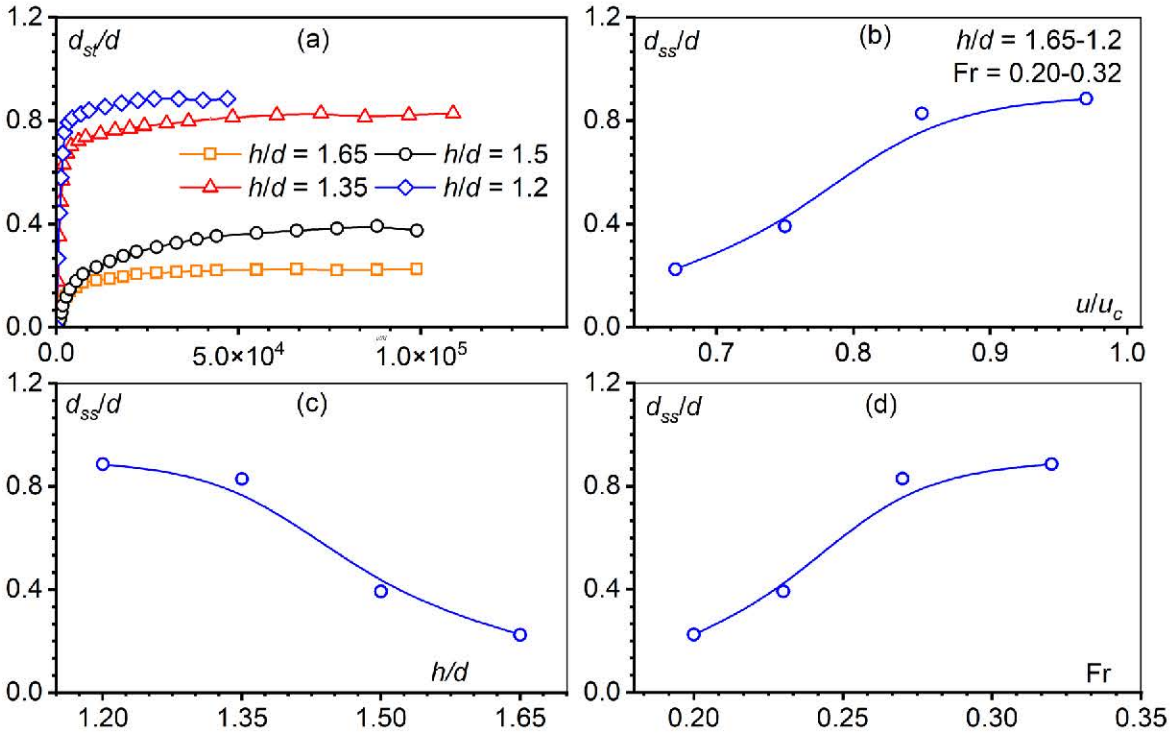

Fig. 8.7. The single pier **(a)** temporal variations for d_s, **(b)** influence of u/u_c, **(c)** influence of h/d, and **(d)** the influence of Fr on the d_{ss}.

Figure 8.8(a-h) shows the variations in dimensionless d_{st} (d_{st}/d) and dimensionless t (ut/d) for each experiment under different flow conditions. The d_{st}/d for each pier is shown separately, indicating that d_s for two piers is always greater than for a single pier under similar flow conditions due to their reinforcing effects nearby (Das et al. 2016, 2019). The maximum and

minimum d_{st1}/d occur at $e = 3d$, $h = 1.2d$, and $e = 3.5d$, $h = 1.65d$, respectively, while maximum and minimum d_{st2}/d values are observed at $e = 2.25d$, $h = 1.2d$, and $e = 2d$, $h = 1.65d$.

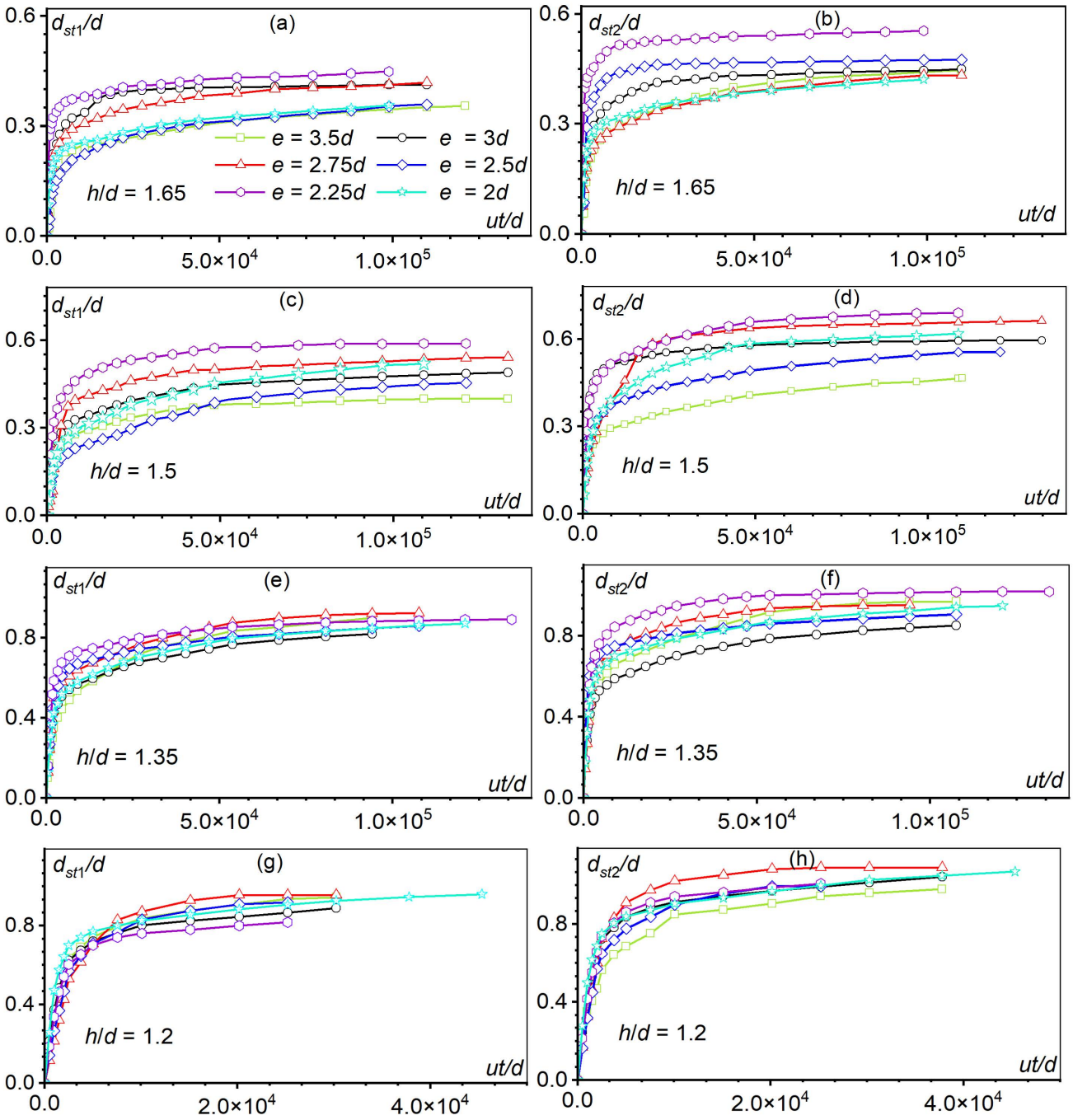

Fig. 8.8. Variation of d_{st1}/d and d_{st2}/d with ut/d at **(a-h)** various h/d.

The minimum values of d_{st1}/d and d_{st2}/d at specific ratios of ut/d and h/d occur due to the complex interaction between the vortices generated by the piers. The d_{st2}/d reduces when the spacing e/d =2.5 and the h/d =1.2, the interference between the horseshoe vortex formed at the

base of the eccentric pier and the wake vortex and reduces the elevation of the midsection and sediment from the front pier transported to the rear pier reduce the scour. This phenomenon is beneficial for the design of eccentric piers in bridges because it results in a lower d_{sm}. These conditions promote safer and more efficient bridge designs, particularly in environments where sediment transport and scour create significant challenges between the two pier groups. When the h/d reduces the scour rate is rapid in the initial stages and in the later stage it flattens and becomes horizontal in less time compared to others, this change is significant for h/d= 1.2 [Fig. 8.8(g-h)].

8.3.2. Influence of hydraulic parameters

The combined influence of different hydraulic parameters such as dimensionless eccentricity (e/d), u/u_c, h/d, and Fr on d_{sm} for each pier in the eccentric arrangement is graphically represented in Fig. 8.9.

The scour effects are minimal when the e is carefully adjusted to specific values. As shown in Fig. 8.9 the dimensionless d_{sm} (d_{sm1}/d for the front pier and d_{sm2}/d for the eccentric pier) vary with changes in parameters like e/d, u/u_c, h/d, and Fr.

For the front pier, d_{sm1}/d initially increases with e and then decreases after e/d= 2.25 under flow conditions where h/d ranges from 1.5 to 1.65, before increasing again beyond e/d = 3. A significant rise in d_{sm1}/d is noted when u/u_c increases from 0.75 to 0.85, leading to a 90% increase in d_s. Similarly, for the eccentric pier, d_{sm2}/d increases by 72% with the same rise in u/u_c.

Minimum d_s occur when e/d = 3.5 and h/d = 1.65 for the front pier, and e/d = 2 and h/d = 1.65b for the eccentric pier. These conditions reduce the scouring effects because the high h/d decreases the u/u_c which will reduce the flow strength mainly and reduce scour, while for the same h/d, the reduced scour can be seen for less than e/d = 2 and beyond the e/d =3.

The sheltering effect is observed when $e < 2$, which reduces scour by minimizing the direct impact of flow on the eccentric pier. However, when the horseshoe vortex from the eccentric pier interacts with the wake from the front pier, it can increase scour due to their combined effects. If the eccentric pier is aligned in the region of shed vortices from the front pier, d_s increases for $2 < e < 3$. Furthermore, the interference of compressed vortices, especially around the eccentric pier, intensifies scouring as the inner arm of the vortices is compressed, increasing the local u. When the eccentricity $e>3d$, the piers behave more independently, with no significant vortex interaction or reinforcement, leading to reduced scour similar to that around a single pier.

Placing eccentric piers closer together with specific l and e can help reduce scour, especially when building a new pier alongside an existing bridge to meet increased traffic demands in urban areas. If there is no need for side-by-side bridges, the new pier can be placed further from the existing pier to enhance stability and safety. Proper placement of piers minimizes erosion risks and extends the lifespan of the bridge.

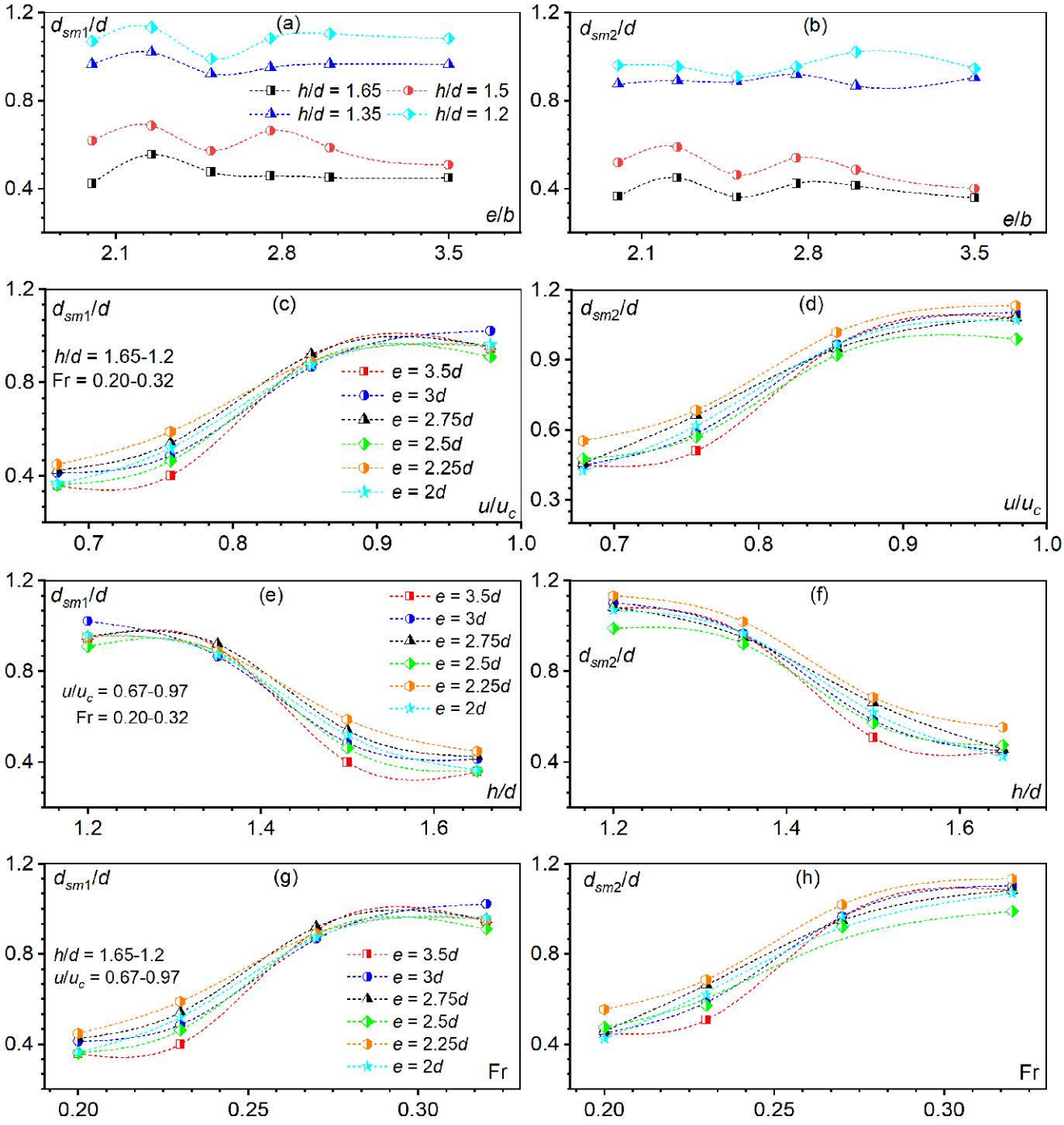

Fig. 8.9. Variations of maximum d_{sm} with different **(a-b)** transverse spacing (e/d), **(c-d)** flow intensity (u/u_c), **(e-f)** flow shallowness (h/d), and **(g-h)** Fr for eccentric piers.

8.3.3. Analysis of bed morphology

The main objective of this attempt is to quantitative analysis of scour affected area, depositons, and volume using a combination of two eccentric piers. The scour volume and impacted area have been recorded for different e and h. By comparing the geometry of the three sections, the current work aims to comprehend the morphology and scour geometry of the bed following each experiment. The sediment scour zone is separated into three areas based on the direction of flow: the left, middle, and right sections (Fig. 8.1b).

(a) Effect of eccentricity on scour length and width

The non-dimensional scour length (l_x/d) and width (w_x/d) vary with different values of e/d and are shown in Fig. 8.10(a-d). An increase in the u/u_c from 0.75 to 0.85 causes a significant increase in l_x/d for the front pier. Specifically, l_x/d increased by 176% on the right side and by 109% on the left side due to a 30% increase in u/u_c, as seen in Fig. 8.10(a) and Fig. 8.10(b), respectively.

However, for w_x/d, the maximum and minimum values occur at different conditions. In the left section, the maximum w_x is observed at e/d = 2.75, h/d = 1.2, and the minimum at e/d = 3, h/d = 1.65. Similarly, in the right section, the minimum width occurs at e/d = 3, h/d = 1.65, and the maximum at the same values [Figs. 8.10(c-d)], when the longitudinal u exceeds the transversal u, sediment transport increases, resulting in a scour hole that is much longer than its w. The variation in e also impacts the dimensions of the scour hole. Minimum l_x and w_x are advantageous as they help prevent bridge pier failure by reducing the impact of erosion.

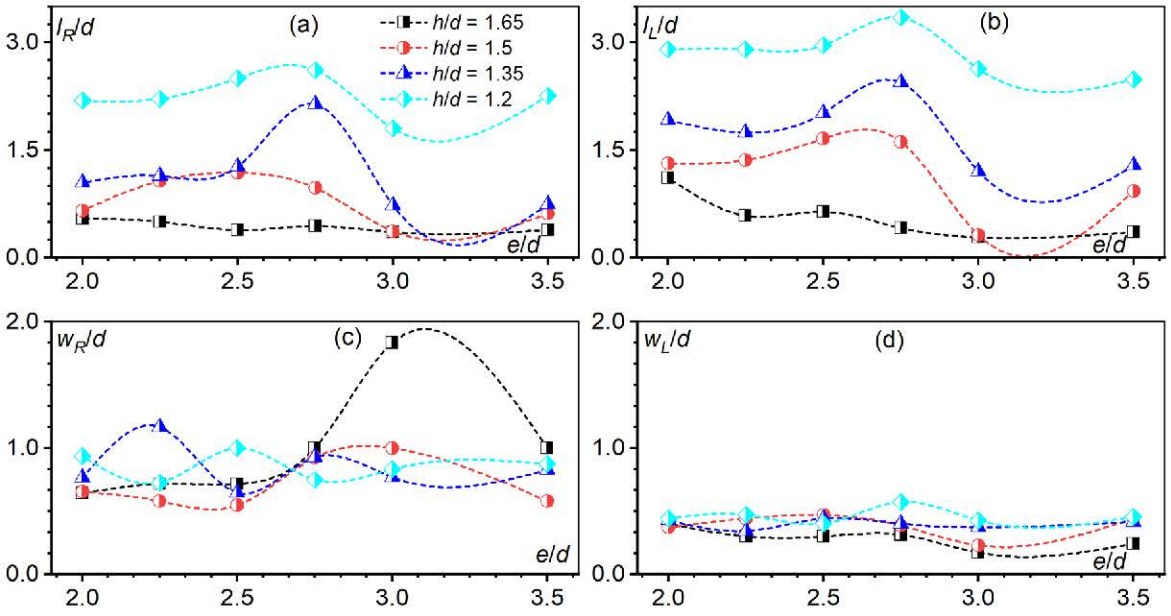

Fig. 8.10. Effect of transverse spacing on maximum scour **(a-b)** length (l_x), and **(c-d)** width (w_x).

Eccentric pier arrangements can cause scour holes to overlap, increasing the d_s and extent of sediment transport. This leads to a longer but narrower scour hole, particularly when h/d increases. Evaluating the minimum l_x and w_x is crucial to ensure the stability and safety of bridge structures. These conditions help in designing piers that are less susceptible to scour-related damage and extensive morphological changes in the river which may reduce risk from the changes in the flow direction, enhancing the overall durability and safety of the bridge.

(b) Influence of eccentricity on scour area and volume

The detailed analysis of scour contour planner area (A_p), and volume ($\forall$) in dimensionless form for different sections indicated in Fig. 8.5, are given in Table 8.3.

Table 8.3. Experimental outcomes based on grid data of deposition in contour graphs.

Exp. no.	e/d	u/u_c	h/d	Fr	A_s/d^2	A_p/d^2	$\forall/d^3$	Left section		Right section		Midsection	
	(--)	(--)	(--)	(--)	(--)	(--)	(--)	A_{pL}/d^2 (--)	$\forall_L/d^3$ (--)	A_{pR}/d^2 (--)	$\forall_R/d^3$ (--)	A_{pM}/d^2 (--)	$\forall_M/d^3$ (--)
1	3.5	0.68	1.65	0.2	53.17	52.97	0.90	21.59	0.13	8.33	0.12	19.04	0.30
2	3	0.68	1.65	0.2	60.67	60.43	1.24	35.12	0.24	36.37	0.46	15.45	0.29
3	2.75	0.68	1.65	0.2	61.47	61.02	2.14	37.22	0.45	9.06	0.22	15.01	0.63
4	2.5	0.68	1.65	0.2	93.79	93.06	4.56	23.83	0.42	12.03	0.20	14.23	0.71
5	2.25	0.68	1.65	0.2	77.74	77.23	3.46	24.93	0.51	38.52	0.45	19.28	0.86
6	2	0.68	1.65	0.2	83.38	82.74	4.12	7.29	0.36	13.11	0.38	12.96	1.25
7	3.5	0.76	1.5	0.23	78.78	78.17	5.64	37.15	1.45	13.65	0.40	22.44	1.74
8	3	0.76	1.5	0.23	53.80	53.30	1.38	11.31	0.39	10.90	0.20	17.10	0.49
9	2.75	0.76	1.5	0.23	168.10	167.03	16.46	11.45	1.93	27.41	1.74	25.01	4.02
10	2.5	0.76	1.5	0.23	195.98	194.82	19.97	37.07	2.99	38.86	1.83	23.88	3.46
11	2.25	0.76	1.5	0.23	166.99	165.57	17.32	32.29	4.59	22.60	3.10	22.42	6.24
12	2	0.76	1.5	0.23	83.33	82.26	6.70	6.57	0.79	23.45	0.76	14.13	1.77
13	3.5	0.85	1.35	0.27	131.95	131.41	5.98	32.55	1.40	34.29	0.66	21.93	1.24
14	3	0.85	1.35	0.27	73.75	73.09	5.99	20.16	2.24	17.89	0.67	22.32	1.91
15	2.75	0.85	1.35	0.27	264.30	263.10	29.69	24.37	4.62	39.73	3.76	37.40	6.80
16	2.5	0.85	1.35	0.27	170.67	169.64	21.48	8.09	1.44	29.51	1.87	21.23	3.21
17	2.25	0.85	1.35	0.27	114.56	113.86	5.99	21.40	0.83	22.01	0.97	17.54	1.98
18	2	0.85	1.35	0.27	167.54	166.27	14.62	23.96	3.84	37.94	1.27	12.72	2.43
19	3.5	0.98	1.2	0.32	178.24	177.68	9.48	20.79	1.15	54.36	1.48	48.46	3.72
20	3	0.98	1.2	0.32	170.40	169.36	17.97	56.91	6.55	69.01	3.04	38.39	5.17
21	2.75	0.98	1.2	0.32	580.65	578.09	108.73	31.16	8.52	56.88	11.09	50.91	14.40
22	2.5	0.98	1.2	0.32	222.38	221.31	16.24	38.86	2.52	62.94	4.17	31.21	4.38
23	2.25	0.98	1.2	0.32	301.23	299.81	43.60	37.93	7.77	62.67	7.25	45.64	10.13
24	2	0.98	1.2	0.32	255.28	254.44	21.37	30.61	3.41	46.82	3.74	26.41	3.94

The percentage change in the section-wise A_p of the scour hole for different e/d is shown in Fig. 8.11(a-c). The percentage of the A_p varies greatly in both the left and right parts depending on the flow conditions. To show the effect of e/d, the percentage change section-wise $\forall$ is shown in Fig. 8.12(a-c). The percentage change section-wise $\forall$ in the left section varies greatly depending on the flow conditions, while in the right section, it is generally higher.

Due to the eccentric pier arrangements, the percentage change in section-wise A_p and $\forall$ is higher throughout the midsection for all cases. The percentage change of A_p for u/u_c ranging from 0.75 to 0.85 is higher than for u/u_c for 0.67 and 0.97 in the left section, as shown in Fig. 8.11(a).

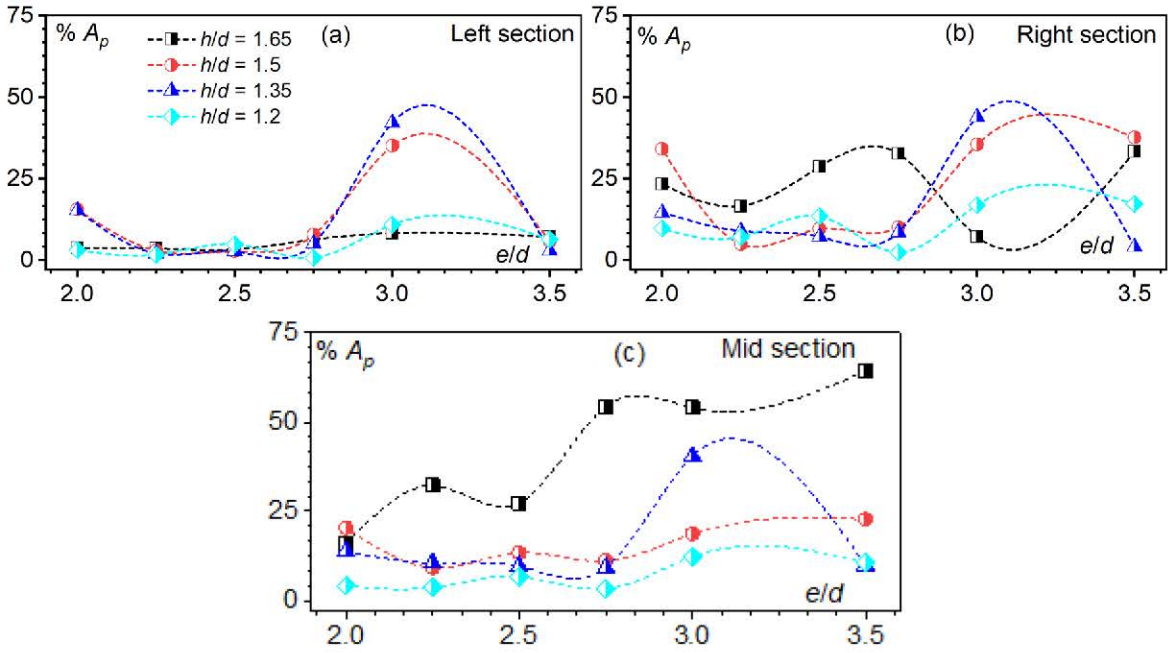

Fig. 8.11. Effect of transverse spacing, e/d on scour **(a-c)** planar area (A_p) for different sections.

The left section at $e/d = 2.75$, $h/d = 1.2$, and $e/d = 2$, $h/d = 1.65$ has the minimum percentage area (Fig. 8.11a) and volume (Fig. 8.12b) among all the experiments. This suggests that sediment transport is lower on the left side as there is no eccentric pier effect. However, on the right side the sediment is shifted by the combined action of the front pier wake and the eccentric pier horseshoe vortex action leading to more scour and the eccentric pier shed vortex is more on the right side than on the left side of the front pier and increase the spread toward the left side. Meanwhile, the maximum scour area is found for $e/d = 3.0$, so as for volume also.

These minimum values are important for engineering assessments, as they help stabilize structures under different hydraulic conditions from the extensive sediment shifting from the pier.

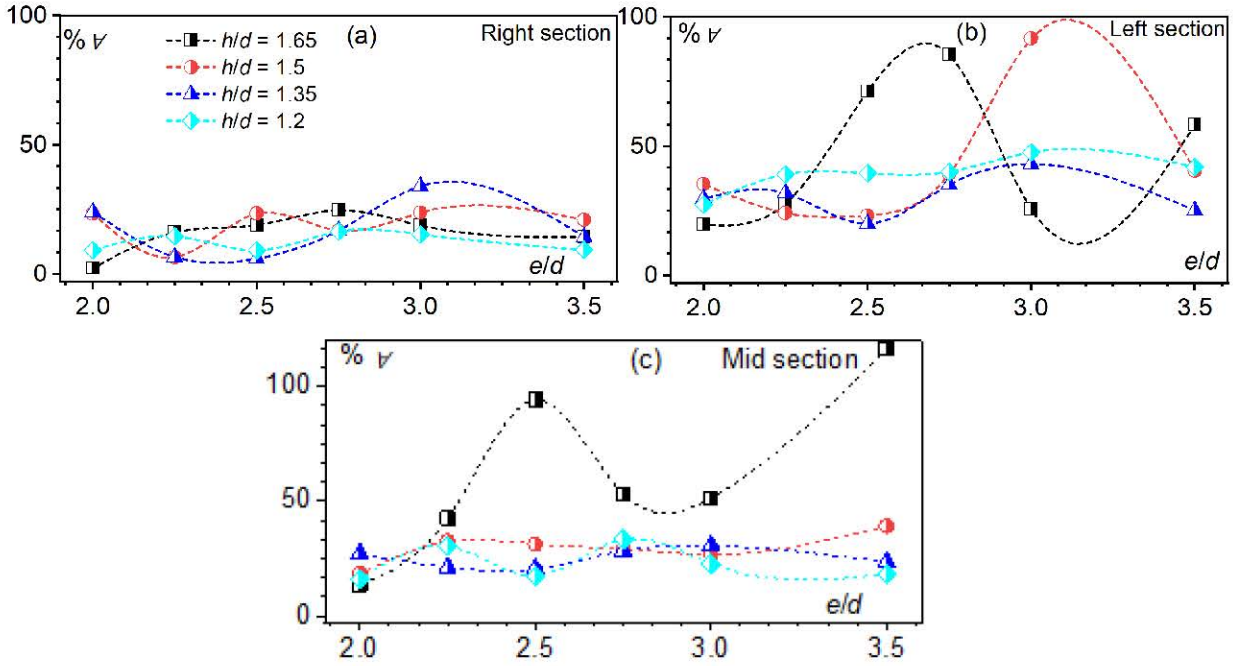

Fig. 8.12. Effect of transverse spacing, *e/d* on scour **(a-c)** volume (∀) for different sections.

8.3.4. Scour depth comparison: single vs. eccentric piers

The d_{sm} recorded at isolated piers d_{ss} and eccentric pier arrangements (d_{sm1} and d_{sm2}) show different hydraulic behaviors. Single-pier setups have a consistent scour distribution, while eccentric pier arrangements cause deeper scour holes due to their interference. The d_{sm} stability is more predictable in single-pier setups than in eccentric ones. This highlights the importance of understanding scour around such bridge foundations.

In Fig. 8.13(a-b), the percentage change in d_{sm} at the front (E_1) and eccentric (E_2) piers in the eccentric arrangements is shown, compared to a single-pier setup with *e/d*. Figure 8.13b shows that E_2 is always greater than E_1 and varies significantly with *e* across all the flow conditions. Compared to the single pier, the maximum increase in d_{sm1} and d_{sm2} in the eccentric arrangement ranges from 60-100% and 90-150%, respectively, for $u/u_c = 0.67$. Similarly, the minimum increase d_{sm1} and d_{sm2} is around 3-16% and 12-30%, respectively, for $u/u_c = 0.97$. A 28% increase in u/u_c leads to a 56% increase in E_1 for the front pier and an 86% increase in E_2 for the eccentric pie. The increase d_{sm1} and d_{sm2} are calculated relative to the d_{ss} using Eq. 8.8. Here, $i = 1, 2$ for the front and eccentric pier.

$$E_i\left(\%\right) = 100 \times \left| d_{smi} - d_{ss} \right| / d_{ss} \tag{8.7}$$

After evaluating all the eccentric pier arrangements based on *e*, the optimal position for minimizing scour and ensuring a secure bridge pier design is when the eccentric pier is placed at $e = 2.5d$, $h = 1.2d$. In this arrangement, the lowest d_s is 94% lower than the d_{sm2} at $e = 2.25d$, $h = 1.65d$.

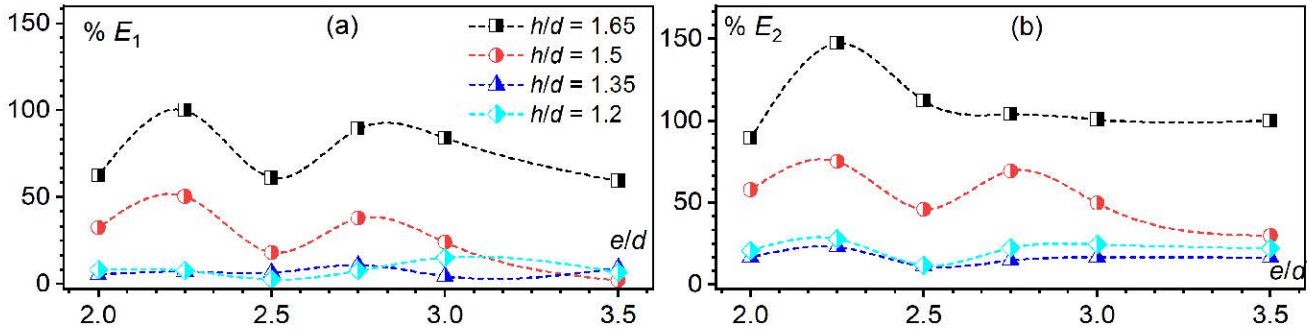

Fig. 8.13. Comparisons of percentage change of d_s between single pier and eccentric pier arrangements for **(a)** front pier (E_1), and **(b)** eccentric pier (E_2).

8.3.5. Comparison of scour depths in this study with literature

The Fig. 8.14(a-b) shows the impact of varying $\varphi°$ on the d_{sm1} and d_{sm2}. It can be seen that for $\varphi \sim 10°$- $40°$ strict increase of d_{sm2} was seen for Beg (2004) and a strict decrease was seen for $\varphi \sim 20°$- $40°$ (Khaple et al. 2017). Some inconsistencies can be seen here so, in the present study the focus given to $\varphi \sim 20°$- $35°$ for more precise and accurate understanding and found the increase d_{sm1} and d_{sm2}, $\varphi \sim 20°$- $25°$ and then decrease and stable in wider angle with e>3.

Comparing this study with other literature, where e/d is varying, the changes between Beg (2004) and this research can be observed in Fig. 8.14(c-d). It can be seen that d_{sm1} increases up to 2.5 and then decreases while d_{sm2} increases monotonically. Here, only one literature varying the e can be found, so the focus is given to more studies on varying e with other hydraulic parameters for the robust study of the impact of e/d and found that the minimum scour can be found $e/d \sim 2$ and e/d >3 maximum can be found in the range of $e/d \sim$ 2-3.

Figure 8.14(e-f) shows the effect of l/d on d_{sm1} and d_{sm2}. While Beg (2004), Das et al. (2016), Khaple et al. (2017), and Das et al. (2019) showed variations in l/d, and Nandi and Das (2024) kept l/d constant. Meanwhile for the present study also l/d is constant. Figure 8.14(g-h) shows how changes in r/d influence. Though Das et al. (2016), Khaple et al. (2017), and Das et al. (2019) showed considerable variation however this is similar to the variation of l/d.

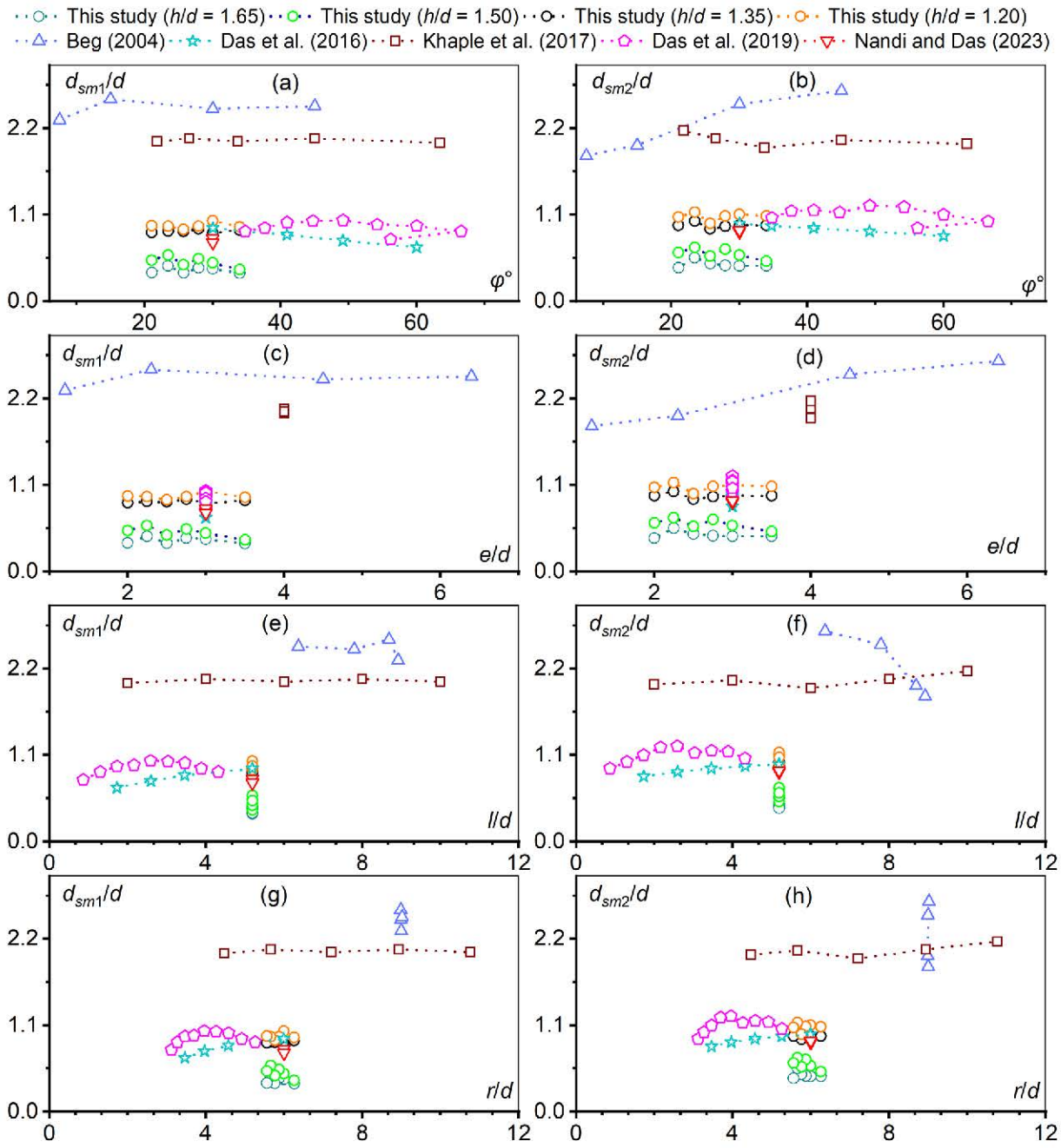

Fig. 8.14. Comparison of d_{sm} variation with **(a-b)** flow skew angle or, eccentric angle ($\varphi°$) **(c-d)** transverse spacing, e/d, **(e-f)** longitudinal spacing, l/d, and **(g-h)** diagonal spacing, r/d of previous literature and present study.

8.3.6. Regression formula for scour depth

Clear-water data from literature and experiments are used to estimate the d_{sm} for both piers using Multi-Linear Regression (MLR) and Multi-Nonlinear Regression (MNLR). Data from 49 experiments (24 from this study and 25 from the literature) are used to develop semi-empirical

formulas. The dataset is split, with 80% used for training the models and 20% for testing. Regression models are calibrated through an iterative process to achieve the desired accuracy using statistical methods.

Regression analysis is employed to obtain coefficients by fitting the model with the dependent and independent variables, selecting the most appropriate coefficients based on the highest R^2 value. The MLR analysis produced two formulas, one for the front pier and one for the eccentric pier. The standard deviations (SD) of the predicted values for these piers are 0.598 and 0.522, respectively, closely matching the observed SD of 0.607 and 0.547, which indicates a good model fit. The Eqs. (8.8-8.9) are derived with coefficients optimized to minimize errors.

$$\frac{d_{sm1}}{d} = -1.679 + 0.81\frac{u}{u_c} + 0.4496\frac{h}{d} + 4.32\mathrm{Fr} - 0.0014\frac{e}{d} - 0.0063\frac{l}{d} + 2.06E^{-07}\frac{ut}{d} \tag{8.8}$$

$$\frac{d_{sm2}}{d} = -1.519 + 0.861\frac{u}{u_c} + 0.3093\frac{h}{d} + 3.82\mathrm{Fr} + 0.0862\frac{e}{d} - 0.0862\frac{e}{d} + 2.38E^{-07}\frac{ut}{d} \tag{8.9}$$

The MNLR produced two formulas for each pier by minimizing errors (Eqs. 8.10-8.11). The predicted SDs for the front and eccentric piers are 0.595 and 0.521, respectively, closely matching the observed SDs of 0.607 and 0.547, which indicates a good fit. The Gauss-Newton algorithm was used to estimate model parameters by minimizing squared residuals, with a convergence tolerance of 0.00001. The models required 29 and 27 iterations respectively for d_{sm1}/d and d_{sm2}/d.

$$\frac{d_{sm1}}{d} = 0.6577\left(\frac{u}{u_c}\right)^{1.6811}\left(\frac{h}{d}\right)^{0.6281}\mathrm{Fr}^{0.6214}\left(\frac{e}{d}\right)^{0.0248}\left(\frac{l}{d}\right)^{-0.0116}\left(\frac{ut}{d}\right)^{0.0928} \tag{8.10}$$

$$\frac{d_{sm2}}{d} = 0.5506\left(\frac{u}{u_c}\right)^{1.5521}\left(\frac{h}{d}\right)^{0.4504}\mathrm{Fr}^{0.4686}\left(\frac{e}{d}\right)^{0.1834}\left(\frac{l}{d}\right)^{-0.013}\left(\frac{ut}{d}\right)^{0.0911} \tag{8.11}$$

(a) Performance evaluation

This section analyzes the results of the proposed empirical formulas. Figure 8.14(a-d) compares the d_{sm} calculated by MLR and MNLR for the front and eccentric piers. The R^2 values for the MLR models are higher than those for the MNLR models, which indicates that MLR provides slightly better predictions for both piers. This suggests that a continuous interpretation of the dependent variable aligns more closely with the data, particularly when linear relationships are present. Imposing a nonlinear method through MNLR can decrease accuracy when a linear description is more appropriate, as demonstrated in Table 8.4. Additionally, the training method produces higher R^2 values and lower MSE, RMSE, and MBE compared to the testing method for both models.

Since the study uses only 49 data points, the limited variability does not show significant nonlinearity, making the MLR model a better fit. However, with more data, the MNLR formula could better capture hidden nonlinear patterns. A comparison is given in Fig. 8.15.

Table 8.4. Evaluation for MLNR and MLR predictors based on performance indicators.

Prediction method	Pier	Training				Testing			
		R^2	MSE	RMSE	MBE	R^2	MSE	RMSE	MBE
MNLR	Front	0.969	0.012	0.11	0.002	0.935	0.020	0.141	-0.024
	Eccentric	0.943	0.017	0.129	0.001	0.928	0.027	0.166	-0.052
MLR	Front	0.975	0.010	0.098	0.001	0.951	0.016	0.126	-0.037
	Eccentric	0.946	0.016	0.126	-0.001	0.949	0.026	0.160	-0.076

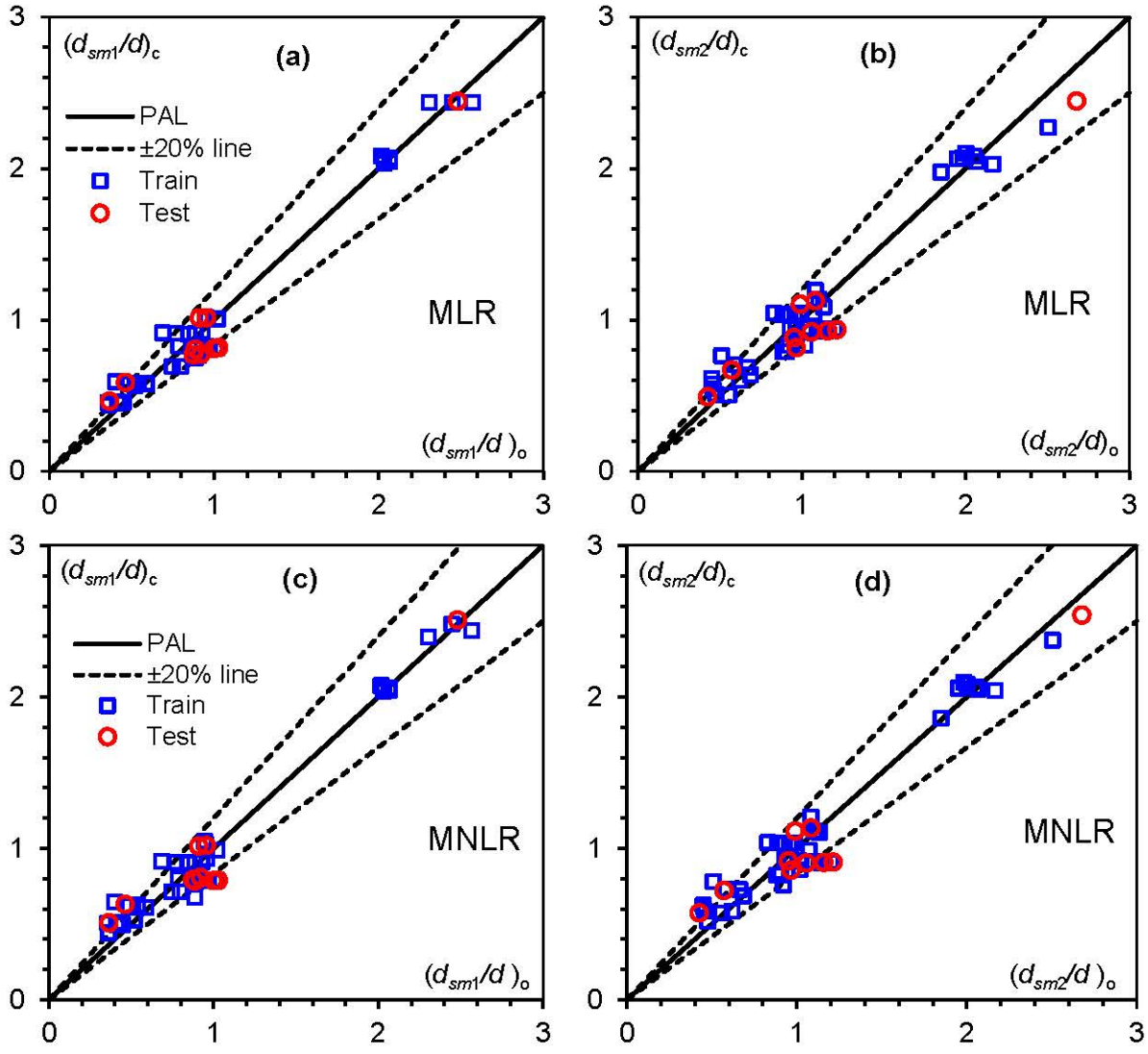

Fig. 8.15. Comparison between calculated and observed d_{sm1} and d_{sm2} by using **(a-b)** MLR formula, and **(c-d)** MNLR formula.

(b) Comparison of new and literature formulas

The measured d_s data are used to compare the newly developed formulas with those proposed in the literature. Figure 8.16 shows the comparison between computed values (from Beg 2004, Das et al. 2016, Khaple et al. 2017, Das et al. 2019, Nandi and Das 2024) and observed d_s data from this study for both eccentric piers. The accuracy of the five literature formulas and the present study is systematically evaluated using various statistical performance indicators.

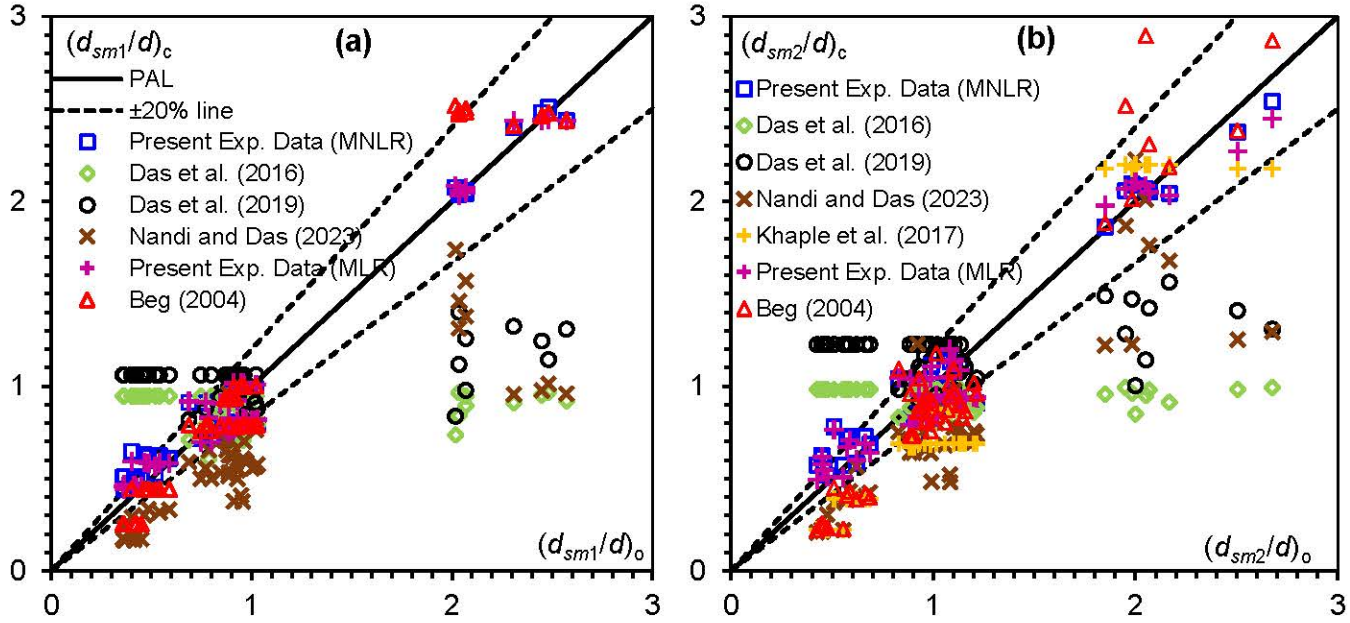

Fig. 8.16. Comparison between proposed and commonly used empirical formulas of various literatures for maximum d_s of **(a)** front pier, and **(b)** eccentric pier.

The newly proposed formulas provide better results than the five formulas from previous literature, each of which is based on limited data. The accuracy of the proposed formulas is more consistent with the collected data. The Fig. 8.16(a) shows that for the front pier, 90%, 76%, 71%, 55%, 47%, and 10% of the data fall within a ±20% error margin for MLR, MNLR, Beg (2004), Das et al. (2016), Das et al. (2019), and Nandi and Das (2024), respectively. For the eccentric pier, 84%, 67%, 49%, 43%, 37%, 25%, and 24% of the data fall within the ±20% error margin for MLR, and MNLR, respectively. Table 8.5 provides a summary of the performance evaluation for single, front, and eccentric piers.

The comparison between the MLR formula and Beg (2004) for the front pier shows a 1.36% increase in R^2, with MSE and RMSE decreasing by 66% and 42%, though MBE is higher for MLR. For the MNLR formula versus Beg (2004), R^2 and MBE increased by 0.52% and 50%, while MSE and RMSE decreased by 56% and 34%. For the eccentric pier, the MLR formula improves R^2 by 2.06%, with MBE, MSE, and RMSE decreasing by 93%, 76%, and 51%. The

MNLR formula improves R^2 by 1.74%, with MBE, MSE, and RMSE decreasing by 95%, 75%, and 50%.

Table 8.5. Overall evaluation of performance indicators of the collected data set of previous literature.

Pier	Reference	Statistical parameters			
		R^2	MSE	RMSE	MBE
Front	MNLR	0.963	0.014	0.117	-0.003
	MLR	0.971	0.011	0.104	-0.007
	Beg (2004)	0.958	0.032	0.178	-0.002
	Das et al. (2016)	0.001	0.398	0.631	-0.137
	Das et al. (2019)	0.200	0.315	0.561	+0.004
	Nandi and Das (2024)	0.714	0.290	0.539	-0.403
Eccentric	MNLR	0.938	0.019	0.137	-0.010
	MLR	0.941	0.018	0.134	-0.015
	Beg (2004)	0.873	0.106	0.326	-0.045
	Das et al. (2016)	0.006	0.332	0.576	-0.158
	Khaple et al. (2017)	0.922	0.076	0.275	-0.199
	Das et al. (2019)	0.137	0.272	0.522	+0.093
	Nandi and Das (2024)	0.728	0.172	0.415	-0.301

Statistically, the MLR formula developed in this study provides the best results, making it the most suitable for estimating d_{sm} for eccentric bridges. The MNLR formula ranks second, with Beg (2004) and Khaple et al. (2017) ranking third for front and eccentric piers, respectively.

However, the limitations of this study include small-scale settings that cannot fully replicate real-world conditions. Each experiment lasted ~10 hours, with the measured d_s reaching a quasi-equilibrium or maximum at the experimented time period. The piers had φ between 21° and 34°. Future research should explore various flow conditions, bed materials, pier shapes, and arrangements, including live-bed scenarios and different attack angles. The interaction of parameters r and $\varphi°$ should also be examined further. Advanced measurement tools can improve understanding of d_s evolution under different parameters.

8.4. Conclusions

Understanding and mitigating the effects of scouring is critical for preserving eccentric piers in two bridge pier arrangements. Few studies have used sediment transport models and semi-empirical approaches to develop formulas for eccentric piers. This study uses data from 49 experiments to validate these formulas, comparing observed and computed maximum scour

depths (d_{sm}) using statistical indicators like MSE, RMSE, MBE, and R^2. The key parameters for interference are transverse spacing (e) and longitudinal spacing (l). Conclusions from the experimental analysis are presented below:

- The key parameters are found h/d, u/u_c, Fr, ut/d, and e/d are influencing d_s around both piers in the eccentric arrangement.
- The minimum d_{sm} for eccentric pier arrangements can guide the construction of safe and cost-effective bridge piers. The minimum d_{sm} front pier (d_{sm1}) is observed at $e = 3.5d$ and $h = 1.65d$, while the maximum d_{sm} for the eccentric pier (d_{sm2}) is 25% higher at the same location. However, minimum d_{sm2} occurred at $e = 2d$ and $h = 1.65d$, with the d_{sm1} being 14% lower at the same position.
- In each arrangement, the single pier (d_{ss}) is used to assess the increase or decrease in d_s for both piers of eccentric arrangements. The lowest scour, suitable for safe bridge design, is found at $e = 2.5d$ and $h = 1.2d$ for the eccentric pier, with a minimum d_{sm2} 94% lower than the maximum d_{sm2} at $e = 2.25d$ and $h = 1.65d$.
- Single-pier arrangements are simpler and environmentally less impactful but may not support all spans and are prone to scour. Eccentric pier arrangements offer better load distribution and stability but increase complexity and environmental impact. The study shows that single-pier arrangements have lower d_s.
- The MLR and MNLR formulas are developed (Eqs. 8.8-8.11) to accurately predict d_{sm} around eccentric piers arrangements. The MLR model outperformed MNLR, with R^2 = 0.941, MSE = 0.018, RMSE = 0.134, and MBE = –0.015.
- Comparing five empirical formulas from the literature, the newly proposed MLR and MNLR formulas showed the best and second-best performance respectively. The formula of Khaple et al. (2017) is the next best for eccentric piers, and Beg (2004) for front piers.

This laboratory study determined the optimum eccentric pier locations by identifying minimum scour in parallel bridge pier models while considering the effects of e, u/u_c, and h/d, Fr. The findings give valuable insights for designers and engineers, enabling the safe and economical placement of new bridge piers alongside existing ones.

References

Amini, A., Melville, B. W., Ali, T. M., and Ghazali, A. H. (2012). Clear-water local scour around pile groups in shallow-water flow. *Journal of Hydraulic Engineering*, *138*(2), 177–185.

Ataie-Ashtiani, B., and Aslani-Kordkandi, A. (2012). Flow field around side-by-side piers with and without a scour hole. *European Journal of Mechanics-B/Fluids*, *36,* 152–166.

Beg, M. (2004). Mutual interference of bridge piers on local scour. In *Proceedings of the Second International Conference on Scour and Erosion, Singapore* (pp. 111–118).

Beg, M., and Beg, S. (2015). Scour hole characteristics of two unequal size bridge piers in tandem arrangement. *ISH Journal of Hydraulic Engineering*, *21*(1), 85–96.

Hannah, C. R. (1978). *Scour at pile groups*. Research Report No. 28–3, Civil Engineering Dept., University of Canterbury, Christchurch, New Zealand.

Chabert, J., and Engeldinger, P. (1956). Etude des affouillements autourdes piles des ponts. Laboratoire d'Hydraulique, Chatou, France (in French)

Das, S., Das, R., and Mazumdar, A. (2016) Comparison of local scour characteristics around two eccentric piers of different shapes. *Arabian Journal of Science and Engineering, 41*(4), 1199–1213.

Das, R., Das, S., Jaman, H., and Mazumdar, A. (2019). Impact of upstream bridge pier on the scouring around adjacent downstream bridge pier. *Arabian Journal for Science and Engineering*, *44*, 4359–4372.

Devi, G., and Kumar, M. (2022). Experimental study of the local scour around the two piers in the tandem arrangement using ultrasonic ranging transducers. *Ocean Engineering*, *266*, 112838.

Fael, C., Lança, R., and Cardoso, A. (2016). Effect of pier shape and pier alignment on the equilibrium scour depth at single piers. *International Journal of Sediment Research*, *31*(3), 244–250.

Franzetti, S., Radice, A., Rebai, D., and Ballio, F. (2022). Clear water scour at circular piers: A new formula fitting laboratory data with less than 25% deviation. *Journal of Hydraulic Engineering*, *148*(10), 04022021.

Hoang, X. (2015). Numerical Simulation 3D of Local Scour around Subsea Caisson Structures in Steady Currents and Waves. In *2015 International Conference on Modeling, Simulation and Applied Mathematics* (pp. 29–32). Atlantis Press.

Khaple, S., Hanmaiahgari, P. R., Gaudio, R., and Dey, S. (2017). Interference of an upstream pier on local scour at downstream piers. *Acta Geophysica*, *65*, 29–46.

Liang, F., Wang, C., and Yu, X. (2019). Performance of existing methods for estimation and mitigation of local scour around bridges: case studies. *Journal of Performance of Constructed Facilities*, *33*(6), 04019060.

Liang, F., Wang, C., Huang, M., and Wang, Y. (2017). Experimental observations and evaluations of formulae for local scour at pile groups in steady currents. *Marine Georesources & Geotechnology*, *35*(2), 245–255.

Liu, Q. S., Tang, H. W., Wang, H., and Xiao, J. F. (2018). Critical velocities for local scour around twin piers in tandem. *Journal of Hydrodynamics*, *30*, 1165–1173.

Malik, R., and Setia, B. (2014). Experimental study on behaviour of closely placed bridge pier models. In *Proceedings of the National Conference in Department of Civil Engineering, National Institute of Technology Kurukshetra, Kurukshetra, India.*

Malik, R., and Setia, B. (2020). Interference between pier models and its effects on scour depth. *SN Applied Sciences*, *2*, 68.

Melville, B. W. (1997). Pier and abutment scour: integrated approach. *Journal of Hydraulic Engineering*, *123*(2), 125–136. Melville, B. W., and Coleman, S. E. (2000). *Bridge scour*. Water Resources Publication.

Monti, R. (1994). Indagine sperimentale delle caratteristiche fluidodinamiche del campo di moto intorno a una pila circolare, Polytechnic of Milan, Milan, Italy (in Italian).

Nandi, B., and Das, S. (2024). Equation for time-dependent local scour at pier-like structures with eccentric in-line arrangements. In *Proceedings of the Institution of Civil Engineers-Water Management*, *177*(6), 361–374.

Raudkivi, A. J., and Ettema, R. (1983). Clear-water scour at cylindrical piers. *Journal of Hydraulic Engineering*, *109*(3), 338–350.

Raudkivi, A.J. (1998). Loose Boundary Hydraulics. A.A. Balkema Publishers, Netherlands.

Richardson, E.V., Simons, D.B. and Lagasse, P.F. (2001). River Engineering for Highway Encroachments - Highways in the River Environment. Federal Highway Administration, Hydraulic Series No.6, FHW A NHI 01-004, Washington, D.C.

Shen, H. W., Schneider, V. R., and Karaki, S. (1969). Local scour around bridge piers. *Journal of the Hydraulics Division*, *95*(6), 1919–1940.

Sheppard, D. M., Melville, B., and Yang, Y. (2023). Local equilibrium sediment scour prediction at bridge piers with complex geometries. *Journal of Hydraulic Engineering*, *149*(4), 04023003.

Sumer, B. M., Fredsøe, J., and Bundgaard, K. (2005). Global and local scour at pile groups. In *ISOPE International Ocean and Polar Engineering Conference* (pp. ISOPE-I). ISOPE.

Wang, C., Yu, X., and Liang, F. (2017). A review of bridge scour: mechanism, estimation, monitoring and countermeasures. *Natural Hazards*, *87*, 1881–1906.

Xiong, W., Cai, C. S., Zhang, R., Shi, H., and Xu, C. (2023). Review of hydraulic bridge failures: Historical statistic analysis, failure modes, and prediction methods. *Journal of Bridge Engineering*, *28*(4), 03123001.

Chapter 9

Overall remarks

9.1. Key findings and recommendations

Scour at bridge piers remains a critical concern for ensuring the stability and longevity of bridges. Different studies have been done on isolated pier scour considering equilibrium conditions. This thesis identifies the promising temporal scour depth (d_{st}) formula and a machine learning technique to predict the maximum scour depth (d_{sm}).

As urbanization drives the construction of new bridges near existing ones, understanding and mitigating the effects of pier interactions becomes increasingly important. The interference of hydraulic parameters, flow patterns, and spacing between piers create complex challenges in an accurate prediction of scour depth (d_s), especially on the two pier groups. This study highlights the need for advanced predictive models, by both traditional semi-empirical methods and modern machine learning techniques, to address the limitations of current approaches. Focusing on comprehensive scour analysis around isolated and two pier groups the following overall remarks can be made:

Firstly, Chapter 3 evaluated 329 data series and over almost ~ 6700 datapoints to measure the accuracy of various formulas to d_{st}. This chapter considers the key influential parameters as flow intensity (u/u_c), flow shallowness (h/d), sediment coarseness (d/d_{50}), constriction ratio (d/W), sediment uniformity (σ), and dimensionless time ($ut/d\Delta^{0.5}$). The finding shows that the formula by Shen et al. (1966) had 21% data lying within the 20% error band which is the lowest among all, while the NCHRP (2011) or Sheppard et al. (2011) formula had the highest at 73%. On average, the error margin for d_{st} predictions across all selected studies was between 31% and 57%. Among the many formulas reviewed, the ones proposed by Melville and Chiew (1999), and NCHRP (2011), remain the most reliable. However, there are challenges in calculating the equilibrium scour depth (d_{se}) and equilibrium time (t_e), to use these formulas. The formula by Franzetti et al. (2022) was noted for initially overestimating d_{st} but later achieving good accuracy within an 80% range. Finally, the new formula derived in this study shows good agreement between calculated and observed d_{st}, outperforming Franzetti et al. (2022) and it simplifies the process by not requiring prior calculations of d_{se} or t_e.

Secondly in Chapter 4, applied advanced methods to 634 data points from 35 different literature sources, developed a robust d_{sm} predictive ensemble model, and compared it to six promising formulas from the literature. The key parameters for predicting d_{sm} are identified as

u/u_c, h/d, d/d_{50}, d/W, σ, $ut/d\Delta^{0.5}$, and Froude number (Fr) through subset regression analysis and KNN. Stochastic Gradient Boosting using Reduced Error Pruning Tree SGB(REPTree), Boosted Regression Trees using Support Vector Machine Regression with Pearson VII Universal Kernel BRT(SVMR-PUK), and again SGB(REPTree) proven top performance when training and testing and overall data set respectively. The formula by Nandi and Das (2023) outperformed the formula from the literature ranking highest in performance indicators across all data sets but gave less performance compared to these ensemble models. Sensitivity analysis shows that σ and u/u_c are the most critical factors for predicting d_{sm} in clear water. Uncertainty analysis highlighted that the SGB(RFR) model had the lowest prediction uncertainty, whereas the formula by Jain and Fischer (1979) had the highest uncertainty. Overall, the study highlights the reliability of machine learning models over traditional formulas, particularly in terms of accuracy and uncertainty in the prediction.

Furthermore, Chapter 5 introduced a novel formula for quasi-equilibrium time (T_e). The parameters affecting T_e are identified as u/u_c, h/d, d/d_{50}, σ, and d/W. The statistical influence parameters in the present time scale formula outperformed those in existing formulas across training and validation. A numerical example demonstrated how to calculate d_{st} as well as d_{sm} using existing formulas from the literature and shows considerable improvement in the estimation of d_s.

Chapter 6 introduces new formulas for predicting d_s around piers arranged side-by-side, in tandem, and eccentrically. For side-by-side piers, the proposed formula is based on key parameters such as u/u_c, h/d, pier spacing (r/d), and $ut/d\Delta^{0.5}$outperformed the existing literature formula. In tandem pier arrangements, key hydraulic parameters are identified as r/d accounting for reinforcing and sheltering effects. The new formula for tandem arrangements outperforms the literature formula. The newly developed formula for d_{sm} *is* influenced by as u/u_c, h/d, d/d_{50}, r/d, flow skew angle ($\varphi°$), and $ut/d\Delta^{0.5}$ for eccentric piers. These formulas demonstrated superior statistical performance compared to the literature. The accuracy of the proposed formulas is assessed by comparing experimental data that lies within ± 20% error band. The side-by-side configuration achieved 100% data falls within this band, while tandem and eccentric configurations exceeded 50% and 65%, respectively. The highest accuracy is noted for the front pier in tandem arrangements, while the rear pier in eccentric arrangements showed the lowest accuracy among the newly developed formula for different arrangements.

Moreover, in Chapter 7, ensemble ML methods like Random Forest (RF) and Extreme Gradient Boosting (XGBoost) and improved scour prediction are found considering two piers are side by side, tandem, and eccentric arrangements across clearwater data. Results demonstrate that RF outperformed XGBoost in both training and testing phases with Random Search cross-validation optimization for both piers using performance indicators. The u/u_c was identified as the most influential variable making the phenomenon highly vulnerable during model training with sequential feature selections (SFS) and SHapley Additive exPlanations (SHAP). PDPs quantitatively depict each parameter the u/u_c shows increasing trends, while d/d_{50}, decreases across models in the considered range which well describes the physical

insights of flow parameters. The φ and r/d match well with the physical insights of such hydraulic parameters. Other parameters do not show a much clearer trend. The recommended ML model for predicting scour is RF-RSCV for Pier-1 and Pier-2.

In addition, Chapter 8 includes an experimental study to find the minimum scour locations in clearwater conditions. The key parameters considered are h/d, u/u_c, Fr, t, and eccentricity (e). The lowest d_{sm} for the front pier occurs when the eccentric pier is located at $e = 3.5d$ and $h = 1.65d$. The lowest d_s for the eccentric pier occur when $e = 2d$ and $h = 1.65d$. Upon considering all pier arrangements in terms of e, the minimum d_s for the safe bridge pier design is found when the eccentric pier is positioned at $e = 2.5d$ and $h = 1.2d$. Based on the integrative data from the literature and this study, the multi-linear regression MLR-based new formula outperformed the multi-non-linear regression MNLR-based formula and all literature formulas for eccentric piers.

9.2. Limitations in the present study

The present study has developed new formulas to predict d_{st} and d_{sm} around isolated piers and d_{sm} arranged side-by-side, in tandem, and eccentrically. These formulas are derived based on a comprehensive analysis of literature experimental data and have shown higher performance compared to the formulas in the literature. Despite these advancements, several limitations should be considered when applying these findings to real-world scenarios.

- The study focuses solely on clear water conditions, both in the development of the formulas and in the experimental studies, limiting its applicability to other flow conditions.
- The ensemble machine learning model used to predict d_{sm} isolated piers was built without tuning hyperparameters, which may affect its optimization.
- A significant limitation is the assumption of threshold observed quasi-equilibrium time (T_e) at 2 days, excluding 90% of the available literature data for estimating quasi-equilibrium time (T_e).
- The accuracy of the proposed formulas for side-by-side and eccentric pier configurations is affected by the limited availability of relevant data and a wide range of hydraulic conditions.
- Only readily available black-box machine learning models are used for d_s prediction, which may limit core advancement in the training algorithm.
- The experimental studies and literature data utilized cohesionless, uniformly graded sand as the bed material, which might not represent more complex sediment conditions.
- The laboratory pier model was installed in an eccentric arrangement with a φ varying between 21° and 34°, which may limit the generalization of findings to other angles.
- The study only considered e ranging from $2d$ to $3.5d$, which could be a limitation in understanding scour behavior across a broader range of spacings.

9.3. Future scopes

The present study has some limitations discussed in the previous sections. However, there are several opportunities for future research to address the above limitations and further enhance the accuracy and applicability of the proposed formulas/models.

- This study may extend considering live bed conditions, as well as incorporating field data to enhance the generalizability of the developed formulas.
- Explore advanced hyperparameter tuning methods to improve the predictive accuracy of ML models for estimating d_{sm} around the isolated pier.
- The present data set can be extended to include a wider range of hydraulic and sediment conditions, which may help to validate the proposed formulas in diverse real-world scenarios.
- Implement more interpretable machine learning models to gain insights into the decision-making process and better understand the factors influencing d_s such as physics-informed deep learning methods that can be used for the same purpose.
- Further investigation to include the effects of different sediment types, including cohesive soils and non-uniformly graded materials, to reflect natural riverbed conditions more accurately.
- Moreover, extensive experiments may be conducted with a broader range of φ and e to obtain a more comprehensive understanding of scour behavior around piers in various configurations.
- Implement long-term monitoring systems for real-world bridge piers to gather data for refining and validating the proposed formulas under different environmental and operational conditions.

BUDDHADEV NANDI

Designation/ Communications	:	**Doctoral Research Fellow,** School of Water Resources Engineering, Jadavpur University, Kolkata– 700032, West Bengal, India.
Nationality	:	Indian
Contact	:	(+91) 9800760156, 8240947390
Email	:	buddhadevn.swre.rs@jadavpuruniversity.in buddhadevnandi95@gmail.com
Website	:	https://sites.google.com/view/b-nandi
WoS Researcher ID	:	ADX-7960-2022
Scopus Author ID	:	57220522364
ORCID iD	:	0000-0002-6320-3556
SciProfiles	:	2726930

Education

2019- Present	***Ph.D. in Engineering*** (Submitted)**.:** School of Water Resources Engineering, Jadavpur University. Proposed Title of Thesis: *Evaluation of Scour around Isolated and Two Circular Piers using Semi-Empirical and Machine Learning Approaches.*
2017-2019	***M.E.*:** School of Water Resources Engineering, Jadavpur University, Kolkata. Subject: **Water Resources & Hydraulic Engineering**, Aggregate: 82.06% (*First Class*). Title of Thesis: *Analysis of Time Variation of Scour around Three Cylindrical Tandem Piers.*
2012- 2016	***B.E.*:** Dept. of Civil Engineering, The University of Burdwan, Subject: **Civil Engineering,** Aggregate: 80.04% (*First Class with Honours*). Project: *Design and analysis of G+4 multi-storey buildings.*
2010- 2012	***Higher Secondary.*:** West Bengal Council of Higher Secondary Education. (*WBCHSE*), Subject: **Science**, Aggregate: 79.2%
2008- 2010	***Secondary.*:** West Bengal Board of Secondary Education. (*WBBSE*), Aggregate: 83.5%

Languages

বাংলা, English, हिंदी.

Additional Qualifications/Skills

GATE	2017(IITR), 2018(IITG)
Software	*CiteNetExplorer*, *CiteSpace*, *VOSviewer* – Bibliometric and scientometrics analysis. *MATLAB* – Machine learning and graphical analysis; *WEKA* – Machine learning algorithms for data mining; *ArcGIS* – Analyze geospatial data, delineate watershed; *Python* – Data analysis and Deep learning; *SPSS*, *Minitab* – Statistical analysis and feature selection; *OriginLab* – Graphical analysis and statistical analysis; *AutoCAD, STAAD.Pro* – Drawings and design; *Inkscape* – Vector graphics editor; *WaterGEMS, EPANET* – Design, and optimize water distribution systems; *HEC-RAS* – Flow hydraulics, Sediment transport; *GeneXproTools* – Data modeling.

Professional Certifications

2023	Mathematics for Machine Learning and Data Science

2023 Machine Learning Specialization

Area of Research Interest

Sediment Transportation and Hydraulics, Fluvial Hydrodynamics, Open Channel Hydraulics, Environmental engineering, Applied Hydrology, Computational Fluid Dynamics, Applied Mathematics, Machine Learning, Deep Learning.

Subject Strength

Fluid Mechanics, Engineering Mechanics, Strength of Material, Applied Hydrology, Irrigation Engineering, Environmental Engineering, Mathematics.

Articles in Journals, Conferences, and Books

Note: * Corresponding author

International Journals

2025 Q1, **Nandi**, **B**., and Das, S*. (2025). Predicting Max Scour Depths near Two-Pier Groups Using Ensemble Machine-Learning Models and Visualizing Feature Importance with Partial Dependence Plots and SHAP. *Journal of Computing in Civil Engineering*, 39(2), 04025007. https://doi.org/10.1061/JCCEE5/CPENG-6150.

2024 Q1, **Nandi**, **B**., Patel, G., Das, S*., 2024. Prediction of maximum scour depth at clear water conditions: Multivariate and robust comparative analysis between empirical equations and machine learning approaches using extensive reference metadata. *Journal of Environmental Management.* 354, 120349. https://doi.org/10.1016/j.jenvman.2024.120349.

2024 Q3, **Nandi**, **B**., and Das, S*. (2024). Equation for localized time-dependent scour at pier-like structures with eccentric inline arrangements. In *Proceedings of the Institution of Civil Engineers-Water Management*, 177(6), 361–374. Emerald Publishing Limited. https://doi.org/10.1680/jwama.23.00006.

2023 Q1, **Nandi**, **B**., and Das, S*. (2023). Identify most promising temporal scour depth formula for circular piers proposed over last six decades. *Ocean Engineering*, 286, 115639. https://doi.org/10.1016/j.oceaneng.2023.115639.

National Journals

2023 Mondal, S., **Nandi, B***. and Das, S. (2023). Evaluation of Water Quality Index to check the Impact of COVID-19 on Water Quality at Gandhighat in Kangsabati River. *Journal of The Institution of Public Health Engineers*, Vol (L1), pp. 5-23.

2022 **Nandi**, **B**., and Das, S*., (2022). Transformative Insights Into Water Distribution Network Modeling and Optimization Through Epanet At Ranibandh and Khatra Blocks in Bankura. *Journal of the Association of Engineers*, India, 92(1-4). Pagination: 11-30.

International Conferences

2024 **Nandi**, **B***., Das, S. (2024). Estimation of Clear Water Maximum Scour Depth At Eccentric Pier Using Light Gradient Boosting Machine and Random Forest Regressor. Presented at the International Conference on Sustainable Materials, Environment and Technologies Under Climate Change Scenario (SMET-2024) (Hybrid Mode), 25th - 27th July, 2024, National Institute of Technology Kurukshetra, India.

2024 **Nandi**, **B***., Das, S. and Chakraborty, D. (2024). Flow Fields around a Cylinder Plate Structure to Harness Green Energy using Vortex-Induced Vibration. International Conference on Green Energy and Sustainable Technologies (ICGEST 2023), 5th -7th January, 2024, NIT Kurukshetra, Kurukshetra, Haryana, India.

2020 **Nandi**, **B***., Das, S. and Mazumdar, A. (2020). Time Variation Analysis of Scour around Eccentrically Placed Three Tandem Cylindrical Piers, *Second ASCE India Conference on*

"Challenges of Resilient and Sustainable Infrastructure Development in Emerging Economies" (CRSIDE2020).

2020 **Nandi**, **B**., Das S.* and Mazumdar A. (2020). Experimental Analysis and Numerical Simulation of Hydraulic Jump, In: *IOP Conference Series: Earth and Environmental Science, 2020 6th International Conference on Environment and Renewable Energy*. (ICERE 2020), Hanoi: Vietnam, 505(1), 012024, 24-26 Feb. 2020. https://dx.doi.org/10.1088/1755-1315/505/1/012024

Chapters

2025 **Nandi**, **B***., Das, S., Paul, S. (2025). Estimation of Clear Water Flow Induced Maximum Scour Depth Using Random Forest and XGBoost. In: *Mukhopadhyay, A., Ghosh, K. (eds) Advances in Thermo-Fluid Engineering. INCOM 2024*. Lecture Notes in Mechanical Engineering. Springer, Singapore. https://doi.org/10.1007/978-981-97-7296-4_6.

2025 **Nandi**, **B***., Das, R., Chowdhury, S., Das, S. (2025). Analyzing Velocity Profiles Around Three Eccentric Inline Submerged Vanes like Sediment Control Structure. In: *Mukhopadhyay, A., Ghosh, K. (eds) Advances in Thermo-Fluid Engineering. INCOM 2024*. Lecture Notes in Mechanical Engineering. Springer, Singapore. https://doi.org/10.1007/978-981-97-7296-4_12.

2024 **Nandi**, **B***., Sasmal, K. and Das, S. (2024). Evolution of Four Formulae Derived Over Five Decades to Predict Temporal Scour at Circular Pier. In: *International Conference on Science, Technology and Engineering*, pp. 131-139. Singapore: Springer Nature Singapore. https://doi.org/10.1007/978-981-99-4665-5_14.

2021 Chowdhury, P*., Das, S., **Nandi**, **B**. and Das, R. (2021). Variation of Clearwater Scouring Geometry at Isolated Structures Obliging in Sediment Shifting. In: *International Conference Sustainable Environmental Engineering and Science*, pp. 45-56. Singapore: Springer Nature Singapore. https://doi.org/10.1007/978-981-99-0823-3_5.

Training/Courses Attended

2025 Course Title: Workshop on Data Science and Technologies: Applications in Atmospheric and Space Sciences – organized by NARL, Gadanki, Tirupati, Andhra Pradesh, India.

2022 Course Title: Physical & Mathematical Modelling of Reservoir and Appurtenant Structures – organized by CWPRS, Khadakwasla, Pune, Maharashtra, India.

2019 Course Title: Hydrodynamics and Sediment Transport in Unsteady Flows (Program Id: IIT/CEP/STC/AQ/2019-2020/CE/300) – organized by IIT KGP, Kharagpur, India.

2015 Training: Vocational Training Under Eastern Railway/Engg. Dept./Malda Divn., the period from 06.01.2015 to 17.01.2015.

Awards /Fellowships/ Projects

2023 Awarded as **Junior Research Fellow** under DST-SERB (SURE Scheme) to work in School of Water Resources Engineering, Jadavpur University, Kolkata, India.

Project Title*: In-situ Pollution Load Assessment of an Ungauged River using Integrated Water Quality and Hydraulic Modelling to Improve Restoration Strategies.*

2021 Awarded **Junior Research Fellow** (JRF) to work in School of Water Resources Engineering under State Government Fellowship Scheme of Jadavpur University, Kolkata, India.

2020 Awarded International **Travel Grant** by the "RUSA 2.0 - Support to Student, Government of India" for presenting a research paper in an International Conference 2020 6th International Conference on Environment and Renewable Energy 24-26 February 2020, Hanoi, Vietnam.

2017 Awarded Graduate Aptitude Test Engineering (**GATE**) fellowship by All India Council for Technical Education (AICTE) during 2017-2019 to study Masters of Engineering in School of Water Rescources Enginneirng, Jadavpur University, Kolkata, India.

Ocean Engineering 286 (2023) 115639

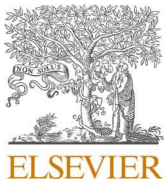

Contents lists available at ScienceDirect

Ocean Engineering

journal homepage: www.elsevier.com/locate/oceaneng

Identify most promising temporal scour depth formula for circular piers proposed over last six decades

Buddhadev Nandi , Subhasish Das *

School of Water Resources Engineering, Jadavpur University, Kolkata, 700032, India

ARTICLE INFO

Handling Editor: Prof. A.I. Incecik

Keywords:
Temporal scour
Clearwater
Compromise programming
CRITIC
Multiple attribute decision-making

ABSTRACT

Temporal scour depth (d_{st}) measurement at bridge piers is a significant issue for application engineers because accurate prediction is required for real-time monitoring. Although several formulas were employed, definitive study is still needed to determine which formula predicts most accurately. Therefore, here, a comparative analysis of d_{st} prediction formulas, at circular piers in clearwater conditions, is performed using laboratory datasets for evolution over 57-years based on seven parameters: sediment coarseness, flow shallowness, constriction ratio, threshold-Froude number, sediment uniformity, relative density, time. Goal is also to select best option that will provide more useful compromise solution concept rather than examining ideal solutions based on inconsistencies. Therefore, useful statistical influence factors are used to perform 11 literature formulas with a newly derived formula in relation to their fitting coefficients. Weightage of each influencing factor is calculated using equal weightage and CRITIC methods. Ranking of each formula is determined using compromise programming. Overall study reveals that NCHRP (2011) formula is still most useful to determine d_{st} if equilibrium scour depth (d_{se}) and equilibrium time (t_e) are known. Melville and Chiew's (1999) formula is very close to NCHRP (2011). But without presuming d_{se} and t_e, the newly proposed formula most accurately predicts the d_{st}.

1. Introduction

Scouring at bridge piers and abutments is the most frequent cause of bridge failures, particularly during flood events. Therefore, local scour at bridge foundations has long caused concern among engineers. When river flow interferes with a vertical obstruction like a bridge pier or abutment, local scouring, an erosion process that occurs near the sediment bed of streams, results in the formation of a three-dimensional vortices system that occurs close to the upstream face of obstructions (Breusers et al., 1977; Breusers and Raudkivi, 1991; Dey et al., 1995; Melville and Coleman, 2000; Dey, 2014) leads to the three dimensional flow separation (Ahmed and Rajaratnam, 1998; Melville and Raudkivi, 1977). Local scour is caused by vortex system-generated shear forces on the bed sediment that are higher than the critical bed-shear stress (τ_{0c}).

In conventional practice, equilibrium conditions are preferred to support overly conservative foundations but temporal conditions are preferred for economical pier construction. The temporal depth of local scour (d_{st}) at bridge piers is calculated using existing formulas, that provide the equilibrium scour depth (d_{se}) and are, therefore, conservative with respect to temporal impacts. The d_{se} is suitable for the live-bed conditions that frequently exist in floods. However, the d_{se} may be excessively conservative in situations where clearwater scour (CWS) conditions exist. The d_{se}, which can take weeks to reach its maximum depth, may represent only a small fraction of the actual d_{se} (Melville and Chiew, 1999).

Due to the considerable scientific interest in the evaluation of d_{st} at circular bridge piers (CBPs), a number of prediction formulas are already available to compute d_{st} (Melville and Chiew, 1999; Shen et al., 1966; Franzetti et al., 1982; Sumer et al., 1992; Sumer et al., 1993; Dey, 1999; Oliveto and Hager, 2002; Oliveto and Hager, 2005; Kothyari et al., 2007; Sheppard et al., 2014; Lança et al., 2013; Choi and Choi, 2016; Aksoy et al., 2017; Franzetti et al., 2022).

Since the pioneering investigations of (Chabert and Engeldinger, 1956; Laursen and Toch, 1956) local scour at CBPs has been the subject of important research for decades over decades. The performances of numerous predictors from the literatures were compared by Vonkeman and Basson (2019), who justified the need for better predictive capabilities, which may also apply to numerical modeling. Experimental investigation was conducted on d_{st} in uniformly layered bed sediments and for steady CWS flow (Chabert and Engeldinger, 1956). Ettema

* Corresponding author.
E-mail addresses: buddhadevn.swre.rs@jadavpuruniversity.in (B. Nandi), subhasish.das@jadavpuruniversity.in (S. Das).

https://doi.org/10.1016/j.oceaneng.2023.115639
Received 15 May 2023; Received in revised form 4 July 2023; Accepted 14 August 2023
Available online 20 August 2023

Evolution of Four Formulae Derived Over Five Decades to Predict Temporal Scour at Circular Pier

Buddhadev Nandi, Krishanu Sasmal, and Subhasish Das

1 Introduction

The interaction of stream flow and a vertical bridge supporting structure which are creating an obstruction to the flow generates erosion of the sediment bed due to complicated three-dimensional flow separation [1]. The transverse resistivity of the soil supporting the foundation decreases substantially with increasing scour depth, resulting in horizontal deflection of the foundation head. The most significant human aspects are: the insufficiency of hydrological data to base flood magnitude estimations for design purposes; the *absence of reliable techniques for estimating scour at bridge piers*; as well as an inability to predict the impact and accumulation of debris against the bridge structure [2]. In front of such obstructions, the flow velocity is less and on the side of the obstruction, the flow velocity increase which reduces the bed shear stress and the sediment lifted by the action of the horseshoe vortex leads the erosion. Most of the widely used empirical formulas for estimating scour depth under clear water equilibrium (CWE) conditions are derived under conditions of extremely long flow periods. Bridge pier footings designed keeping CWE condition, scour depths can offer significantly higher values than when the flow lasts for a shorter period of time. Smaller scour depths can be attained for a limited time to the peak value of the planned flood hydrograph, thus minimizing the total construction costs. As a result, it is critical to investigate the temporal variation of CWE scour. However, time-dependent studies on the local scouring phenomenon are few.

To determine the maximum depth of scour at bridge piers, several computational and laboratory investigations were conducted. But based on these concepts, bridge pier design may not be cost-effective. Thus, the concept of temporal scour depth (S_{dt}) is established. The S_{dt} is a crucial requirement for safe and cost-effective construction of bridge piers [3]. Due to the gradually increasing scientific interest in evaluating

B. Nandi (✉) · K. Sasmal · S. Das
School of Water Resources Engineering, Jadavpur University, Kolkata, West Bengal, India
e-mail: buddhadevnandi95@gmail.com

B. P. Swain and U. S. Dixit (eds.), *Recent Advances in Civil Engineering*, Lecture Notes in Civil Engineering 431, https://doi.org/10.1007/978-981-99-4665-5_14

Journal of Environmental Management 354 (2024) 120349

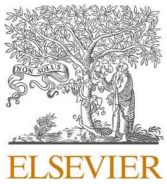

Contents lists available at ScienceDirect

Journal of Environmental Management

journal homepage: www.elsevier.com/locate/jenvman

Research article

Prediction of maximum scour depth at clear water conditions: Multivariate and robust comparative analysis between empirical equations and machine learning approaches using extensive reference metadata

Buddhadev Nandi, Gaurav Patel, Subhasish Das *

School of Water Resources Engineering, Jadavpur University, Kolkata 700032, India

ARTICLE INFO

Handling Editor: Raf Dewil

Keywords:
Clear water scour
Machine learning
Random forest
Support vector regression
Bagging
Boosting

ABSTRACT

Flow obstructed by bridge piers can increase sediment transport leading to local scour. This local scour poses a risk to the stability of bridge structures, which could lead to structural failures. There are two main approaches for evaluating the scour depth (d_s) of bridge piers. The first is based on understanding hydraulic phenomena and developing relationships with properties affecting scour. The second uses data-driven soft computing models that lack physical interpretations but rely on algorithms to predict outcomes. Methods are chosen by researchers based on their goals and resources. This study aims to create innovative ensemble frameworks comprising support vector machine for regression (SVMR), random forest regression (RFR), and reduced error pruning tree (REPTree) as base learners, alongside bagging regression tree (BRT) and stochastic gradient boosting (SGB) as meta learners. These ensembles were developed to analyse maximum scour depths (d_{sm}) in clear water conditions, utilizing 35 literature's experimental data published in last 63 years. The performance of each machine learning (ML) approach was assessed using statistical performance indicators. The proposed model was also compared with top six empirical equations with strong predictive ability. Results show that among these empirical equations, the equation from Nandi and Das (2023) performs best. Performance evaluation considering training, testing, and the entire dataset, SGB (REPTree), BRT(SVMR-PUK), and SGB (REPTree) exhibited the highest performance, securing the top rank among all ML models and empirical equations. Sensitivity analysis identified sediment gradation and flow intensity as the most influential variables for predicting d_{sm} during both training and testing phases, respectively.

1. Introduction

In hydraulic environments, obstructions in streams for bridge piers are susceptible for which sediment being washed away by the rapidly flowing water around them. Unique flow fields form locally around piers, and subsequent flow patterns around such piers are found noticeably different. The presence of such obstructions alters the flow patterns in their immediate vicinity, resulting in either flow contraction, formation of horseshoe vortices upstream of such obstructions, formation of lee-wake vortices downstream of such structures, generation of turbulence or occurrence of reflection and diffraction of waves, occurrence of these changes generally increase the local sediment transport capacity, resulting in scour. Scour can cause hydraulic and maritime constructions to fail. As a result, the stability of the bridge structure may be compromised (Sumer, 2007). *How can scour depth be reliably assessed and what are the competing methods used by researchers?*

Researchers have used two main approaches recently to estimate maximum scour depths (d_{sm}) at bridge piers. The first method involves establishing *functional relationships* by considering physical hydraulic phenomena. Researchers in this group plunge into the hydraulic processes and provide a detailed understanding of the variables affecting the d_{sm}. The second method employs *soft computing models*. These models focus on data-driven approaches without explicitly describing the physical hydraulic processes or providing a clear interpretation of the d_{sm} affecting variables. Instead, they rely on algorithms and data inputs to predict the d_{sm}. Both approaches have their merits, with the former offering a deep understanding of the underlying physics, while the latter leverages computational techniques for prediction. Researchers choose

* Corresponding author. School of Water Resources Engineering, Jadavpur University, Kolkata 700032, India.
E-mail addresses: buddhadevn.swre.rs@jadavpuruniversity.in (B. Nandi), gauravp.wre.rs@jadavpuruniversity.in (G. Patel), subhasish.das@jadavpuruniversity.in (S. Das).

https://doi.org/10.1016/j.jenvman.2024.120349
Received 4 October 2023; Received in revised form 2 January 2024; Accepted 8 February 2024
Available online 24 February 2024

Estimation of Clear Water Flow Induced Maximum Scour Depth Using Random Forest and XGBoost

Buddhadev Nandi, Subhasish Das, and Subhalakshi Paul

Abstract Bridge piers in hydraulic environments are vulnerable to local scour. Water flow causes erosion of adjacent sediment vicinity of the piers leads a risk to bridge structure. This results in unique flow patterns near the bridge piers. Soft computing models that are data-driven and efficient are used by researchers nowadays to predict local scour. A total of 180 data sets from the previous literature over four decades were collected. Ensemble frameworks, such as Random Forest Regression (RF) and Extreme Gradient Boosting (XGBoost), are utilized in this study to compute the maximum local scour depth in clear water flow conditions. As independent variables, there are five input parameters: flow strength, flow shallowness, sediment gradation, sediment coarseness, and dimensionless time were considered. A total of three performance indicators were used namely Coefficient of Determination (R^2), Mean Absolute Error (MAE), and Root Mean Squared Error (RMSE) to assess the effectiveness of these two machine learning models. Three literature equations with high potential have been taken into account for comparison with the current machine learning model about performance indicators. The results of the study show that the XGBoost performs better during the training stage with $R^2 = 0.983$, MAE = 0.066, and RMSE = 0.086, while the RF performs best during the testing scenario with $R^2 = 0.765$, MAE = 0.221 and RMSE = 0.299, The features importance found using XGBoost which indicates that flow intensity to be the most important variable that causes this phenomenon most vulnerable.

Keywords Random forest · Extreme gradient boosting · Scour · Machine learning

B. Nandi (✉) · S. Das · S. Paul
School of Water Resources Engineering, Jadavpur University, Kolkata, India
e-mail: buddhadevn.swre.rs@jadavpuruniversity.in

A. Mukhopadhyay and K. Ghosh (eds.), *Advances in Thermo-Fluid Engineering*,
Lecture Notes in Mechanical Engineering,
https://doi.org/10.1007/978-981-97-7296-4_6

ASCE

Predicting Max Scour Depths near Two-Pier Groups Using Ensemble Machine-Learning Models and Visualizing Feature Importance with Partial Dependence Plots and SHAP

Buddhadev Nandi, Aff.M.ASCE[1]; and Subhasish Das, Ph.D.[2]

Abstract: Assessing scour depth (S_d) near side-by-side, tandem, and eccentric bridge piers is crucial for designing resilient structures. Researchers employed soft computing techniques to enhance S_d prediction models, focusing on ensemble machine learning (ML) methods for isolated piers. However, this research is limited on such two-pier groups, which necessitates a detailed study of how pier spacing and positioning collectively affect S_d predictions. A thorough examination is needed to analyze scouring patterns and the collective two-pier impact on estimating S_d using ensemble ML models. This study employs two ensemble ML models, random forest (RF) and extreme gradient boosting (XGBoost), to collectively predict circular two-pier S_d. Input parameters such as flow characteristics, sediment properties, time, pier gaps, and flow skew angle are rigorously evaluated to assess their combined impact on S_d. Partial dependence plots (PDP) and SHapley Additive exPlanations (SHAP) are used to visualize feature importance and effects on predicting S_d after training ML models, providing insights into individual features' influence on predictions. Performance indicators [coefficient of determination (R^2), mean absolute error, and root mean squared error] assess the ML models' performance. Results demonstrate that XGBoost outperformed RF in training and testing phases with random search cross validation (CV) optimization for both piers. However, RF excelled over XGBoost in training using grid search CV and random search CV for both piers. Flow intensity was identified as the most influential variable, making the phenomenon highly vulnerable during model training with SFS and SHAP. Using ensemble ML models with detailed parameter evaluations and visualizations, engineers can predict S_d more effectively, thus enhancing scouring pattern understanding to design resilient structures. **DOI: 10.1061/JCCEE5.CPENG-6150.** *© 2025 American Society of Civil Engineers.*

Practical Applications: The practical application of this study shows where new bridges are needed next to old bridges for traffic in rapidly populating cities. Bridge piers are placed side-by-side, in tandem, or eccentrically. Scour depth can increase or decrease due to dynamic interference if these piers are not studied properly. This study examines how interference impacts scour depth in various positions and estimates it using an ensemble ML model. This ensemble model accurately predicts scour depth around such interfering piers, which outperforms the classic model. Partial dependence plots show how parameters affect scour depth, considering interference effects. The model shows how interference impacts the scour depth for designing such piers. This model can be used to analyze the impact of such two-pier configurations after integrating the field data for studying field installation effects. Experts and practitioners can utilize the model to improve bridge placements by predicting how pier interference affects scour depth, thus enhancing safety in the design process.

Author keywords: Bridge pier; Maximum scour; Random forest; Extreme gradient boosting (XGBoost); Partial dependence plots; SHapley Additive exPlanations (SHAP).

Introduction

Scouring at bridge piers is driven by changes in flow patterns, increasing local shear stress and dislodging sediment particles from the river bed. The erosion of sediments surrounding bridge piers due to river flow poses a significant risk to bridge stability. Flood-scour-related cases constitute 53% of the total causes of failures (Wardhana and Hadipriono 2003). It is crucial to distinguish between clear-water scour and live-bed scour. The evolution of scour holes over time and the correlation between scour depth and approach flow velocity vary depending on the type of scour (Chabert and Engeldinger 1956). Understanding the flow patterns and coherent structures around piers is essential for comprehending scour development (Das et al. 2013; Dey and Ali 2024; Kalidindi and Khosa 2024). Local scour around groups of piers (cylindrical or other shapes) and flow structures, including reinforcing, sheltering, shed vortices, and compressed horseshoe vortices are crucial for scour pattern and scour depth (S_d) changes (Hannah 1978; Ataie-Ashtiani and Aslani-Kordkandi 2013; Mamoon et al. 2022). Detailed examination of scour patterns under different conditions (ice cover, open flow) on side-by-side piers was studied (Namaee and Sui 2019; Sahu et al. 2023); however, these studies have yet to capture all the complexities of natural river environments. Numerical modeling in

[1]Doctoral Research Fellow, School of Water Resources Engineering, Jadavpur Univ., Kolkata, West Bengal 700032, India. ORCID: https://orcid.org/0000-0002-6320-3556. Email: buddhadevn.swre.rs@jadavpuruniversity.in

[2]Associate Professor and Joint Director, School of Water Resources Engineering, Jadavpur Univ., Kolkata, West Bengal 700032, India (corresponding author). ORCID: https://orcid.org/0000-0002-6512-7454. Email: subhasish.das@jadavpuruniversity.in

Note. This manuscript was submitted on April 27, 2024; approved on September 27, 2024; published online on January 11, 2025. Discussion period open until June 11, 2025; separate discussions must be submitted for individual papers. This paper is part of the ***Journal of Computing in Civil Engineering***, © ASCE, ISSN 0887-3801.

Cite this article
Nandi B and Das S
Equation for time-dependent local scour at pier-like structures with eccentric in-line arrangements.
Proceedings of the Institution of Civil Engineers – Water Management,
https://doi.org/10.1680/jwama.23.00006

Research Article
Paper 2300006
Received 05/02/2023;
Accepted 12/09/2023;
First published online 19/09/2023

Equation for time-dependent local scour at pier-like structures with eccentric in-line arrangements

Buddhadev Nandi ME
Doctoral Research Fellow, School of Water Resources Engineering, Jadavpur University, Kolkata, India (Orcid:0000-0002-6320-3556)

Subhasish Das PhD
Associate Professor, School of Water Resources Engineering, Jadavpur University, Kolkata, India (Orcid:0000-0002-6512-7454) (corresponding author: subhasish.das@jadavpuruniversity.in)

Excess scour developing around tandem and eccentric piers of side-by-side bridges may aggravate bridge failure. Thinking differently, this combination of pier-like structures may increase scour and shift sediments towards the bank, which may help in self-dredging. Therefore, accurate estimation of temporal scour depth (d_{st}) around such piers has a very high priority nowadays. However, little work has been done in this regard. Most of the previous equations predict d_{st} only for an isolated pier. Here, two to three piers are placed eccentrically in line in addition to isolated piers to derive equations empirically for accurate prediction of d_{st} considering circular, triangular and square pier shapes. The present experimental results for an isolated circular pier are validated using equations from the literature, cross-validated with other published experimental data. Predictive equations are proposed for two to three piers with eccentrically in-line arrangements, taking their intermediate spacings as key variables. These equations are established based on dimensional analysis and non-linear regression. Overall analysis reveals that the estimated temporal scour depths based on the proposed integrated equation are closely within the ±80% accuracy band. The proposed equations can be used to predict temporal scour accurately for selected combinations of piers within the given experimental ranges.

Keywords: eccentricity/hydraulics & hydrodynamics/pier/sedimentation/shallow water/temporal scour

Notation

B	pier diameter/width (L)
B_e	effective pier diameter/width (L)
D_{50}	median diameter of sand (L)
d_{se}	maximum scour depth at isolated pier (L)
d_{st}	temporal scour depth (L)
$d_{st\text{-}1f}$	d_{st} at front pier for isolated pier (L)
$d_{st\text{-}2e}$	d_{st} at eccentric pier for eccentric arrangement (L)
$d_{st\text{-}2f}$	d_{st} at front pier for eccentric arrangement (L)
$d_{st\text{-}3e}$	d_{st} at eccentric pier for in-line eccentric arrangement (L)
$d_{st\text{-}3e}$	d_{st} at rear pier for in-line eccentric arrangement (L)
$d_{st\text{-}3f}$	d_{st} at front pier for in-line eccentric arrangement (L)
Fr	Froude number
g	gravitational acceleration (LT^{-2})
H	approach flow depth (L)
L_d	diagonal distance between two eccentric piers (L)
L_o	longitudinal distance between the piers (L)
Re	flow Reynolds number ($= VH/\upsilon$)
Re_p	pier Reynolds number ($= VB/\upsilon$)
S	bed slope
T	time scale (T)
	time (T)
t_e	time to reach equilibrium scour (T)
V	depth-averaged approaching flow velocity (LT^{-1})
V_*	shear velocity (LT^{-1})
V_c	critical velocity (LT^{-1})
V_{*c}	critical shear velocity (LT^{-1})
α	angle of attack
β	correction factor for pier alignment
γ	specific weight of fluid ($ML^{-2}T^{-2}$)
υ	kinematic viscosity (L^2T^{-1})
ρ	mass density of fluid (ML^{-3})
ρ_s	mass density of sediment (ML^{-3})
σ	geometric standard deviation

1. Introduction

When a pier blocks a stream's flow, a scour hole forms locally around the pier. Examples are piers of new bridges, which are usually wide these days, and comprise two piers aligned along the flow to support the structure's loading simultaneously. New bridges constructed parallel to existing bridges also give rise to the complex pier condition studied (Ashtiani and Beheshti, 2006; Das and Mazumdar, 2015; Das *et al.*, 2016; Keshavarzi *et al.*, 2018; Malik and Setia, 2020; Memar *et al.*, 2020; Moreno *et al.*, 2017; Yang *et al.*, 2019, 2020; Yilmaz *et al.*, 2017). Study of complex piers is needed for the safe and cost-effective design of bridges and offshore structures and for mitigating bridge failure. Eccentrically in-line piers can enhance sediment shifting by increasing scour towards the channel bank (Das *et al.*, 2016, 2019; Jaman *et al.*, 2017; Michael *et al.*, 1991).

It is crucial to know how long the local scour near a bridge pier lasts. For time-dependent local scour surrounding isolated piers, only a few equations have been suggested (Melville and Chiew,

Buddhadev Nandi
27.01.2025

Ph.D. Thesis

ORIGINALITY REPORT

6%
SIMILARITY INDEX

PRIMARY SOURCES

1	hdl.handle.net Internet	849 words — 1%
2	Mohammad Khail, Waheedullah. "Açık kanal genişliğinin köprü ayakları etrafında oluşan oyulmalara etkisi", Izmir Katip Celebi University (Turkey), 2024 ProQuest	210 words — < 1%
3	www.researchgate.net Internet	206 words — < 1%
4	link.springer.com Internet	159 words — < 1%
5	discovery.ucl.ac.uk Internet	146 words — < 1%
6	www.cwc.gov.in Internet	145 words — < 1%
7	arcabc.ca Internet	131 words — < 1%
8	Bento, Ana Margarida Lopes Saraiva Alves. "Risk-Based Analysis of Bridge Scour Prediction", Universidade do Porto (Portugal), 2024 ProQuest	125 words — < 1%

Subhasish Das 01 27/01/25

Dr. Subhasish Das
Associate Professor & Joint Director
School of Water Resources Engineering
Jadavpur University
Kolkata - 700032

Rajib Das 27/01/2025

Dr. RAJIB DAS
Assistant Professor
School of Water Resources Engineering
Jadavpur University
Kolkata-700 032

Buddhadev Nandi
27.01.2025